Development and Characterisation of Site-Controlled Quantum Dot Waveguides for Nanophotonics Devices

Chak Lam Chan

A thesis submitted in partial fulfilment of the requirements for the degree of
Doctor of Philosophy

The University of Sheffield
Faculty of Engineering
Department/School of Electrical and Electronic Engineering

April 2024

Abstract

The objective of this study is to investigate the growth and optical properties of positioned InAs quantum dots (QDs) on GaAs (001) substrates, grown by molecular beam epitaxy for nanophotonic applications. The research presents the impact of growth techniques, such as growth interrupt and indium flushing on site-controlled structures, and demonstrates the ability to reduce the size distribution of QDs within a patterned array and control QD emissions with the use of such growth techniques. Low-temperature micro-photoluminescence was used to characterise positioned InAs QDs, including QD occupancy and single dot emissions, excitonic states and fine structure splitting. Site-selected arrays was also presented as a QD map, showing groups of neighbouring QDs with comparable optical properties which could be tuned using stark effect in a doped structure. Following from the successful undoped structures, the growth of doped site-controlled waveguides was presented and successfully fabricated into mesa diodes. With a diode structure, an electric field was applied providing the ability to tune multiple QDs into the same wavelength. In addition, the use of post-growth method to control QD emissions was presented. The use of rapid thermal annealing with different capping methods on InAs/InP QDs was demonstrated and the ability to control emissions wavelength using annealing temperature between 750°C and 800°C with a SiO_2 cap was demonstrated. The QD properties such as integrated PL intensity, wavelength shifting, and FWHM have also been shown to improve after RTA. Low-temperature micro-photoluminescence of the annealed structures showed similar improvements to single QD emissions where wavelength shifting of single dots and reduction to QD linewidths is achieved.

Acknowledgements

I want to take this opportunity to thank everyone who has helped me over this period and to show my appreciation for their continual support during this journey. Thank you, Dr Charlotte Ovenden, as without your enthusiasm and high recommendation to do a PhD, I would not have taken this opportunity and path. A big thanks to my supervisor, Prof. Jon Heffernan, for providing me with this opportunity and the support you have provided over the last few years. It has been a pleasure to have been part of the team.

I am incredibly grateful to numerous people within NEF and the research group. Thank you, Dr Edmund Clarke, for guiding me from the very beginning and putting up with the endless streams of questions and the assistance you have provided through the last few years. A big shout out to the rest of the growth team, Dr Aris Trapalis, Dr Ian Farrer, Dr Akshay Verma, Dr Pallavi Patil, Richard Firth, and Dr Nick Bailey for your support in the day-to-day operations and teaching me about the reactors, characterisation equipment, as well as your wisdom in all manner of things. Thank you to Dr Elisa Sala for providing me with the InP samples for RTA experiments and also for the support in this area of research. Thank you to Dr Paul Fry, for teaching and supporting me in all manners of characterisation and you have been a solid pillar of support when it comes to characterisation. I would also like to thank the physics department, specifically Dr. Dominic Hallett and Dr. René Dost, for the help they have provided on the site-control fabrication and optical measurements.

To my parents, Ka Man Fung and Hoi Yip Chan, and brothers, Anthony Chan, and Alex Chan, thank you for the countless support and love over the years. All of you are my main support pillars that I can always rely on, and always being there when I need it. None of this would have been possible without you all being here with me. Thank you to all my friends and their bad fortune in having to listen to me explain and vent about all the difficult problems I have been having on any particular day, particularly to my oldest friends, Jacob Armer and Harry Kullman, who have treated me like family.

List of publications

C. L. Chan, E. M. Sala, E. Clarke, J. Heffernan, 'Effects of Rapid Thermal Annealing on Telecom C-band InAs Quantum Dots on InP (100) Grown by Droplet Epitaxy'. *Submitted.*

C. L. Chan, A. K. Verma, A. Trapalis, C. Ovenden, D. Hallett, E. Clarke, I. Farrer, M. S. Skolnick, J. Heffernan, 'Demonstration of quantum confinement stark effect on multiple site-controlled quantum dot'. *In preparation.*

Presentation

C. L. Chan, A. K. Verma, A. Trapalis, C. Ovenden, D. Hallett, E. Clarke, I. Farrer, M. S. Skolnick, J. Heffernan, Site-controlled InAs/GaAs Quantum Dot arrays for nanophotonics, UKSemiconductor 2023, Sheffield.

C. L. Chan, A. K. Verma, A. Trapalis, C. Ovenden, D. Hallett, E. Clarke, I. Farrer, M. S. Skolnick, J. Heffernan, Site-controlled InAs/GaAs Quantum Dot arrays for nanophotonics, CMQM 2023, Birmingham.

Poster

C. L. Chan, A. K. Verma, A. Trapalis, C. Ovenden, D. Hallett, E. Clarke, I. Farrer, M. S. Skolnick, J. Heffernan, 'Site-controlled InAs/GaAs Quantum Dot arrays for nanophotonics', QD2024, Munich. *Upcoming.*

C. L. Chan, A. Trapalis, E. Clarke, I. Farrer, J. Heffernan, 'MBE growth and characterisation of indium droplets on GaAs (001) by droplet epitaxy', ICMBE 2022, Sheffield

List of contents

List of contents

I, the author, confirm that the Thesis is my own work. I am aware of the University's Guidance on the Use of Unfair Means (www.sheffield.ac.uk/ssid/unfair-means). This work has not previously been presented for an award at this, or any other, university.

1 Introduction

The concept of quantum computing was first proposed in the 1980s by Richard Feynman [1], but it was not until 2000 that a series of necessary conditions for constructing quantum computing, also known as DiVincenzo's criteria, were proposed [2]. This quickly became an attractive alternative solution when compared to classical computers seen in modern technology [3]. Moore's law [4] predicts that the size of transistors should be halved every two years, but physical limitations are becoming the common roadblocks people cannot bypass. The key difference between classical and quantum computers is the use of quantum bits (qubits), a basic unit where the quantum mechanical phenomena of superpositions are achieved where it exists in both states of 1 and 0 of a classical bit. The benefit of qubits is the potential ability to perform calculations exponentially quicker by taking advantage of the superpositions effect. The principal operation of the qubit and the possible application it can be applied has since gained tremendous development within the research community. One candidate which could act as qubits is quantum dots (QDs), which have already been shown to meet DiVincenzo's criteria as a solid-state qubit [5]. The progression in areas such as fabrication and growth of the QDs in achieving single devices have been promising [6]; however, to realise the actual application of quantum computing requires scalability and repeatability which is the current bottleneck for further progress and optimisation.

The growth of high-quality semiconductor materials can be achieved using a well-established technique also known as Molecular beam epitaxy (MBE). Stranski-Krastanov (S-K) growth mode is a widely accepted method for randomly nucleated QD growth by MBE with various successful implementations towards different applications, including indistinguishable photon pairs [7], single photon purity [8], single-photon source [5], strong coupling [9] and chirality [10]. One challenge in the development of QD applications is the low device yield due to the random positioning of QDs. Although methods such as dot registration [11] have been demonstrated for determining their positions, they lack scalability. This increases the complexity during fabrication and limits the number of QDs that can be used per device (multi-dot applications). One proposed solution is the use of site-control QDs, which produce etched pits for deterministic QD formations. Site-controlled QDs are also formed within patterned surfaces with different markers, allowing easy identification and alignment to the positions and enabling scalability. To date, reports of site-controlled QDs integrated into photonic devices such as photonic cavities [12] and optical resonators [13] have been achieved. However, the use of a patterned surface introduces new challenges, such as maintaining high single QD occupancy within the nanoholes and uniform QD properties across the pattern, including wavelength and linewidths.

1 Introduction

In this thesis, we focus on improving the existing fabrication and growth methods to produce high-quality and deterministically positioned indium arsenide QD on GaAs, suitable for scalable quantum circuits. The ideal characteristics for positioned QD arrays include uniform wavelength emissions, high brightness, and low linewidths. For our intended applications as building blocks for qubit applications, we focus on growth development and optimising of existing techniques such as indium flushing and growth interrupts for waveguide structures targeting 930 nm. At this emission range, devices produced from this structure are suitable for existing characterisation equipment, requiring no changes in optical setup for characterisation. Chapter 2 provides background information on III-V semiconductor QDs, the growth of QDs with molecular beam epitaxy with a specific focus on site-controlled growth and suitable post-growth methods for tuning and controlling QD emissions. Chapter 3 details the type of processes and methods used for the fabrication and growth of site-control QDs and the characterisation equipment used to facilitate site-controlled InAs/ GaAs growth and InAs/InP QDs. Chapter 4 delves into growth optimisation and characterisation of site-controlled QD growth in an undoped waveguide structure. Focusing on the implementation of growth techniques such as growth interrupts and indium flushing, with analysis on the ability to control QD properties. Chapter 5 uses the optimised growth structure for undoped waveguide structures and characterises single dot emissions within an array. Here, we discuss the installation of a high precision positioning stage and the array selection process to identify suitable QD arrays for device fabrication, followed by an initial analysis of single dot properties such as fine structure splitting, exciton-biexciton excitation and present a series of neighbouring QD positions with comparable emission suitable for device fabrication. Chapter 6 develops growth on doped site-control waveguide structures to allow for electrical tuning and excitation. With the doped structure, lack of planarisation was also investigated, with different parameters which would impact the planarisation presented. A successful growth attempt and characterisation of a doped site-control waveguide in a diode structure followed this. The use of quantum confinement stark effect to tune multiple dots within an array in the same wavelength is achieved. Lastly, Chapter 7 explores the possibility of rapid thermal annealing as a post-growth method for tuning single QDs on InAs/InP structures. Room temperature and low-temperature photoluminescence are presented, detailing the effects of rapid thermal annealing on ensemble and single dot emissions.

2 Background

Over the last few years, III-V semiconductor quantum dots (QDs) have seen big leaps and advancements due to their potential to produce indistinguishable photon pairs and achieve entanglement. This chapter introduces epitaxial QDs, how such structures are formed, and advanced techniques such as site-control employed to create deterministic positioned dots. The material properties of III-V semiconductors, including their crystal structure and different types of low-dimensional structures, are also detailed. Lastly, post-growth methods for tuning optical properties are explored.

Zinc blende structure

A sphalerite or zinc-blende form is a standard crystal structure of III-V compound semiconductors, including GaAs and InP, as shown in Figure 2- 1. This is the same as a diamond structure, except the structure is made up of two different atoms instead. In a unit cell, this consists of a face-centred cubic structure where an arsenic (phosphorus) atom is bonded to 4 gallium (indium) atoms. Repeating the unit cell forms the crystal structure comprising rich gallium or arsenic configurations, which are favourable for unbonded electrons. Due to the electron configuration, the unbonded electrons energetically favour the arsenic atom over the gallium atoms. This changes the band structure on a GaAs structure and lattice distortion, otherwise known as band bending [14]. At the surface of the structure, the rich gallium or arsenic configurations can form reconstructions, which are used during epitaxial growth by Reflection High-Energy Electron Diffraction (RHEED) to determine layer formation. The lattice constant, a, is defined by the length of a unit cell, where a_{GaAs} = 5.65 Å and a_{InAs} = 6.058 Å, resulting in a ~7.2% lattice mismatch allowing the use of Stranski-Krastanov (S-K) growth mode for QD formation (discussed later).
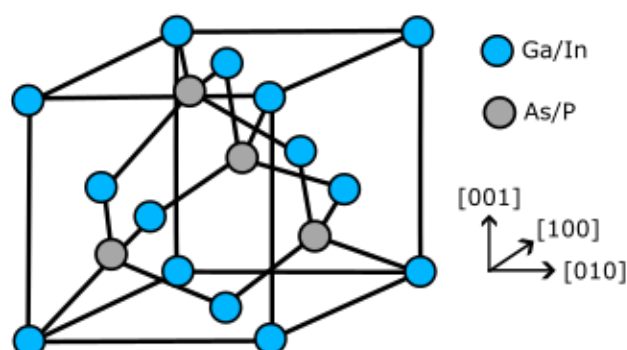

Figure 2- 1 A 3D representation of the unit cell of GaAs or InP, showing the configuration of arsenic (phosphorus) atom bonded to 4 gallium (indium) atoms.

Low dimensional structures/ III-V Quantum dots

When the confining area of carriers are similar to the de-Broglie wavelength, the confinement of carriers can be defined by:

$$\lambda = \frac{h}{p} = \frac{h}{\sqrt{3m_{eff}k_b T}}$$

Where p is the momentum, h is the Planks constant, m_{eff} is the effective mass of the carriers, k_b is the Boltzmann constant, and T is temperature. The different levels of DOS with varying degrees of dimensionality are shown in Figure 2- 2. The level of confinement of electrons determines the density of states (DOS), where bulk material has no confinement and results in a continuous energy level compared to three-dimensional confinement (0D structures) produces discrete energy states. QDs are an example of 0D structures achieved by surrounding InAs QDs with GaAs (or InP).
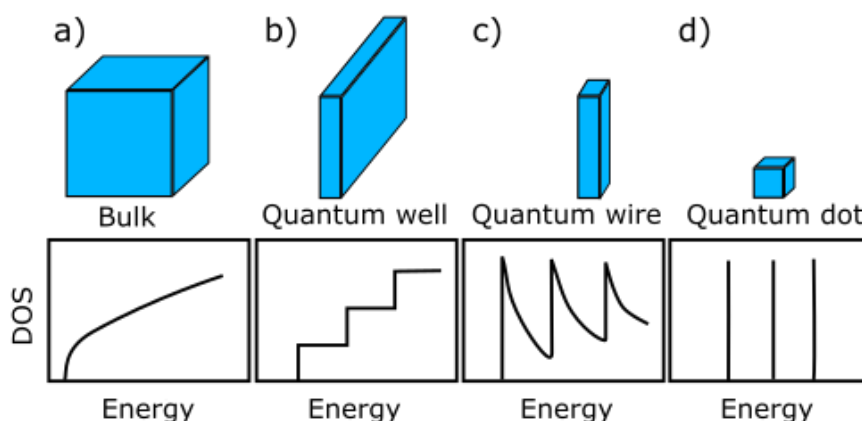

Figure 2- 2 The density of states (DOS) for a range of confinement directions: (a) bulk, (b) quantum well, (c) quantum wire, (d) quantum dot. As each state is reduced, the confinement increases up to the quantum dot, where confinement is in 3 dimensions and produces atomic-like energy levels (delta function)

QDs are typically referred to as artificial atoms due to their atom-like properties, such as discrete energy levels [15]. With its unique properties, particular interest towards incorporating them into various devices, such as single photon emitters [16], lasers [17], quantum relays [18], and solar cells [19], has been investigated. When visualising QDs emissions, it can be simplified into a two-level system consisting of a single ground state and a single excited state, as shown in Figure 2- 3. An excited emission is generated when an electron is promoted to the excited state, and it maintains in this state until spontaneous emissions occur. This is otherwise known as electron-hole recombine, resulting in a photon emission (hv) where the energy emitted is the difference between the ground state and excited state—such emission results in a population decay rate that determines the QD's lifetime. The QD's bandgap is dependent on QD's size, where smaller dots have big band gaps, while large dots have smaller band gaps [20]. The QD composition and strain environments also play essential roles in QDs

band energy [21]. For photonic devices, controlling the emissions is important thus, the controlling of QD size, shape and compositions is critical towards realising ideal QDs for nanophotonics. Therefore, QDs need to have high uniformity with low defect content and sufficiently deep localising potential [22].
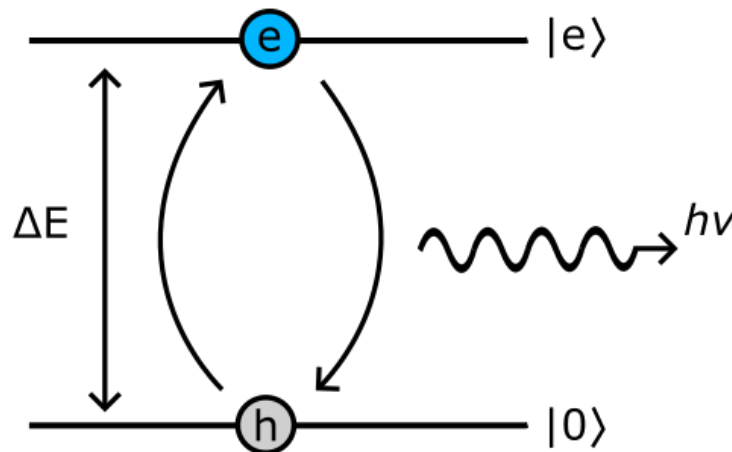

Figure 2- 3 A simple example of a two-level system of exciton formation and relaxation, emitting a photon in a QD, where ΔE is the band gap, hv is the photon energy, |0⟩ is the ground state, and |e⟩ is the first excited state of the QD.

QD's optical properties are also affected by the surrounding environments, including defects and contamination. Introduced during growth, these negatively impact emissions by introducing charge traps, otherwise known as charge noise, which cause the broadening of emission linewidths [23]. The asymmetric shape of the QD also broadens the emission linewidth and is an unwanted property for quantum applications as it produces large fine structure splitting (FSS) [24].

Quantum dot transition

When sufficient energy is provided this results in a transition where an electron-hole (e-h) pair is generated from a QD. When the e-h pair recombines under relaxation, this will generate a photon emission which is equal to the bandgap of the QD, also known as an exciton. Within this single type of exchange a series of charge state can also be produced within the QD. Figure 2-4 shows a range of possible configurations and corresponding polarisation of emitted photons. When an exciton interacts with the surrounding charge this ultimately forms charged excitons called trions. Trions are configurations which composes of two identical Fermi particles bounded by Coulomb forces and on the third particle it possesses a charge which is equal in magnitude but opposite in charge. If the bound e-h complexes involve two electrons and a hole , this is a trion X^-, while if its two holes and an electron, then this is a trion X^+.

The electrostatic forces of the e-h pair when confined into the dot leads to a binding energy associated with the formation of biexciton, or in this case of two e-h pairs. These excision complexes are thus

equivalent to a hydrogen atom or more complex molecules and ions. The biexciton state decays by the recombination of a single pair with the emission of a single photon, transitioning to a single exciton state. Further decay occurs by the emission of another single photon, and this process is otherwise known as the biexciton-exciton cascade. In the biexciton states, there are the two excited electrons with a spin quantum number of $m_z = \pm 1/2$ and the heavy hole state of $m_z = \pm 3/2$. In an ideal condition, this results in perfectly entangled photons and indistinguishable photon pairs; however, variables such as asymmetrical QD shape and the anisotropic piezoelectric potential are introduced during QD formation [25]. This degrades entanglements due to introduction of a fine structure splitting (FSS) between the different possible spin states in the biexciton cascade process. This is caused by small energy difference between the asymmetrical interaction between the spin of the electron and the magnetic field produced by the orbital motion of the electrons. Figure 2- 4 When FSS is sufficiently large, photons produced by the QDs are not indistinguishable, making them unsuitable for quantum applications which require high indistinguishability [26] [27]. To reduce FSS, various growth optimisation and growth techniques can be employed to produce more symmetrical QDs [24] [28].

State name	Charge config	Quantum state	Linear Transition
Biexciton		$\lvert XX\rangle$	
Negative trion		$\lvert X^-\rangle$	
Positive trion		$\lvert X^+\rangle$	H
		$\lvert Y_b\rangle$	V
Exciton		$\lvert X_b\rangle$	
		$\lvert Y_d\rangle$	
		$\lvert X_d\rangle$	H V
Electron		$\lvert g\rangle$	
Hole		$\lvert g^+\rangle$	
Ground state		$\lvert g^-\rangle$	

Figure 2- 4 The electronic configuration of a QD in a range of confined states for electron (blue) and holes (red). The biexciton may decay to one of two bright exciton states by emission of a horizontal or vertical polarised photon.

Quantum dot growth

Semiconductor QDs are nanoscale materials which are only a few orders of magnitude larger than a typical atomic radius. These clusters are composed of 10^2 to 10^5 atoms, which are sufficiently small to provide confinement of electrons and holes in three dimensions. The wave functions and energies of the quantum confined states are adjusted by changing the size, composition, and shape of a QD. The formation of semiconductor QDs is typically formed by epitaxial growth. This has the benefit of being able to integrate into high-quality crystalline heterostructure structures, which enables the fabrication of electrical and optical devices. The material structures that have been investigated include InAs QD on GaAs [29] [30] and InP [31] [32]. The combination of materials is ideal for different applications and emission ranges and introduces different challenges during growth due to the material properties. One main difference is the lattice mismatch between InAs to GaAs (~7%) and InP (~3.2%), resulting in a difference in strain field when depositing InAs, thereby changing the critical thickness required for QD formation. Figure 2- 5 illustrates the band gap as a function of lattice constant for a variety of III-V materials.
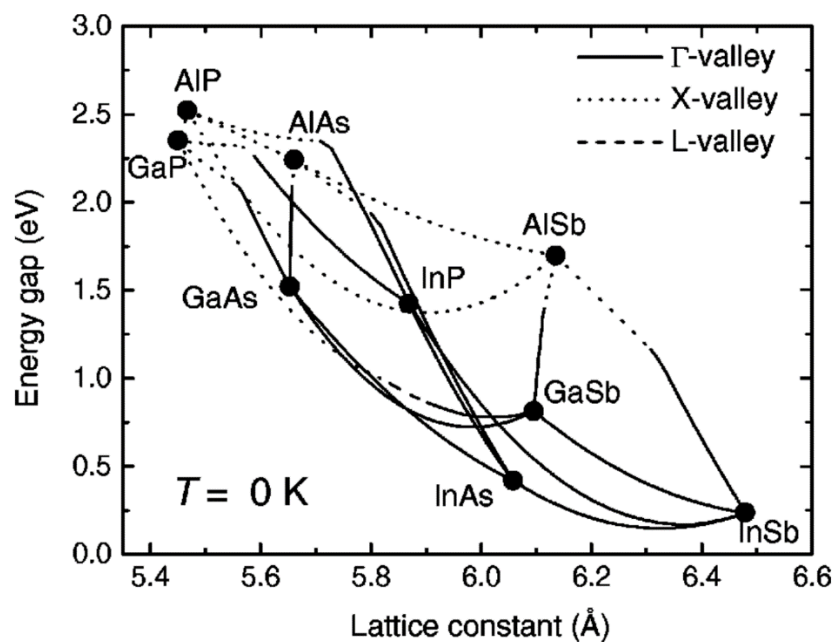
Figure 2- 5 Lowest forbidden gap as a function of lattice constant for non-nitride III-V at zero temperature. The materials with Γ-, X-, and L-valley gaps are indicated by solid, dotted, and dashed lines, respectively. Reprinted with permission from the author, I. Vurgaftman, J. R. Meyer, L. R. Ram-Mohan; Band parameters for III–V compound semiconductors and their alloys. J. Appl. Phys. 1 June 2001; 89 (11): 5815–5875. https://doi.org/10.1063/1.1368156 [14]

To form QDs in semiconductor materials, Molecular Beam Epitaxy (MBE) is a commonly used technique for epitaxial growth in an ultra-high vacuum (10^{-11} Torr) environment. This, combined with the use of effusion cells to generate molecular beams of group III and group V atoms from solid

material, allows precise compound crystalline layers to be deposited in the scale of monolayers. For InAs/GaAs QD structure, temperatures of 580°C to 640°C are typically used during growth. The use of the S-K growth mode in MBE allows for self-assembled QDs by taking advantage of lattice-mismatched at the interface between two materials to achieve high-quality and dislocation-free QDs. More details regarding the functionality of MBE can be found in Chapter 3. To form deterministically positioned QDs, the growth of site-controlled QD is investigated by molecular beam epitaxy (MBE) using Stranski-Krastanov (SK) growth mode for form QDs.

Growth modes and Stranski-Krastanov QDs

For epitaxial growth with MBE, typically, this can be defined into three different growth modes, which is illustrated in Figure 2- 6. Frank Van der Merwe (FM), also known as layer-by-layer growth, is used when depositing lattice-matched materials [33]. One example of this growth mode is GaAs depositing on GaAs substrate. Volmer-Weber (VW), known as island growth, occurs if the deposited atoms are strongly bonded to each other rather than the substrate. Due to lattice mismatching, these clusters of atoms nucleate before growing into 3D structures in the form of islands. One example of islanding is droplet epitaxy, first presented in 1991 by Koguchi et al [34]. This method first deposits group III material, such as gallium or indium, onto the substrate in the form of metallic droplets. These droplets are nano-size structures which have high surface tension and are controlled by diffusion across the surface. When exposed to high pressure of group V atoms, the droplets are then crystallised to form QDs. By controlling different growth parameters such as temperature [35] [36], control of arsenic [37] and deposition amount [38], the size and shape of droplet epitaxy QD can be controlled [39] [40] [41].
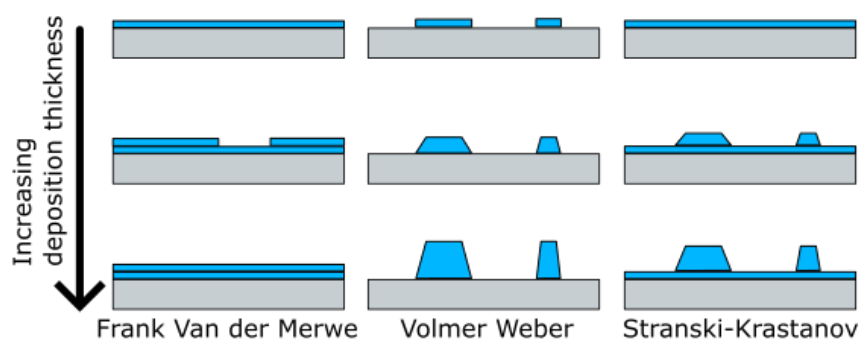
Figure 2- 6 Different types of growth modes, Frank Van der Merwe (Layer-by-layer), Volmer Weber and Stranski-Krastanov (S-K) and the layer formation with increasing deposition amounts.

Lastly, the S-K growth mode also makes use of lattice mismatch between the QD material and substrate. Figure 2- 7 shows an AFM image of an uncapped InAs QD grown by S-K growth mode on a GaAs substrate. Initially, the S-K growth mode deposited material layer-by-layer where strain energy builds up. With more material deposition, this continues to build up until the critical thickness, which is determined by the lattice mismatch between the QD material and buffer layer. At this critical

thickness, the surface has built up sufficient strain that the surface cannot accommodate more strain elastically [42]. Further deposition of the surface will cause the surface to release this strain in two ways: either generating misfit dislocation on the surface [43] or the ideal scenario where 3D islands are formed. S-K growth mode differs from droplet epitaxy, as this formation of QDs forms 2D wetting layers in the process of forming 3D islands due to the strain build-up from layer-by-layer [44]. Similar to droplet epitaxy, by controlling the temperature [22], deposition rate [45], and deposition amount [20], it is possible to control the size [19], density [46], and shape of the QD [47].
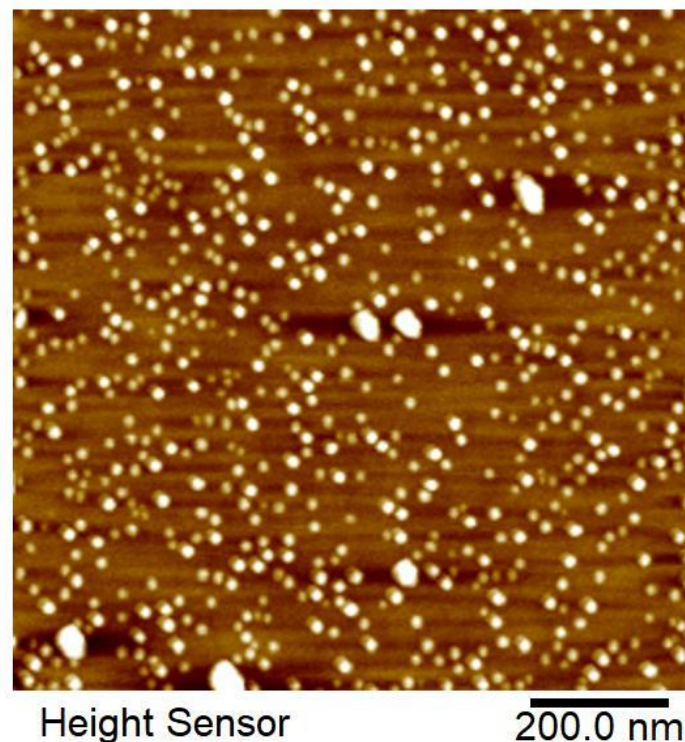
Figure 2- 7 An example of a 1 x 1 μm² AFM image of an InAs/GaAs quantum dots grown by molecular beam epitaxy (MBE).

QD growth by MBE

Molecular beam epitaxy is an epitaxy method which excels in thin-film depositions; therefore, planar surfaces produced with this method often have exceptionally low roughness. For self-assembled QD, this has been vastly reported on, mainly focused on MBE growth where controlling various parameters, including growth temperature [22], growth rate [45], growth interrupt [48, 49], and amount of material deposited [20]. These conditions can be optimised and control different QD properties, including QD density [47], volume [20], emissions intensity [22], and ensemble linewidth [50]. For different applications, different limitations can be imposed during growth due to device limitations. This includes but is not limited to complex structures, reactor limitations, or specific structural requirements. Therefore, understanding the effects of the different growth parameters on QD properties is important for optimisation [7] [21].

One objective is the improvement of site-controlled QD growth to be applied to quantum applications. For waveguide applications, a total structure thickness restriction of 170 nm is imposed for site-control waveguide structures as this is optimised for 930 nm emission wavelengths [51]. The QD is positioned in the centre of this structure with a thick sacrificial layer underneath, which can be removed during device fabrication. With a thin structure, this introduces a series of challenges, one example being low linewidths (sub 10 µeV) QDs. This limits the number of growth techniques that can be used to improve QD uniformity. Low QD linewidths results in small FSS, which is key for indistinguishable photon pairs [7] [52]. Literature has reported on the effects of different patterned surface in achieving uniform height distribution [21] [50], an important feature for FSS as highly uniformity QD shape reduces FSS [24] and use of other growth conditions can also be used to improve this further [47]. Seguin et al, reported on the size-dependent effect of FSS on self-assembled InAs QDs on GaAs where varying the size of the QDs, FSS can be controlled between 520 µeV and 80 µeV [53]. These results are also complemented with model calculations using the eight-band **k·p** theory to rule out the large FSS caused by the elongation of the QD shape. Other optical properties that QD size controls, including emission wavelength and intensity, are also crucial properties to improve and have been reported to be controllable by altering the size of QDs [54] [55] [56].

Additional techniques that can be employed to control QD size includes indium flushing [57] and stacked QD structure [58]. Partial capping involves modifying the QD shape where a thin buffer layer is deposited after the QD layer, followed by indium flushing. This controls the height of the QDs to the thin buffer layer and has been reported to contribute to highly uniform QD shape [57]. By controlling the indium flushing temperature, shifting of wavelength emission and improvement of FWHM can be achieved [32]. Similar results can also be achieved by controlling the thickness of the thin buffer layer thickness between 1.4 nm to 5.6nm [57] [59]. When the thin layers are used in a stacked QD structure, the first layer of QD deposition acts as the seed layer, and the position of these QDs in this layer help localise the position of the subsequent QD layers [20]. Precise control of the thickness of the buffer layer in the stack enables subsequent QD layers to be stacked on top of each other with high precision [21] [60]. The repetitive ordering of thin layers, followed by the QD layer also have other benefits such as an improvement in optical properties. By controlling the number of stacks of QDs and the buffer layer thickness, QD brightness and low linewidths can be achieved [32] [61] [62] and have an impact on the electrical properties of the QDs in doped structures [63]. With additional stacks of InAs QDs within the stack has also demonstrated to cause redshifting of wavelength emission due to the increased amount of indium deposited across the stack structure [61] [64]. To achieve a specific emission wavelength, a balance is required between the number of layers and the total indium deposited. This method is commonly used in site-controlled QD growth as vertical strain tuning of the

stacked QDs helps maintain the positioning of the QDs within the pattern and allows for a thicker structure to be grown on a patterned substrate [63] [65] [66], however this is unsuitable for waveguide structure where thickness limitation are imposed.

Site-controlled QD growth

Site-controlled QDs produce deterministic positioned QDs with the use of a patterned substrate during growth. This consists of predefined QD nucleation points with low surface potential in the form of etched pits, thereby becoming preferential nucleation sites. This encourages indium to migrate from the planar surface towards the etched pits, increasing the growth rates within the nanohole compared to the rest of the surface [67]. These nucleation sites are a series of etched pits consisting of numerous step edges, which reduce the strain energy and the surface free energy of the QD [55] [68]. The formation of the etched pits and other features of the pattern can be fabricated through a series of methods, both in-situ [69] and ex-situ [70] of the MBE reactor. In this study, the patterned substrate is produced using an ex-situ method involving e-beam lithography (EBL) and inductively coupled plasma-reactive ion etching (ICP-RIE). To produce a patterned substrate with this method, a photoresist is applied to the substrate, where a pattern can be developed using EBL. The pattern can then be developed and etched with the use of an ICP-RIE, which is a dry etching process. A series of cleaning steps are then used to remove the residual photoresist and other contaminants by solvent and acid cleaning. Full details on the fabrication of the patterned substrate will be discussed later in 3 Methods.

The advantage of dry etching with ICP-RIE is the quick processing speed when forming the etch pits while still maintaining good control over the depth and diameter of the nanohole by controlling the conditions of the plasma power and duration [71]. The etched pits are formed with sharp step edges, which increases the strain energy at the step interface [55] [68]. Using ex-situ methods to generate a patterned substrate also introduces contamination from the chemicals used and oxide formation when exposed to air, which must be removed with the cleaning process. These unwanted contaminants impact the optical properties by broadening emission linewidth and increasing non-radiative recombination [72] [73]. One solution to mitigate these issues is the use of a thick buffer and improve optical properties by being further away from the contaminated surface. This has a limited effect when designing waveguide structures due to the thickness limitation to achieve a specific wavelength emission [51]. On the other hand, in-situ methods mitigate these issues as no organic resist or cleaning chemical is used to form the pattern surface. Regardless of the method used, the formation of nanoholes still causes damage to the substrate surface, which will impact QD formation [74].

Another aspect to consider when growing on pattern substrates is controlling the planarisation of the nanoholes. This is a control between maintaining the preferential nucleation points generated from the pattern for QD growth but still producing a planar sample after all the layers are grown. Figure 2-8 shows a simple diagram of a typical site-controlled growth structure. With the growth rate within the nanohole being greater than the growth rate on a planar surface, understanding the parameters which control the infilling of the etched pit is important. Depositing materials after the patterning process will change the nanohole shape and size, including the elongation along the [1-10] orientation [55] [75]. The nanohole profile controls the nucleation of QD and the overall size and shape of the QDs, which impacts QD properties [76] [77].
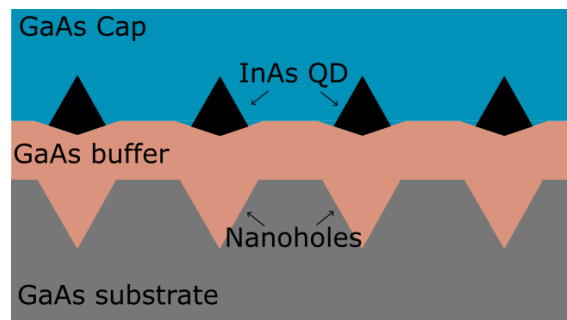

Figure 2- 8 A simple diagram of the site-control growth structure, showing the different interfaces during different stages of the site-control process and growth.

The etched pit produced can vary from parabola-shaped [75] to pyramidal-shaped [78] and the different nanohole shape is formed through different methods and substrate types providing different advantages. Pyramidal-shaped nanoholes have well-defined facets and are symmetrical due to their shape, which produces QDs with low linewidths. From the literature, these nanoholes can produce QDs with FSS as low as 5 μeV and with QD linewidths of 18 μeV [79] [80]. The formation of pyramidal-shaped nanoholes is only reported on GaAs (111) B substrates, which have lower growth temperatures when compared to self-assembled QDs [69] [81]. Despite this advantage, the fabrication of pyramidal-shaped nanoholes is limited to GaAs (111) B due to the difference in surface orientation and cannot be replicated on GaAs (001). Instead, parabola-shaped nanoholes are the standard nanohole shapes formed in GaAs (001) and are easily formed through different etch methods; the most common methods include wet chemical etching [76] or dry etching [70]. The QDs deposited under these fabrication conditions have also been successful, with linewidths of 6 μeV to 50 μeV achieved depending on the structure grown [78] [82]. The nanohole enlarges during growth because of anisotropic surface migration dynamics of GaAs during the buffer layer growth [68] [73]. However, the enlargement is not uniform on all sides and typically elongates more in one direction, which depends on the crystal orientation of the substrate. For GaAs (001), elongation of up to 10% along the [110] crystallographic direction has previously been reported [75]. The impact of increasing the nanohole

sizes on QD occupancy within nanoholes is shown in Figure 2- 9. Controlling the density of QDs in nanoholes is crucial for single-dot occupancy, and the depth of a nanohole plays a significant role in achieving this [70]. The inadequate depth of nanoholes reduces the nucleation of QD within nanoholes and increases the density of random nucleated QDs [83].
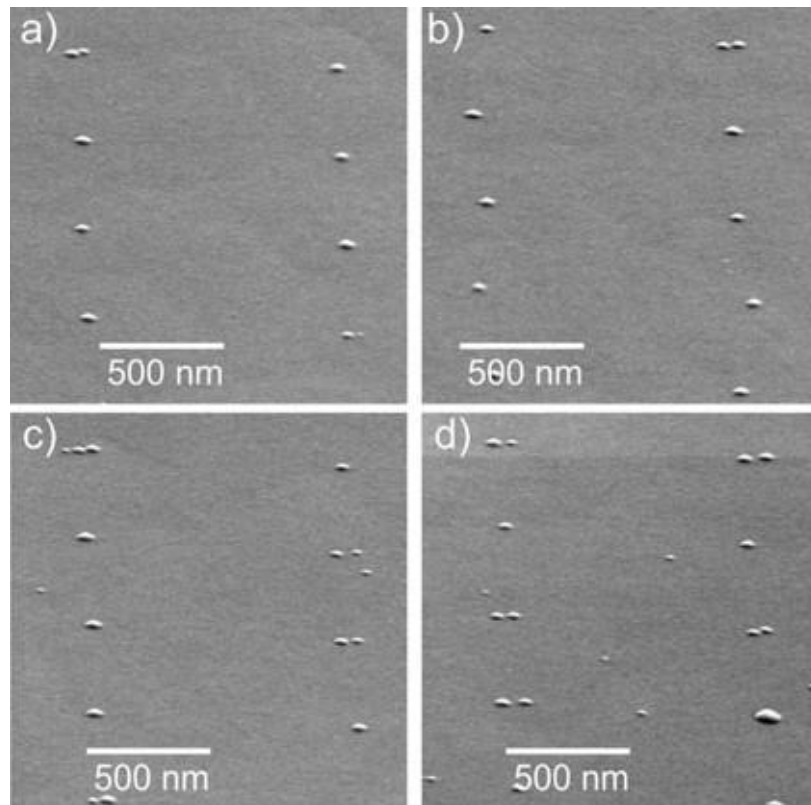
Figure 2- 9 SEM image of SCQD morphology dependent on the nanohole size, showing occupancy with multiple QDs per nanohole is increased for larger nucleation centres (from a to d). Reprint with permission from the author, Schneider, C., Huggenberger, A., Gschrey, M., Gold, P., Rodt, S., Forchel, A., Reitzenstein, S., Höfling, S. and Kamp, M. (2012), In(Ga)As/GaAs site-controlled quantum dots with tailored morphology and high optical quality. Phys. Status Solidi A, 209: 2379-2386. https://doi.org/10.1002/pssa.201228373 [68].

Kiravittaya et al, reported on the indium diffusion rate on a patterned surface, and evidence that nanoholes are the preferential nucleation sites [76]. With sufficient time to diffuse across the pattern surface, this increases QD occupancy by allowing indium to occupy neighbouring nanoholes. However, such long migration of indium across the surface can also result in indium desorbing. Depending on the amount deposited, single dot occupation can be achieved. Literature has presented crystallisation of InAs QDs within a patterned substrate with InAs amount varied between 1.2 ML and 2.0ML [84]. With 1.2ML InAs deposition, this results in the bimodal formation of QDs and subsequent increase in InAs deposition, the bimodal QDs merge into a single large QD and are positioned in the centre of the nanohole. When depositing InAs at high temperatures, desorption of InAs and intermixing with the adjacent layer are important mechanisms in QD nucleation [68]. This changes the composition of QDs and, when combined with the preferential diffusion of indium to the holes, impacts the total amount

of InAs needed for QD formation [85]. Under these conditions, a 13% reduction of the critical thickness has been reported when compared to nucleation on a planar surface [21] [70]. For SCQD growth, the growth temperature used is generally lower than conventional planar surface growth, with values ranging between 470°C to 530°C to prevent damage to the pattern [70] [86]. For self-assembled QD growth temperatures, values of up to 600°C can be used as this does not damage the surface [32]. A study on local anodic oxidation patterned QDs with varying growth temperatures has been reported [87]. The size and shape of the QD within an etch pit can be adjusted by controlling the growth temperature between 460°C to 520°C. In addition, the QD height and width can be tuned by increasing the growth temperature, with the height ranging from approximately 1 nm to 60 nm.

Various methods can be employed to form a patterned surface: EBL in combination with dry etch [12] [70] [88] and wet chemical etch [78] [82] are ex-situ methods previously discussed. Other methods include local anodic oxidation [75] [89], in-situ laser interference patterning [69], and focused ion beam etching (FIB) [90] [91]. Table I provides a summary of the different published methods of SC pattern along with difference in growth conditions, QD occupancy.

Table I – Summary of key literature for site-control QD, detailing QD occupancy, and growth conditions including buffer layer and QD growth.

Ref	Fabication method	Occupancy	QD growth		Buffer growth		Stack	Additional Note
		AFM	Rate	Temp (°C)	Thicknes(nm)	Temp (°C)		
[55]	EBL, Dry etch			500	12	500	Y	
[68]	EBL, Dry etch		0.005 - 0.010 nm/s	530	20		Y	
[84]	EBL, Dry etch	1.2ML InAs :Small double QDs 1.7ML: single QDs 2.0ML: large single QDs	0.01ML/s	470/500	5.4	500	Y	
[88]	EBL, Dry etch	10-90%	0.02ML/s	515	100	580	Y	
[167]	EBL, Dry etch		31nm/hr	470	15		N	
[13]	EBL, Wet etch	50%	0.013ML/s	500	30		Y	
[67]	EBL, Wet etch	49 to 77%		545	20		Y	
[68]	EBL, Wet etch		0.0006nm/s	530	34		Y	
[82]	EBL, Wet etch	40%	0.01ML/s	510	22	510	Y	
[152]	EBL, Wet etch			520	90	550	N	
[75]	LAO	89%	0.01ML/s	510	15	450	N	
		75%	0.01ML/s	510	20	450	Y	
		64%	0.01ML/s	510	30	450	Y	
[87]	LAO				7	480	N	
[89]	LAO	50 to 90%	Varied	510	100		N	
[69]	in-situ laser interference patterning	Multi-occupancy ~100%	0.026ML/s	500	500	600	N	a laser fluence of approximately 15mJ/cm2
[91]	FIB		2.7ML/s	485	300	590	N	GaAs layer for QD

From all the methods available, EBL with wet chemical etching is well-developed with detailed reported of QD occupancy with up to 77% QD occupancy, and under resonant excitation produced linewidth as low as 6 µeV is achieved [82]. The majority of the work relating to wet etching also uses a stacked QDs with partial capping approach which has demonstrated to improve linewidth and blueshift emissions [50] [92]. Stacking QDs can control the position of the QD deposited by using a seeded layer initially followed by controlled buffer layer deposition to tune the QD emissions, as

previously discussed [21] [75]. Partial capping is a well-known technique which uses a thin capping layer to control the height of QDs, improving QD uniformity and emission shifting [59] [93].

For dry etching, a mixture of single stack and multi stack QDs are used with a maximum QD occupancy of 90% has been achieved [88]. Kiravittaya et al, also studies the SCQD formation with different amount of InAs deposited, 1.2 ML, 1.7 ML and 2.0ML at 0.01ML/s was used. This demostated that with low amount of InAs deposited resulted in multi-dot occupation and above 1.7ML resulted in single dot occupation with varying sizes.

While promising results has been demostrated across different fabrications and growth techniques, the required values for each SCQD paramaters depend on the appliations the QDs are used will be used for. The application which would be used from the output of this research is the creation of entangled state between photons emitted from multiple QDs. This challenge with this applcations is all photons emitting from QDs must be identical to each other (i.e. the same energy). Grim et al, has demonstrated that by using a strain tuning method, they achieved a runing range of over 65meV over 3 QD [94]. With this level of tuning, this demonstrates, that SCQD with good yield previously reported can be fabriacted into complex structure using multiple QD and can be tuned into resonance [82][88]. However, this does add a additional level of complexity which is not ideal for scalable goals. For research applications typical QD occupanction of 40% or greater provide signifcant benefits for detail analysis of QD uniformity and multi-dot applications. However, to move to scalable appliations or mass production, having yield above 70% is preferred. From Table I, each different method demosntrates this 70% target, however, in each literature initial PL spectrums is provided but does not comment on the wavelength uniformity or suitable linewidth (<10 μeV).

Site-controlled QD in device structures

To achieve scalable SCQD growth, it is crucial to attain a high yield of single dot occupation. This enables high device yields and the ability to fabricate a device which uses multiple QDs. Having known locations and multiple QDs leads to the development of more complex systems, generating increased interest. These systems are analogous to molecules and are often referred to as QD molecules [95]. SCQD requires a very narrow distribution in emission wavelength to enable the possibility to tune individual QDs into the same wavelength and in an ideal situation all the QDs within an array has the same wavelength. To achieve this in growth means that all QDs have to be similar in size and composition. With an optimised growth condition, additional complexity to the overall structure can be used to enhance the optical properties further for certain applications. When implementing SCQD into device structures, the doped layers can act as charge barriers within the structure, where an applied electric field across a device structure reduces non-radiative recombination [96].

Coupling SCQDs into a variety of structures has previously been reported, including photonic cavity [12], QD-in-nanowire [97], micropillars [98] and optical resonators [13]. The implementation of SCQDs into devices enables improvements in the optical quality of SCQDs by exciting them either optically or electrically. Other known benefits include increased radiative recombination rate of the QD [99] [100], improved speed and brightness of the QD emissions and reduced negative effects of dephasing [101] [102]. Huggenberger et al, report SCQDs inside a photonic crystal cavity with a good linewidth of 38 μeV and FSS of ~32 μeV, which are comparable to self-assembled QDs in a cavity structure [13]. Alternatively, QD-in-nanowires demonstrate the benefits of deterministic positioned QDs with linewidths of 87 μeV [95] but require improvement to match self-assembled QDs properties [103]. Other applications, including the use of two deterministic positions SCQDs on the L3 cavity with good position accuracy and the ability to tune the two QDs into the same wavelength with temperature dependence measurements, are presented [12]. This allows weak coupling of both QDs exciton peaks and enhances the QD emission. The PL spectrum of two QDs coupled to the same photonic cavity is shown in Figure 2- 10. Single photon emissions with SCQD coupled into a cavity system have also been reported with promising $g^2(0)$ = 0.12 and emitting at the 930 nm range [86]. Alternative approaches to microcavities are electrically driven SCQDs on cavity have also been reported with some degradation of the linewidth of 170 μeV observed on XX emission with a large linewidth of ~250 μeV on X emissions. However, the single dot emission from an electrically driven still shows good $g^2(0)$ = 0.42 [104]. In all examples, the demonstration of highly accurate deterministic QD positions is important not only for device yields but also for reducing inhomogeneous broadening of emissions [105].
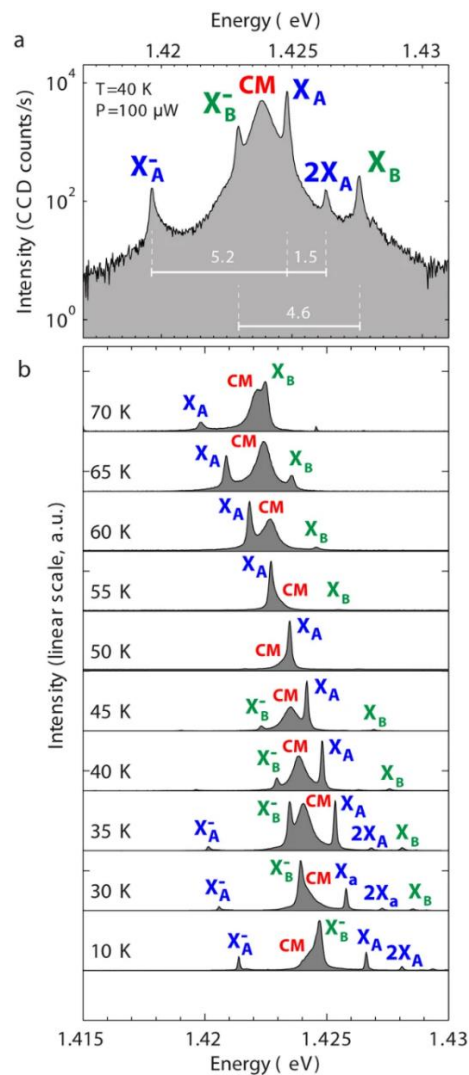
Figure 2- 10 PL spectrum of two QDs coupled to the same PhC cavity mode. (a) Semi-logarithmic plot showing the cavity mode CM tuned spectrally in between the exciton lines belonging to two spatially separated QDs A and B. Energy separations are indicated in meV. (b) Temperature dependence (10–70 K) of the PL spectrum (normalised to maximum intensity). Reprint with permissions granted licensed under a Creative Commons Attribution 4.0 International License, Calic, M., Jarlov, C., Gallo, P. et al. Deterministic radiative coupling of two semiconductor quantum dots to the optical mode of a photonic crystal nanocavity. Sci Rep 7, 4100 (2017). https://doi.org/10.1038/s41598-017-03989-y [12]

Diode structures using site-controlled QDs achieving electrical operation as single photon emitting devices have been reported [106]. An oxide aperture acts as a buried stressor structure to force QD formation. This allows the QD position to be within the current path during vertical current injection. This technique within a diode structure yields an exciton FSS of (84 ± 2) µeV at 960 nm to 967 nm emission range and an anti-bunching value of $g^2(0) = 0.05$ under direct current injection. The lowest linewidth recorded with the diode was on negatively charged exciton with a linewidth of 25 µeV. Single pyramidal QDs [107] and FIB SCQD [108] have also seen integration into diode devices, showing comparable electroluminescence of single QDs for injection current as low as 150 nA.

An overview of the literature towards site-controlled QD growth and device integration demonstrates the ability to achieve low linewidth by a combination of wet chemical etch processing and a stacked

QD system with partial capping. The use of a stacked system improves QD occupancy and size uniformity, which are ideal for nanophotonic devices. Other methods of fabrication have also been reported; however, they are still lacking with larger linewidths (~25 µeV) or poor QD occupation. The ability to produce SCQDs with comparable quality and optical properties of self-assembled QDs has been achieved. The structure proposed in the literature is not suitable for our application due to the use of stacked QD structures exceeding the total thickness requirement. In this thesis, we focus development of waveguide structures with a maximum thickness of 170 nm to optimise QD emissions at 930 nm. Within this limitation, while maintaining the position of InAs, QDs become vital as it is required to be in the centre of the structure to provide optimal emissions. This results in additional challenges regarding growth as these limits the doping layer thickness and the implementation of multiple techniques to improve QDs' properties (such as partial capping or stacked QDs). Instead, the general growth conditions such as growth temperature, deposition amount, and additional growth techniques are used to provide a good foundation to achieve planarised single-stacked QDs with low linewidth and high QD occupancy. Initial implementation of SCQD into device structures has also been reviewed with good improvements to emission intensity and tune-ability between two QDs. However, to-date literature only details single devices and does not mention the ability to scale and repeatability of the methodology used.

Site-control patterning process

The fabrication method used in this research to produce patterned substrate involves a dry etch process using EBL for patterning the substrate and ICP to etch the substrate, for details involving the fabrication process, see Chapter 3. Ovenden et al, previously reported on optimising the fabrication process used in this research, detailing different pattern parameters affecting the formation of the etched pits and initial growth characterisation of site-controlled QDs are reported [109]. The optimised fabrication process produced nanoholes with an average depth of 19.8 ± 0.6 nm with a position deviation of ± 55nm and ±18 nm in the [110] and [1-10] orientation with 43% single dot occupancy by an atomic force microscope (AFM). Dry etching is then compared to another fabrication method, local anodic oxidation (LAO). This uses an AFM to pass a small electrical current from the tip to the sample surface to form an oxide on the surface followed by a thermal or chemical treatment to form the etched pit. The use of LAO formed nanoholes with a depth of 11.0 ± 0.9 nm with ± 56nm and ± 38 nm positioning deviation along the [110] and [1-10] orientation, with a significantly work single dot occupancy of 20% when measured with the AFM [89]. Figure 2-11 provides a summary between two nanohole fabrication methods and the characteristics of the nanohole profile and post regrowth QDs characteristics previously studied.

Parameter	EBL (50D2)	LAO
Linewidth (mean)	55 ± 25 µeV	83 ± 36 µeV
Linewidth (mode)	44 µeV	62 µeV
Linewidth (minimum)	26 µeV	33 µeV
Mean wavelength	970 ± 30 nm	968 ± 34 nm
QD height	9.8 ± 2.4 nm	7.9 ± 2.1 nm
PL occupancy (imaging)	28%	25%
PL occupancy (spectrometer)	21%	25%
AFM single occupancy	43%	20%
Positioning deviation [110]	± 55 nm	± 56 nm
Positioning deviation [1-10]	± 18 nm	± 38 nm
Nanohole diameter (before)	57.9 ± 2.7 nm	359.4 ± 16.4 nm
Nanohole depth (before)	19.8 ± 0.6 nm	11.0 ± 0.9 nm

Figure 2- 11 Summary between EBL-ICP and LAO fabrication methods for patterned substrates for the physical dimensions of the nanoholes, the post-regrowth QD occupation and QD characteristic. Reprinted with permissions from C. Ovenden, "Development and characterisation of site-controlled quantum dot arrays," White Rose eTheses Online, Sheffield, 2021 [109].

From the investigation between different methods of achieving patterned substrates, EBL-ICP fabrication method was chosen as the preferred method of choice. This was chosen as the depth variation and nanohole diameter was more consistent compared to LAO, higher single dot occupancy and high quality QD characteristics. This method also enable future to develop towards more complex devices which requires more complex fabrication process such as two stage etch process to achieve two different etch profiles and precise control of the etch depth by controlling the ICP etching conditions.

Post growth methods

The use of post-growth techniques is a good additional step for altering the structure of the QDs to achieve more favourable optical properties for photonics applications. A common example is when as-grown QDs show a spectral distribution longer than the target wavelength. The use of post-growth methods, such as ion implantation [110], electric fields [111], and optical stark effect [112], have all been shown to control the QDs emission wavelength [113], brightness [110] and FSS [111]. These improvements provide suitable methods for tuning QDs outside of the growth environments.

Quantum-Confined Stark Effect

A QD in a diode can be applied with an external electric field to induce electroluminescence (EL) in forward bias to allow for emission wavelength tuning by Quantum Confinement Stark Effect (QCSE) [114]. Typically performed in reverse bias, this enable tuning of QDs by reducing charge fluctuations as defect states becomes filled [103]. The diode structure consists of positively (p) and negatively (n) doped regions sandwiched together by an intrinsic (i) layer, which contains the QDs forming a p-i-n diode. When the external voltage applied is greater than the built-in voltage, EL can occur where the

exchange of electrons from n to p regions and holes from p to n region, populating QDs within the i region. This alters the bandgaps as electron and holes are pushed to the opposite edges of the QDs, resulting in a band-shift. Figure 2- 12 provides a diagram of the band structure and band-shifting process induced by an electric field. The use of QCSE has been demonstrated to tune InAs/GaAs QD emissions wavelength up to 25meV using AlGaAs barriers [115]. The size of the QDs has also been reported to have an impact on tuning where the QD height of ~10 nm requires a high order of defect-free surface compared to 7 nm tall QDs, which can accommodate 3 times greater defects or charge traps, reducing the tunability of the QDs [116]. In addition to the ability to tune the wavelength of QDs, QCSE was also demonstrated to reduce emission linewidths below 6 μeV [103]. The theoretical study suggests that the minimum FSS that can be obtained is 3 μeV due to the symmetry of the crystal [117]. Bennett et al, has also reported on the use of QCSE and demonstrated the ability to reduce FSS from a single dot to as low as 0.7 μeV [118].
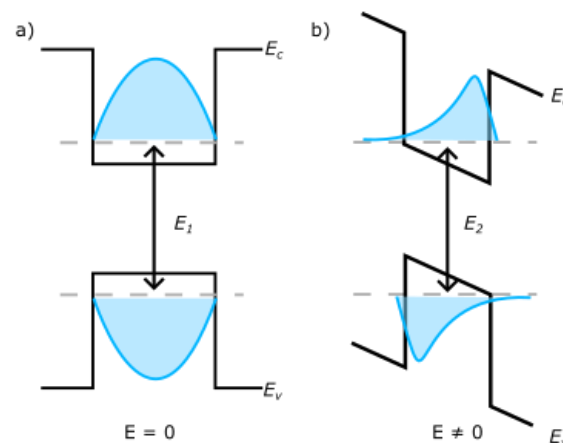

Figure 2- 12 A band structure representation of QCSE with (a) no electric field (E=0) with an energy gap of E_1 and (b) an electric field applied (E≠0) with an energy gap of E_2. The conduction band and valence band change under the electric field are also presented.

Rapid Thermal Annealing

Rapid thermal annealing (RTA) is a technique where samples are exposed to high temperatures (>600°C) for short periods. This is a well-known technique that alters the composition and shape of QDs to modify the optical properties of QDs [119]. Emission shifting is the main feature with RTA due to the compositional and size change induced by the intermixing of atoms between adjacent layers [54]. When annealing an additional improvement observed are the narrowing of ensemble PL FWHM and is dependent on the annealing temperature [120] [121]. This typically involved Ga/In atoms for InAs/GaAs QDs [122] or As/P atoms for InAs/InP [120]. Compositional change across layers gives chances to remove defects by infilling caused by interdiffusion mechanisms, which also assist in emission shifting [123], removing wetting layer emissions [112] and brightness enhancement but

reducing charge noise [113]. For this method, the annealing temperature, annealing duration, and the types of capping methods are parameters that can be changed. Annealing temperatures typically vary between 600°C to 950°C [122] [124], with annealing duration varying from as little as 30 seconds to 300 seconds [125]. The effects of annealing temperature and different capping methods on optical properties for InAs/GaAs self-assembled QDs are summarised in Figure 2- 13.
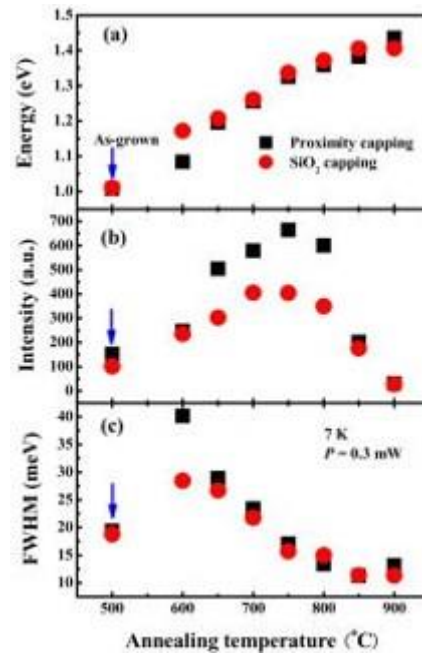

Figure 2- 13 Peak energy, integrated intensity, and FWHM of the peaks plotted as a function of annealing temperature. Solid squares indicate the data for the samples with the GaAs proximity capping, while solid circles stand for the samples with the capping. Reprinted with the permission of the author, Tao Yang, Jun Tatebayashi, Kanna Aoki, Masao Nishioka, Yasuhiko Arakawa; Effects of rapid thermal annealing on the emission properties of highly uniform self-assembled InAs/GaAs quantum dots emitting at 1.3 µm. Appl. Phys. Lett. 12 March 2007; 90 (11): 111912. https://doi.org/10.1063/1.2713135 [126]

This technique for InAs QD has been comprehensively studied with unique methods of introducing thermal treatments with ion implantation [110], proximity capping [122] [126], superlattice capping [127] and dielectric capping methods such as SiO_2 [128] or iterative laser annealing [129]. Different capping methods introduced help reduce the outdiffusion of atoms from the surface of the substrate. Proximity capping is one example which suppresses the outdiffusion of atoms [113]. While SiO_2 dielectric capping methods allow some degree of outdiffusion but help protect the surface from defect generation at high temperatures. For GaAs-based QD structures, the annealing mechanisms have been well characterised, with emission shifting up to ~350meV with annealing temperatures up to 950°C [113]. Narrowing linewidth of ~40meV [130] with growth temperatures up to 850°C has also been achieved [124] [131]. For InP-based QD structures, the introductory investigation into the effects of RTA is reported. These include the use of different capping methods [125] detailing the behaviour of

the intermixing effect [120] in correlation to the effects of ensemble PL emissions [120] [125]. Annealing of lower dimensional structures such as quantum wires is also reported with the use of an InAlAs buffer layer to lattice match InAs to InP [132]. Details of the thermal thresholds required with InP-based structures are discussed, with a minimum annealing temperature of 750°C required before any intermixing occurs. This is explained by the strong bonds of Al-As, which require higher thresholds. Barik et al, use SiO_2 and TiO_2 as a capping layer to study the effects of impurity-free disordering and the effect of emission shifting while maintaining good emission intensity. Varying the annealing temperature, a maximum emission shifting of 74 meV and 157 meV is obtained with SiO_2 and TiO_2 capping layers, respectively [133]. All literature on InAs/InP QD is also focused on ensemble PL emissions. The effects of annealing towards single dot emissions have not been reported despite the significant improvements reported under ensemble emissions. Comparatively, SCQD's effects with similar thermal treatments are also not reported for both ensemble emissions and single dots.

3 Methods

In this project, various experimental methods is used to fabricate an array of nanoholes and alignment markers and characterised QD emissions. The main method of producing sample is the use of molecular beam epitaxy, including in-situ equipment used during growth, the methods used to characterise growth samples before and after growth to ensure a high-quality pattern substrate. Furthermore, the characterisation of nanohole arrays will be explored, including single dot characterisation and initial diode characterisation. Followed by details of the post-growth method, rapid thermal annealing, and the equipment used in the process. A range of samples was used in this project; all GaAs-based samples (PRXXX) were grown using the DCA Instruments MBE in collaboration with Dr Ian Farrer, Dr Aristotelis Trapalis and Dr Akshay Verma. InP-based samples (JRXXX) were grown on an Aixtron 3*2 MOVPE Reactor by Dr Elisa M. Sala.

This research project has a primary objective of optimising the fabrication and growth process for etch nanoholes to make them suitable for waveguide structures suitable for quantum applications. The process involves producing the etch nanoholes in a pattern called site-control (SC), allowing for deterministic positioning of QDs. The pattern controls the nanohole diameter, the spacing between nanoholes (pitch) and the dosage of EBL patterning, allowing for direct comparison between these parameters. The goal for SC QD growth and characterisation is to achieve an ideal solution for deterministic QDs that are usable for nanophotonic devices. To use site-controlled QD in scalable qubit circuits, undoped and doped waveguide structures need to be used for device characterisation. When making modifications to the structure, it is essential to consider how it will affect the distribution of QD wavelength, site occupation and uniformity. We also investigate InAs/InP QD substrates and the post-growth methods' ability to control QD optical properties.

Fabrications

Nanohole fabrication uses a dry etching approach of e-beam lithography (EBL) and inductively coupled plasma (ICP) etching. A large pattern was used with variations in nanohole diameter, pitch, and e-beam dose to allow for direct comparison between these parameters. Alignment markers and text are used to allow easy identification of different regions of the pattern and for easy alignment during characterisation. A series of solvent and acid cleaning is then used to remove any photoresist, oxide, or contamination on the patterned surface. A summary flow diagram of the fabrication process is shown in Figure 3-1.
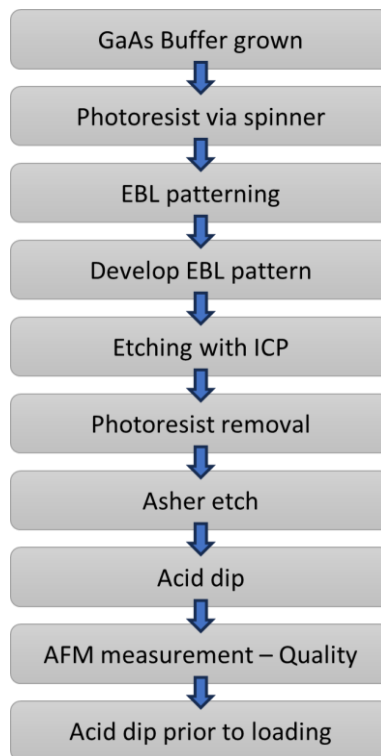
Figure 3- 1 Flow diagram of the EBL-ICP fabrication process from the initial buffer regrowth up to reloading into the MBE reactor for regrowth of the QDs and capping layers.

After the growth of the 100nm GaAs buffer layers by MBE, the wafer is removed from the reactor for SC pattern fabrication. First the substrates are coated using 100nm of positive organic resist poly(α-methylstyrene-co-methyl-chloroacrylate) (CSAR62). To achieve this thickness, CSAR62 was diluted with anisole in a 1:2 ratio and applied with a photoresist spinner, using a spin speed of 4000rpm for 30 seconds. The use of CSAR62 over conventional resist such as poly-methyl methacrylate (PMMA) is due to its ability to create narrow radii and its resolution enhancement [134]. The sample is loaded into the electron beam lithography to develop the pattern.

Electron Beam Lithography (EBL)

EBL is a commonly used lithographic technique to produce photolithographic mask plates, but it is a viable solution for nano-sized features such as nanohole arrays and other photonic devices. To form a pattern on the photoresist, using EBL, a stream of high-energy electrons is directed through an aperture onto the photoresist, which follows a pre-defined pattern generated using the Graphic Data System file II (GSDII). This is a digital design file that controls the path the electron beam will take, the intensity and duration allowing for repeatability of the same pattern. The electron energy (also known as dose) is adjusted to enable bond scission (positive tone) or Crosslinking (negative tone) throughout the resist's depth by overcoming the activation energy. The system can control the feature's position, drawn size and shape; the following equation can represent this.

$$D = \frac{I \times t}{A}$$

Where D is the dose, I is the beam current, t is the exposure time, and A is the area exposed.

When using the EBL for fabrications, the feature size matters as this can affect the resolution of the pattern. When an electron incident on a resist, this causes bond scission to occur; however, an alternative reaction is ionisation, where the interaction is inelastic [135]. This causes an emission of a second electron from the resist, enabling further reactions to the resist as these electrons have sufficient energy to break the bonds of the resist [136]. This is an especially common effect for larger features; therefore, it requires the use of a proximity correction algorithm to minimise such effects. Meanwhile, smaller features, depending on the spacing between each other's features, will either need no corrections or increased applied dosage to increase the number of electron interactions for bond scission. This interaction between an electron on the resist changes the solubility of the photoresist in the pattern regions by changing the molecular weight of the resist at the specific areas.

The Raith EBL system was utilised for all EBL patterning, operating with a beam voltage of 50kV in lower current mode with an aperture of 60μm. The base dose of ~300μCcm^{-2} was used and scaled based on this value (e.g. a scaled dose of 0.5 would give 150 μCcm^{-2}). A basic schematic of the EBL pattern used is shown in Figure 3- 2. The notation used for different arrays in this pattern is defined by *XXDY*, where *XX* is the nanohole diameter (drawn size), *D* stands for dose, and *Y* is the dose reference based on the scaled e-beam dose. (e.g. 32D7 is 32 nm diameter nanoholes with e-beam scaled dose 7)
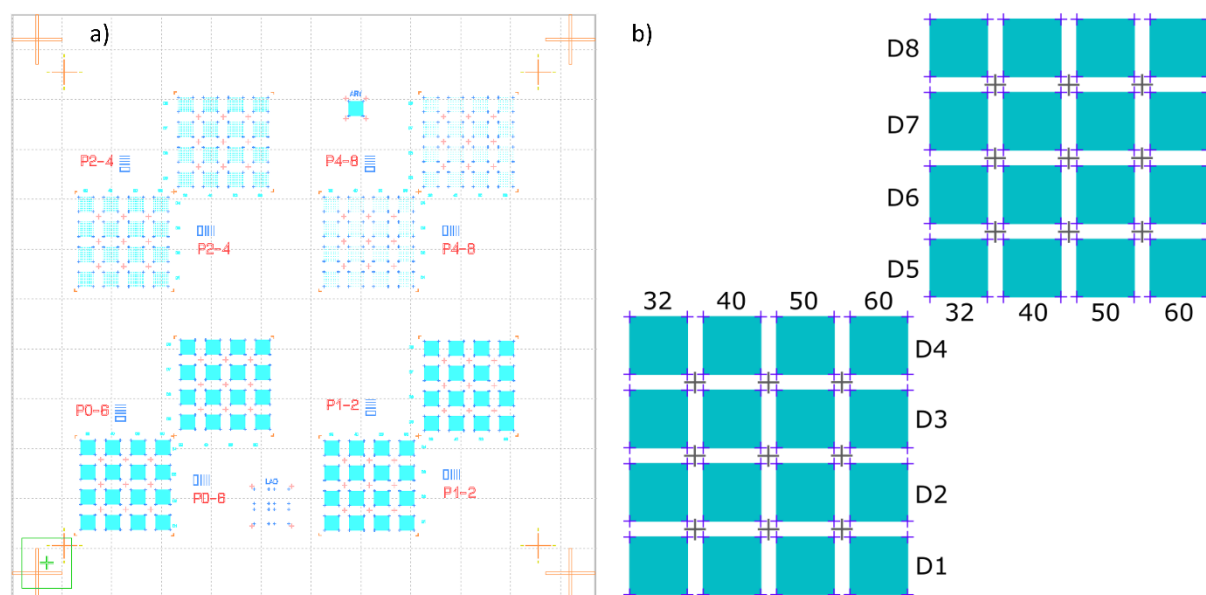
Figure 3- 2 a) An EBL schematic of the site-control pattern used in this work, exported from Raith EBL design software, b) a simple diagram equivalent from a single pitch detailing the variation in nanohole size and e-beam dose.

Inductively Coupled Plasma (ICP)

Prior to the etching of the wafer, development is essential to remove the resist of patterned areas. As EBL causes the solubility of the resist to change, these areas react with the developer and are dissolved from the rest of the resist. The developer used is xylene, which is heated to 23°C, and the wafer is submerged for 60 seconds before rinsing in isopropyl alcohol (IPA) to stop any additional reaction from taking place instantly. Prolonged exposure can cause overexposure, which is dependent on how easily it is to penetrate the solid polymer, the number of interactions and the concentration of the solvent. Based on these properties, this determines whether the solvent will develop or strip the resist. For development, in areas that have a series of chain scissions (patterned regions), the diffusion of solvent occurs at a faster rate than in non-irradiated areas (off-pattern regions). In practical terms, precise control over the solvent temperature (23°C) and exposure duration (60 second) of the sample to the solvent is critical in ensuring a well-developed pattern.

ICP is a dry etching technique where a radio frequency (RF) source inductively generates the ICP power for etching. The schematic diagram of the ICP is shown in Figure 3-3 . The etchant gas is introduced in an evacuated chamber to generate plasma for etching. The RF source induces an alternating magnetic field, which generates an electric field under Faraday's law. This generates plasma based on the etchant gas and electric field by ionising gas molecules and atoms, parameters which control the etch rate. ICP-RIE's advantage over RIE is the independent RF generator connected to the wafer clamp, which attracts ions to the wafer—allowing decoupling of the ion current and ion energy to be applied to the sample. Attracting ions onto the sample induces ion bombardment, resulting in etching on the

sample surface, which is a mixture of a chemical reaction and a sputtering process. Varying the RF power can help maintain high aspect ratios by preventing lateral etching and improving the etch rate [71] [137], while low energy improves selectivity and reduces substrate damage. With the thickness limitation of the structure, controlling the etch rate, which is governed by the ion density of the plasma and the reactive ion species produced, is essential. The etching gas used was Cl_2 with Argon, which, when optimised with other parameters, allows for good selectivity and minimal damage to the sample [138].
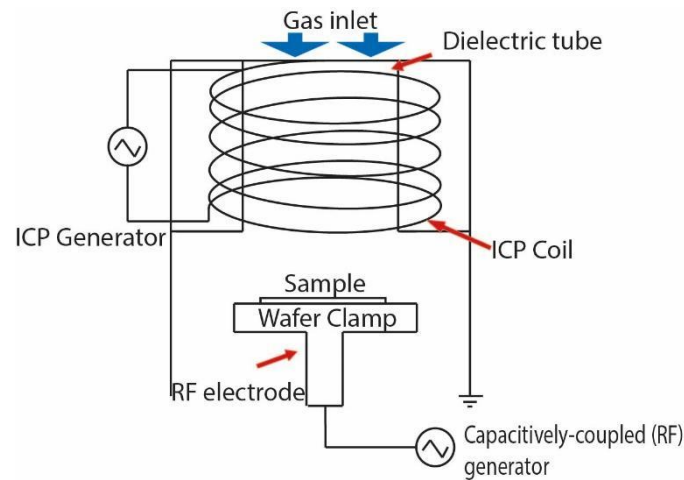

Figure 3- 3 A basic schematic of the ICP-RIE with different key components labelled.

For the etching recipe, a flow of 25 sccm and 2 sccm for Ar and Cl_2 gas was used respectively and for the RF and ICP power, 48 W and 240 W was used respectively. This resulted in a etch rate ~ 120nm/min. During the etching process, exposed areas in the form of the pattern are translated onto the sample, while areas covered with the resist are protected. In this particular work, an Oxford Instrument ICP-RIE with Argon/Chlorine gas was used in this fabrication process. This instrument used is exclusively for InP-based and GaAs-based materials, which reduces the possibility of cross-contamination from other fabrication processes from other unique materials such as GaN.

Post etch cleaning process

While etching will remove most of the photoresist from the sample, residual photoresist will remain and must be removed as this affects the surface quality, which impedes QDs properties. Cleaning the

sample comes in 3 stages: wet chemical clean, dry plasma ashing, and an acid dip. The detailed cleaning process is shown in Figure 3- 4.
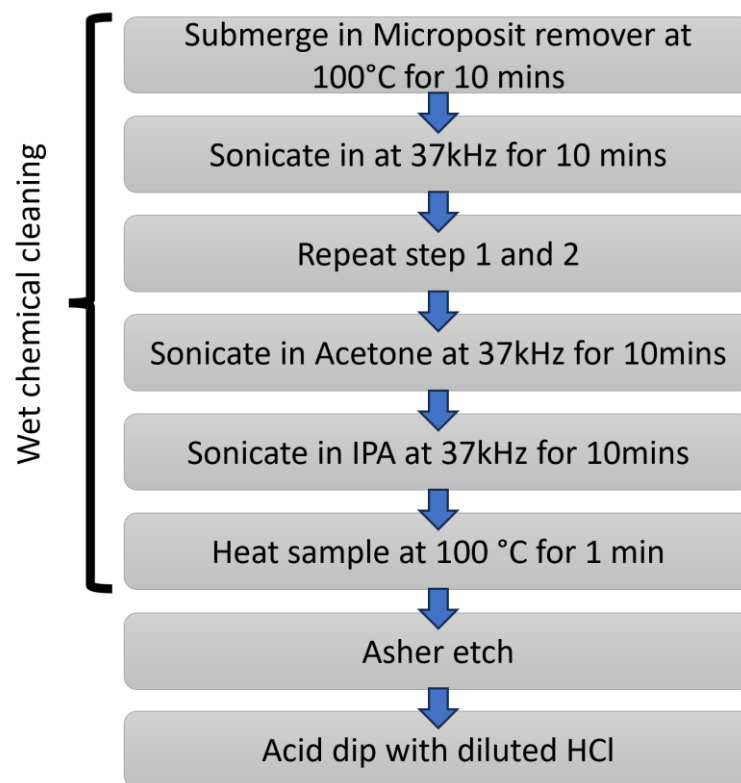

Figure 3- 4 Flow diagram on the key information for the solvent cleaning process to remove remaining resist and other contaminants.

To remove the residual photoresist, microposit remover 1165 (resist remover) was used, which consists of 99% 1-methyl-2-pyrrolidinone. This is a commercially available resist stripper targeted towards sensitive substrates. First, the sample is submerged under a resist remover at 100°C on a hot plate for 10 minutes. The manufacturer recommends this as it encourages a reaction between the photoresist and resists remover. The sample still submerged is then sonicated at 37kHz for 10 minutes to ensure the removal of contamination from nanoholes. This is repeated with a new breaker of resist remover to ensure complete removal of photoresist, especially within the etched nanoholes. The sample is then submerged and sonicated in acetone followed by IPA for 10 minutes at 37kHz in each solvent. The use of acetone removes any general organic contaminants, such as oils and grease, but leaves behind a dry stain. The use of IPA removes the dry stains and acts as a rinsing step for any containments remaining on the surface. The wafer is then placed onto the hotplate for 60 seconds at 100°C to remove excess moisture and form a thin layer of unwanted oxide. A plasma Asher is then used for 60 seconds to remove any remaining photoresist. Finally, the wafer is dipped into 1:4 HCl to Deionised water (DI water) for 60 seconds and rinsed off with DI water. This removes most of the oxides once the sample has been exposed to air and during the hot plate step.

After cleaning, the sample undergoes AFM surface characterisation for surface quality control. This verifies that contaminants have been removed and that the nanohole size, shape, and depth are within acceptable expectations. The series of steps to remove all contaminants and photoresists is an important step. An insufficiently clean sample will introduce contamination within the reactor and potentially compromise the pressure in the chamber. This will also affect the material quality of the structure grown on the patterned surface; therefore, for uncleaned samples, the cleaning process is repeated.

Prior to loading into the MBE system for regrowth, a final acid dip is performed following the same procedure detailed above. This final acid dip is to remove an oxide that may have formed while exposed to the air in the period between the last acid dip and loading into the MBE system. The loaded samples are degassed by the standard procedure and heated to 150°C and 400°C for a minimum of 12 hours. Prior to growth, as the sample is a patterned surface, the conventional thermal treatment is unsuitable. Instead, atomic hydrogen cleaning was used to remove oxide and prepare the surface within a vacuum. The sample is measured with secondary ion mass spectrometry (SIMS) before and after hydrogen cleaning to track the removal of oxide and contaminates. Details of both these processes are discussed in the later sections.

The Molecular Beam Epitaxy (MBE) system

MBE is an epitaxy growth method which allows for very precise layer deposition in the scale of monolayer (ML). This level of precision is achieved using beams of atoms or molecules directed at the sample surface with a specific flux while under ultra-high vacuum (UHV). The growth rate is related to the flux and is controlled by the source temperature. Samples grown in this study are primarily focused on III/V materials containing gallium, indium, and arsenic. Each material source is heated within a Knudsen cell, and material deposition is controlled by a series of shutters in front of the cells, allowing for precise deposition of material. Figure 3- 5a shows a standard growth chamber schematic. During growth, arsenic is constantly supplied into the chamber, and arsenic desorption helps prevent material degradation of the substrate surface (GaAs). The formation of the GaAs layer is enabled when there is enough migration of Arsenic and Gallium across the surface till Arsenic atoms bond with Gallium atoms to form monolayers. The duration of the gallium shutter cells remaining open controls the amount of GaAs deposited, which is calculated by the growth rate and the layer thickness required. For QD growth, a similar process was used, where indium was used instead of gallium. However, due to the lattice mismatch of InAs to GaAs, once the critical thickness is reached (nominal thickness 1.7ML), the InAs layer relaxes due to excessive strain build-up and forms 3D islands [44].

3 Methods

The DCA instruments, P600 cluster tool, and MBE reactor are used to grow site-control structures and GaAs-based materials. The layout of the DCA MBE system can be seen in Figure 3- 5b, where several chambers surround a central distribution centre (CDC); all chambers except for the storage racks have a gate valve to maintain vacuum and prevent cross-chamber contamination. The MBE system is under ultra-high vacuum (UHV) for high-quality materials to be produced, and CDC is used to transfer samples between chambers. At the same time, the load lock (LL) allows samples to be loaded and unloaded from the system to prevent a breaking vacuum.
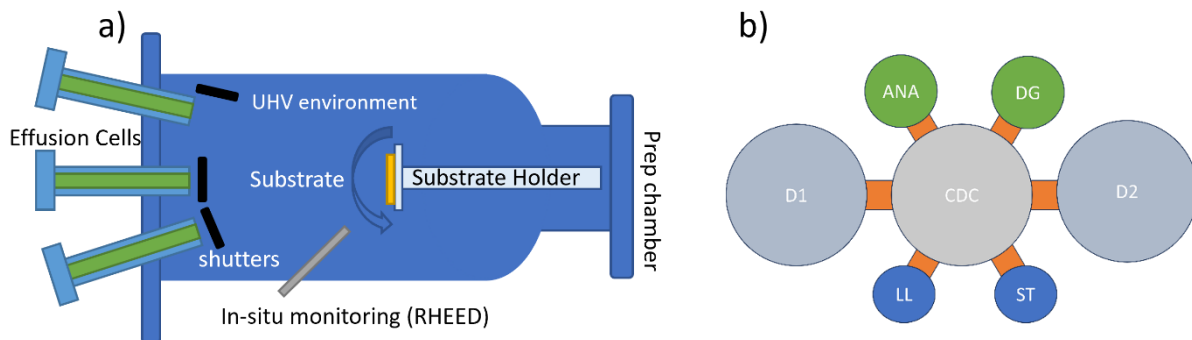

Figure 3- 5 A simplified schematic of a) a standard growth chamber and b) a DCA cluster tool MBE system. The chambers of the system consist of a main growth chamber (D1), atomic hydrogen cleaning chamber (D2), degas chamber (DG), degas chamber with SIMS (ANA), Load lock (LL), Storage rack (ST) and central distribution centre (CDC)

For the DCA system, when the sample is loaded into the system, it undergoes degas for 12 hours at 150°C, followed by another 8 to 12 hours at 400°C in DG or ANA. The degassing steps are used to thermally desorb decontaminates and remove residue. Temperature monitoring is typically done by various methods based on the chamber used; in the case of degas, thermocouples are used. For growth, the use of k-space Associates Band Edge Thermometer (BandiT) was used to measure the sample [139]. The BandiT uses an optical absorption edge measured in real-time to determine the actual temperature of the substrate. The substrate heater is controlled by a feedback loop using a thermocouple placed near the substrate holder. Therefore, mapping of the band edge's movements to the substrate temperature is required, where this is dependent on the material and substrate temperature. Other factors such as sample size, doping, polish, and thickness also affect the temperature control, but these can be calibrated based on each substrate type.

Reflection High Energy Electron Diffraction

Reflection High Energy Electron Diffraction (RHEED) is a handy in-situ metrology tool used in MBE. This allows the characterisation of the crystalline structure and quality of the surface in real-time to measure growth rates accurately, characterise the III/V ratio, and calibrate growth temperature [140]. An electron gun generates a stream of high-energy electrons that is directed onto the sample surface

and diffracts at a shallow angle. This scatters electrons from the sample surface and is detected by a phosphor screen. Figure 3- 6 shows the simplified operations of an RHEED.
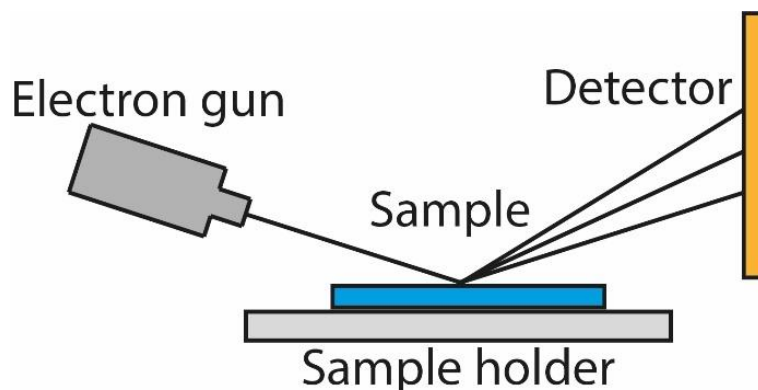

Figure 3- 6 A simplified view of the operations of RHEED used in MBE.

The surface quality affects the RHEED patterns produced. For instance, if the sample is flat and has an atomic terrace, this produces a streaky pattern. Meanwhile, for non-uniform surface or oxide removal, RHEED intensity is reduced, and diffuse scattering takes place. The number of intermediate lines present in the RHEED pattern can distinguish the reconstruction pattern. The notation for reconstruction is denoted by (n x m), where n and m are representations of the number of repeats of the surface unit cells in two different unit cell vectors, [110] and [1-10], respectively, for GaAs (100) substrate. The formation of QDs during growth can be determined by the 2D to 3D transition time, where 2D layers turn into 3D islands. The RHEED pattern produces a unique pattern with an additional bright spot caused by the diffraction of 3D islands formed. An example of the RHEED pattern of a smooth GaAs surface is shown in Figure 3- 7. This can be used to calibrate the BandiT temperature results as the GaAs transition from a (4 x 4) to (2 x 4) reconstruction occurs around 500°C for the reactor used in this study [141].
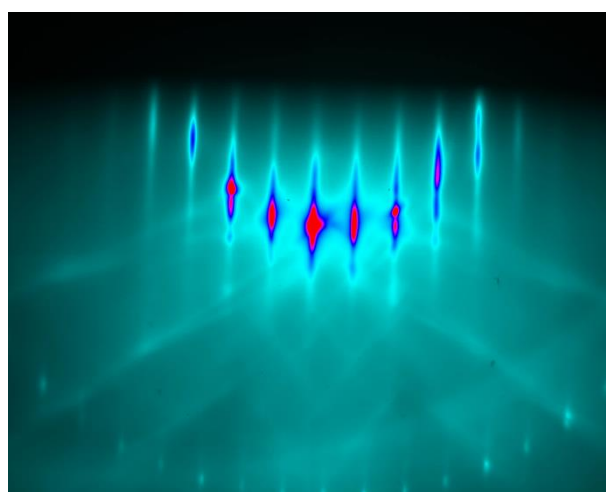

Figure 3- 7 RHEED pattern taken in the [110] direction at 490°C of a smooth GaAs buffer surface.

Secondary ion mass spectrometry (SIMS) – ANA chamber

Secondary ion mass spectrometry (SIMS) is a destructive surface analysis technique that measures the composition of a sample surface. Figure 3- 8 shows a schematic of the basic operation of a SIMS which is built into the ANA degas chamber. This setup in the reactor is orientated so that it can be operated with samples facing in the direction of the floor, following the orientation configuration used in growth. A beam of primary ions is generated via an ion gun with the use of Argon gas. The splutter beam bombards the sample surface, creating secondary ions in the form of charge fragments. With a series of lenses, the charge fragments are guided towards the mass spectrometer, providing information on the composition. A quadrupole mass spectrometer used is made up of two pairs of poles where an alternating RF signal can be applied to send ions into a spiral motion. A DC bias is then applied, which drives the motions of the spiralling ions down the quadrupole towards the detector.
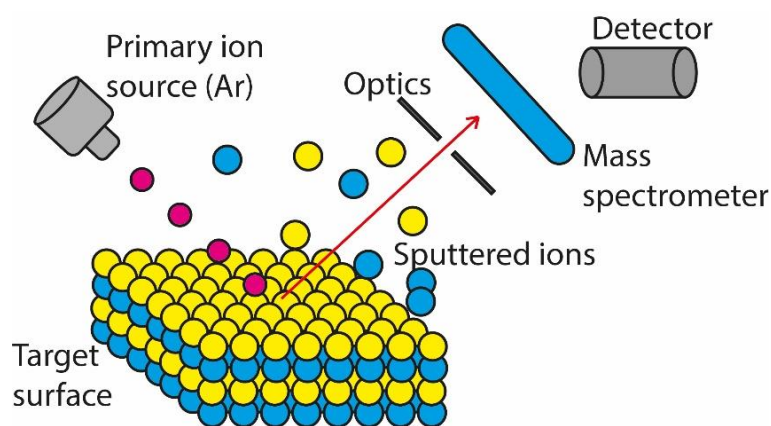

Figure 3- 8 A schematic of the basic operation of Secondary Ion Mass Spectrometry with key components of the device.

The diameter of the ion spiral is defined by the mass/charge (m/z) ratio and can be tuned by the quadrupole. This allows ions with the correct m/z ratio to travel down the pole towards the detector. In contrast, ions with incorrect m/z ratio will have larger (or smaller) spiral diameters and impact the poles during travel. To measure a range of m/z, the quadrupole is controlled to allow specific m/z ratios to be measured over a region of interest covering both the positively charged and negatively charged ions of the surface species, otherwise known as positive and negative modes, respectively.

SIMS measurements are done before and after in-situ atomic hydrogen cleaning to identify the changes to individual species varying in between the range of 0 and 200 amu. Figure 3- 9 shows an example spectrum of a positive and negative mode on a patterned substrate. Appendix A shows the sub-list of m/z that would be expected within this work. For this work, the use of SIMS is to identify

the removal of oxides, including Gallium Oxide (GaO, Ga₂O₃), but also other material peaks (e.g., Oxygen, Gallium, etc.) to determine the cleanliness of the sample surface for growth.
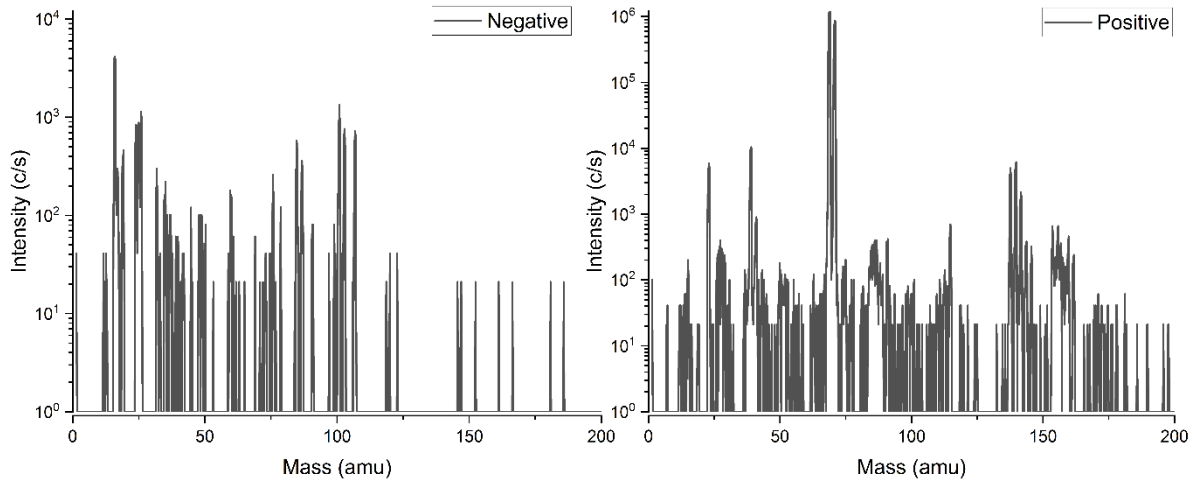

Figure 3- 9 SIMS spectrum in a) negative mode, b) positive mode of a pre-hydrogen clean GaAs sample with a patterned surface

Atomic hydrogen cleaning

Atomic hydrogen cleaning (AHC) is an in-situ surface preparation method that can replace conventional thermal treatment to remove native oxides and carbon contaminations. For thermal desorption, around 540°C is required to remove native oxides [142], while with AHC, temperatures around 400°C can be used, which reduces the risk of damaging the patterned surface. At this temperature, this provides a good balance of complete oxide removal within a reasonable period (1hr). The specific thermal and kinetic interactions between hydrogen and GaAs have previously been studied by Burke et al, [143]. This provides an excellent foundation to determine the specific chemical reaction and surface reconstructions after AHC [144]. During AHC, a hydrogen radical is a highly reactive species that bonds with surface oxides and contaminants. The highly reactive nature of hydrogen allows for lower temperatures to be used for the desorption and removal of species without any damage to the surface. AHC was also previously reported to aid in reducing surface defect density and surface contamination before and after growth [145]. Controlling the hydrogen cleaning process is determined by flux, hydrogen cracking efficiency, oxide thickness and consistency [146] [147] [148]. The rate of oxide removal is controlled by the chemical desorption of the reaction products, chemical reactions and diffusion on the GaAs oxide surface, and the adsorption of atomic hydrogen radicals. In this work, the hydrogen atomic beam source (HABS) used is by MBE Komponenten, and detailed characterisation of this source has been reported previously [89] [149] [150].

3 Methods

Atomic hydrogen is generated when H_2 gas passes over a heated tungsten filament, otherwise known as cracking. Hydrogen atoms are directed towards the sample surface as a beam of gaseous material. The hydrogen flux and the filament temperature govern the cracking efficiency, which is controlled by the HABS temperature. The HABS temperature is current controlled and the relationship between current and HABS temperature is shown in Figure 3- 10. The standard method of measuring cracking efficiency is the use of a beam flux monitor (BFM). By measuring the change in intensity of the H-2 peak, the cracking efficiency and number of hydrogen atoms can be calculated. The fall in intensity in the H-2 peak is measured in place of the rise in the H-1 peak, as the BFM cannot measure this. The following equation defines the cracking efficiency (η):

$$\eta \, (\mathrm{T}) = \frac{Q_{H_2}^{uc} - Q_{H_2}(T)}{Q_{H_2}^{uc}}$$

where $Q_{H_2}^{uc}$ is the uncracked H_2 signal and Q_{H_2} is the cracked H_2 signal [151] and is HABS temperature controlled. However, due to the difference between individual reactor setups, it is not possible to use literature values directly. Instead, it was used as a reference in addition to experimental values to create a baseline calibration where a flow of 0.5 sccm was calculated for the highest number of hydrogen atoms produced.
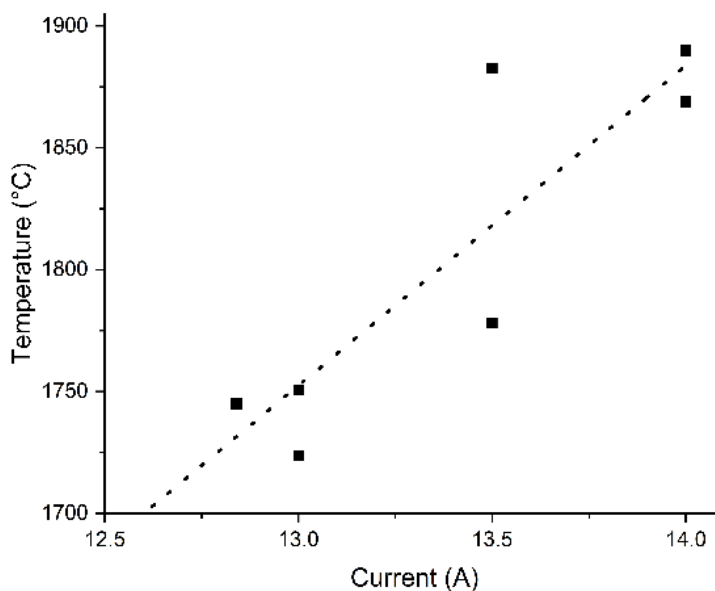

Figure 3- 10 Relationship between HABS temperature and supply current, dash line shows the average across multiple measurements.

Characterisation

Atomic Force Microscopy (AFM)

AFM is a non-destructive type of scanning probe microscopy capable of characterising surfaces with a high spectral resolution. Alternatively, it can also perform surface modification, such as local anodic oxidation [89], as the probes used are incredibly sharp with a tip radius of 2 to 30nm, and a current can be applied. Figure 3- 11 shows a basic schematic setup of the AFM and the basic operation features. The AFM is composed of a tip mounted on a cantilever, laser, and position-sensitive detector photodiode (PSDP) to perform measurements. The tip is connected to the cantilever with a known spring constant, which is defined by the type of tip used. They allow a predictable deflection on the cantilever when the tip runs across the surface and cause a change in height due to surface features. To track the deflection, a laser is reflected off the back of the cantilever onto a PSPD, which is made up of four quadrants. This deflection is caused by a laser reflected off the back of the cantilever and directed towards the PSPD, which is made up of four quadrants. The different quadrants generate different electrical signals, which are converted into an image by the computer. The tip radius determines the resolution of the image, but small features are vibration-sensitive.
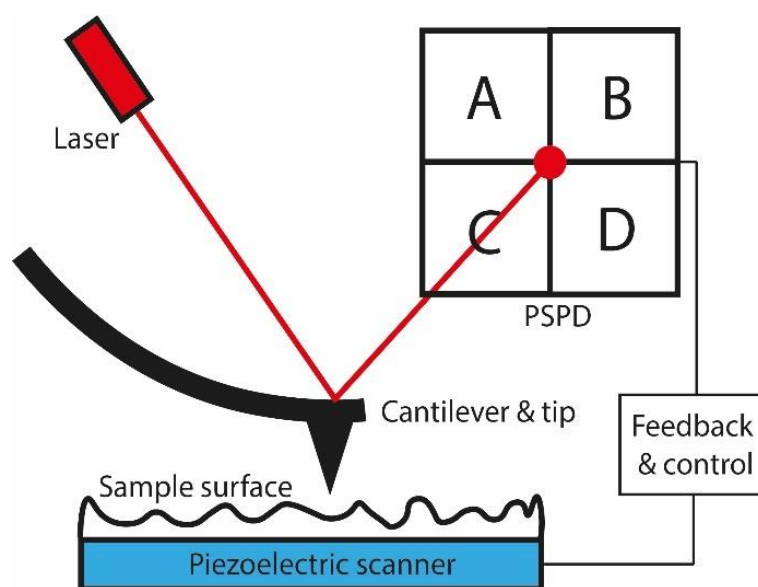

Figure 3- 11 A basic schematic of an AFM setup is required to capture images of the target surface.

The Bruker Dimension ICON AFM was used with a silicon nitride SNL-10 tip as it has a super high resolution 2 nm radius, frequency of 65 kHz and spring constant of 0.35 N/m. The tip is coated in reflective gold to provide a stable reflection due to its inert nature. The AFM operates in ScanAsyst tapping mode, which drives the tip speed near the resonant frequency, resulting in rapid oscillation in the z-direction. This mode is an advanced tapping mode developed by Bruker and is used exclusively

for all AFM images shown unless stated otherwise. NanoScope Analysis 2.0 software provided with the Bruker Dimension ICON AFM was used to analyse and extract data from the AFM images.

Figure 3- 12 shows an example of an AFM image produced using the Bruker Dimension ICON AFM. The AFM can reconstruct the surface morphology and generate 2D and 3D images with atomic-scale precisions. Other advantages include no sample preparation, reproducible and accurate, making it an ideal characterisation choice for nanoholes and QD samples. A closed-loop positioning stage allows reproducible movements to a specific location. This allows the ability to use the "Programmed Move" function, which creates and saves referenced points for more straightforward mapping of multiple locations. With a patterned surface, this enables repeatable and reproducible monitoring of specific locations of the sample, allowing tracking of the nanohole shape, size and depth change before and after QD growth. The use of SNL-10 tips with a 2 nm tip radius is also essential for nanohole measurements, as if the tip radius is larger than the nanohole radius, it will be unable to produce the correct deflection. This results in a false measurement of the nanohole with shallower and sharper profiles, as a large radius tip would obstruct itself from reaching the bottom nanoholes.
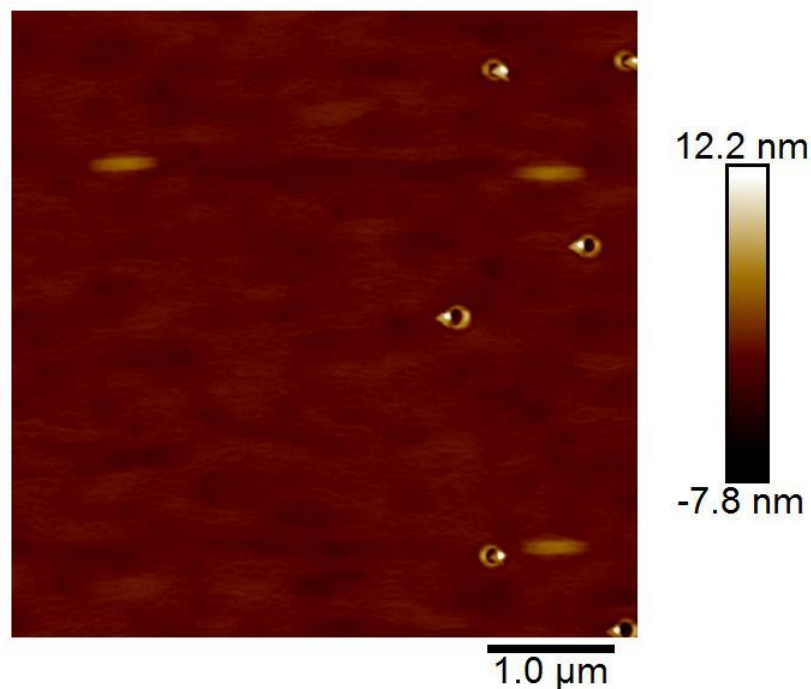

Figure 3- 12 An example of a 5 x 5 μm² AFM image of local droplet etching of aluminium droplets and buried InAs quantum dots on GaAs substrate.

Photoluminescence (PL)

Photoluminescence (PL) spectroscopy is an optical characterisation method which is contactless and non-destructive. In principle, focused light is directed onto the sample surface, where it is absorbed and promotes electrons to an excited state, otherwise known as photoexcitation. When the electrons

relax and recombine, this results in light emission, where the energy is equal to the difference between the excited state and the relaxed state. Excess energy produced during the recombination process is lost due to impurities and defects. The emission of light is collected by the photodetector and directed toward the spectrometer to be measured. The PL spectrum is controlled by a range of factors, such as impurities and defects, which alter the radiative transitions [152]. The peak wavelength of the PL spectrum is equal to the band gap energy, which is the standard excitation mechanism where an electron is promoted (and relaxes) between the valence band and the conduction band. At the same time, the PL's high intensity and low linewidth is an indication of good material quality.

In this work, a series of PL setups are used: a room temperature PL (RT-PL) for bulk and extended emission range (>1600 nm) measurements and two different low-temperature micro-PL (LT-µPL) setups with different capabilities. The LT-µPL setup (*Setup 1*) available within the research group includes an InGaAs and silicon detector with coarse movement to allow for multiple samples to be measured simultaneously. This setup was used to characterise InP-based samples and initial site-controlled QDs samples. The other LT-µPL setup (*Setup 2*) is an imaging and spectrometer setup used in collaboration with Dr Dominic Hallett and the Department of Physics for site-control QD imaging and device characterisation. This setup is optimised for ranges between 900 nm and 1000 nm and allows for a wide area excitation with the use of an LED.

RT-PL setup is used to generate full wafer mapping, including various parameters, by measuring the optical emissions from the sample at room temperature. This is achieved by measuring multiple spectrums across the wafer to form the full map, which is acquired using an Accent RPM2000 PL mapper. To excite the wafer, a 656 nm diode laser with ~36.4mW excitation power is used with a 150 g/mm grating and detected with a Hamamatsu G9208 InGaAs detector with an extended response up to 2200 nm. Room temperature measurements offer rapid feedback in emission wavelength but lack high PL intensity caused by non-radiative recombination centres and additional peaks due to carriers escaping to higher energy levels. This was used to measure rapid thermal annealing samples to provide a quick characterisation of the annealing effects.

For µPL, *Setup 1*, samples are excited via a fibre-coupled 635 nm red diode laser with a power density of approximately 4.5 W/cm^2, which is controlled with a neutral density filter wheel. A Princeton Instruments SP2750 spectrometer includes a cryogenically cooled PyLoN IR InGaAs detector at 600 lines/mm grating and a PyLoN Silicon detector at 1200 lines/mm grating. Other configurations with the detectors and gratings are possible for higher spectral resolution depending on the wavelength range required and application. This allows measurements of emission wavelength from 800 nm to 1600nm with high collection efficiency when both detectors are used. The response of the InGaAs

detector on the LT-µPL system is limited to 1600 nm, so single QD emission at longer wavelengths may not be detected. A white light source and CMOS camera are also installed to illuminate and visualise the sample surface to position the setup to a desired location. A series of beam splitters are used to direct the laser beam and white light into the objective lens and focus on the sample, one is installed at the start of the excitation path to enable the laser and WLS source to be direction into the same optical path. The second beam splitter is at the collection of the of the optical setup to split the collection path into two: one to the CMOS camera and one to the collimator to the spectrometer. Within this setup, a series of open-loop linear actuators (N-470.V Piezo Mike) is used for each axis (XYZ) allows for a larger range of moments across the sample plate with a controller with 20 nm step size or manual adjustments with up to 300 mm movement. These actuators are installed at the base of the optical setup to enable translation of the optical cage rather than the cryostat. The disadvantage of this method of movement is that it lacks the precision and feedback loop on each movement to be able to repeatability and reliably move back onto the same positions within a sample, and improvements to this are introduced later. In addition, for fine structure measurements, a polariser can be installed into the setup when required. All samples are bonded onto a copper sample plate using silver paint, which can be installed into the cryostat. The cryostat is then purged with nitrogen, and when under vacuum, the sample plate is cooled down to 5K by a closed loop compressor before measurements are performed. Figure 3- 13 shows the schematic of Setup 1. In this setup, measurements are performed for single dot characterisation for InP-based samples with the InGaAs detector. For GaAs-based samples, additional QD mapping of site-controlled QDs and FSS measurements are also performed.
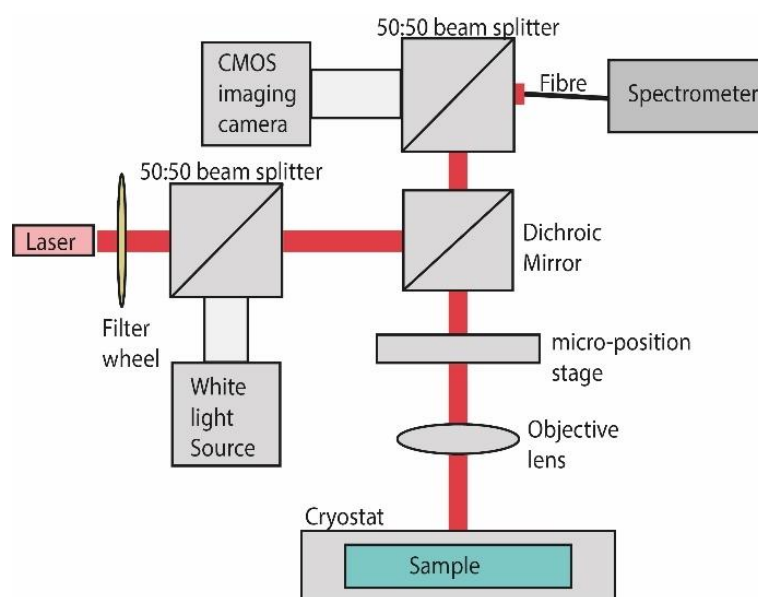

Figure 3- 13 A schematic diagram of µPL (Setup 1) within the research group used for ensemble dot measurements, single dot mapping, which is capable of measuring QD ranging from 800 nm to 1600 nm.

Setup 2 is more focused on InAs/GaAs QD samples and optimised for emissions between 900 nm and 1000 nm with capabilities including voltage biasing devices and PL imaging. Figure 3- 14 shows a complete schematic of Setup 2. For the excitation source, an 810 nm light emitting diode (LED) was used, which causes above-band excitation and can excite a larger area than a laser. The LED excitation source was voltage-controlled, but the typical excitation power used has a power density of ~5.9 W/cm^2 at 2.8V. The excitation path then reach a beam splitter which reflects the light towards the sample by an objective lens. The setup includes an adjustable filter used in between two beam splitters to block the LED light from reaching the camera. Light is then directed towards a PyLoN Silicon detector and a sensitive imaging Si CCD camera. A closed loop positioning stage is also installed to allow the sample to be moved under the setup, allowing for single QDs to be measured and collected by the fibre. Samples are mounted by silver paint onto a cold finger, which is cooled by a continuous flow helium cryostat.
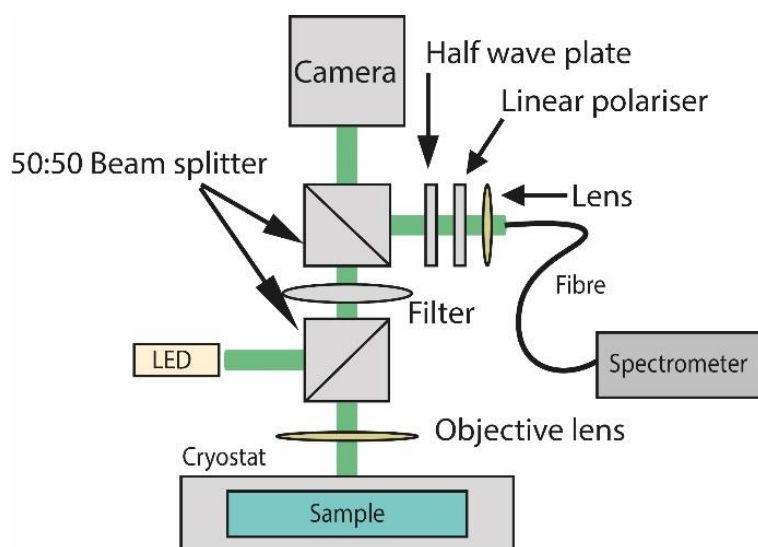

Figure 3- 14 A schematic diagram of μPL (Setup 2) located in D49 in the Department of Physics used for PL imaging and PL measurements targeted wavelength emission between 900 nm to 1050 nm.

Rapid Thermal annealing (RTA)

Rapid Thermal annealing (RTA) is a post-growth method that rapidly heats semiconductor samples to high temperatures (>1000 K) in a short period, from a few seconds up to 30 minutes. This allows changes to the material properties of a sample, which are controlled by the temperature, annealing duration, ramp time and ambient gas. A typical setup will have a high-intensity heat source in the form of an IR lamp or tungsten-halogen lamp placed near the sample surface. To control temperature pyrometers and thermocouples are used to measure the sample's temperature. A method of cooling is required to control the rate of heating to prevent sample breakage and dislocation forming. RTA is a conventional method for the activation of dopants and the interfacial reaction of metal contacts. However, as a post-growth method, the use of high-temperature annealing is to encourage

intermixing and outdiffusion of atoms within the material structure to change the optical characteristics of the sample.

For this work, an ECM JetFirst RTP system was used to anneal InAs/InP QD samples. This system is a lamp furnace with a pyrometer and 3 thermocouples are placed across the silicon carrier wafer for higher temperatures up to 900°C. The system also contains a PID control system that is calibrated to a 4-inch silicon wafer to enable precise temperature control. Figure 3- 15 shows a schematic diagram of the RTA system used. During annealing, the chamber is filled with N_2 gas (2000 sccm) while ramping to a starting temperature of 200°C before ramping and holding at the desired temperature before cooling down to room temperature. This system's ramp rates will vary based on the target temperature as the ramping duration; in our experiment, 30 seconds was used. Controlling the cooling of the sample is essential, as rapid cooling can cause thermal shock and the formation of unwanted dislocations, and to prevent this, samples are slowly cool down over 3 minutes to room temperature.
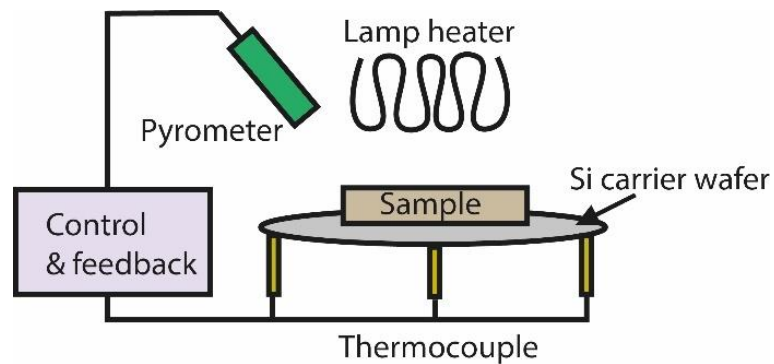

Figure 3- 15 A basic schematic for ECM JetFirst RTP system with the key components labelled.

4 Growth and characterisation: undoped Site-Control waveguides

Site-controlled QDs (SCQDs) have the benefit of being deterministically positioned, making them suitable for use in quantum photonic devices as building blocks for photonic qubits. Other suitable devices using SCQDs have been demonstrated, including photonic cavities [12], Schottky diodes [153], and photonic resonators [154]. A high yield of usable SCQDs is crucial for scalability technologies, allowing for mass manufacturing and complex device fabricating using multiple QDs. To achieve these conditions, the ability to reproduce samples with high QD occupancy with site-control is important. Jöns et al, have presented high quality SCQD, with linewidth as low as 6 µeV suitable for single photons sources but no details regarding neighbouring QDs with comparable optical properties was reported [82]. Ovenden et al, have previously demonstrated the ability to achieve high occupancy SCQDs (>90%) with initial optical characterisation on standard GaAs capped structures [109] but the structures used contained only GaAs layers with InAs QDs unsuitable for device fabrication. In this chapter, waveguide structure, shown in Figure 4- 1a, was used, which differs from previous studies performed by Charlotte et al [109], by the addition of a sacrificial AlGaAs layer to allow for the fabrication of free-standing waveguide devices. We also investigated the use of growth techniques such as growth interrupt (GI) and indium flushing to enable the control of optical properties in this chapter.

Figure 4- 1b-c shows the structures required to investigate these growth techniques (GI and indium flushing) whilst keeping the total thickness of the structure the same; the details of the growth conditions are discussed later. GI is a technique which pauses the growth after the InAs deposition for a short period to allow for indium migration across the surface [48]. This enables more uniform deposition of indium across the surface and on a patterned surface assist indium in migrating into nanoholes for high occupancy [155]. On the other hand, indium flushing controls the height of the QDs by introducing a thin layer of GaAs after QD deposition and removes exposed areas of QDs with high growth temperature and high arsenic flux [57]. This addition of this techniques, improve the QD shape uniformity, and improve uniformity of QD properties [50] [77]. In this chapter, the use of these techniques are investigated, and the effects on the pattern parameter are determined.
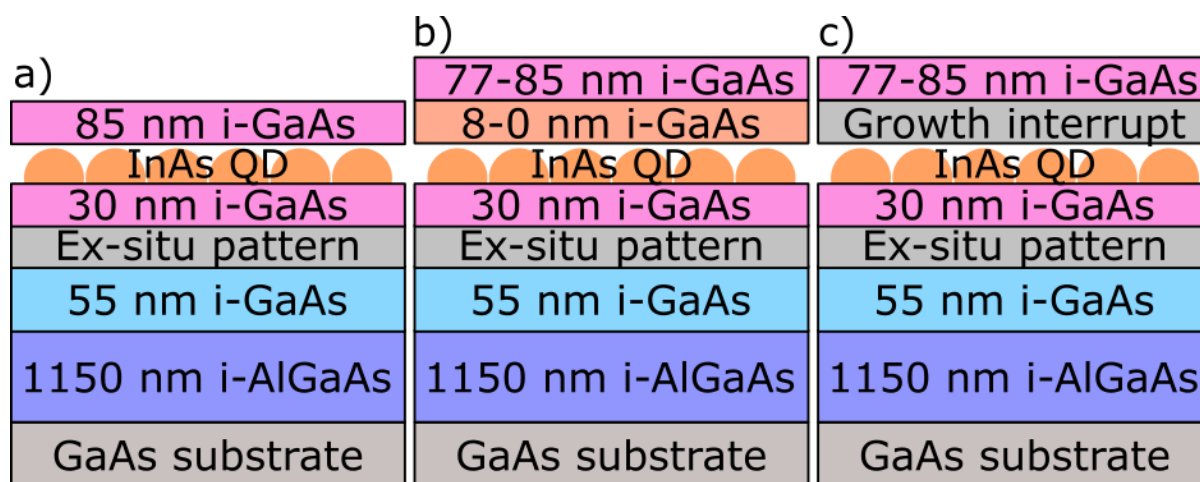
Figure 4- 1 Simple diagram of the undoped waveguide structure used, a) GaAs-only capping, b) partial capping structure with 0 to 8 nm partial capping and corresponding capping layer to equal a total thickness of 85nm and c) GaAs capping structure with growth interrupt.

Undoped SC waveguide growth process

The growth structure used in this chapter is an undoped waveguide structure on GaAs (100), shown in Figure 4- 1a. Initially, an 1150 nm thick AlGaAs sacrificial layer is deposited at 590°C, followed by a 55nm GaAs buffer layer at 590°C. The sample is then removed from the reactor, and the surface is patterned using EBL-ICP; specific details of the process are detailed in Chapter 3. The patterned sample is then re-introduced into the reactor, and the subsequent growth procedure is outlined in Figure 4- 2. The oxide removal step (thermal degas) was carried out at 580°C to maintain the patterned surface since we know that too high temperature leads to surface damage and degradation of the pattern [156]. Prior to QD deposition, 55 nm of GaAs regrowth buffer is deposited at 540°C. This layer is deposited to move the QD deposition away from the original interface, preventing any impurities and damage from being introduced in the QD layer. This also allows partial infilling of nanoholes to help planarise the pattern region in subsequent layer growth. InAs QD are deposited at 500°C for 163s at a rate of 11 nm/h. After the QD layer is deposited, growth interrupt and indium flushing were used to improve QD uniformity and quality, and to control the dot size to achieve the target emission wavelength of around 930 nm. This is an ideal emission range for highly efficient Si detectors [157]. Following QD growth, a layer of GaAs is deposited as a cap, with a thickness of 77-85 nm, depending on the growth technique used. For growth interrupt (GI) studies, the interrupt durations used are 30, 60, 180 and 300 seconds, while for indium flushing, the GaAs thin layer is varied from 0, 2, 4, to 8 nm thick. A summary of all the structures grown is shown in Table I, while Figure 4- 1 shows a simple diagram of the structures used.
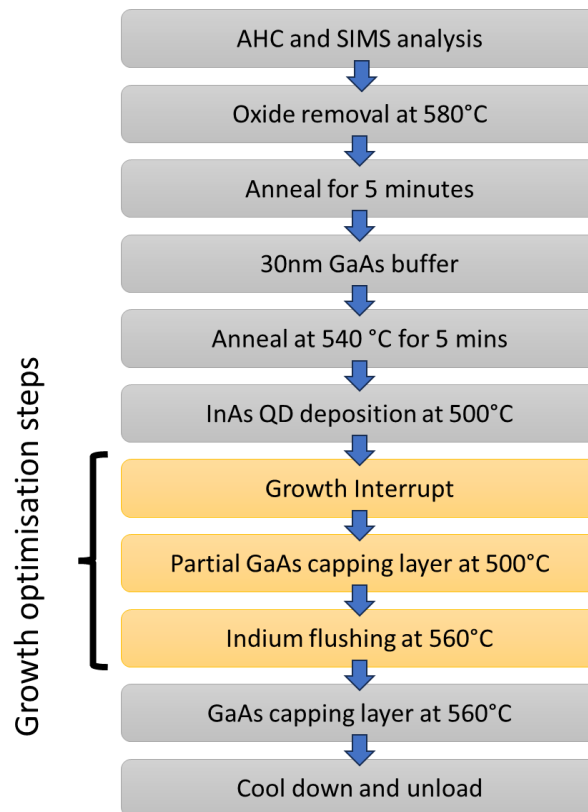
Figure 4- 2 Overview of the overgrowth of the patterned waveguides: grey boxes are standard growth steps (unchanged), and yellow boxes are additional growth steps that are investigated.

Table II A list of site-control growth structures used in this chapter; samples are ordered by the sample number.

Sample number	Control parameter	Structure	Growth interrupt (s)	Partial capping thickness (nm)	Characterisation methods
PR0144	Reference	Undoped waveguide	0	0	PL image/ Ensemble PL
PR0183	Growth interrupt	Undoped waveguide	30	0	PL image/ Ensemble PL
PR0186	Growth interrupt	Undoped waveguide	300	0	PL image/ Ensemble PL
PR0187	Growth interrupt	Undoped waveguide	60	0	PL image/ Ensemble PL
PR0188	Growth interrupt	Undoped waveguide	180	0	PL image/ Ensemble PL
PR0260	Indium flush	Undoped waveguide	60	2	PL image/ Ensemble PL
PR0261	Indium flush	Undoped waveguide	60	4	PL image/ Ensemble PL
PR0262	Indium flush	Undoped waveguide	60	8	PL image/ Ensemble PL Single dot/mapping*

*Single dot/mapping is not presented in this chapter; instead, it is discussed in 5 Single dot characterisations on undoped waveguides.

The capping layer thickness is varied to maintain a total thickness of the waveguide structure of 170nm, keeping the QD position also in the centre of the structure. To effectively confine the single photons into a single optical mode, the thickness of the waveguide structure is defined by $\lambda/2n$, where λ is the target emission wavelength and n is the refractive index of GaAs (n_{GaAs} = 3.4). Thus, for 930 nm emission, the waveguide should be 137 nm thick. This was later revised to a thickness of 170 nm to allow sufficient space for the implementation of growth techniques and planarisation of the pattern surface without significant losses the efficiency of QD emissions [51]. A thicker structure traps higher-order optical mode within the structure and therefore, does not pose a major problem for the optical properties of QDs and waveguiding of single photons.

µPL measurements using *Setup 1* was used to investigate the effects of different growth techniques by observing large groups of single dots emissions with low excitation power (100 µW). For this type of measurement, the objective lens is changed to a 10x lens to allow a large area coverage of a 50 µm diameter laser spot on the sample surface, reducing the power density. To excite the surface, a red diode laser with an excitation power of 100 µW was used. *Setup 2* was also used for rapid feedback by PL imaging and provides a visual aid to determine QD occupancy. To visualise the presence of positioned QD within the array, techniques were employed to filter out unwanted emission ranges (< 1050 nm). The presence of a high density of long wavelength dots reduces the visualisation of single QD emissions within the ordered arrays. To remove these long wavelength emissions (< 1050 nm), the addition of a low pass filter in these measurements helps identify the uniformity of QD emissions. It should be noted that the absence of emissions from the images and in nanohole positions does not imply the lack of QD occupation. For full details regarding the differences between the different µPL used in this section, we refer to Chapter 3 for the specific details.

Undoped site-control waveguide reference sample

An undoped SC waveguide with a standard GaAs cap was used as a reference (See Figure 4- 1a). PL images with different pitches of the reference structure are shown in Figure 4- 3. Regardless of the pitch, high-level QD occupancy is achieved while maintaining good imaging of the pattern. At 0.6 µm pitch, high QD occupancy is achieved regardless of the e-beam dose and nanohole size, but for higher pitch sizes, the nanohole size and e-beam dose have an impact on QD emissions. For pitches larger than 0.6 µm and smaller nanohole size arrays, the presence of QD emissions decreases, whilst the larger nanohole sizes preserve high QD occupancy. The QD occupancy across the arrays suggests uniform deposition of InAs across the pattern regions, including depositions within the alignment markers, is achieved. This is evident by the uniform intensity observed from the PL images, as alignment makers often act as preferred nucleation sites, and more InAs deposition is deposited in these areas over the nanohole arrays, resulting in bright emissions. Maintaining a uniform QD

occupancy at larger pitches is important as the laser spot of the setup used is ~5 μm diameter (with 100x objective lens), which makes it suitable for single dot measurements at the 4.8 μm pitch. In contrast, smaller pitches will result in multiple dots being measured, making them more suitable to characterise as ensemble emissions.
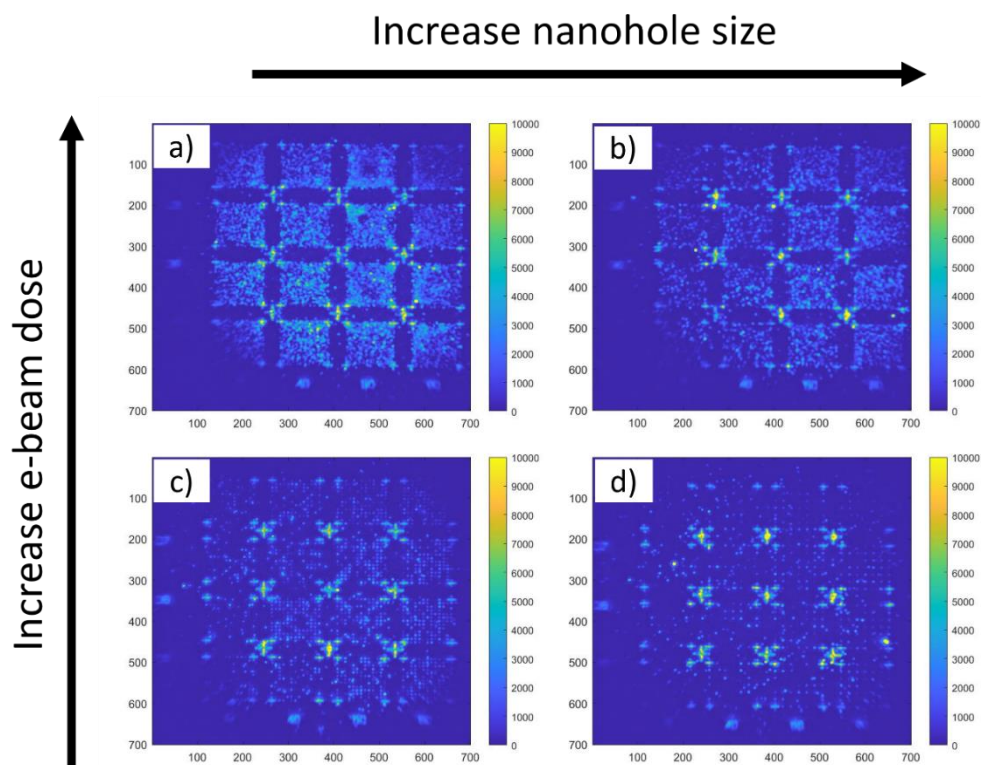

Figure 4- 3 PL image of SC QD growth without any growth techniques at a) 0.6 μm pitch, b) 1.2 μm pitch, c) 2.4 μm pitch, d) 4.8 μm pitch. The arrays show an increase in nanohole size from left to right and an increase in e-beam dose from bottom to top.

Figure 4- 4 show the integral intensity of individual arrays from the PL images. As the pitch increases, the integral intensity decreases due to the number of etched pitches available within each array, which determine the QD density. For example, 0.6 μm pitch has 49 x 49 nanoholes vs 4.8 μm pitch, which has a 7 x 7, 49 times decrease in QD density. The difference in pitch shows a decrease in integral intensity by ~8 times, but this is lower than expected, suggesting a variation in occupancy between the pitch is present. This is reinforced by the non-uniform intensity of individual arrays within a set pitch, with the brightest arrays at the centre of the pattern with 50D2 (50 nm diameter nanoholes with e-beam dose 2) array being the brightest and the corners arrays showing poor integral intensity in most of the pitches investigated. This variation in intensity suggests indium deposition favouring arrays in the centre of the pattern compared to the edges of the pattern, due to the larger density of facets in the vicinity. Alternatively, this could suggest that the patterning parameters at the corners 32D1, 32D4, and 60D8 are not ideal pattern parameter conditions to enhance QD occupation.
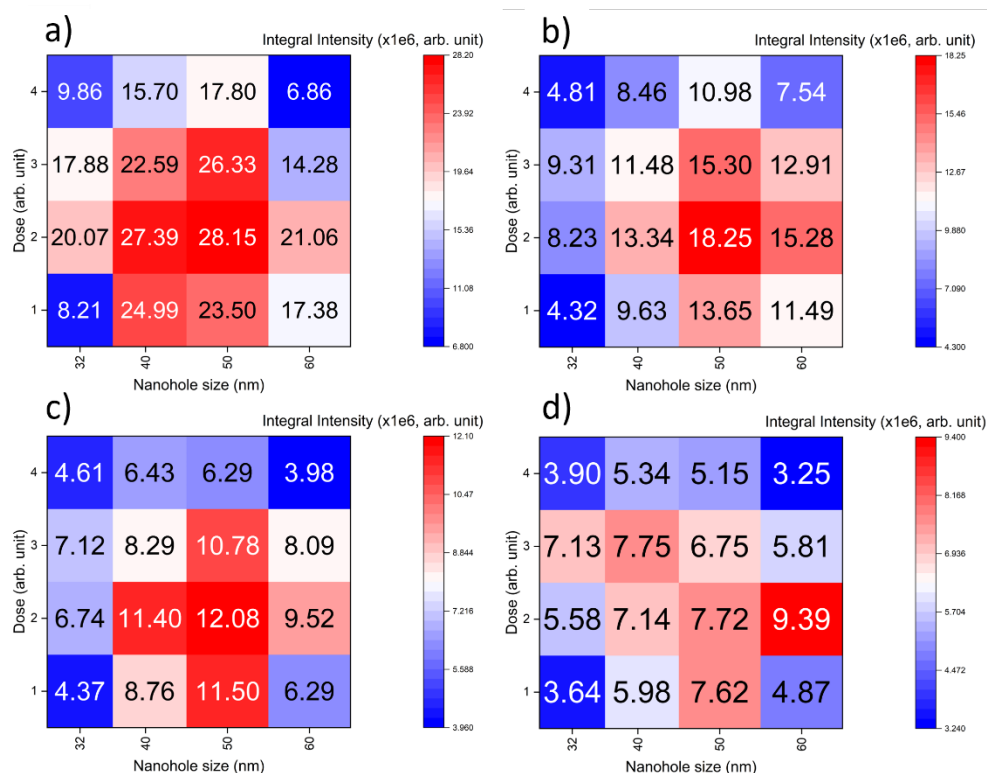
Figure 4- 4 Integral intensity of individual arrays of the control sample across the different pitches: a) 0.6 µm, b) 1.2 µm pitch, c) 2.4 µm, d) 4.8 µm.

Figure 4- 5 shows an example of the ensemble PL spectrum of an array at 0.6 µm pitch. A broad ensemble emission is obtained ranging between 910 nm to 1030 nm, an indication that the QD present within the arrays has a large size distribution [45]. As the control sample, this demonstrates that SCQD growth without any optimisation to control the QD size and shape with significant improvement is required. The broad ensemble emission, with an FWHM of ~100 nm, makes this approach unsuitable for tuning QDs into the same emission wavelength via quantum confinement stark effect as there is a maximum shift of 25 meV achievable [158]. We, therefore, investigated a range of growth techniques to control and improve the distribution of QD shapes and quality in the arrays. In terms of growth optimisation, the use of growth interrupt [48] or partial capping with indium flushing [93] has previously been demonstrated to be a suitable technique to improve the QD shape and size, which helps narrow ensemble emissions.
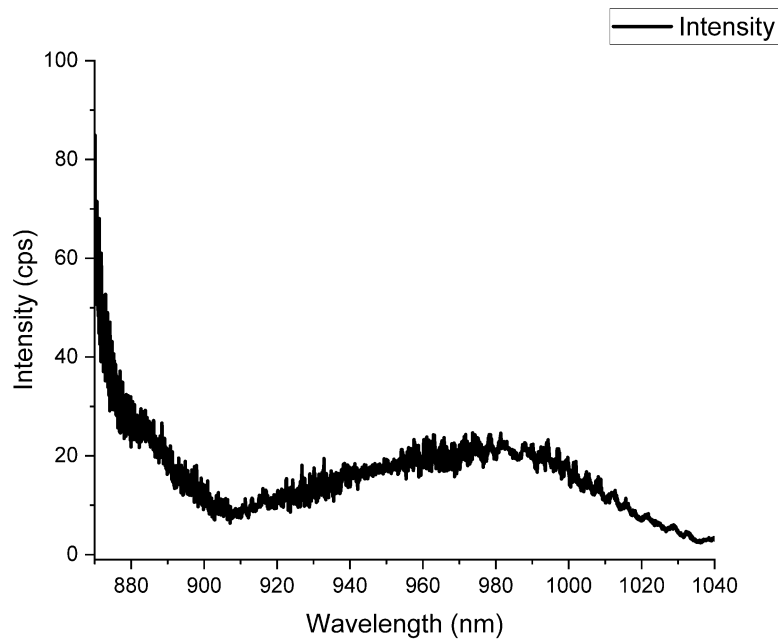
Figure 4- 5 Ensemble PL spectrum of SCQD growth with a GaAs-only capping structure at 0.6 μm pitch, 40D7 array.

Growth optimisation: Growth interrupt

GI is a highly effective technique in enhancing optical properties by improving the QD aspect ratio (height/width) [49]. This technique was used after the deposition of InAs QDs, where a short period of interruption is introduced that enables annealing of the dots at the same temperature and similar As flux. This gives time for indium atoms to reorganise into a more stable position. The arsenic shutter remains open with a constant flux until the growth of the GaAs capping layer. By changing the GI duration, the amount of indium migration can be controlled, which impacts the size and shape of the QDs [159]. This also reduces the density of QDs as smaller InAs QDs can migrate across the surface and coalesce together to achieve In-rich QDs with very uniform size distribution [48]. For the remainder of this chapter, unless stated otherwise, all PL images will be from the 2.4 μm pitch as good visibility of single dot positions within the array is presented, as demonstrated in Figure 4- 3c.

The PL images of the site-control pattern after regrowth with different GI (30 seconds to 300 seconds) are shown in Figure 4- 6. The introduction of GI does not degrade the presence of QD within an ordered array and the presence of the pattern is maintained with clear identification between the alignment markers and QDs. The QD emissions is a mixture of random positions and ordered QDs, and the density is dependent on the GI used. The presence of randomly nucleated QDs around the pattern region increases with increasing GI. Below 180 second GI, the visibility of the positioned QDs are hindered by the bright alignment markers, which is a contrast to the growth without any growth techniques (see Figure 4- 3c). When GI is above 180 second, the visibility between the positioned QDs and the alignment markers improves significantly. We believe that the PL intensity from the alignment

markers decreases significantly and becomes more comparable with positioned QDs emissions, as the positioned QD emission is shifted into our detection range with higher GI duration. The longer GI duration allows indium atoms to migrate for longer distances, increasing InAs distribution across the pattern region with the etched pits acting as a preferential nucleation site [76]. As shown in the literature, the QD formation with GI has also been demonstrated to be altered by allowing the migration of indium atoms and coalescence under Ostwald-type ripening [160]. In addition, by increasing the size and quality controls (reduction in defect density), QD emissions shift emissions towards the detectable range (< 1050 nm) [7]. The lack of emissions from the QD arrays is not direct evidence of no QD occupancy. Instead, this could be a lack of optically active QDs or QD emitting outside the range of the detector could also be contributing factors.
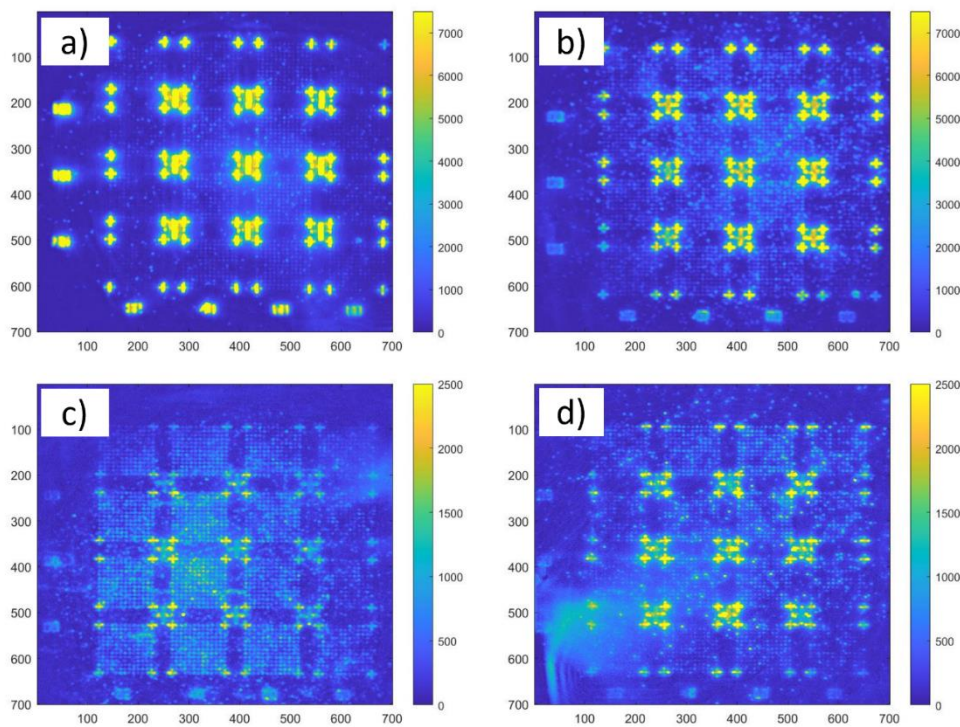

Figure 4- 6 PL image of site-control QDs with a pitch of 2.4 µm with varying growth interrupt, a) 30 seconds, b) 60 seconds, c) 180 seconds, d) 300 seconds. The arrays show an increase in nanohole size from left to right and an increase in e-beam dose from bottom to top.

To investigate the intensity of the arrays between different pattern parameters, integral PL intensity was measured for each array. Figure 4- 7 shows the integral intensity of individual arrays with pattern parameters and different GI durations. With GI above 180 seconds, the integral intensity is decreased by a factor of 3, which could be attributed to the desorption of indium with high GI duration. Pohl et al, have demonstrated the effects of desorption to reduce the density of optically active QDs and shift emissions [160]. We believe a similar observation is observed where the desorption reduces the amount of indium within the etched nanoholes, which results in a decrease in PL intensity. The

brightness uniformity between individual arrays is also improved by ~50 % with the introduction of GI when compared to the control sample (see Figure 4- 3c). The position of the brightest array for any GI is found to be within the centre regions of the pattern, but with varying GI, exact array changes from between the centre arrays (40D2, 40D3, 50D2 and 50D3). Based on the variation between different GI durations, this reinforces the previous assumption that indium deposition is influenced by the large number of pattern facets where the centre of the pattern has the highest density. The larger number of facets within the centre region could be acting as a higher preferred nucleation site compared to the edge arrays. In summary:

- High QD occupation with a good visual of the pattern is maintained.
- A high density of randomly nucleated QDs within the pattern regions is introduced.
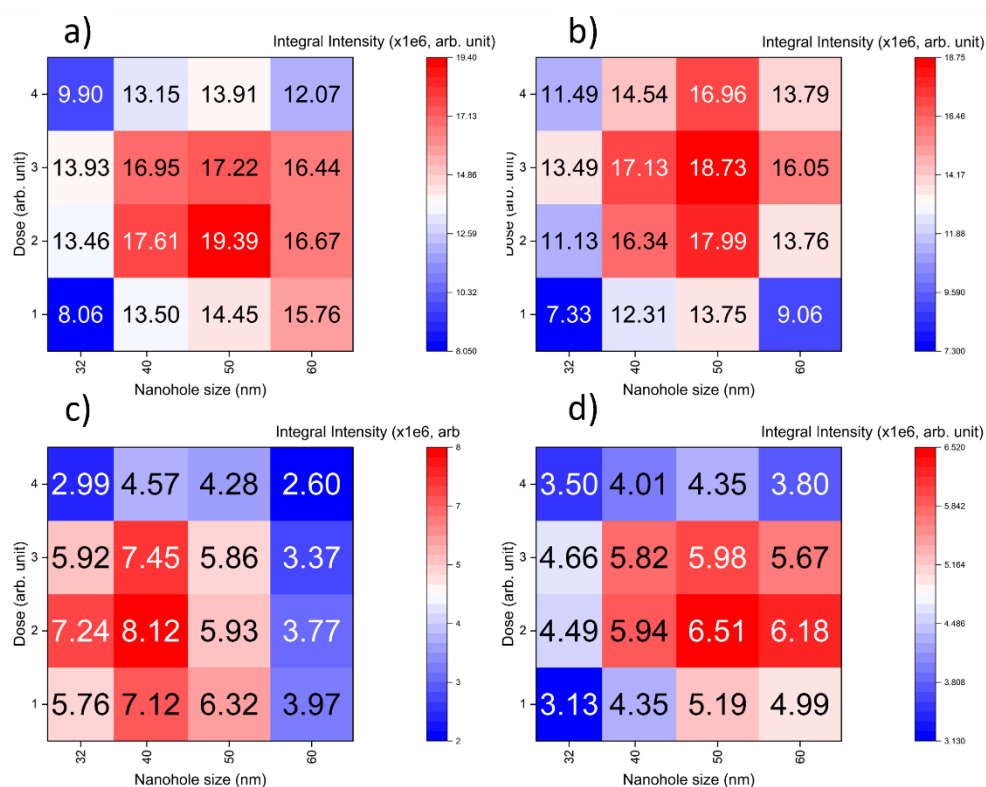- PL intensity within the arrays improves compared to the control sample.

Figure 4- 7 Integral intensity of individual arrays at 2.4 µm with different growth interrupts: a) 30 seconds, b) 60 seconds, c) 180 seconds, d) 300 seconds.

Figure 4-8a-d shows the ensemble PL spectrum with varying GI between 30 seconds and 300 seconds. The use of GI has resulted in a significant narrowing of ensemble emissions achieved when compared to the control sample, shown in Figure 4- 3. At the shortest GI (30 seconds), the FWHM has dramatically reduced by 75 nm compared to the control sample to 90.0 nm, and the subsequent increase in the GI duration results in a controllable broadening of ensemble emissions to a maximum

FWHM of 41.3 nm (180 seconds GI). At a longer GI (300 seconds), the emission again narrows to a FWHM of 32.4 nm. The narrowing of ensemble emissions is evidence that the size of the QD ensemble is very uniform [48] [155]. At the longer GI, indium atoms can migrate over longer distances, resulting in a larger QD size and aspect ratio [7], which will broaden the ensemble emissions [159]. The shifting of the peak ensemble also follows a similar trend, where between 30 seconds and 180 seconds, a controllable redshifting of up to 70 nm is achieved, but at 300 seconds GI, a blueshift of 40 nm is observed. Figure 4-8 summarises these changes to the ensemble peak with different GI durations. The increase in QD size previously discussed is also the contributing factor to the redshifting of the ensemble [48] [160], with GI between 30 seconds and 180 seconds. Convertino et al, report indium desorption becomes the dominating mechanism when GI exceed 200 seconds, causing rapid degradation of QD morphology [161] and redshift ensemble emission [160] and reducing the density of optically active QDs [161]. From the ensemble from all GI samples, peak emissions are emitting below 1050 nm, which eliminates the possibility of optically inactive QDs within the ordered array. The suitable sample identified for additional investigation is the 60 second GI sample, as this sample provided the best PL intensity while maintaining a low FWHM and comparable ensemble emission close to the 930 nm target. To potentially improve the optical properties and allow an additional degree of control, an investigation into the effect of different pattern parameters, such as nanohole size and e-beam dose, on optical properties is needed. In summary:

- The addition of GI improves ensemble QD properties significantly.
- Varying GI duration controls emission shifting up to 70 nm and FWHM by 41.3 nm.
- Above 180 seconds GI, indium is desorbing which causes blueshift to QD emissions.
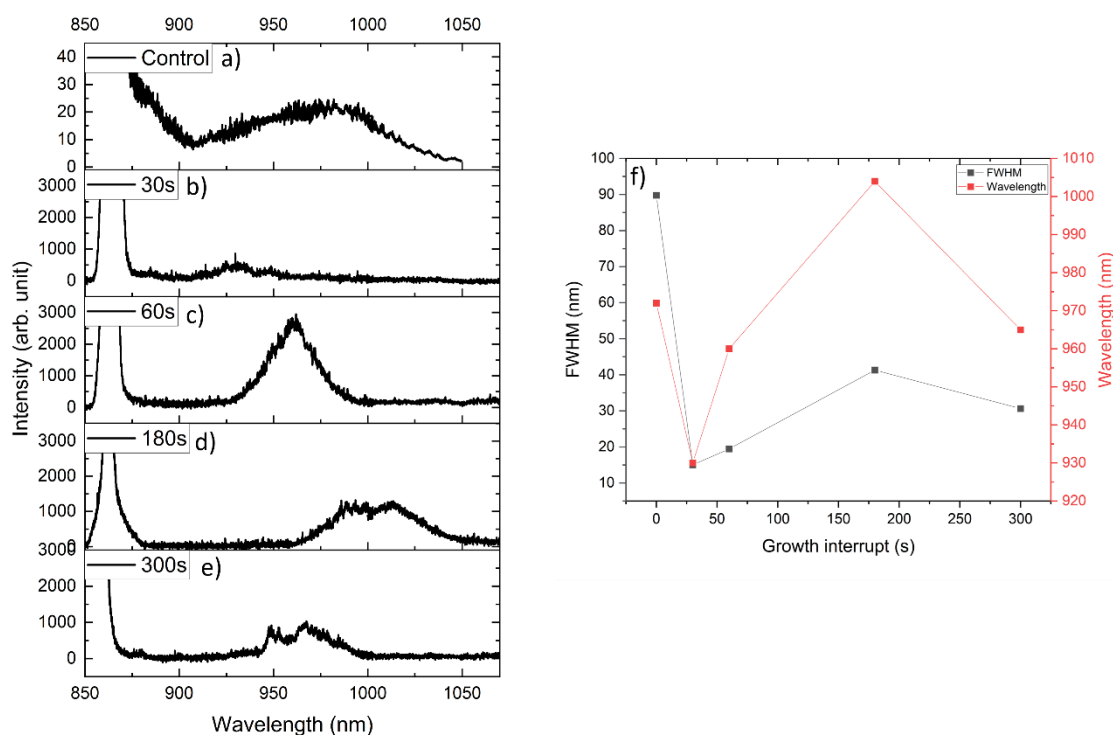
Figure 4- 8 Ensemble PL spectrum of growth interrupt a) control sample b)30 seconds c) 60 seconds d) 180 seconds e) 300 seconds and f) analysis of ensemble PL spectrum on FWHM and peak wavelength for varying growth interrupt.

The effects of different e-beam doses with 60 seconds GI is shown in Figure 4-9a-d, where (a) dose 4, (b) dose 3, (c) dose 2 and (d) dose 1. With decreasing e-beam dose, the ensemble emission degrades until 32D1 with no QD emission. The decrease in PL intensity suggests an increase in defect density [7]. At 32D2, the ensemble is still present; however, the emissions have broadened significantly with poor PL intensity. The ensemble emissions observed between 32D3 and 32D4 arrays (32 nm diameter nanoholes with e-beam dose 3 and 4, respectively) show an improved PL intensity by 3 times and FWHM by ~50 nm, with an emission shift of 10 nm. The summary of the peak emission and FWHM dependent on the e-beam dose are shown in Figure 4-9e. As such, the largest dose (dose 4) is identified as the suitable array, due to brighter emissions and better ensemble properties, suitable for further investigation where different nanohole sizes are compared. In summary, by varying the e-beam dose with 60 seconds GI:

- PL intensity is dependent on e-beam dose.
- A maximum of 10 nm emission shifting with varying e-beam dose.
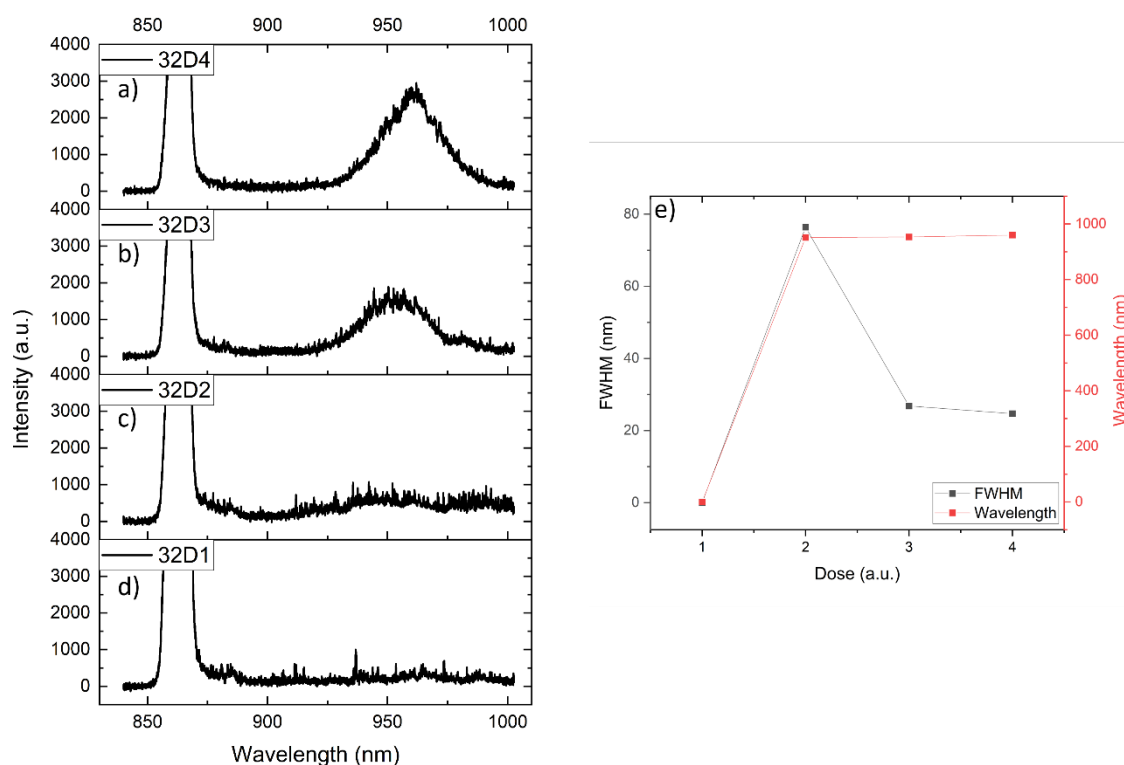- FWHM degrades significantly at 32D2.

Figure 4- 9 Ensemble PL spectrum with 60 seconds growth interrupt, comparing different e-beam doses a) 32D4, b) 32D3, c) 32D2, d) 32D1, and e) analysis of ensemble PL spectrum on FWHM and peak wavelength.

Figure 4-10a-d presents ensemble emissions comparing the different nanohole sizes between 32 nm and 60 nm with a 60 second GI. At the smallest nanohole array (32D4), the ensemble emissions are centred at 963 nm and increasing the nanohole size to 40 nm results in a redshift in the ensemble by 10 nm to 973 nm. A further increase in the nanohole size allows a controllable blueshift of the ensemble emission by up to 15 nm. A comparable trend is found with the FWHM where between 32 nm and 40 nm nanohole size, the ensemble emission broadens by 5 nm and increasing nanohole size beyond 40 nm will cause the narrowing of the ensemble by ~6 nm at 60 nm nanohole diameter. The graph in Figure 4-10e shows the summary of FWHM and peak ensemble with respect to the nanohole size. Both the shifting of emissions and FWHM have been determined to be controllable by the nanohole size, as this controls the formation of the QDs. During the GI step, indium diffuses across the surface, enabling smaller QD to coalesce into larger QDs within nanoholes. However, the QD size is limited to the smallest nanohole (32nm), and the nanohole size becomes a determining factor in the QD properties. In contrast, larger nanoholes enable multiple dots to form within a single large nanohole with sufficient space to diffuse uniformly, improving FWHM. Figure 4-10f shows the expected effect of increasing nanohole diameter and correlation to multi-dot occupation *[109]*. Mayer et al have previously demonstrated the influence of nanohole shape and multi-dot occupancy, with

70nm diameter nanoholes having up to 3 QDs *[55]*. Ovenden et al, have also reported multi-dot occupancy and the size of QDs within a etch pit relationship to QD emissions *[109]*. From the different nanohole sizes investigated, 60D4 presented is the most promising array, as it has the narrowest FWHM ensemble (23.8 nm) with a peak emission of 953 nm, which is the closest to the 930 nm target. In summary, with varying nanohole sizes:

- At the smallest nanoholes, QDs are limited by the nanohole.
- At 40 nm diameter, QDs are not limited by the nanohole and redshift of QD emissions.
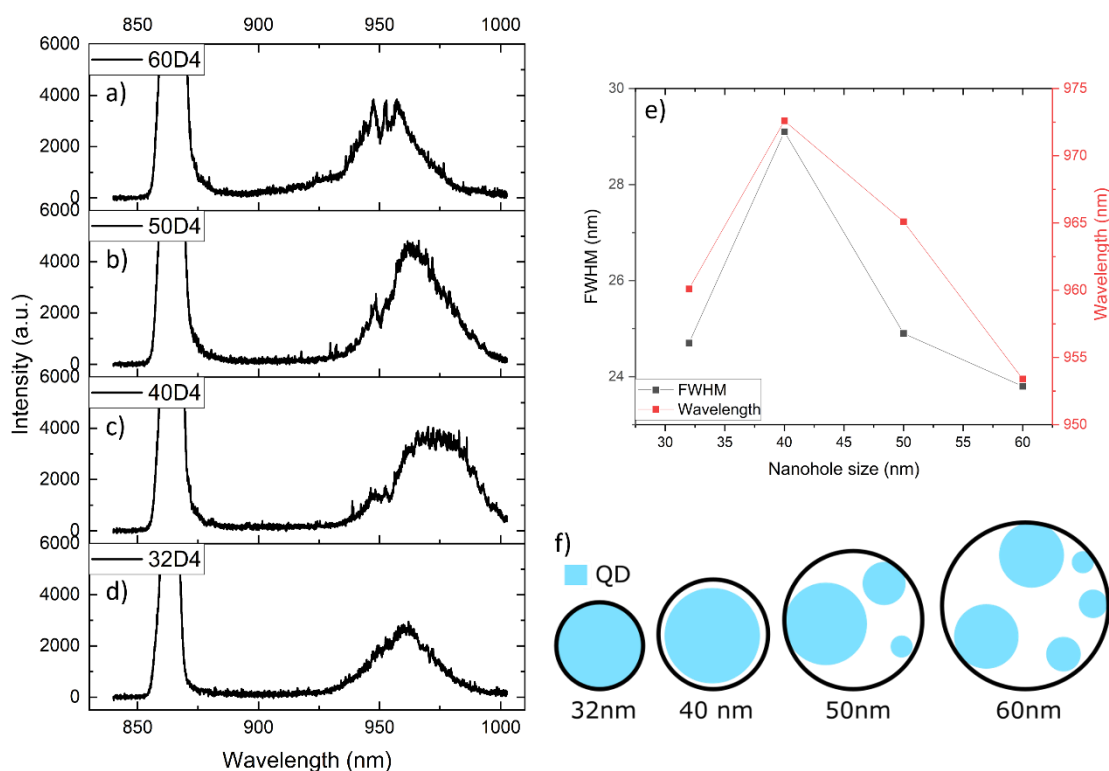- Above 40 nm diameter nanoholes, QD emission blueshifts because of multi-dot occupation.

Figure 4- 10 Ensemble PL spectrum with 60s growth interrupt, comparing different nanohole diameters a) 60D4, b) 50D4, c) 40D4, d) 32D40, e) analysis of ensemble PL spectrum on FWHM and peak wavelength and f) a simple diagram of the expected QD occupation with increasing nanohole size. With a 32nm diameter, the size of the QD is limited by the size of the nanohole, while at the largest nanoholes (60 nm), there is the multi-dot occupations of smaller QDs.

The introduction of GI can reduce size dispersion and allow for highly uniform QD emissions, as shown by the reduction of FWHM from 89 nm (without GI) to 19 nm (60 seconds GI) in Figure 4-8. Increasing the GI duration up to 180 seconds results in a larger FWHM along with a redshift of the ensemble by 70 nm. Additional control over the ensemble emissions by 20 nm is found when different nanohole sizes are investigated. On the other hand, increasing the e-beam dose improves the PL intensity, but at a low dose (dose 1), no ensemble emissions are observed, indicating that a larger e-beam dose is

preferred for good QD emissions. Based on the results presented, the use of a 60 second GI provides a good balance between the improved optical properties and QD occupancy, and within this sample, 60D4 arrays showed the most promise, with ensemble emission centred at 953 nm with a low FWHM of 23.8 nm. However, further improvement by introducing an indium flush could lower FWHM and control the shifting of the peak emissions towards 930 nm and was investigated next [59].

Growth optimisation: Indium flushing

Indium flushing is another technique that is being investigated, which alters the size of QDs and improves QD uniformity [57]. This technique exposes QDs to high arsenic flux at higher temperatures after a thin GaAs cap is deposited, which allows indium to desorb and control the shape of the QDs [93] [162]. During indium flushing, the arsenic flux and growth temperatures are conditions which control the rate of desorption and interdiffusion of atoms [59] [163]. The thin GaAs layer thickness can also be altered prior to indium flushing to control QD height [57] [59]. Figure 4- 11 demonstrates the effect of indium flushing with a thin GaAs layer on different QD sizes. Small QDs are often eliminated after indium flushing, while larger QDs reduce in size, enabling a blueshift in emissions [57] [164]. Currently, the use of indium flushing is mainly reported in stacked SCQD, which prevents the formation of randomly nucleated QD while controlling QD emissions [50] [77], however we believe using this in a single stack still have benefits to improve optical properties. In this investigation, 60 seconds GI was used to ensure good size distribution (optimised from the previous investigation), followed by partial capping (PC) with varying GaAs thicknesses of 2 nm, 4 nm, and 8 nm for indium flushing at 560°C and arsenic flux of 3.8E-6 Torr for 5 minutes, as shown in Figure 4- 1b.
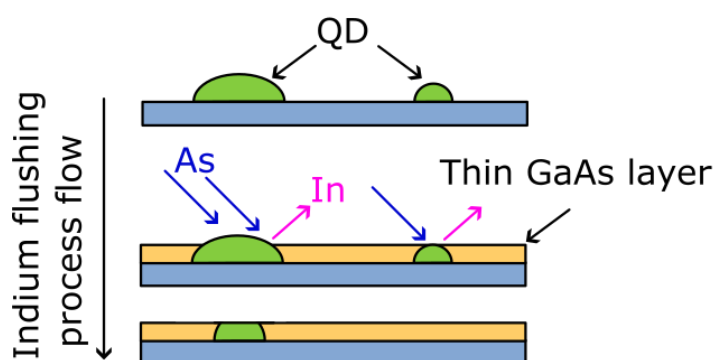

Figure 4- 11 Simple diagram of the indium flushing process with a thin GaAs layer and the changes this technique will affect different QD sizes.

PL images of the site-control QD arrays with varying PC thicknesses are shown in Figure 4- 12. The visibility of the pattern region is maintained after the addition of this technique, which is evident by the presence of ordered arrays of QD emissions and alignment markers. High QD occupancy and single dot emissions are observed in the fully capped sample (control sample) and after the use of indium flushing, the presence of highly ordered QD emissions is reduced. With a PC thickness of 8 nm, the overall positioned QD density decreases, but it cannot be confirmed whether the lack of emissions

within the array is due to a lack of QD occupation during growth or QDs emission emitting beyond 1050 nm. Decreasing the PC to 4 nm, the trend of low density of ordered QD emissions is maintained, and at 2nm PC, a significant increase in QD emission within the pattern region is presented, but it is hard to distinguish between site-controlled QDs or randomly nucleated QDs. The decrease in the presence of QD emissions is attributed to the indium flush step as the fully capped sample maintains high QD occupancy. Lowering the height of QDs leads to a reduction in the volume of smaller QDs at a faster rate than larger ones and, ultimately, results in a decrease in overall QD density because the smallest of dots are eliminated by this step [57] [165]. The brightness between QDs and alignment markers also differs significantly, which is an effect caused by the introduction of GI (see Growth optimisation: Growth interrupt for details). The indium flush affects the PL intensity by allowing previously larger and optically inactive QDs to reduce in size by desorption and become optically active [59]. This mechanism of shrinking larger dots to smaller dots are observed in alignment markers as the numerous facets encouraged more indium to be deposited in this feature over nanoholes during growth [166]. This resulted in the overall integrated brightness of the PL images with indium flushing to increase by 5 times when compared to the full capped (discussed later). We believe for small nanoholes sizes (32nm/40nm), this follows the same mechanics where the previously size limited QDs due to the nanohole is reduced in size and becomes optically active, enabling QD emissions. While for larger nanohole arrays, the formation of multi-dot occupancy of smaller QDs are eliminated with the use of indium flush. A diagram depicting the behaviour of positioned QDs within nanoholes are shown in Figure 4- 13.
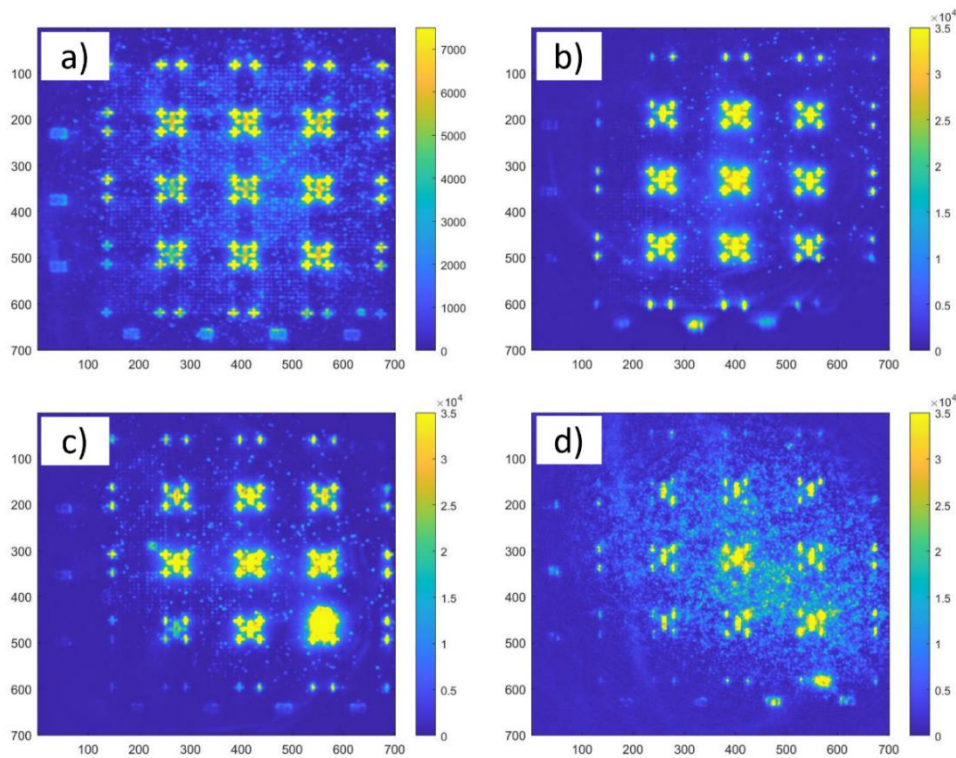
Figure 4- 12 PL image of site-control QD arrays with a pitch of 2.4 μm with varying partial capping thickness a) fully capped, b) 8 nm, c) 4 nm, d) 2 nm. The arrays show an increase in nanohole size from left to right and an increase in e-beam dose from bottom to top.
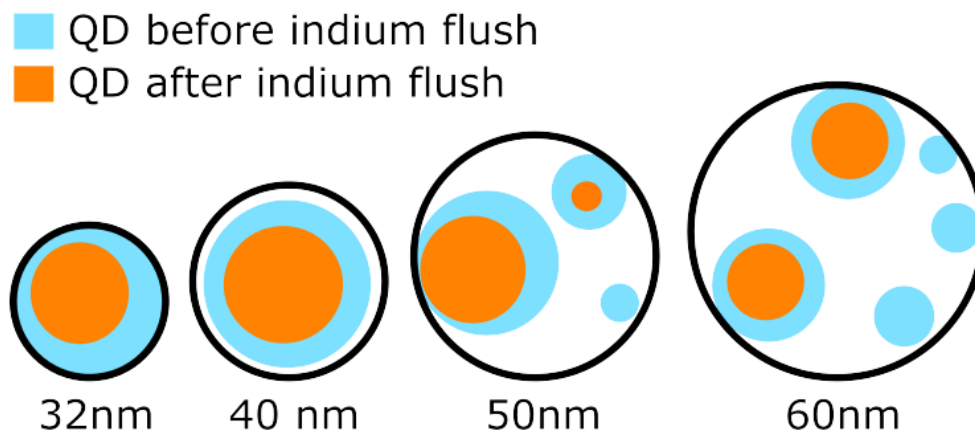

Figure 4- 13 Simple diagram of the expected behaviour to positioned QDs within a nanohole after the implementation of indium flushing for different nanohole sizes (32nm to 60nm).

Figure 4- 14 show the integral intensity of individual arrays with varying PC thicknesses. The high density of QD emissions observed with 2nm PC thickness is represented in the integral intensity with a dramatic increase by 7 times compared to the fully capped sample. While with a thicker PC layer, the integral intensity increased by 4 times to the fully capped sample. This suggest that this technique is also a good solution to improve QD intensity which is caused by the interdiffusion of atoms and reduction of defect density around the arrays during indium flushing [7]. The brightest arrays with indium flushing maintains the trend previously observed (see Figure 4- 4 and Figure 4- 7), where the

brighter arrays are positions centre of the pattern. However, it is notable that the brightest array is not consistently as the 50D2 array, suggesting that the pattern parameters maybe influencing the bright emission and instead are caused by preferential nucleation towards the centre of the array due to an increase number of facets compared to the edges [76] rather than being optimal pattern parameters for QD nucleation. In summary with varying the thin GaAs layer with indium flushing:

- Brightness increases significantly with a thin GaAs layer.

- Decrease in QD occupation with the addition of indium flushing into the growth process.

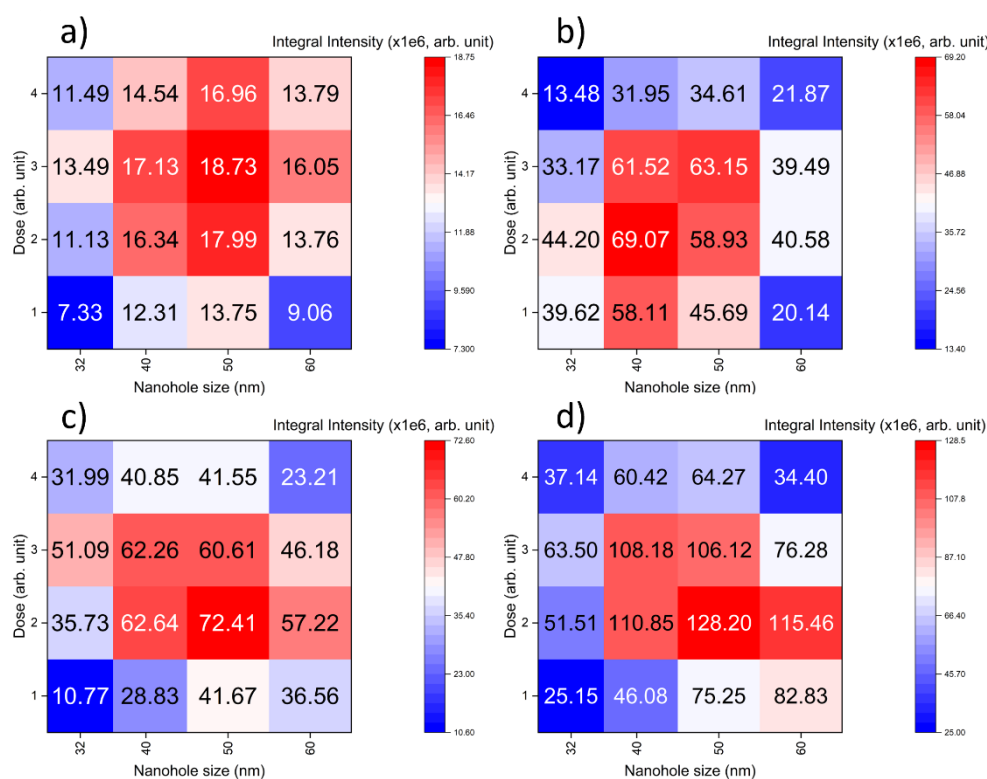- With 2 nm PC for indium flushing results in high density of QD around the pattern region.

Figure 4- 14 Integral intensity of individual arrays from the PL image with varying partial capping thickness a) fully capped, b) 8 nm, c) 4 nm, d) 2 nm.

The effect of varying partial capping was also investigated optically by comparing the ensemble PL spectrum shown in Figure 4-15 a-d. With the largest PC of 8 nm, the ensemble emissions doubles in PL intensity and blueshift by 15 nm, suggesting a thicker PC could be a direction to optimise optical properties further. The thickness of the PC plays a vital role in controlling the QD properties as a decrease in PC thickness to 2 nm leads to a linear blueshift of ~80 nm, and achieves an ensemble emission at 877 nm. For FWHM, a linear trend with an improvement of ~14 nm is shown with decreasing PC thickness. The improvement to FWHM suggests that changes to QD shape still occur during the indium flushing step by controlling the height of the QD, resulting in highly symmetrical QDs [165]. Sasakura et al, report similar improvements to FWHM with the introduction of indium

flushing due to maintaining high structural uniformity of QDs [59]. Figure 4-15e presented a summary of the FWHM and emissions wavelengths dependent on partial capping thickness. The integral intensity of the ensemble also increases with partial capping thickness up to 8 nm. Iizuka et al, attribute increase the in PL intensity due to improvement in QD height uniformity [87]. Similar observation is also seen with thicker PC (4 nm /8 nm), where the height of larger dots are limited to the PC thickness while smaller dots are removed. While for thinner PC thicknesses, larger proportion of QD is exposed and would be desorbed with this technique resulting decrease PL intensity and lower QD occupation [59].

When the PL image (Figure 4- 12) and ensemble PL spectrum are analysed together, this provides a good overview of the benefits. Utilising PC thickness between 4 nm and 8 nm can significantly decrease the number of randomly nucleated QD while retaining ensemble emission of arrays within the 930 nm range. At these two thicknesses for PC, the ability to identify positioned QD emissions from other features (such as alignment marker) is improved, along with good ensemble emission at the 930 nm range, which is a good indicator of suitable growth conditions. The difference between the two PC thicknesses is the absence of QD emissions in some arrays where 4 nm PC shows a higher rate of positioned QD emissions. Nevertheless, the combination of GI and indium flushing has allowed for the control of the shifting of emissions and the improvement of FWHM. With the current aim of optimisation towards the 930 nm range, this approach has proven successful overall, but we now look at the variation of pattern parameters and their effect on dots with indium flushing.

- Emissions shifting of the ensemble by 80 nm with indium flushing.
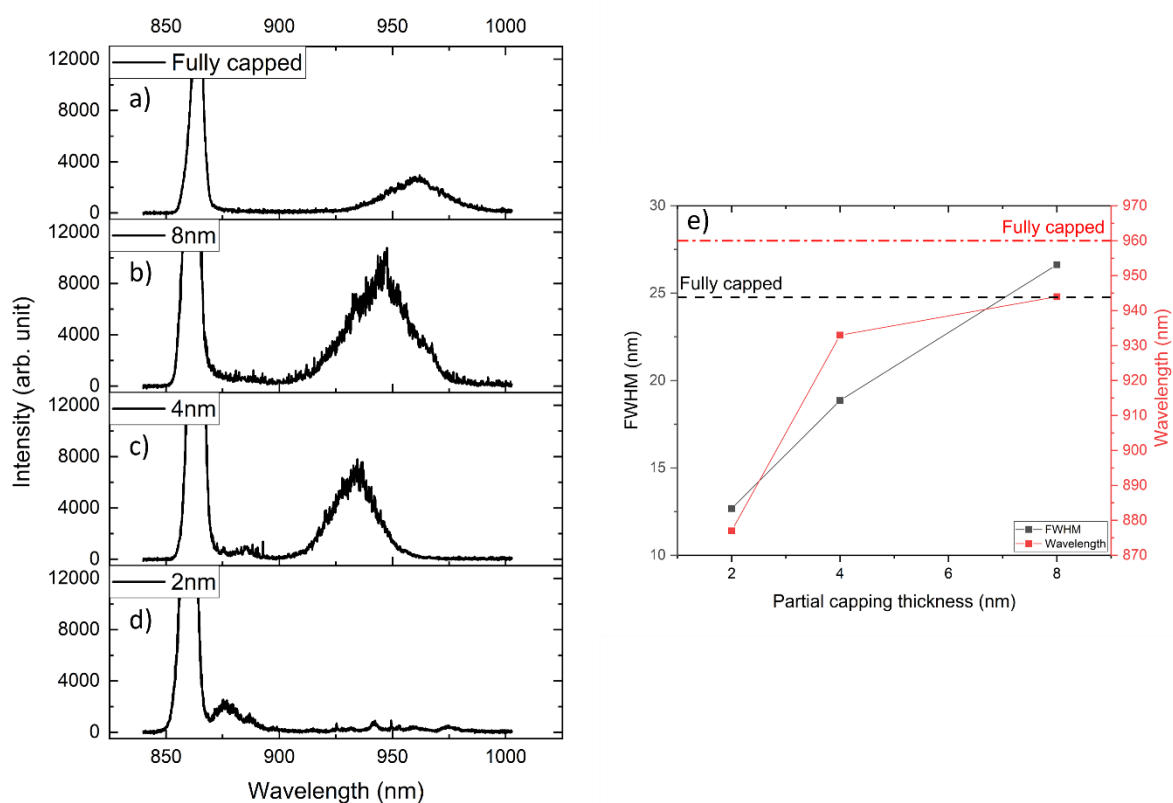- FWHM improves by 14 nm with a thin GaAs layer up to 2nm.

Figure 4- 15 Ensemble PL spectrum with different partial capping thicknesses a) full capped, b) 8 nm, c) 4 nm, d) 2 nm, and e) analysis of ensemble PL spectrum of the FWHM and peak wavelength with the dashed line as full capping

Using a 4nm capped sample, the variation in e-beam dose between dose 1 to dose 4 is shown in Figure 4-16 a-d. When decreasing the dose, the ensemble emission degrades until 32D1, where the ensemble emissions disappear. The best emissions are observed at 32D4, with an emission centred at 930 nm and an FWHM of 18.3 nm. The variation in dose is comparable to GI, where no significant emission shifting is presented, with the largest shifting of 4 nm at 32D2. Therefore, it can be concluded that the emission shifting is not dependent on the e-beam dose. Literature indicates that emission shifting is controlled by the size of the QD, which suggests that variation in the e-beam dose does not drastically alter QD size [57]. Similarly, FWHM across the different doses also does not change drastically or in a controlled manner. The analysis of the effect of e-beam dose on emission wavelength and FWHM is presented in Figure 4-16e. Overall, variation e-beam dose does not alter the ensemble emission properties, but a minimum e-beam dose is required to enable QD emissions.

- Varying e-beam dose, control the emission brightness by up to 4 times
- Minor emission shifting of 4 nm and change in FWHM is observed
- 32D4 arrays the identified as a suitable array and best e-beam dose for further investigation
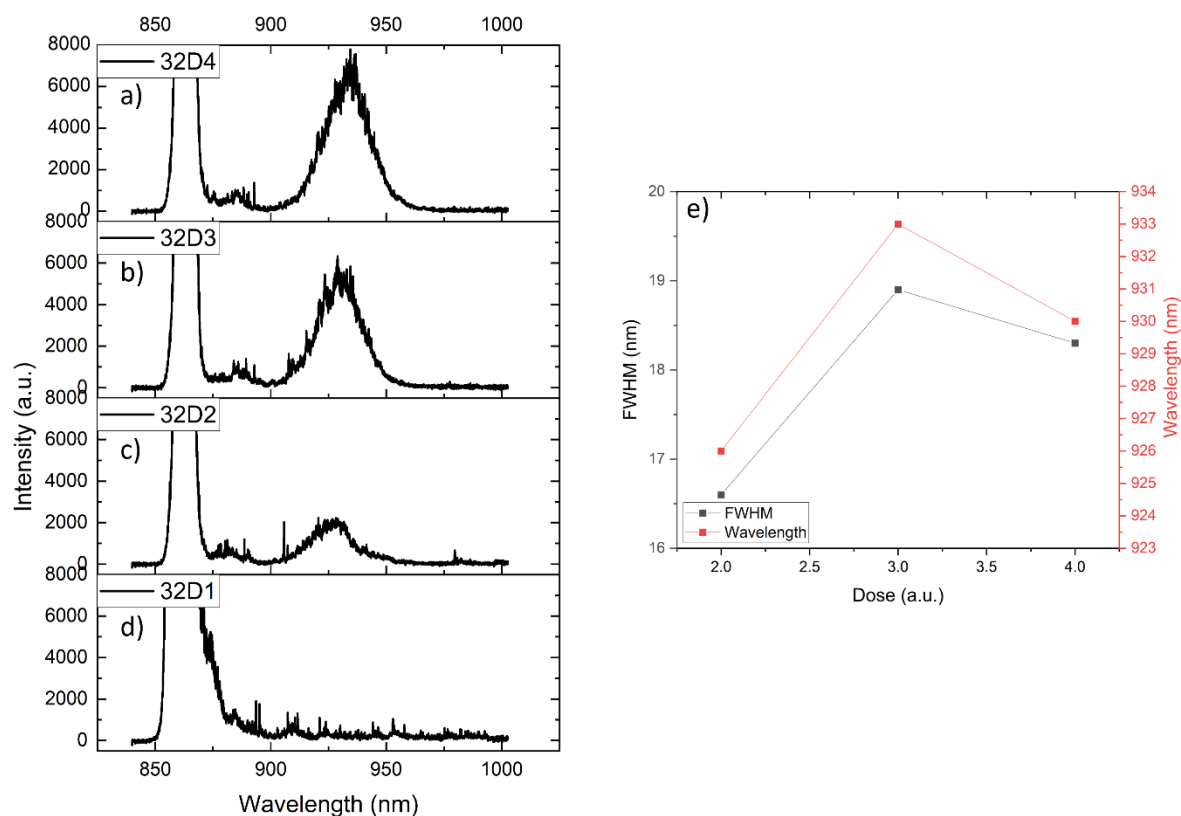
Figure 4- 16 Ensemble PL spectrum on 4nm partial capping, comparing different e-beam doses a) 32D4, b) 32D3, c) 32D2, d) 32D1, and e) analysis of ensemble PL spectrum the FWHM and peak wavelength.

Taking the e-beam dose (dose 4) with the best ensemble emission, we then vary the nanohole diameter and the effect on the ensemble emissions. Figure 4- 17a-d compares PL emission before and after the use of indium flushing with varying nanohole size. With the use of indium flushing and increasing the nanohole diameter, the ensemble emission degrades up to the 60D4 array, where the ensemble emissions disappear and, in its place, dot-like emissions are presented. Figure 4- 11 provides a simple diagram of the expected behaviour of QDs with the introduction of indium flushing. With a nanohole size of 32 nm, the previously size-limited QDs reduce in size overall due to desorption and become optically active as a result. The size uniformity of QDs in this nanohole size is comparable to each other as the amount of indium that could be deposited in these nanoholes during growth are limited to the same. Increasing nanohole size, results in multi-dot occupation in the nanohole with smaller QDs, and with indium flushing, similar behaviour of size reduction is observed. At the largest nanohole, where the QDs are sufficiently small, QDs are removed completely due to desorption. The smaller QDs that remain causes a blueshift with increasing nanohole size, with a maximum shifting of 14 nm at 50D4. This could be supported when comparing the ensemble emissions with the same structure but without the use of the indium flushing technique. The introduction of indium flushing

results in a blueshift in ensemble emission, which supports the evidence that QDs are reducing in size [57]. While at the largest nanohole, the disappearance of the ensemble peak supports multi-dot occupations which are eliminated. Figure 4- 17e shows the summary of the peak emissions and FWHM dependent on the nanohole size.

Based on the expected effects of indium flushing on QD size, this should result in a reduction in FWHM. However, the opposite effect is observed where at 32D4, an FWHM of 18.9 nm is achieved, which degrades to an FWHM of 27.3 nm for 50D4. The broadening of FWHM is evidence of an increase in the size distribution, paired with the PL intensity also degrading suggesting QDs becoming optically inactive. This suggests QDs are reducing in size, but instead of desorbing, interdiffusion of indium/gallium to adjacent layers is taking place [167]. Sasakura et al, have previously reported that indium flushing at a higher temperature compared to QD growth temperature can result in unwanted interdiffusion, which reduces the uniformity of QD emissions [59]. The atoms migrate from the InAs QDs into the adjacent GaAs layer. This suggestion refines the proposed effect of indium flushing, where a mixture of interdiffusion and desorption is taking place during the indium flushing step, which, for larger QDs, is reduced in size but becomes optically active, typically found in the smallest nanohole arrays. Medium-sized QDs, either eliminated or remain just large enough to emit, are not uniform in size and small QDs, which are found in larger nanohole sizes. When compared the PL images, the decreased QD occupancy with the introduction of indium flush provides additional evidence of evidence on the proposed effect. Only larger nanohole arrays show a decrease in QD emission within the array. The results presented show the ability to control ensemble emission by decreasing nanohole size, with 32D4 identified as the array with the best ensemble emission across all arrays measured.

- The addition of indium flushing enables controlling of the ensemble wavelength.
- Varying nanohole size also enables controlling of the peak ensemble, enabling emission shifting by 35 nm.
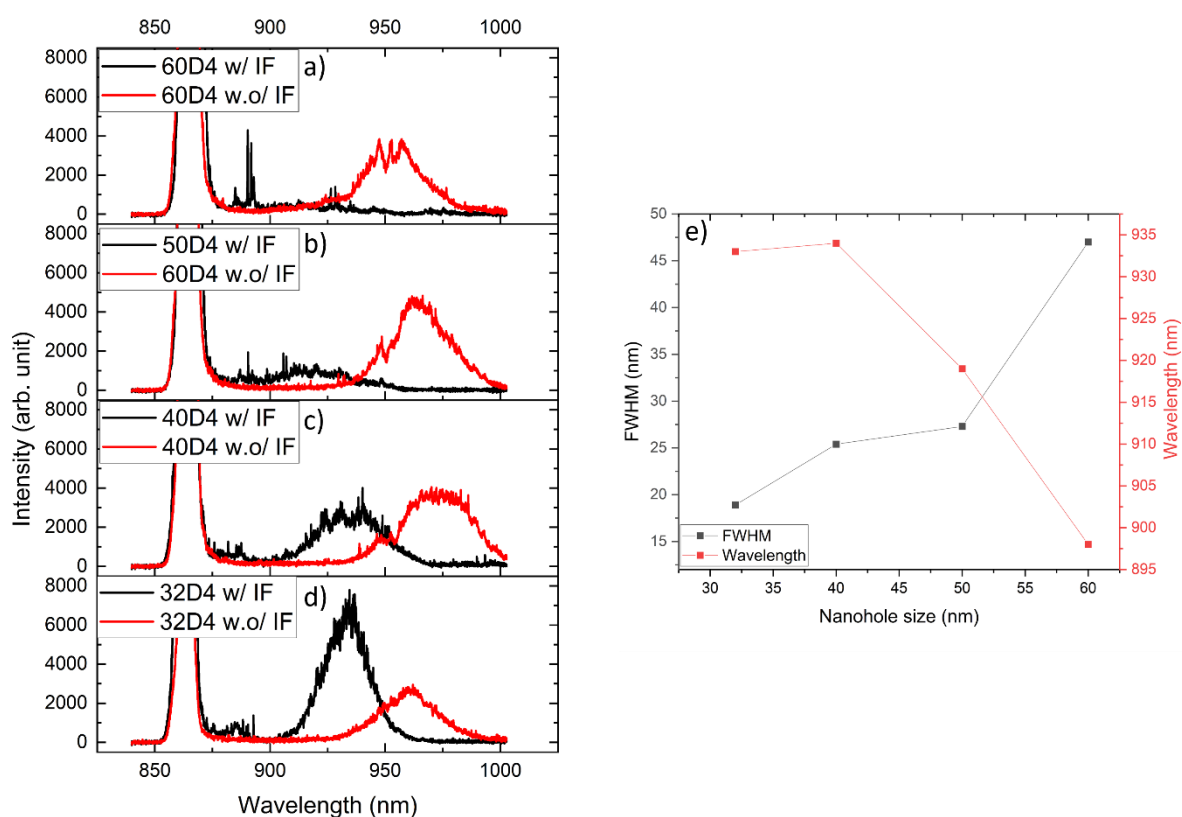- With a smaller nanohole size, FWHM is improved by ~10nm.

Figure 4- 17 Comparing the ensemble PL spectrum between the with (w/) and without (w.o/) indium flushing (IF) with the following pattern parameters e-beam dose 4 arrays with different nanohole diameters a) 60D4, b) 50D4, c) 40D4, d) 32D40, and e) summary of ensemble PL spectrum with IF on FWHM and peak wavelength.

Summary

In conclusion, by implementing various growth techniques, the QD properties can be tuned into a desirable range. The use of growth interrupt has proven to reduce the size distribution while maintaining high QD occupancy. The emission wavelength and the FWHM are also dependent on the growth interrupt (up to 180 seconds). Varying the partial capping can further shift emissions towards the 930 nm range at the cost of reduced QD occupancy, specifically for larger nanohole sizes. Further investigation of the pattern parameters shows that variation in e-beam dose does not control QD emission for both growth techniques. While nanohole size variation allows for emission shifting up to 20 nm. With the results of this study showing that variation in pattern parameters, combined with additional growth techniques can be used to achieve our objectives in terms of dot occupancy, FWHM, brightness and spectral centring, the next step is measuring single-dot emissions. While it is feasibly possible to measure a series of single dots manually, this is a time-consuming and inefficient solution to measuring large numbers of single dot arrays for characterisation. For example, the smallest arrays are at 4.8 μm pitch with 7 x 7 nanohole arrays. With 16 such arrays, each with varying conditions would consume weeks of measurements. To resolve this issue, requires a method of array selection to narrow down suitable arrays for detailed measurements. It also requires the development of the

setup to allow for the acquisition of multiple single dot locations automatically but also the ability to return to designed locations. As such, the installation of a nano-positioning stage was proposed, which allows for movement with nanometre precision and position feedback.

5 Single dot characterisations on undoped waveguides

In this chapter, we focus on the single dot characterisation and QD mapping of undoped waveguides containing SCQDs previously detailed in Chapter 4. Prior to the characterisation, the deployment of the nano-position stage into the research group's µPL setup (Setup 1) was required to allow for single dot characterisation. For specific details regarding the setup prior to the upgrade, please refer to Chapter 3. The modification to include the nano-position stage was designed by Dr Aristotelis Trapalis and was implemented in collaboration with the author. The software development for the nano-position stage, including the ability to perform QD mapping, was developed for use in this PhD project by the author. With the upgraded setup, an in-depth analysis of arrays from an optimised SC sample was conducted, with the effects of different pattern parameters outlined and analysed. Suitable arrays with good optical properties were identified, and mapping of these arrays and single dot characterisation was carried out. We identify different excitonic states from single dot emissions and confirm the presence of multiple dots with comparable emission (± 2 nm) where quantum confinement stark effect (QSCE) could be used to tune these QD positions into the same wavelength.

Nano-position stage implementation

The capabilities of the group's µPL setup (Setup 1) were previously limited to 20 nm step movements in any direction and without feedback on the current position. As a result, this limits the ability to perform automated scans of large numbers of QDs within an array, as the movement of the linear actuators was not tracked. To enable position tracking, a PIMars Nanopositioning stage by PI instruments was installed with a corresponding controller (E-727.xF Digital Multi-Channel Piezo Controller). This enabled position feedback that is highly accurate and is responsive to movements of up to ± 2 nm within a 300 µm scanning range in 3 axes direction. Figure 5- 1 shows (a) the design schematics and (b) the practical installation of the nano-position stage onto the µPL setup. Post-installation, tuning and calibration of the piezo actuators on the nano-position stage were required to ensure correct feedback on the stage's positions. This step of the installation is important as insufficient suppression of background vibrations will result in oscillation effects when the stage is moving, impacting the movement accuracy. Vibrations originate from several sources, including the cryostats when turned on for low-temperature measurements, as well as other external vibrations from labs, such as pumps or the operation of heavy machinery/equipment within the building. To resolve this problem, additional damping solutions, such as floating the optical table, were used to suppress vibrations, improving steady-state conditions.
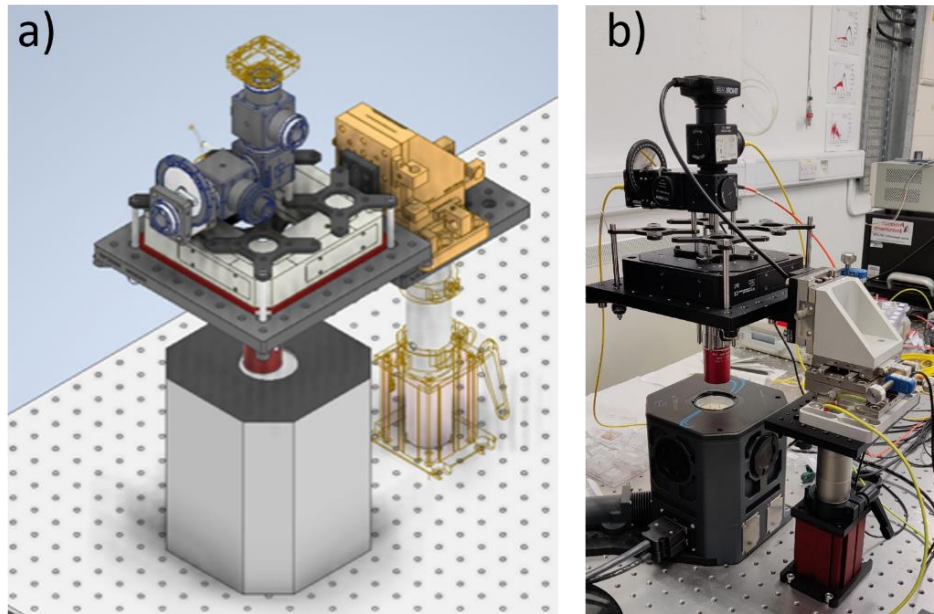
Figure 5- 1 The implementation of the nano-position stage into the group's µPL setup, a) the 3D model and schematics produced by Dr Aristotelis Trapalis, b) practical installation of the nano-position stage.

QD mapping software development

With a functional nano-position stage and calibrated piezo actuators, the next step was software development with the goal of moving the stage with position feedback and functionality that allows multiple locations to be measured automatically. PI instruments provided a library with a range of basic functions from closed-loop movement to reading actuators' position. To develop a QD mapping software, a graphical programming environment, NI LabVIEW 2022 Q3 (64-bit) was used.

Software overview

Figure 5- 2 shows the user interface of the final QD mapping software, with various functionality milestones highlighted with different colours. The first milestone (highlighted in orange) includes extremely basic movement of the nano-position stage in the form of relative movement; this allows users to control the movement speed and direction of the stage and manually move the collection area to a desired location and adjust the focus with Z-axis movement. This added the ability to free move the stage and provided a better understanding of the range of functions provided by the included function library. The next key feature (highlighted in green) is integrating the acquisition software, Lightfield, to allow the acquisition of the spectrums while using the same interface. This also allows users to turn on/off different hardware independently and select pre-defined "experiments" for Lightfield. This inclusion was needed as various projects and applications are used with this setup for different target wavelengths. In Lightfield software, the user can define the acquisition settings to use. The wide range of capabilities, including the type of detector used and grating used, is pre-defined to prevent end-users from customising new configurations and potentially damaging the stage. The

ability to turn on/off the controller and Lightfield separately allows users to take advantage of nano-position stage movement while being able to use other acquisition software (e.g. vista control) for different requirements.

With the basic features such as movement and acquisition of spectrums achieved, the next milestone is automated movement and acquisition together, under "non-referenced move", highlighted in purple. This makes use of the previously developed relative move function with minor adjustments to allow automated movements for a (N×N) arrays, where N is the size of the array. This allows for relative movement in the form of a grid with a set distance between each position. When Lightfield is also turned on, a PL spectrum can be acquired for each position within the array. As the first iteration for automated movement and acquisition, this is a big advancement towards automated single QD characterisation and PL mapping. The ability to define the step distance eliminates the possibility of overlapping of excitation area (5 μm diameter laser spot) as sufficiently large movement for each step can be configured. However, this is not suitable QD mapping of ordered arrays as there is no angle compensation for these automated movements, and it is not possible to perfectly align the arrays to the axes of the nano-position stage. To correct the angle offset, the use of several setpoints is required where the absolute position from the nano-position stage can be stored and returned to when required (highlighted in yellow). Lastly, these setpoints can be used in the QD mapping sections of the program (highlighted in blue) to calculate the angle offset to compensate for this issue and set the starting position. An additional feature added for QD mapping is the ability to adjust to the array size (N×N), how much to move between each position (i.e. the pitch of the nanohole array), returning the absolute positions for each location and the direction the nano-position stage moves. For full details on the programming scripts and functionality, we refer to Appendix B for the backend of the program.
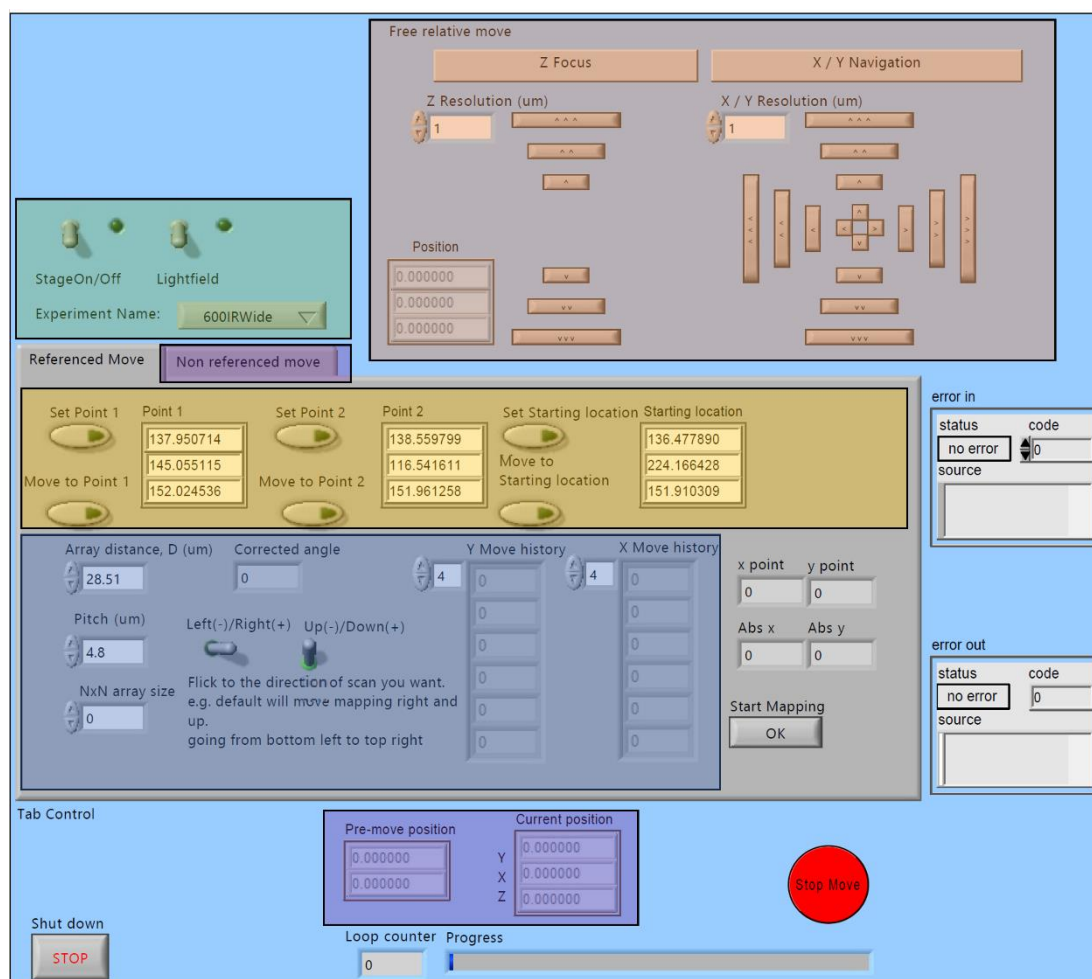
Figure 5- 2 Overview of the user interface of QD mapping software with various development milestones, free relative move (Orange), ability to turn on/off difference devices and PL spectrum acquisition capabilities (Green), basic programmable movement with movement history (Purple), Saving multiple positions and return to positions (Yellow), QD mapping function (Blue)

Angle compensation

The challenge to overcome for QD mapping is correcting the offset angle introduced by various steps from fabrications to PL measurements. Some examples include the pattern fabrication process, sample cleaving and mounting onto the cryostat, where each of these will introduce some tilt between the patterned array and the axis movement that will need to be compensated for. Figure 5- 3 illustrates the effects introduced with the angle offset with respect to the movement of the axis of the nano-position stage. To move between nanoholes requires compensations on two axes (x and y axes), and the defining offset angle is key in allowing all subsequent movement to be compensated. The offset angle will change for each instance where the sample or optical setup is moved; thus, methods of quickly calculating the offset angle are important.
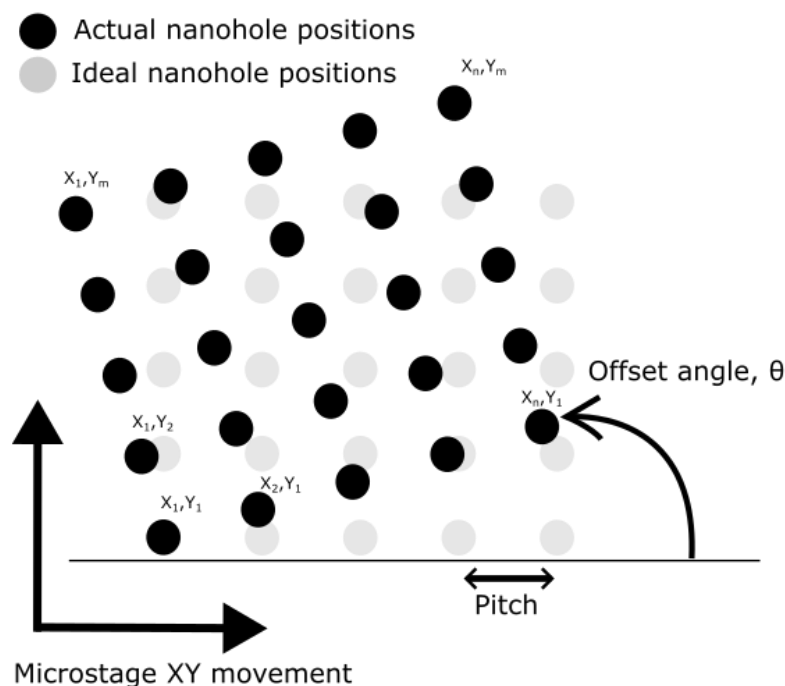
Figure 5- 3 Illustration of the effects on the angle offset to the patterned substrate compared to the movement of the micro stage where the position of each nanohole is defined by (X_n, Y_m), where n is the nanohole position.

To define the offset angle (θ), the distance between two known points is required; for this example, the distance between two nanoholes was used, otherwise known as the pitch. This provides two different distance values: the ideal distance between two nanoholes (D_{ideal}) and the actual distance between nanoholes (D_{actual}). D_{ideal} is predefined as the pitch of the array, while D_{actual} is defined by the distance between two measured positions along one axis (the x-axis was used in this example). The two absolute positions of the nano-position stage are labelled as (X_1, Y_1) and (X_n, Y_m) for simplicity. The position (X_1, Y_1) is defined as the origin point, otherwise known as the first nanohole measured, while (X_n, Y_m) is the position of another nanohole; here, let us assume this next position is (X_2, Y_1) to match with the pitch distance, shown in Figure 5- 3. The offset angle, θ, between these two nanohole positions can be represented in cartesian form, shown in Equation (1). The offset angle accuracy can be improved by increasing the distance between the two points measured. One alternative is using two alignment markers (max distance of 300 μm), which also have known distances and can improve the offset angle accuracy due to the larger distances between the two positions.

With the offset angle defined, to find the absolute position of any nanohole positions on the same row, the corresponding coordinate is defined in Equation (2) - (3), where (x_0, y_0) is for non-zero origin points and the D_{ideal} is the distance between the number of nanoholes (n - 1) multiplied by the pitch. (e.g. The distance from the origin to the 6th position nanohole in the same row (n = 6) at 2.4 μm pitch, D_{ideal} = (6 − 1) × 2.4 = 12 μm)

5 Single dot characterisations on undoped waveguides

$$\theta = cos^{-1}\left|\frac{D_{ideal}}{D_{actual}}\right| = cos^{-1}\left|\frac{Pitch}{X_2 - X_1}\right| \tag{1}$$

$$x_{n,1} = D_{ideal} \times cos\,\theta = (n-1) \times pitch \times cos\,\theta + x_0 \tag{2}$$

$$y_{n,1} = D_{ideal} \times sin\,\theta = (n-1) \times pitch \times sin\,\theta + y_0 \tag{3}$$

Similarly, to move between nanoholes positions within the same column, the same equation can be used, but the offset angle is shifted by an additional 90° (θ -> θ + 90°) shown in Equation (4) - (5). These equations defined only allow for movement between nanoholes within the same row or column but not beyond that. To move across an (N × M) array from the origin point requires the consideration of the vertical and horizontal movement. This can be achieved by combining the movement equations derived and combining Equation (2) - (5) together. The movement across any positions within an (N × M) array is shown in Equation (6) - (7).

$$x_{1,m} = D_{ideal} \times cos(\theta + 90) = (m-1) \times pitch \times sin\,\theta + x_0 \tag{4}$$

$$y_{1,m} = D_{ideal} \times sin(\theta + 90) = (m-1) \times pitch \times cos\,\theta + y_0 \tag{5}$$

$$x_{n,m} = (n-1) \times pitch \times cos\,\theta + (m-1) \times pitch \times sin\,\theta + x_0 \tag{6}$$

$$y_{n,m} = (n-1) \times pitch \times sin\,\theta + (m-1) \times pitch \times cos\,\theta + y_0 \tag{7}$$

This provides the absolute coordinates for any nanohole position within an array from an origin point after compensating for the angle offset, thereby allowing the ability to perform a QD map of any sized array with a constant pitch between each position. This method of using absolute positions rather than a relative movement from a starting location allows easier identification of specific nanohole positions. In addition, easier accessibility to previous locations also allows for additional measurements at any point and does not require moving back to the origin to move back to a specific position. For arrays that are close together, this also enables measurements of multiple arrays to be measured before further analysis of specific positions if needed, provided the optical setup is not moved.

Validation of software and calibration settings
The nano-position stage's calibration was confirmed by moving the XY-axis continuously between two locations. The positions are 100 μm apart, with a 3-second pause in between to allow for stabilisation of the stage post-movement. Figure 5- 4 displays the change in position read-out from the controller for one iteration of this test with a 3-second pause. The behaviour observed is within the expectations of a calibrated system, with a large change in position during the movement of the stage to a different position. The stability is restored quickly before a steady state is achieved, an indicator that the

calibration is performed correctly and the stage is not oscillating radically. One aspect which is still lacking is the range in which the steady-state values are maintained where roughly ± 5 nm change in position over the 3 seconds is observed. This discrepancy is caused by existing background vibration caused by the cryostat located on the same optical table when measuring at low temperatures. While efforts have been made to suppress these vibrations (floating the table), it is impossible to suppress this completely without removing the cryostat pumps from the table. Nonetheless, this slight decrease in position accuracy is negligible when considering the accuracy required for measuring nanoholes within the array, with the smallest pitch size being 600 nm.
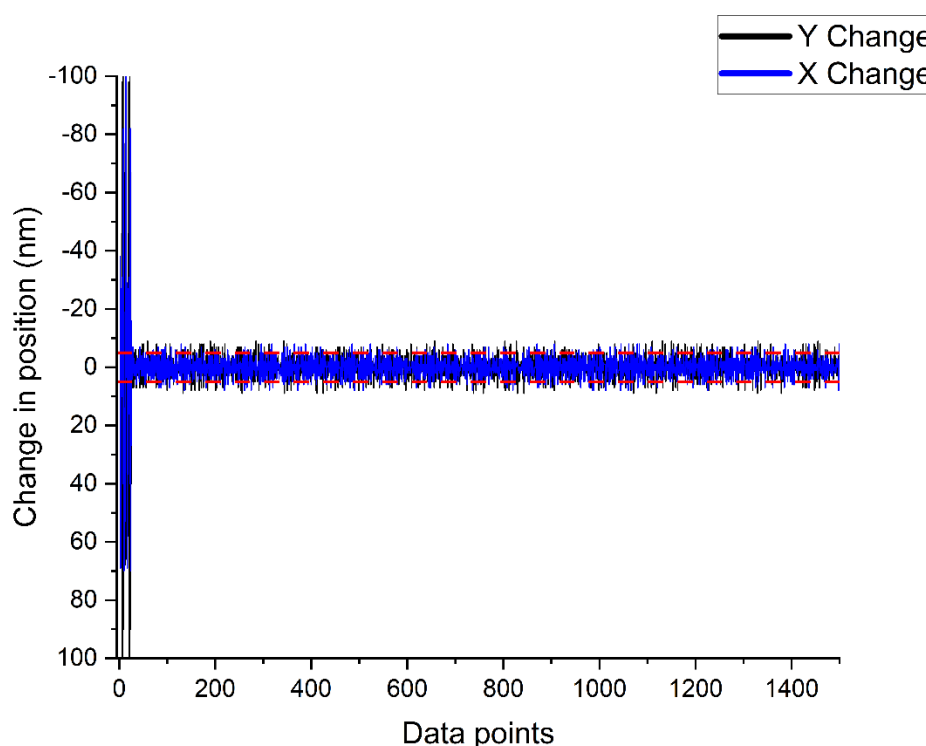

Figure 5- 4 The change in absolute position from the nano-position stage along the X-axis and Y-axis when moved to another position (100 μm) with a reference of the ± 5 nm movement accuracy (red dashed lines)

To verify the accuracy of the angle correction formula, a position within the nanohole array was measured multiple times with different conditions. One method of verifying was measuring the sample positions by changing the mapping path. This is possible by changing the starting positions for the QD map and then comparing the same positions. Figure 5- 5 shows the μPL spectrum from the same nanohole position but obtained from two different scanning directions. The emission peaks presented are identical, with no additional peaks from either repeat. This suggests that no additional dot emissions were detected, and the angle offset was accurately compensated. The current mapping solution lacks compensation to the Z-axis variation across the array, which could impact the QD

intensity. However, this test also confirms that the height change needed across an array is negligible, with a maximum variation of 5% for any given emission peak.
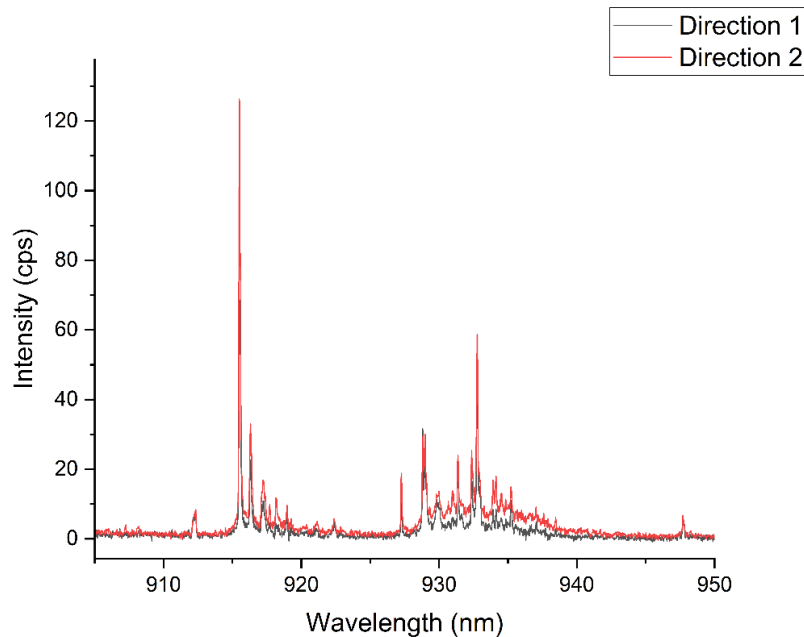

Figure 5- 5 PL spectrum of the same QD position (4,3) when measured with different starting locations within the array.

In summary, a nanopositioning stage and the software controls successfully allowed automation of µPL measurements for single dot measurements. This enables detailed studies of high-quality QD locations with the option to investigate multiple suitable locations found. The QD mapping functionality considers the angle offset and allows the ability to measure QDs within an ordered pattern. This is designed specifically for SCQD arrays, as there is a pattern with a pre-defined distance between each nanohole and each array, allowing easy navigation across the sample. The benefits allow the ability to compare QDs within individual arrays but also direct comparison across multiple arrays with different pattern parameters if needed. At the same time, other non-SC samples can also use the mapping script to create a spectral map for areas up to 300 x 300 µm^2.

Site-control array selection

The development of software controls for functions such as QD mapping minimises manual intervention required to measure a large number of single-dot emissions. However, there is still a limitation on the number of QDs that can be measured within a day due to the time required per scan (up to 15 minutes per scan). As such, methods of selecting suitable arrays for single dot measurements are still required as no optimal pattern parameters have been defined. Optimisation of the growth structure and initial investigation of the effect of pattern parameters (including nanohole size and e-

beam dose) was previously studied and presented in Chapter 4 Growth and characterisation: undoped Site-Control waveguides. For the site selection, we investigated across all arrays within a specific pitch (0.6 μm) to determine suitable pattern parameters for single dot characterisation. The growth structure used were an undoped site-control waveguide with a 60-second growth interrupt and 8 nm partial capping (see Figure 4- 1b). For the μPL measurements, a red diode laser at 100μW for 20 seconds was used as the excitation conditions alongside a silicon detector with 600 lines/mm grating for detection. To be able to capture large numbers of QD emissions, a 10x objective lens was used, which enlarges the excitation area to 50 μm diameter (from 5 μm diameter) for ensemble PL measurements.

Figure 5- 6 compares the ensemble emission with varying e-beam dose. At the lowest dose (dose 1), no ensemble emissions are observed, and when increasing up to dose 3, the presence of ensemble emissions is detected. At dose 2, bimodal emissions are observed around 930 nm, suggesting the formation of two different QD shape profiles [157] [160]. While a single ensemble peak at 930 nm is then detected with dose 3, indicating an improvement to QD shape uniformity where an FWHM of ~10 nm is found. Increasing the e-beam dose higher, the ensemble emissions vanish and are replaced by background noise. The lack of ensemble emission observed at higher doses suggest either a lack of QD occupation or optically inactive QD occupation. This indicates at low e-beam dose are more suitable to enable QD emissions. At higher dose, one possibility is the size of the QD are affected by as slightly large nanohole are formed. This results in multiple-small dot occupation within the nanoholes where the use of indium flushing will eliminate smaller dots through desorption while reducing the size of larger dots by controlling height [57] [165]. For more details about indium flushing as a growth technique, see Chapter 4: Growth optimisation: Indium flushing section for specific details.
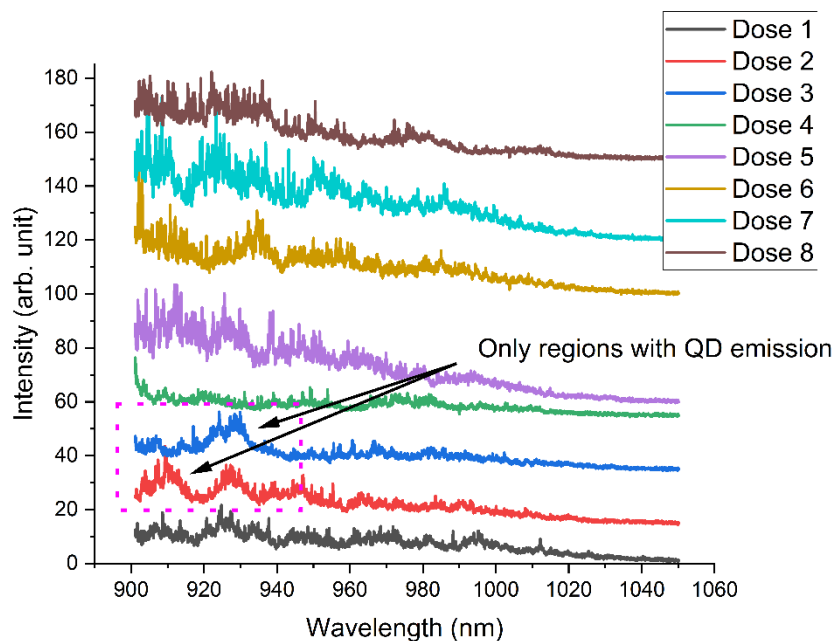
Figure 5- 6 Ensemble PL spectrum of undoped waveguide with 50 nm nanohole diameter with variation e-beam dosage from Dose 1 to Dose 8.

The effect of altering the size of nanoholes on the PL ensemble was also studied as part of the site-selection process. From the previous results, e-beam dose 3 was used as it produced the narrowest ensemble emission. Figure 5- 7 shows the PL emissions for nanohole diameter between 32 nm and 60 nm. When the nanohole diameter is 32 nm, no ensemble emissions are observed, with background noises that can be seen at 930nm and 980nm. Increasing the nanohole size to 40nm leads to the emergence of a single ensemble that is centred at 945 nm with an FWHM of 15nm. The presence of the single ensemble is maintained when a nanohole size is increased to 50 nm with some enhancement to the ensemble, including a blueshift by 20 nm (to 925 nm) and narrowing of FWHM by 7 nm (to 8nm). At the largest nanohole size of 60 nm, the ensemble emission disappears, and a broad background noise reappears. The change in nanohole size has presented the ability to control the ensemble emissions, and this can be understood when observing the QD occupation.

To understand how QD occupies the etched nanoholes with different nanohole size, Figure 5- 8 show a series of nanohole size's effect on QD formation, with and without indium flushing after QD deposition. With smallest nanoholes (32 nm), the QD formation is limited by the nanohole size prior to any growth techniques. This enables single dot occupation as the size is limited to amount of indium deposited in the small nanohole and when indium flushing technique was used, this reduces the size of QDs through desorption and interdiffusion [57] and enables QD emissions [55]. For intermediate-sized nanoholes (40 nm and 50 nm), QD emissions are blueshifted as QD formation is not restricted by the nanohole size, allowing them to be bigger [7] [161]. In addition, this could also be a mixture of

single occupation of larger QDs or multi-dot coalesce into one larger dot by being close to each other. At the largest nanohole sizes (60 nm), this produces multi-dot occupancy of smaller QDs but does not coalesce into large QDs due to large separation. When indium flushing is added to the growth process, these smaller dots will desorb and interdiffusion into the surrounding, which will eliminate the QDs or make them sufficiently small that they are optically inactive [57]. The size and shape of the QDs have previously been reported to be important parameters controlling QD emission [16], and the addition of nanoholes is an additional parameter that controls QD size and effects the optical properties of the QDs.
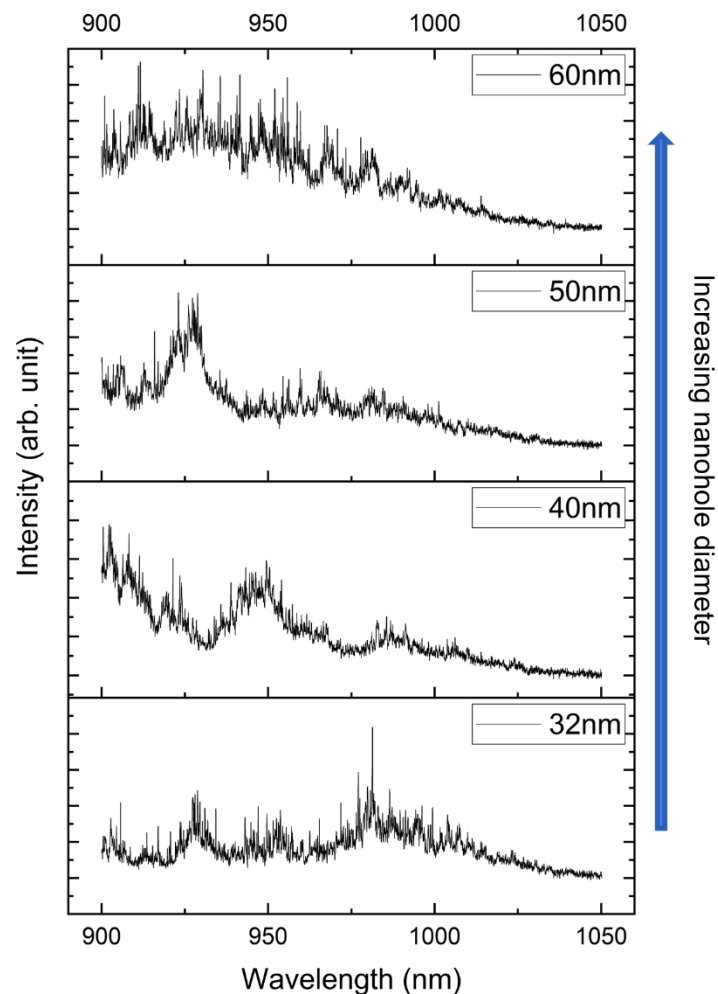

Figure 5- 7 Ensemble PL spectrum of the undoped waveguide from arrays fabricated with e-beam dose 3 and variation in nanohole size from 32 nm to 60 nm diameter.
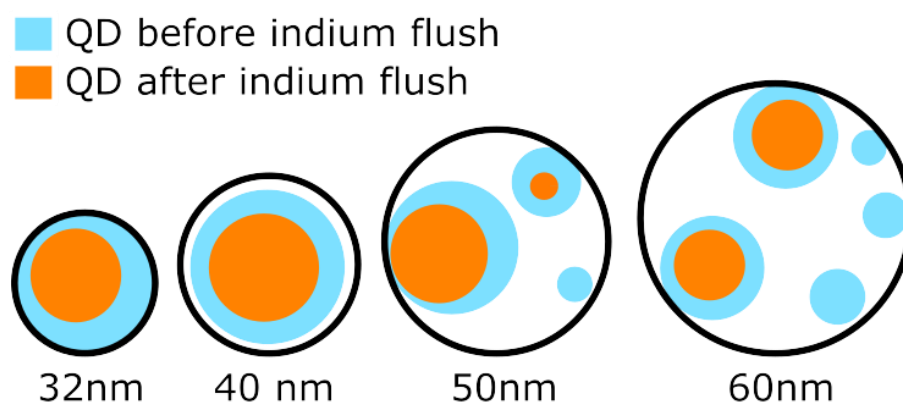
Figure 5- 8 Basic diagram of QD occupation with increasing nanohole size, and the effects of indium flush has on QDs in a nanohole. We expect that at small nanohole, QDs are limited by the nanohole while for larger nanohole multi-dot occupation are driving factors for the blueshift of emissions observed.

From the site selection process, the 40D3 and 50D3 (e.g. 40D3 are 40 nm nanohole diameter with e-beam dose 3) arrays have been identified with ensemble emissions suitable for single dot characterisation. Both arrays produced clear and narrow ensemble peaks, an indication of good QD size uniformity across the array. Ensemble emissions are obtained from 0.6 µm pitch arrays to allow for the use of the ensemble PL emissions technique to identify the best QD arrays. However, for single dot characterisation, the 4.8 µm pitch arrays are used as the distance between each dot is sufficiently large that the laser spot (5 µm diameter) enables no overlap between any positions and provides an accurate measurement of individual QD emissions at these positions. Additional verification by PL images was also used to confirm the presence of ordered QD emissions and was compared to e-beam dose 2 to demonstrate the benefits of the site-selection process. Figure 5- 9 presents the PL images for the nanohole pattern with 40/50 nm nanoholes with e-beam dose 2/3 at the 4.8 µm pitch arrays. The benefit of using the site-selection process in identifying arrays with high QD occupation is demonstrated when comparing the dose 2 array with the site-selected dose 3 arrays. With the presence of ordered arrays of dot emissions with high QD occupancy in dose 3 arrays. While for 2 arrays low QD occupancy is observed, which reducing the number of usable QD with comparable optical properties.
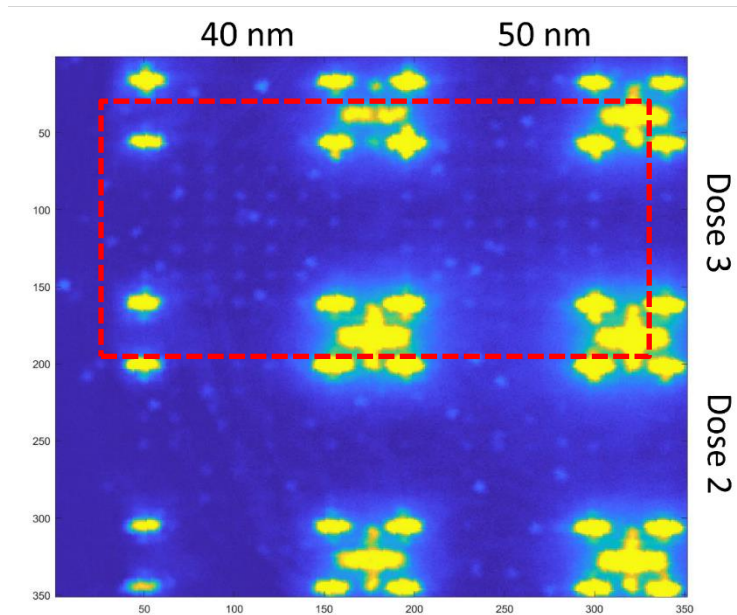
Figure 5- 9 PL Imaging of undoped waveguide structure at 4.8 μm pitch with 4 different arrays with 40/50 nm diameter nanoholes with e-beam dose 2/3. 40D3 and 50D3 are arrays which show the most promise and will be used for single dot measurements.

Single dot measurements

With two potential arrays with good QD occupancy and optimised ensemble PL emissions, the new nano-positioner was used to measure single dot emissions from these arrays to identify nanohole positions with single dot emissions with one example of a single dot emissions within a nanohole is presented. For power dependence measurements for a single dot, the excitation duration is maintained at 20 seconds, and the excitation power is varied between 0.1 μW to 30 μW. To accurately capture linewidths of single dots, a silicon detector with 1200 lines/mm grating was used alongside a 100x objective lens, with an excitation area of 5 μm diameter on the sample to ensure single dot measurements with no overlap with adjacent nanoholes. All nanohole positions were measured to identify the presence of QD emissions within the array and determine occupancy. This allows for suitable QD positions to be measured in more detail, including FSS measurements.

The measurement of a single dot position on the 40D3 array is presented in Figure 5- 10a with a selection of different power excitations used. Starting at the lowest power of 0.1 μW, a single peak emission is found at 905.67 nm, which is identified as the neutral exciton. As the excitation power increases, emission peaks at 906.39 nm and 906.63 nm appear at 1 μW and 15 μW, respectively. The emission lines are clearly visible and narrow, which are identified as different excitation states from a single QD emission. The appearance of these state was identified as the neutral exciton, followed by the biexciton and the charged exciton. It is common for the biexciton to be at a lower energy when compared to the neutral exciton. The position order of each excited state is comparable to the position demonstrated in the literature [168], but the position of the transition states has also been shown to

vary depending on the QD size [169] [170]. The emission intensity from the biexciton is initially lower than the neutral exciton, but as excitation power is increased, biexciton increases in intensity at a higher rate than the exciton state until both states begin to saturate. The different states are confirmed by Figure 5- 10b, where the PL intensity of each state is shown as a function of excitation power, with a total of 24 different powers measured. For each state, saturation of the PL intensity at high power is also observed. Exciton states are identified with similar power coefficient due to carrier capture statistic where both show a linear dependence [171]. While biexciton has a quadratic dependence in carrier capture statistics, require twice as much as compared to excitons [172].
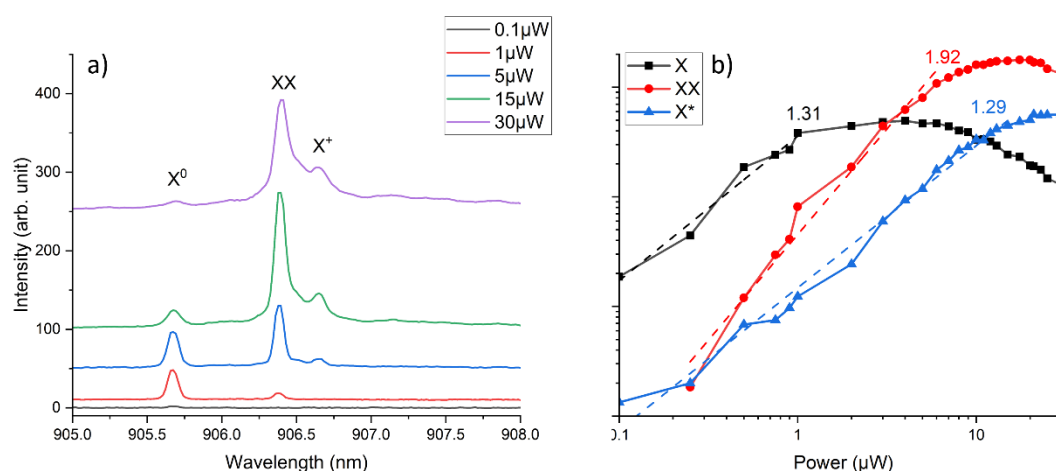

Figure 5- 10 Power dependence measurements on a single nanohole position from a 40D3 array. a) a selection of the spectrum acquired with μPL, showing the appearance of neutral exciton, biexciton, and charged exciton b) Summary of power dependence measurements as a function of excitation power with fitted lines for each state (dashed line).

With a 5 μW excitation power, the linewidth measured from the transition states are 30.9 μeV (neutral exciton) and 53.9 μeV (biexciton), which is comparable to literature with good QD symmetry and low linewidth [172] [168]. The neutral exciton and biexciton can also be identified by the presence of fine structure splitting (FSS). To measure FSS, a polarisation PL measurement takes place where the luminescence emissions are analysed with a λ/4 wave plate and linear polariser to distinguish different polarisation components. Figure 5- 11 shows the polarisation spectrum with a 90-degree rotation difference. The FSS is linked to the lateral anisotropy of the confining potential the different excitonic state previous identified shows a FSS of 33.7 μeV (neutral exciton) and 46.4 μeV (biexciton). The difference in FSS between the exciton and biexciton points towards two different QD formation, however no other dot-like peaks are found between 900 nm and 1000 nm. Literature has also shown that the wavelength difference between the neutral exciton and biexciton peak does not exceed ± 5 nm [24] [53] [170]. Meanwhile, the emission peak at 906.63 nm did not exhibit fine structure splitting; therefore, it is assigned as the charged exciton. No other plausible reasonable causes of the different FSS has been identified. The neutral exciton FSS reported is comparable to the literature [168], but

still requires improvement to achieve values of 10 μeV or lower to be useable for indistinguishable photon pairs [173]. The uniformity of QDs has been shown to control the FSS, where elongated QDs have resulted in larger FSS [16] [174]. Therefore, future improvement to the QD shape uniformity is needed to lower FSS but provide good evidence for improving optical properties with a dry etching fabrication process has been achieved. One possible solution is using droplet epitaxy rather than S-K for QD formation as this has been shown to produce highly symmetrical QDs as it does not use strain to form QDs [26].
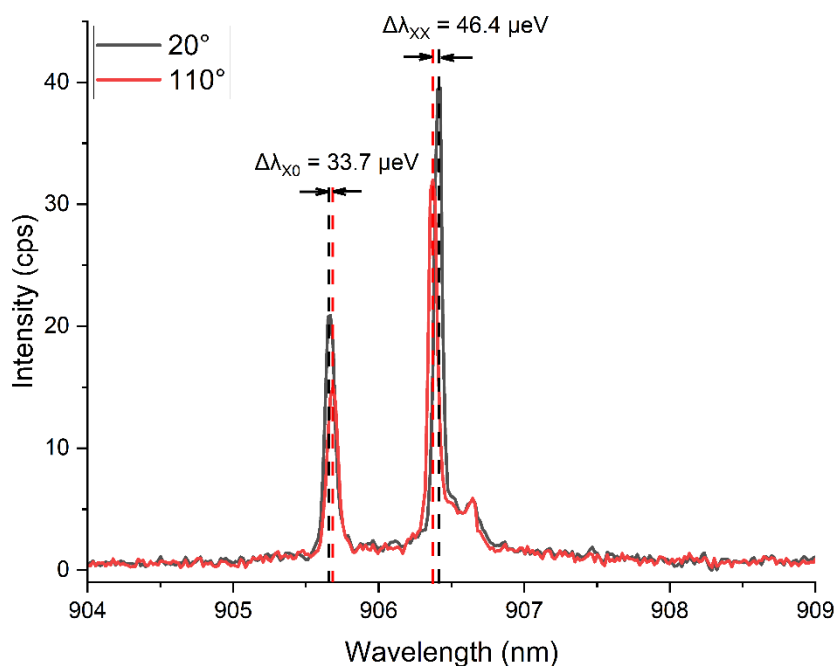
Figure 5- 11 Polarisation measurements with 5 μW excitation power and 90-degree angle difference to demonstrate fine structure splitting with an energy splitting of 33.7 μeV (Exciton) and 46.4 μeV (Biexciton).

Figure 5- 12a shows a selection of the temperature-dependence measurements and the emission shifting of the individual peaks. The previously identified transition states are demonstrated to redshift with increasing temperature. At high temperatures (60 K), only single exciton (X) peaks remain visible in the spectrum but have broadened significantly and poor PL intensity. The other transition states disappear at different temperatures; the biexciton disappears at 50 K, while the charged exciton disappears at 40 K. For temperatures above 70 K, all peak emissions are no longer visible. Kim et al, reported on the disappearance of excitons comparable to the results presented and this is attributed to broadening of linewidth and requiring higher activation energy at higher temperatures [175]. Figure 5- 12b shows the summary of the peak wavelength of each transition state as a function of temperature. For temperatures below 30 K, the peak emission follows the temperature dependency of the InAs bandgap energy under Varshni's law (solid line), shown in Equation (8) [176]. While

increase in temperature above 30K results in a slight deviation from Varshni's relation. This deviation could be linked to the increased numbers of carrier transfers from the wetting layer to the QD resulting in a higher degree of redshifting compared to Varshni's law [177]. Other possibilities include the parameter values used in Varshni's law (α = 0.27 meV/K and β = 93-135 K), which states different values depending on the literature reference used [14] [178].

$$E_g(T) = E_0 - \frac{\alpha T^2}{T + \beta} \tag{8}$$
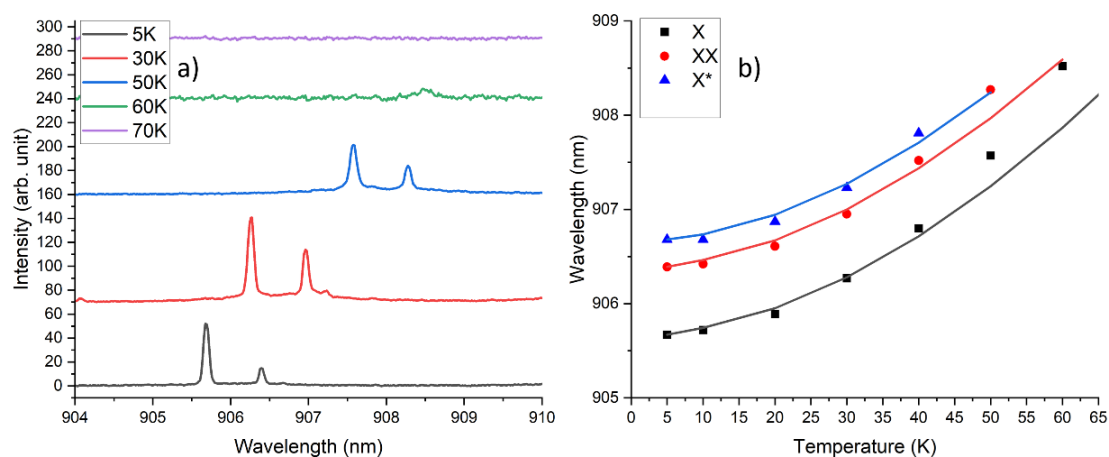
Figure 5- 12 Temperature dependence measurements with 1 µW excitation laser for the 60 seconds between 5 K to 70 K, where a) a selection of the temperature dependence spectrum, demonstration emission shifting with temperature. b) Summary the wavelength of each state as a function of temperature with the slope of the temperature dependency of the InAs bandgap energy obtained by Varshni's law (solid line) where α = 0.27 meV/K and β = 135 K.

Figure 5- 13 summarises the neutral exciton linewidth and emission intensity (inset) as a function of temperature. The lowest linewidth recorded was at 10 K, with 32.1 µeV, which is greater than above the spectral resolution of the detector (20.9 µeV). Between 5 K and 20 K, the linewidth is well-maintained before a dramatic broadening to 150 µeV between 30 K and 60 K caused by phonon scattering [179]. The broadening of the exciton emission is dependent on the temperature, which is also consistent with other studies on both SCQD [180] [181] and self-assembled QD [182]. The increase in intensity at 30K and 40K is attributed to the increased number of carrier transfers from the wetting layer to the QD [177]. When compared to the literature, the intensity trend of the exciton transition as a function of temperature is also comparable to similar studies presented on high-quality SCQD emissions [183] [184].

Figure 5- 13 Linewidth of the neutral exciton transition as a function of temperature, calculated with a Lorentzian fit at the peak of the exciton peak. The inset includes the emissions intensity as a function of temperature for the exciton peak.

QD mapping

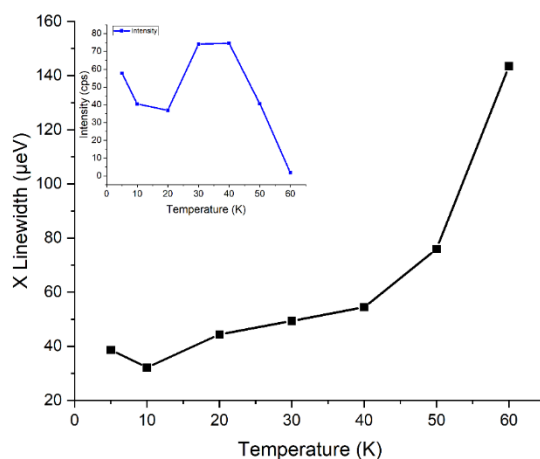Now we have established the optical properties of a single QDs in nanoholes, we move on to the comparison of multiple dots within an array and finding suitable groups of QDs with comparable optical properties. The QD map presents in this section, focuses of identify groups of QDs with good linewidth with comparable wavelength suitable for additional measurements such as Hong-Ou Mandel experiments. For Hong-Ou Mandel experiments, linewidths of dot-like emission must have narrow linewidths (>10 µeV) [185]. In addition, to tune comparable QDs into the same wavelength, quantum confinement stark effect (QCSE) can be used but the limits of the wavelength difference are set at ± 2 nm. In addition, for the end applications of SCQD being quantum applications, achieving low linewidth is important for indistinguishable photon pairs, as such the QD maps will present wavelength and linewidth (as subscript in µeV) of the narrowest dot-like emissions rather than the brightest emissions. The corners of these arrays are excluded from this analysis as alignment markers overlap these nanohole positions. This is due to the presence of multi-dot occupation from alignment markers, making it difficult to determine the origins of the QD emissions at these positions. The position of each nanohole within a QD map will be referred to by position (m, n) where m is the x-axis position, and n is the y-axis position (e.g. position (5, 2) is the x-axis position number 5 and y-axis position number 2).

Taking all the single dot measurements within an array, a QD mapping can be produced, as shown in Figure 5- 14. The 40D3 QD map shows a QD occupancy rate of 51% (23 out of the 45 positions), which is a dramatic decrease in QD occupancy when compared to PL imaging previously shown in Figure 5- 9. The difference in occupancy is a combination of a lack of QD emission from certain positions and the elimination of emissions with exceeding large linewidth (>150 µeV), which is filtered out as non-QD emissions. Despite the low QD occupancy rate, there is good uniformity of QD emissions, with

many pairs or clusters of QD identified with comparable wavelength within the array (colour-coded). The QD position which was previously discussed in the previous section (see Single dot measurements) is position (5, 2) (highlighted in orange), where the closest comparable QD emission is at position (6, 1). However, due to the large wavelength difference (>2 nm), no further investigation on these positions are performed since it does not match the requirements to be able to tune QDs into the same wavelength by QCSE. The ideal pair of QDs is found at positions (7, 4) and (7, 5), which have the same wavelength emissions and comparable linewidth. The single dot measurements of this pair of QD alongside power dependence measurements (inset) are shown in Figure 5- 15. From both positions, the emissions identified in the QD map originate from the exciton states (a charged exciton and a neutral exciton). From the power measurements of these two emission states, two different trends are shown at position (7, 4), the charged exciton states at 903.0 nm saturate as low as 5 µW and presents a comparable trend to the neutral exciton. The biexciton peak is also easily identified as it exhibits a super linear trend and does not saturate even at high power. In comparison, at position (7, 5), the peak at 903.0 nm (neutral exciton) follows the same trend as all other dot-like peaks identified with no signs of saturation. The other peaks are currently identified as charged excitons as they follow the same linear trend as the neutral exciton but do not appear until 1 µW, where the neutral exciton appears as low as 0.1 µW. We also rule out biexciton emissions as no super linear trend is observed and the increase in intensity with power is comparable between the two charged exciton peaks. This suggests the possibility of multi-dot occupation or multiple charges excitons (X^-, X^+). One major setback of these two positions is the large linewidths (> 50 µeV), which are unsuitable for experiments such as Hong-Ou-Mandel experiments [185].
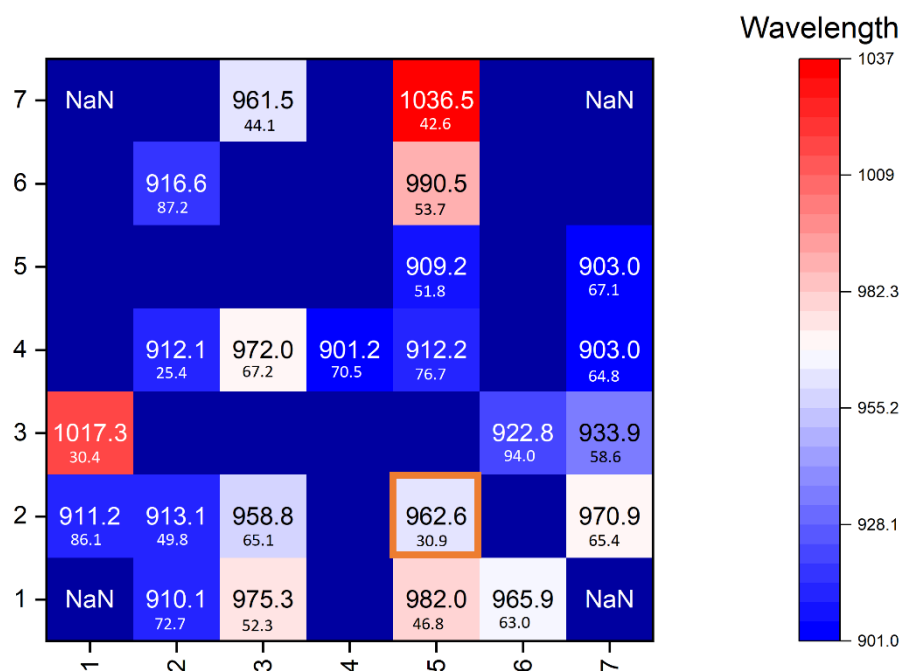
Figure 5- 14 QD mapping of the wavelength (main) and linewidth (subscript) in µeV of the 40D3 array. The corners are excluded from this mapping as the alignment markers overlap these nanohole positions. The previously discussed single dot characterisation position is highlighted in orange.
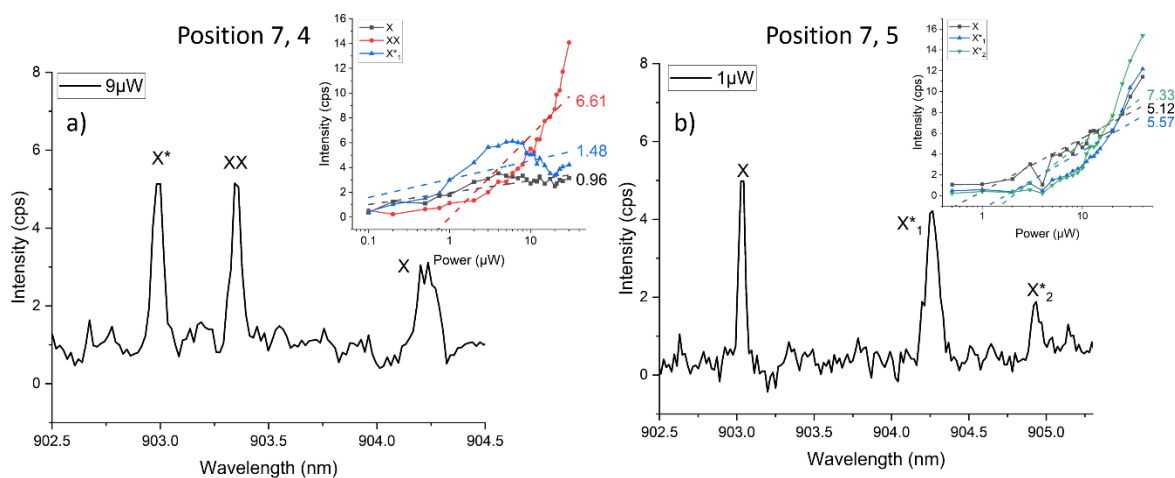
Figure 5- 15 PL spectrum of the ideal pair of QD indicating neutral exciton, biexciton, and charged exciton with power dependence measurements (inset) at a) position (7, 4) with 9 µW excitation power and b) position (7, 5) with 1 µW excitation power for 10 seconds.

Figure 5- 16 presents the wavelength and linewidth distribution of all dot-like emissions captured from the QD position within the 40D3 array. Notably, the large number of dot-like emissions exceed the number of nanoholes implies the presence of multiple dot-like emissions in each position. This is probably a combination of multi-dot occupation and multiple-state emission (neutral exciton, charged exciton, biexciton) within each position. In addition, QD linewidth above 150 µeV is excluded from the distribution as they are deemed to be not dot-like emission. The linewidths of positioned QDs within the arrays present a normal distribution, with the average linewidth being 75.3 µeV. The lowest

linewidth recorded is 25.4 µeV at position (2, 4), with comparable emissions (up to 2nm) observed from neighbouring positions (1, 2), (2, 1) and (2, 2). Although a series of QD pairs with comparable wavelengths are presented, the large linewidth is a limiting factor, particularly towards applications requiring indistinguishable photon pairs with a maximum linewidth requirement of 50 µeV. Position (2, 2) is the only QD position which passes this requirement. The wavelength distribution shows that most QD emissions are around 900 nm to 920 nm, and when all dot emissions are accounted for, the average wavelength is 939.12 nm. This indicates that QDs within this array are highly uniform, which can be attributed to a combination of the nanohole size with the addition of growth interrupt and indium flushing by modifying QD shape to control QD properties [87].

Figure 5- 16 Statistical study of all dot-like emissions at 40D3 array mapping measured at 1 µW for 10 seconds. The variation in a) linewidth with a fitted curve and b) wavelength, with the minimum, mean and standard deviation.

Similarly, the QD mapping for the 50D3 array with each position presenting the narrowest linewidth is shown in Figure 5- 17. Again, the corner of the array is excluded due to overlapping with the alignment marker, producing a high density of dot-like emissions. The QD occupation of this array is 24 out of 45 positions (53%), which is comparable to the 40D3 QD map. The lowest linewidth recorded in this array is also the lowest for SCQD within this research group, recorded at 22.4 µeV (detector resolution limit of 20.9 µeV). From the literature, the lowest linewidth achieved is 6 µeV for pattern substrate fabricated by EBL and wet etch process with a stacked QDs structure [82]. For our dry etching method, the linewidth achieved is comparable to the literature, with the lowest linewidth of 27 µeV and an average value of 120 µeV [186]. The QD map also presents several pairs of QDs with comparable emissions and linewidths. The ideal QD pair is identified at positions (4,3) and (4,4), with a wavelength difference of 0.6 nm and linewidth difference of 11.1 µeV but unsuitable for additional investigation due to large linewidth (> 50 µeV). The average linewidth across the occupied positions is 75.5 µeV, which presents possible growth improvements to reduce linewidths further. Several QD positions with linewidths below 50 µeV are promising positions that could be used for other photonic

applications such as photonic cavity structures [13] or quantum resonators [154]. The linewidth distribution of all QD emissions within the 50D3 array is shown in Figure 5- 18a. When compared with 40D3 arrays, the linewidth uniformity is almost identical, suggesting good shape uniformity is maintained across the two arrays. On the other hand, the wavelength distribution does not follow the same trend seen in the 40D3 array. Figure 5-18b presents the distribution of wavelengths of positioned QD within the 50D3 array, with an average wavelength of 939.7 nm. The wide range of wavelengths presented suggests the sizes of QD vary significantly [45] but maintain good shape uniformity.

Figure 5- 17 QD mapping of the wavelength (main) and linewidth (subscript) in µeV of the 50D3 array. The corners are excluded from this mapping as the alignment markers overlap these nanohole positions. The shortest linewidth recorded of 22.4 µeV at position (2,3) is shown.
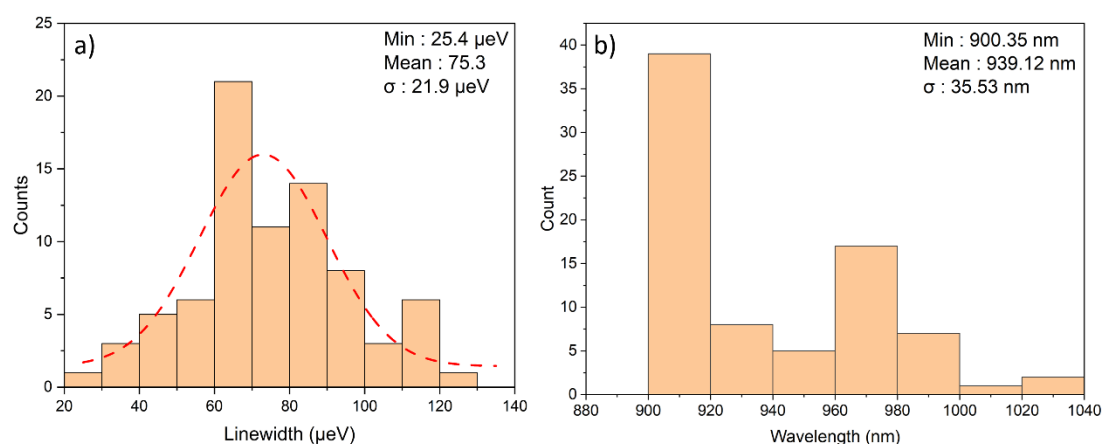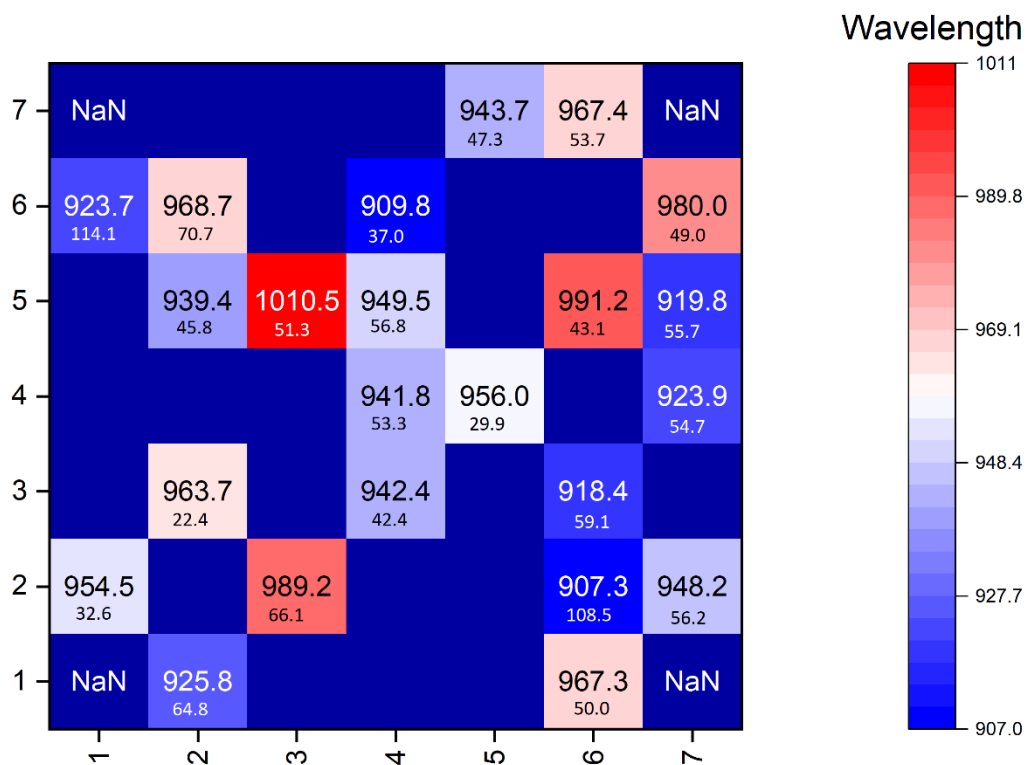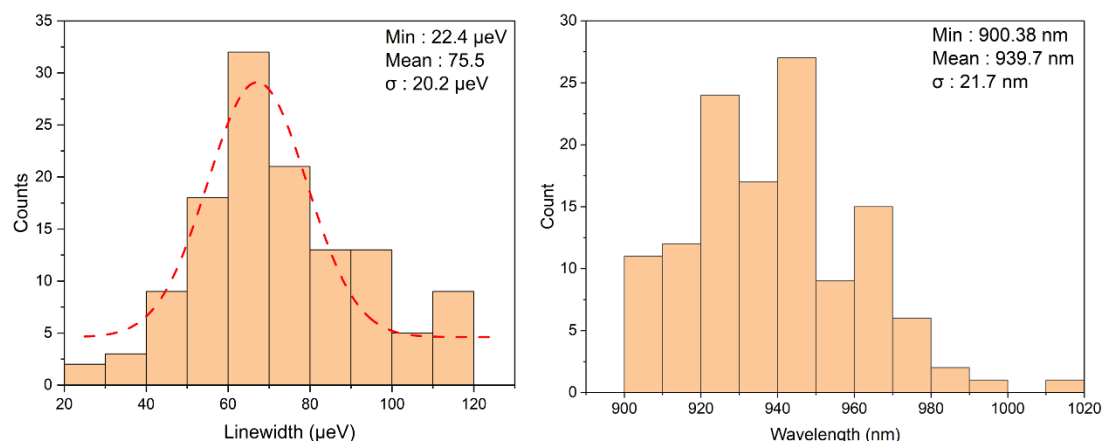
Figure 5- 18 Statistical study of all dot-like emissions at 50D3 array mapping measured at 1 μW for 10 seconds. The variation in a) linewidth with a fitted curve and b) wavelength, with the minimum, mean and standard deviation.

Summary

The μPL setup within the research group was successfully implemented with a nano-position stage, which has increased the capability for mapping arrays. This enabled the ability to perform single dot measurements and QD mapping of arrays of positioned QDs within an array. However, due to time limitations, as each array can take up to 7 hours, it is unsuitable to measure every array from one sample. Instead, site selections are still required to narrow down arrays for single dot measurements, and arrays are shortlisted using ensemble PL measurements with the optimal nanohole size and e-beam dose being identified. From the site-selection process, the PL intensity is dependent on e-beam dose and only dose 2 and dose 3 arrays have shown ensemble emissions. From the two dose, dose 3 was selected for further investigation. By varying nanohole sizes between 32 nm to 60 nm demonstrated the ability to control the optical with 40 nm and 50 nm presenting ensemble emissions that would be suitable for single dot measurements. Initial characterisation of the linewidth, FSS and identifying the exciton and biexciton states of a single QD emission are presented. For 40D3 and 50D3 arrays, a QD map showing a series of neighbouring QDs with comparable optical properties, such as wavelength and linewidth, was shown that has the potential to be used in nanophotonics devices. The lowest recorded linewidth of 22.4 μeV on a positioned QD was achieved with the EBL-dry etching fabrication method. This linewidth achieved is comparable to the linewidth presented in the literature [186]. We believe that with the use of resonance fluorescence measurement it is possible to improve the linewidth to below 10 μeV required for indistinguishable photon pairs [7] [187].

While the QD map presented positioned QDs which are not suitable for QCSE tuning or Hong-Ou Mandel experiment, Huggenberger et al, has previously demonstrated that site-controlled QDs with comparable linewidths presented in this chapter can be used in device structures and suggest that

these QDs are suitable to be integrated into cavities of micropillar resonators and photonic cavity structure [13]. From the successful results of site-controlled QDs presented in this chapter, device fabrication of nanobeam devices with these QDs was performed requiring optical characterisation (not yet been performed). Figure 5- 19 shows SEM images of the newly fabricated nanobeam devices on a site-control pattern. On the other hand, having shown undoped site-controlled QDs with narrow linewidths but lacking in the ability to tune QDs into the same wavelength. One proposed solution is the use of QCSE but this requires the use of a doped structures. With such requirements, the use of a p-i-n diode structure is designed to allow for an applied electrical field to tune QD wavelength and linewidth by shifting the band structure under the QCSE [103] [188]. A maximum ± 2nm shift is achievable with QCSE, enabling neighbouring QDs with similar wavelengths to be tuned into the same wavelength.
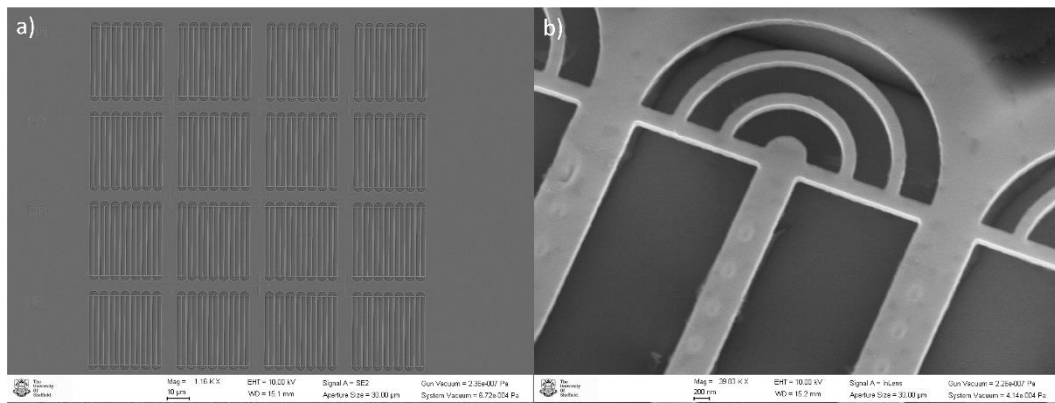

Figure 5- 19 SEM image of nanobeam devices from undoped site-controlled QDs waveguide structure, a) top-down view, b) angled at 30° from top-down of a single nanobeam, with clear visibility of site-controlled QDs on nanobeam. The SEM images was provided with permissions by Dr. Dominic Hallet and Dr. René Dost fabricated the device.

6 Doped site-control quantum dot growth and characterisation

With promising results achieved when adding growth interrupt and indium flushing into the growth structure, we turn out attention towards doped site-control structure for electrical characterisation and tuning. The fabrication methodology for undoped samples requires modification to reduce the etched pits' depth to be suitable for doped structures. With a deep etch, the previous process places the QD depositions too close to the sacrificial layer and, more crucially, the doped layer. This is one of the challenges addressed in this chapter with doped waveguide growth. Controlling the planarisation on patterned substrates is another important aspect, as a lack of planarisation also impacts the position of QD deposition. Therefore, varying different parameters to control planarisation are discussed in this chapter. Site-control QD with good optical emissions including low linewidth has been realised in recent years [107] [154]. However, the lack of scalable devices and the use of multiple SCQDs within devices have yet to be reported. This is a challenging requirement to control as even under site control, variations in the fabrication and growth will impact the size and shape of QDs and occupation, which alter QD wavelengths. An alternative solution would be tuning QDs to emit at the same wavelength with the use of quantum confinement stark effect (QSCE). To realise this requirement, a series of QDs within an array emission with comparable wavelength range is needed. With an applied electric field in the device structure can enable controlled spectral alignment of QD emissions if the dots are within ± 2 nm of each other in the unbiased devices. A doped waveguide structure was therefore fabricated into mesa diodes to study the capabilities of site-controlled QDs under QSCE.

Doped SC Waveguide Growth

For doped SC waveguide growths, the optimisation of the initial growth conditions is based on parameters detailed in Chapter 4 with the addition of the doped layers. For all doped SC waveguide structures, an undoped GaAs (100) substrate was used. After degassing, 300 nm of the i-GaAs buffer layer was grown. Followed by 950 nm i-AlGaAs and 200 nm n-AlGaAs sacrificial layer was deposited. Finally, 25nm of n-GaAs and 20 nm of i-GaAs were deposited before being cooled down and removed from the reactor for pattern fabrication. For all layers grown, the substrate temperature was 600°C, and for all n-doped layers, a target doping concentration of $3\times10^{18}\,cm^{-3}$ was deposited using a Si doping cell.

The standard fabrication process and sample preparation previously detailed in 3 Methods are used in these samples to apply the pattern and prepare the sample for the regrowth of the remaining structure. For the regrowth structure, three different structures were proposed and grown for each campaign. Figure 6- 1 shows simple diagrams of the three different growth structures: a) standard

GaAs-only capping structure, b) 5nm GaAs/3 nm AlAs barrier layers and c) 5 nm thin GaAs layer (for indium flushing) with GaAs/AlAs barriers. For GaAs only capping structure (Sample 1), 30 nm i-GaAs was deposited onto the patterned surface at 550°C. InAs QD were then deposited at 500°C for 162 seconds at a rate of 0.011μm/h, then capped with 55 nm of i-GaAs and 30 nm p-GaAs capping layer at 500°C. For the GaAs/AlAs barrier sample (Sample 2), the 22 nm i-GaAs layer is deposited onto the patterned substrate, followed by 3 nm and 5 nm of AlAs and GaAs, respectively, at 550°C InAs QD is then deposited at 500°C for 162 seconds at a rate of 0.011μm/h and is followed by 5 nm GaAs deposited at 500°C. At this stage, for the indium flushing sample (Sample 3), the growth temperature is ramped up to 550°C for 3 minutes for indium flushing before cooling back down to 500°C for the remainder of the structure. Both structures, Sample 2 and Sample 3 then continue with a 3 nm AlAs layer deposited to complete the barrier structure, followed by 47 nm and 30 nm of i-GaAs and p-GaAs, respectively, at 500°C. Carbon doping was used for all p-type doping with a target doping concentration of 2×10^{19} cm^{-3}. A full list of all the structures presented in this chapter is detailed in Table III.
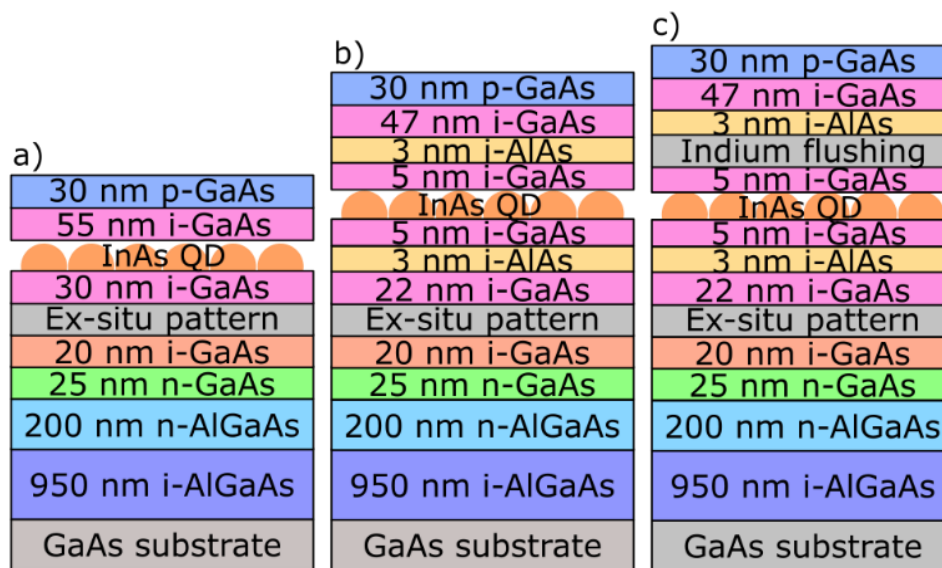
Figure 6- 1 Simple diagrams for different doped SC waveguide growth structures, a) GaAs only structure, b) 5 nm GaAs/ 3nm AlAs barrier structure, c) GaAs/AlAs barrier with 5 nm thin GaAs for indium flushing.

Table III A list of site-control growth structures used in this chapter; samples are ordered by the sample number.

Sample number	Control parameter	Regrowth structure	Regrowth sample	Etch duration (s)	Characterisation methods	Growth temperature (°C)	QD transition time (s)
PR0098	N/A	Optical structure	PR0078B	20	AFM/LT µPL	540	148
PR0265	Doped waveguide – GaAs only capping	Optical structure	PR0182A	20	LT µPL	550	162
PR0257	Doped waveguide – Barrier only	Optical structure	PR0182C	20	LT µPL	550	162
PR0268	Doped waveguide – Barrier with indium flushing (5 nm)	Optical structure	PR0182D	20	LT µPL	550	162
PR0279A	AHC (13 A)		PR0279A	20	AFM/SIMS		
PR0279B	AHC (13.5 A)		PR0279B	20	AFM/SIMS		
PR0301	Growth temperature	40 nm GaAs buffer	PR0164D	20	AFM	550	
PR0302	Thin GaAs layers (20x 2nm)	40 nm GaAs buffer	PR0164D	20	AFM	550	
PR0303	Growth temperature	40 nm GaAs buffer	PR0164D	20	AFM	580	
PR0304	Growth temperature	40 nm GaAs buffer	PR0164D	20	AFM	600	
PR0305	Etch duration	40 nm GaAs buffer	PR0290A	15	AFM	550	
PR0306	Etch duration	40 nm GaAs buffer	PR0290B	10	AFM	550	
PR0307	Etch duration	40 nm GaAs buffer	PR0290D	5	AFM	550	
PR0310	V/III ratio (11:1)	40 nm GaAs buffer	PR0279C	20	AFM	550	
PR0311	V/III ratio (10:1)	40 nm GaAs buffer	PR0279D	20	AFM	550	
PR0316	QD deposition	Optical structure	PR0308C	20	LT µPL	550	163
PR0317	QD deposition	Optical structure	PR0308D	20	LT µPL	550	167
PR0318	Doped waveguide – GaAs only capping	Optical structure	PR0295A	9	LT µPL	550	163
PR0319	Doped waveguide – Barrier only	Optical structure	PR0295B	9	LT µPL	550	163
PR0320	Doped waveguide – Barrier with indium flushing (5 nm)	Optical structure	PR0295D	9	LT µPL	550	163

The samples were then removed from the reactor and fabricated into mesa diodes for optical and electrical characterisation. The fabrication process was completed by Dr René Dost, where first the sample was cleaned using n-butyl acetate, acetone and IPA to remove any dirt and contamination from the surface. Then a 100 nm of CSAR photoresist is applied onto the surface using a spinner at 4000 RPM for 30 seconds. The sample is then baked for 60 seconds at 100°C before the back contact pattern is developed on the wafer using photolithograph. This is then etched onto the wafer using ICP where the etching gas used was Cl_2 and $SiCl_4$ with Argon. The residual resist is then removed using resist remover 1165, n-butyl acetate, acetone and IPA. Next the surface contacts is deposited onto the wafer, by a second round of photoresist and photolithography for the surface contacts using the same conditions. Followed by the deposition of Ti/Au contacts using a splutter. The fabricated diode is then mounted onto a custom-made PCB where the top contacts are wire bonded to the PCB track pad.

The mesa diode was then measured using µPL *Setup 2* for optical characterisation and device characterisation, including the ability to bias a diode to tune QD emissions (refer to Photoluminescence (PL) for the specific details of the setup). To check the fabrication process, an IV curve was obtained on the Sample 3 diode shown in Figure 6- 2a. This actually shows a poor IV curves for this device with a low turn-on voltage of 1V. The current saturating quickly with a max current of1200 µA, and a high current draw suggesting a short circuit within the device structure. Similar IV curves are also obtained for all diodes fabricated from the other structures showing these diodes have poor electrical connection. The device could also be excited optically with the use of a LED as the excitation source to observe QD properties within the array when biased at 0V. Figure 6- 2b shows an example of a PL image with 0V bias for a 0.6 µm pitch array from the Sample 3. The presence of QD emission is observed, with the majority of emissions originating from the alignment markers. Low density QD emissions is also observed, but it is difficult to determine if they are positioned or randomly nucleated QDs. Similar results of low-density QD emissions or even no QD emissions were found in the other doped structures. The initial conjecture is that poor QD emissions originates from the device fabrication process due to the poor IV curves. Therefore, a second attempt to fabricate a mesa diode with different arrays was performed which produced good IV curves, however no optical emissions from ordered QDs was observed. This indicates that the lack of QD emissions in the ordered array is caused by other factors linked to the growth process.

The possible cause of the absence of positioned QD emissions could be explained by the optical image shown in Figure 6- 3, a dark field optical image of the post-regrowth surface from the Sample 3. This image presents a well-defined and easily visible pattern, including the alignment markers and nanohole arrays. The clearly visible arrays of nanohole positions is not translated in the PL images

previously shown (see Figure 6- 2b), which suggests either QD emissions are not optically active or this is evidence of the etched nanohole remaining on the surface (i.e. unplanarised nanoholes). For patterned substrates, capped QD deposition has previously been demonstrated to form a small mound protruding from the surface as evidence of buried QDs on the surface [189]. However, the dark field image presented does not match the evidence presented in the literature, further indicating the presence of unplanarised nanoholes and the absence of QD in the nanohole. To confirm this theory, in the next section the surface morphology is investigated with AFM and checked against with older successful SC samples with QD emissions.
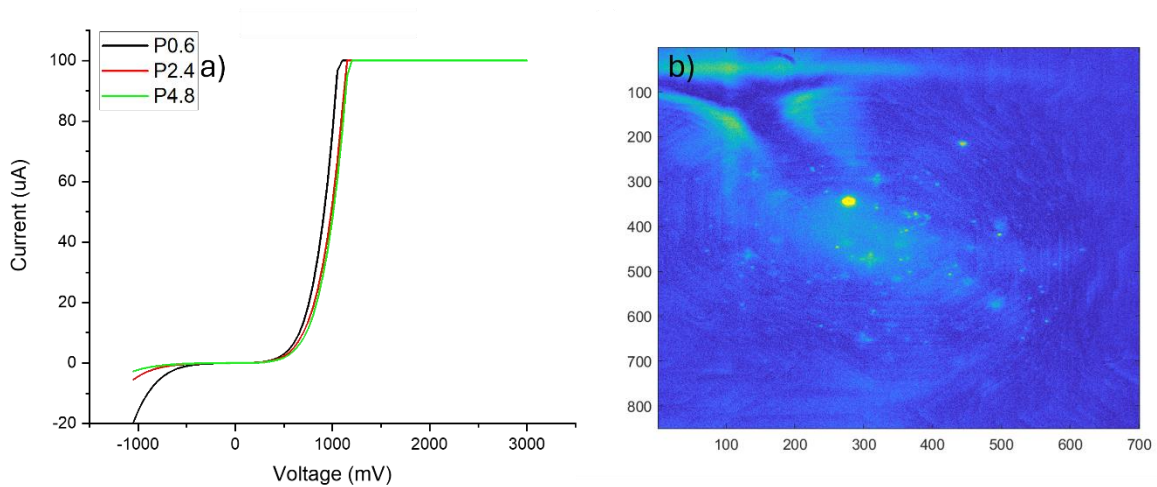

Figure 6- 2 Characterisation of Sample 3, where a) IV curve of the mesa diode for arrays with different pitches, b) PL image with 0V bias was taken from P0.6 arrays, where poor emission across the pattern regions is observed and are random or from alignment markers.
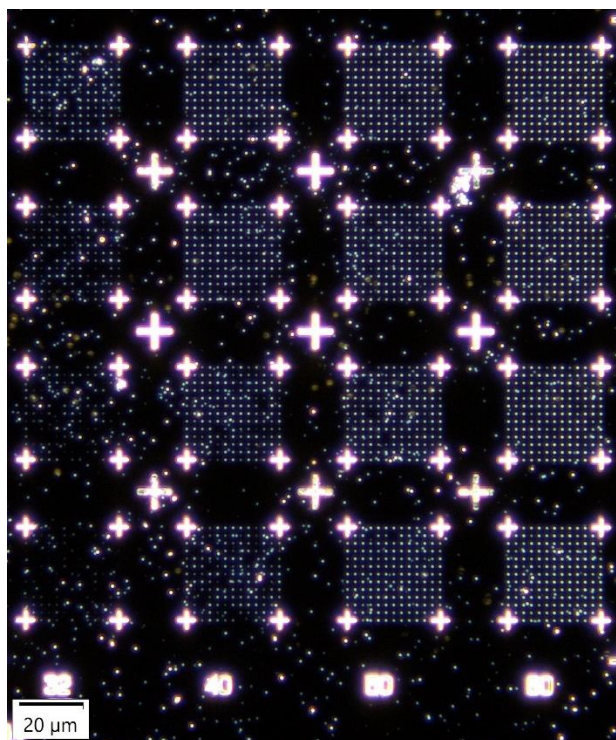
Figure 6- 3 Dark field optical microscope image of Sample 3 with 2.4 µm pitch arrays with 32 nm to 60 nm diameter nanoholes with e-beam dose 5 to 8. The image shows good retention of the pattern surface after growth with the presence of surface contamination randomly positioned.

Planarisation of site-control pattern

To understand the change in nanohole morphology after regrowth (growth after ex-situ fabrication of the pattern), AFM images were taken from the same arrays (60D8) in the pattern before and after regrowth, allowing for comparison in the change in nanoholes. For this chapter, the definition of "pre-regrowth" is defined as the stage where the sample has undergone pattern fabrication and cleaning process prior to sample loading into the reactor. While "post-regrowth" is defined as the stage where the sample has just completed the growth after the substrate has been patterned.

Figure 6- 4 compares the (1×1) µm^2 AFM image of pre-regrowth and post-regrowth of the Sample 1. The pre-regrowth surface shows a clean and well-etched pattern, suitable for regrowth. The nanohole depths from the pre-regrowth AFM images are uniform, with an average depth of (32.4 ± 0.9) nm, indicating that the etching process was also uniformly applied. For post-regrowth, nanoholes are elongated along the [1-10] orientation, which has previously been reported to be caused by growth anisotropy during growth on nanoholes [75]. With a 6nm infill within the nanohole is observed, the average depth of the nanoholes is (108.4 ± 17.1) nm after 115 nm of material growth. The lack of planarisation observed appears only to affect the etched nanoholes as other non-patterned region has normal layer growth. This suggest that the lack of planarisation arises unknow changes during fabrication or growth, leading to the lack of material deposition within the etched nanoholes. The current assumption is either the nanohole shape profile has changed which discourages material

depositions within the nanohole, or the growth conditions or etching process was altered such that no diffusion of the indium or gallium atoms into the nanohole is achieved.
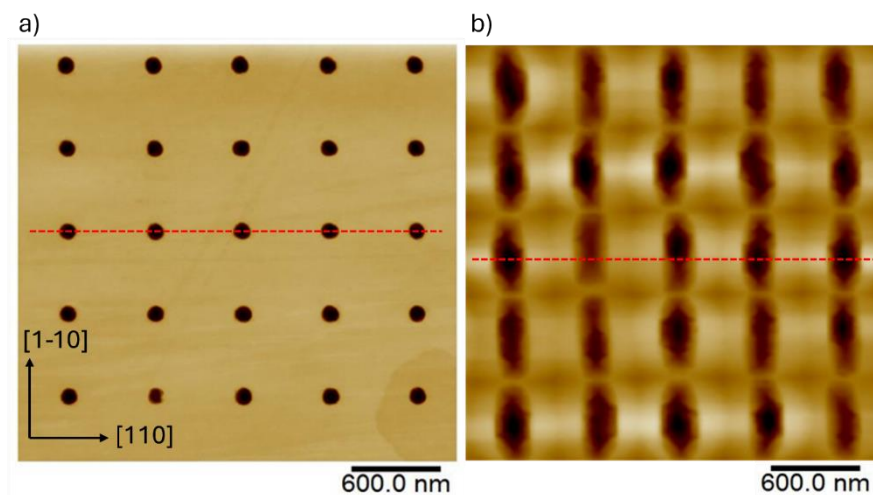
Figure 6- 4 AFM images (1 × 1 µm²) comparing the 60D8 arrays of Sample 1 before and after regrowth where AFM images, a) the surface of the patterned substrate before regrowth, b) the surface of the patterned substrate after regrowth. The location of the sets of nanoholes is within the 60D8 arrays but not of the same set of nanoholes.

The shape profile of the nanohole is outlined by a line profile from both AFM images is shown in Figure 6- 5. The additional growth of 115 nm is also taken into account in the line profiles to demonstrate the lack of planarisation. Post-regrowth line profile shows a large depth variation with some etch pit depth comparable to the initial depth plus the additional layer grown during regrowth (115 nm total thickness deposited). This observation of lack of planarisation is unexpected as typically the nanoholes act as preferential nucleation sites where the deposition rate within the nanohole is higher than the planar surface, as the indium will prefer to diffuse into the etch pits over the planar surface [76]. Instead, the opposite is observed likely due to the change in surface energy on the planar surface is more energetically favourable compared to the etch pit for layer-by-layer growth [164]. One possibility is this could be introduced during the atomic hydrogen cleaning (AHC) step which is known to be an abrasive step and will damage the surface.

An additional observation is the initial etch nanohole depth where the bottom of the etch pit is within the doped layer. Figure 6- 5 provides a simple diagram illustrating the nanohole depth with respect to the rest of the structure. This meant that the etch pit prior to regrowth already encroached onto the n-doped GaAs layer by ~12 nm and after 115 nm of regrowth, a total of 6nm infill of etch pits which is insufficient to have QD deposition away from the n-doped layer. This meant that at the QD deposition step, InAs deposition is either on the planar surface, randomly positioned away from the doped layer, or within etched nanoholes but in the doped layer region. For the QDs within the etch pit, these QDs are optically inactive due to the doped layer supressing QD emissions due to charge suppression [190].

While the randomly nucleated QDs deposited on the surface will emit light by being far away from the doped layers, as seen by the randomly positioned QDs shown in Figure 6- 2b. The issues of etching into the doped region was previously not considered as if the nanoholes was planarised as intended the QD deposition would be up to 30 nm away from the doped layer to enable QD emission. Evidence to support this claim is the QD emission from randomly nucleated QD (see Figure 6- 2b). Therefore, investigation into SC samples which was previously planarised is required to compare the growth conditions and fabrication methods.
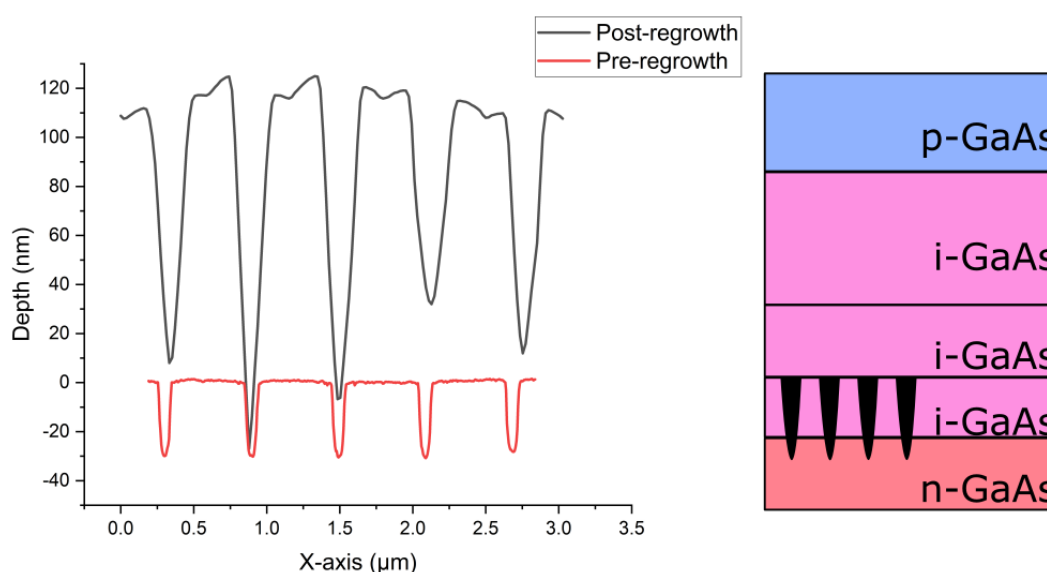
Figure 6- 5 A-line profile comparing the nanohole depth of pre- and post-regrowth in the [110] direction denoted by the red dash line in Figure 6- 5. The array used of the 60D8 array of Sample 1. An equivalent, to-scale comparison of the intrinsic region and adjacent layers of structure growth (excluding the QD layer) is presented, showing that the etching depth also encroached on the n-doped layers.

A successful site-control structure which contained GaAs only layers sandwiched in between InAs SCQDs (see Figure 4- 1a without the AlGaAs sacrificial layer) showed high QD occupancy and QD emissions within the arrays was used to compare with the SC waveguide structures. The pre-growth and post-regrowth AFM images from Sample 1 , are shown in Figure 6- 6a-b. The pre-growth surface is comparable to the doped waveguide structures with a clean surface, and well-defined etch pits with an average depth of (31.2 ± 1.1) nm. The post-regrowth AFM images of the undoped GaAs capped structure show reduced elongation of the nanohole along the [1-10] orientation that is attributed to the infilling of the etched pits. The depth of these planarised pits has an average depth of (2.7 ± 0.7) nm and is sufficiently far from the fabricated surface. Figure 6- 6c shows the line profile of etch pits from the pre- and post-regrowth surface with the total thickness grown (180 nm) included. However, the buffer layer grown remains unchanged with 30 nm of i-GaAs prior to QD growth. This buffer layer

is the main growth step, which moves the QD depositions away from the patterned surface. Infilling of the nanoholes during this step is crucial for QDs, as if this was in a doped waveguide structure this moves the bottom the nanohole away from the doped layer and centres the QD position in the middle of the waveguide structure. The additional 65 nm layer growth caused planarisation was also determined not impact planarisation as in the current doped SC structure after 115 nm of layer growth, the nanohole was infilled by 6 nm and increase the layer growth by 65 nm (~50%) will only increase infilling to 9 nm (or 3 nm of additional infilling), which will not be enough to planarised the sample. The growth presented in this section, demonstrate that we previously have achieved planarisation of etched nanoholes, but additional investigation is required determine the cause of the lack of planarisation observed in the doped SC structure.
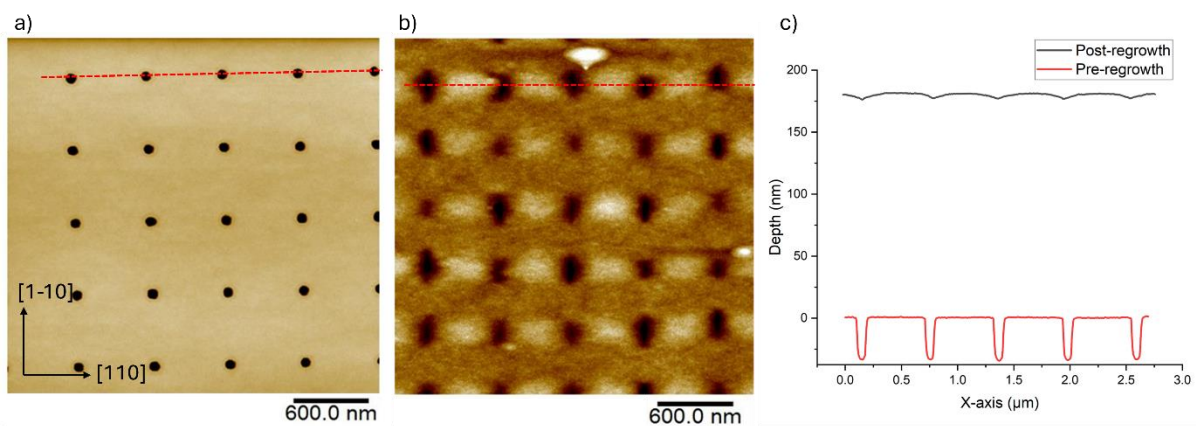
Figure 6- 6 Surface analysis of a GaAs capped SC structure, where 1 × 1 μm² AFM images of a) pre-regrowth surface, b) post-regrowth surface, c) Line profile comparison between two arbitrary rows from the AFM along the [110] orientation, denoted by the red dash line. The additional thickness grown by regrowth is also compensated.

Parameters affecting nanohole infilling

The lack of SCQD emissions from the doped structure has been identified to be caused by the lack of infilling of the etch pits, which results in QD deposition within the doped layers and suppressing QD emissions. Therefore, various factors influencing the infilling of etch pits have been investigated. To observe the infilling mechanism, only the regrowth buffer layer is deposited onto the patterned surface in an undoped GaAs structure. The amount of GaAs deposited is also increased from 30 nm to 40 nm compared to previous growth, to ensure enough material is deposited for planarisation to take place. All AFM images shown are (1 × 1) μm² and are taken from the 0.6 μm pitch, 60D8 array for consistency.

Etch duration dependence

Adjusting the etch duration controls the etch depth, minimising the amount of material depositions needed for planarisation. This is also useful in doped structures as this would move away from the doped layers, which act as charge traps for QD emissions. In this set of samples, the etch duration is

reduced from 20 seconds to 5 seconds, and the GaAs layer is grown at 550°C. Figure 6- 7 provides a summary of the etching depth as a function of etch duration across the various samples in this section. The depth variation at 20 seconds etch indicates that the ICP-RIE process is repeatable and produces minor variation (2 – 3 nm), which proves that the etching recipe is reliable. It is also noted that in the future doped SC waveguide growth process, the etch pits are formed with a 9-second etch for a 10 nm etch depth. This is to ensure the bottom of the etch pit does not encroach into the doped layer, eliminating the possibility that QD emissions being supressed by the doped layer.
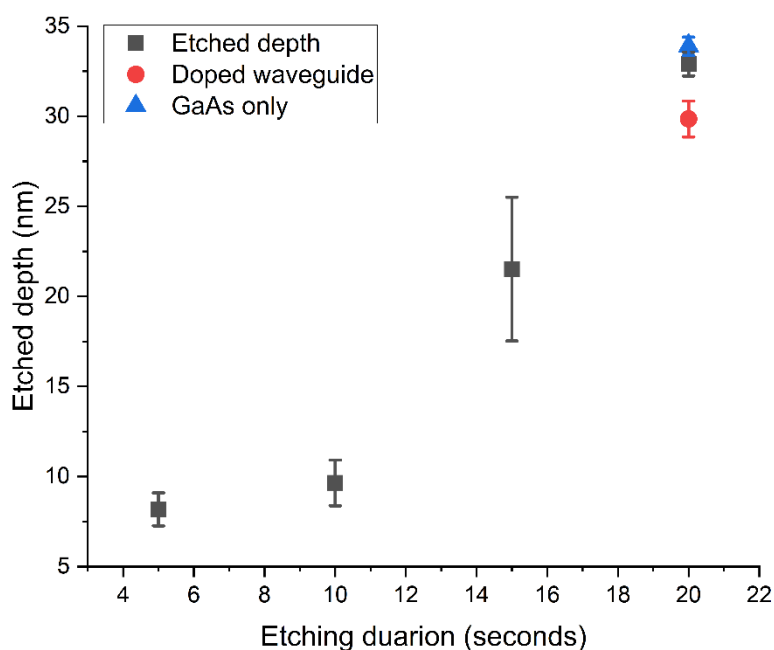
Figure 6- 7 Summarising the relationship between etch duration and etch depth between 5 seconds to 20 seconds with previous growth, including doped waveguide structure (Circle) and GaAs-capped structure (Triangle).

Figure 6- 8 shows a summary of the effects of varying etch duration comparing the pre-regrowth and post-regrowth profiles. For 20 second etch duration, this is the same etching duration in previous samples discussed in this chapter, which will act as a control sample and was used to compared with other parameters throughout the study. The pre-regrowth surfaces at this etch duration are within the expectation of previous growth with a clean surface and well-defined etched nanoholes. The average depth of the pre-regrowth etched pits is (32.9 ± 0.66) nm and, with the additional GaAs buffer thickness (40 nm), shows ~13 nm infilling within the nanohole with an average post-regrowth depth of (59.04 ± 5.33) nm. The post-regrowth surface also remains defect-free and flat, with the nanoholes showing elongation along the [1-10] orientation due to growth anisotropy during regrowth on nanoholes [75].
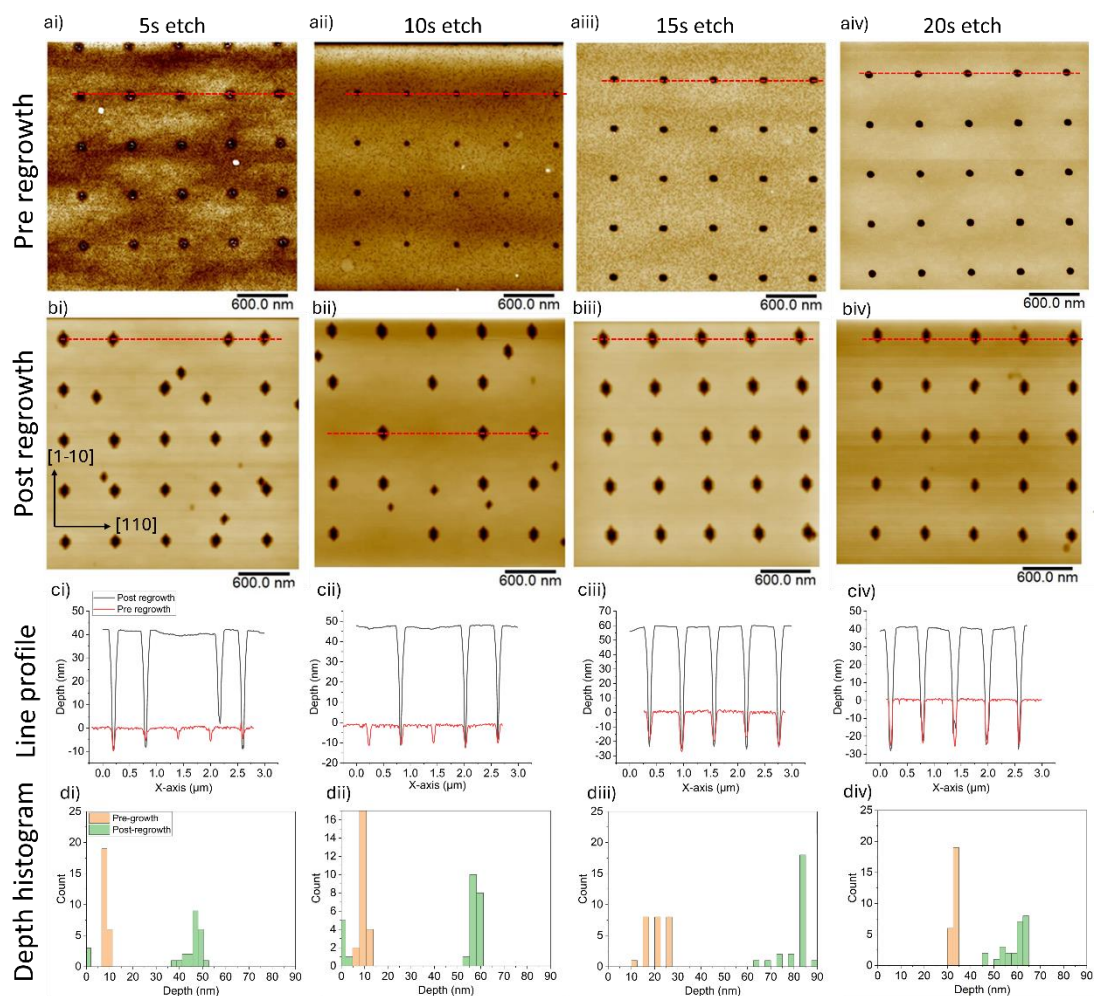
Figure 6- 8 Summary of etch depth variations showing a) pre-regrowth AFM, b) post-regrowth AFM, c) line profile of one row of nanoholes in the [110] orientation between regrowth (highlighted in dashed lines) and d) histogram summary of the nanohole depths from the AFM images. Etching duration of i) 5 seconds, ii) 10 seconds, iii) 15 seconds and iv) 20 seconds.

For a 15-second etch, the nanohole depth changes from (21.52 ± 3.99) nm to (79.88 ± 5.67) nm. This is an unexpected behaviour as the final depth is larger than the sum of the original depth plus the 40 nm buffer. It suggests that a total of 58 nm of GaAs is deposited during the regrowth, an additional 18 nm. For improving the infilling of the nanoholes, a 5-second reduction has the opposite effects, and the depth is increased. There are two possible explanations; the first is the simplest: a thicker GaAs was deposited from 40 nm to ~60 nm caused by changes in growth conditions, calibration, or human error. However, this is unlikely to be the cause as reviewing the growth logs and checking the recipe used, the correct conditions and the target depth were used. The second possibility is that the in-situ surface cleaning with AHC has altered the surface energy within the sample. AHC is known to be an abrasive cleaning technique however the exact changes to the surface profile is hard to determine, which could have affected the subsequent deposition. Atkinson et al, has previously shown that the use of hydrogen-assisted deoxidation (similar to AHC) to remove surface oxide, increases the hole

depth by ~3 nm [77]. Therefore the increase in depth to the nanohole could be linked to the variation in surface energy between the sample fabrication process and regrowth step.

For a 10-second etch duration, some residual contaminations remain prior to regrowth, and these have propagated through to the post-regrowth surface and formed randomly etched pits across the patterned surface. The formation of these randomly etched pits by contamination is evidenced by the fact that all etched nanoholes (site-control or random) are elongated in the [1-10] orientation which show that these are formed prior to any layer growth. For the patterned nanoholes, 6 out of 25 nanoholes (24%) show a flush surface, which is evidence of planarised nanoholes. However, the remaining nanoholes remain unplanarised and show similar result as the 20/15 second etch duration. The average post-regrowth depth is (44.16 ± 24.59) nm, a ~35 nm increase in depth, which is comparable to the total amount of GaAs deposited. This implies that some nanoholes are more likely to have material deposited within the nanohole, which could be linked to different etched hole profiles [166].

For a 5-second etch, pre-regrowth AFM shows residue of the resist or contamination remains within the nanohole. Therefore, another round of solvent and acid cleaning was performed on the sample before loading into the reactor for regrowth. Subsequent SIMS measurements and hydrogen cleaning also confirm the removal of the contaminates. However, post-regrowth AFM presents a different result, where the randomly etched pits are still visible within the pattern region after growth. The density of random etched pits is increased by ~40% when compared to the 10-second etch, and the change in etch pits' shape is the same as patterned nanoholes where elongation along the [1-10] is observed. This suggests that the formation of random pits is prior to the overgrowth of the GaAs layer, a sign of either contamination maintained on the surface or the hydrogen cleaning is introducing additional etched pits, this would support the results presented with 15 second etch with formed deeper nanohole that expected. Therefore, further investigation of the hydrogen cleaning step is required to ensure, this cleaning step is not introduction additional etching step to the surface (discussed later). The planarisation of some of the nanohole with the array is presented, with 3 out of 25 positions (12%) showing a flushed surface. In terms of change in depths after growth, the pre-regrowth depth is (8.18 ± 0.91) nm and after 40nm of GaAs deposited, the post-regrowth depth has increased to (41.12 ± 15.47) nm, a change in depth of ~33 nm, suggesting 7 nm of infilling with nanohole pattern. With such shallow etches, we would expect complete planarisation of the nanoholes, which is visible in some locations. In contrast, based on the results it indicates that some other condition is preventing material depositions within the nanohole, which limits planarisation.

Figure 6- 8c shows the line profile for each etch duration comparing pre- and post-regrowth with consideration of the GaAs layer deposited. The change in post-regrowth profiles are consistent across the different etch durations and the nanohole elongation results in a hexagonal shape on the surface. Figure 6-8d shows the depth distribution of the nanohole across the AFM images captured, comparing pre- and post-regrowth. The majority of the nanoholes presented remain unplanarised, with an increase in depth corresponding to the total material deposited. The depth distribution suggests that infilling of nanoholes is random and another parameter is affecting the ability for material infilling. One example is the wall facets such as (5 3 3)B and (3 1 1)B, have previously been reported to influence infilling [191]. Lower durations produce similar facets which are less abrupt due to shallow holes, which improves the infilling rate. Ikpi et al, also describe gallium migration with a shallow facet, where there is a net migration of gallium adatoms from the bottom of the nanoholes to the side walls [166]. This means could suggest that for shallow etched holes, gallium is more likely to remain within the nanoholes rather than the planar surface. With deeper nanoholes, steeper facets are produced, which restricts the infilling as the surface energy at vertical facets are not favourable to gallium migration towards the sidewall, and the nanohole remains unplanarised.

The results presented in this section, indicate that a shallow etch depth can cause pit infilling of planarising random nanohole positions. However, this effect observed is not an ideal solution as we cannot control the planarisation uniformly across the array, which limits the scalability of site-control therefore, other parameters are investigated which could improve uniform planarisation.

Atomic hydrogen cleaning

When investigating the effects of etch duration on planarisation at lower etch duration, post-regrowth surface contained randomly etched nanoholes that could have been introduced during the atomic hydrogen cleaning (AHC) process. Therefore, investigation to ensure the AHC process are cleaning the samples without causing etching pits is needed. AHC was used as the alternative method to thermal treatment to produce clean surfaces and remove oxides ready for growth and is particularly useful for patterned substrates [192]. AHC is known to require lower substrate temperature to clean substrates but more importantly to prevent the pattern surface from degrading [193]. The efficiency of hydrogen generation, also known as the cracking efficiency, is determined by the cracker temperature. Therefore, controlling the current to the cracker controls the cracking efficiency. Figure 6- 9 shows the relationship between the hydrogen cracker temperature and cracking efficiency [151]. To study the effects of AHC, two different cell currents were used: 13A (1723.6°C) and 13.5A (1778.2°C) during the cleaning process at a substrate temperature of 535°C for 1 hour. SIMS measurements and AFM images were taken before and after AHC to identify the type of molecules removed and to examine the change

to the pattern surface. This study examined the possibility that the cleaning process introduces additional etch pits or generates defects on the surface prior to regrowth.
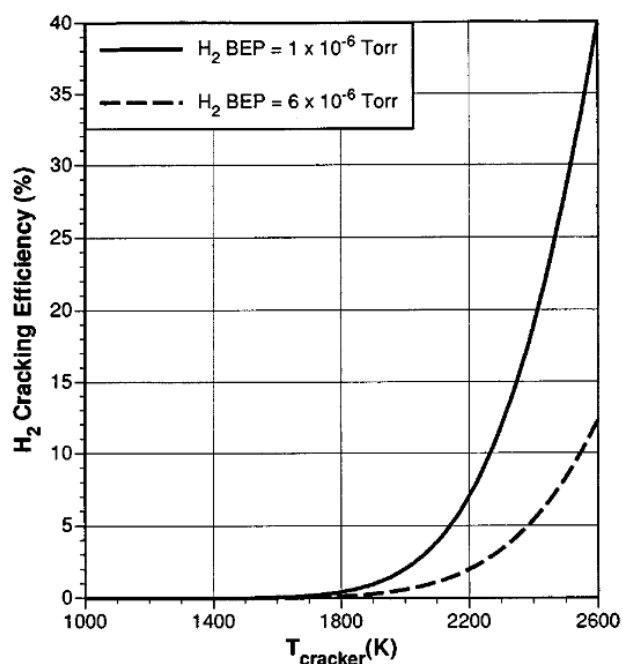
Figure 6- 9 shows the Cracking efficiencies of an atomic hydrogen source as a function of temperature. Two different hydrogen flow rates are indicated. This is a reprint with permission from the author: G. W. Wicks, E. R. Rueckwald, and M. W. Koch. Analysis of cracking efficiency of an atomic hydrogen source and its effect on desorption of $Al_xGa_{1-x}As$ native oxides. J. Vac. Sci. Technol. B 1 May 1996; 14 (3): 2184–2186. https://doi.org/10.1116/1.588895 [151].

Figure 6- 10a, b shows the comparison of the pattern surface before and after AHC at different cracking currents (temperatures). Varying between the two cracking currents, the surface does not introduce randomly etched nanoholes while maintaining a parabola-shaped patterned nanohole. According to literature, the shape of the nanohole only changes after material depositions during regrowth [68] which currently our results presents similar observations. On the other hand, the nanohole depth is reduced by 6.89 nm and 9.79 nm for 13 A and 13.5A, respectively, shown in Figure 6- 10c. With a higher current (higher temperature) will allow for higher cracking efficiency where more hydrogen atoms are generated, which can react with contaminates and the surface increasing the change in depth.

The distribution of the nanohole depths is shown in Figure 6- 10d, where the difference in abrasiveness between the two currents is demonstrated. The depth reduction within the nanohole is also an indication that some of the material removed from the sample surface and is reduced by up to 6 nm and 9nm, respectively. The change in depth to the pattern substrate is a known affect when hydrogen is used to remove oxide [77]. Kiravittaya et al, has demonstrated that use of hydrogen

cleaning and a short anneal reduces the pattern's depth due to out diffusion of material in order to smooth material [84] [194]. The surface roughness, excluding the pattern, is also improved, where a current of 13 A shows a reduction in surface roughness from 1.66 nm to 1.48 nm and 13.5 A from 1.64 nm to 1.52 nm. From a surface morphology perspective, these samples are clean to an exceedingly high standard, which is suitable for site-control growth without introducing additional etched nanohole.
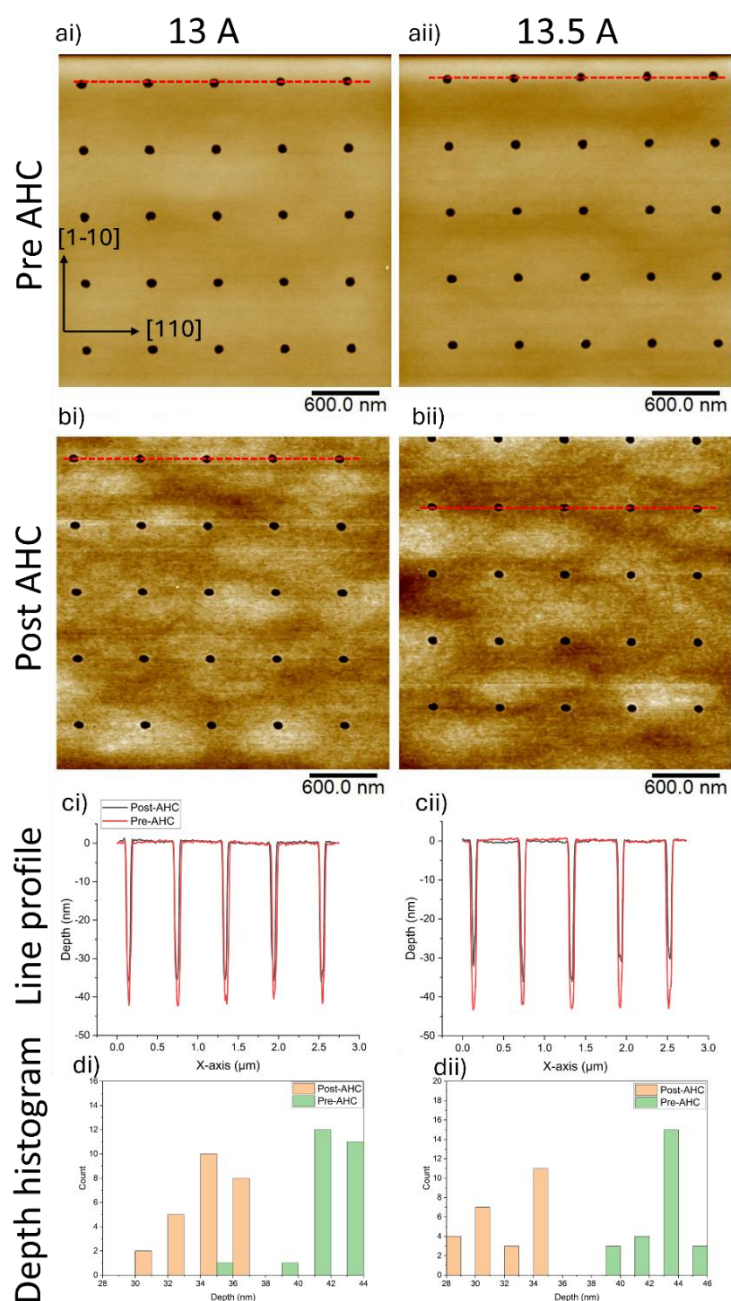
Figure 6- 10 Comparison of AFM images a) before and b) after AHC, c) line profile and d) histogram distribution between two different cracking currents (cracking temperature), i) 13 A (1723.6℃), ii) 13.5 A (1778.2℃). The post-AHC off-pattern roughness of 0.394 nm and 0.665 nm for 13 A and 13.5 A, respectively.

Figure 6- 11 compares the SIMS spectrum at the specific masses of interest between the two different cracker currents in the negative and positive modes. The pre-AHC and post-AHC are contrasted in the removal of certain molecules. The use of hydrogen cleaning was used to remove residual oxides that remain on the surface which caused rough surfaces prior to growth. This cleaning method has been shown to remove contaminants such as oxygen from the surface. After AHC, the presence of oxygen and hydroxide decreased significantly, likely to have reacted with the hydrogen atoms during AHC with a small trace remaining, which is normal. The decrease in intensity of both molecules is within an acceptable range when compared to previous AHC attempts of older site-control samples. GaO^- and GaO_2^- have been completely removed with AHC, and equivalent results are obtained for the AsO^- and AsO_2^-, and the effective removal of oxides is attributed to the combination of the acid dip and hydrogen clean. Other negative molecules are decreased by an order of magnitude, including carbon-based ions. Ionic salts presented, Na^+, K^+ and Ca^+, show negligible change after cleaning, suggesting that some contamination is still present and was introduced from the acid solution. The presence of Ga atoms remains strong despite the decrease in Ga intensity by an order of magnitude; this is expected when compared to previous hydrogen cleaning attempts on patterned substrates. Overall, the removal of unwanted oxides is confirmed, and no significant difference between the two currents used is found. The surface remains defect-free and prevents additional etched nanoholes from forming. As such, the AHC cleaning process was kept the same for subsequent experiments, with cleaning at 13 A for 1 hr.
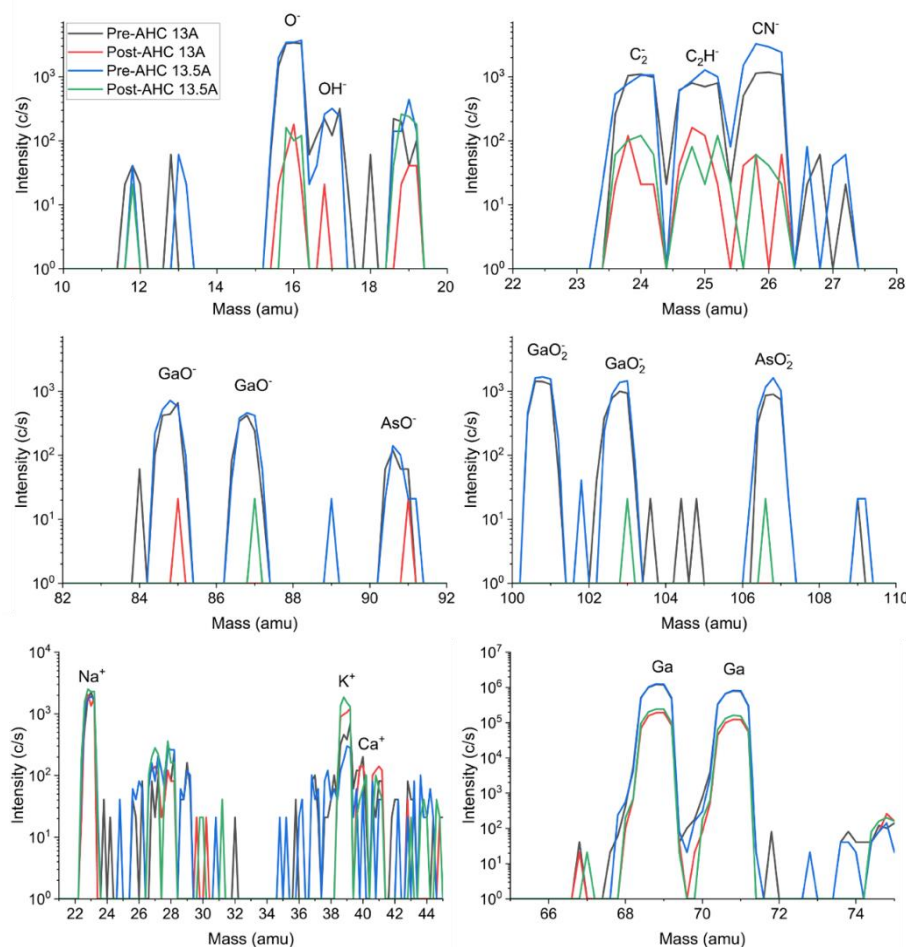
Figure 6- 11 shows the SIMS spectrum for selected masses for different cracker currents (temperature): 13 A (1723.6°C) and 13.5 A (1778.2°C) pre-AHC and post-AHC across the negative and positive modes.

Growth temperature variation

Growth temperature is one of the key growth conditions encouraging indium diffusion across the surface to improve the planarisation of the pits [87]. Figure 6- 12 shows the AFM image comparisons pre- and post-regrowth with growth temperatures between 550°C to 600°C. All pre-regrowth AFM was consistent with a flat surface and free from contamination, conditions which are suitable to load into the reactor for regrowth. When depositing 40 nm GaAs, increasing growth temperature up to 600°C shows no significant change to the nanohole shape besides elongation towards the [1-10] orientation as previously seen. At 550°C, the control sample growth temperature, the nanohole depth measured is comparable to the etch depth plus the GaAs buffer growth. The profile of the nanoholes within the array remains comparable to previous control sample images. At 580°C, subtle changes to the nanohole profile are found when compared to 550°C. One difference is the presence of randomly etched holes with the pattern regions. Otherwise, no major difference is seen when comparing the line profiles to the control sample. At 600°C, the surface remains defect-free, which suggests the random nanoholes found at 580°C are due to contamination and not introduced with higher growth

temperatures. The patterned nanoholes show random planarisation of positioned nanoholes, resulting in a variety of depths within an array. On the other hand, the shape of the nanohole is maintained at this temperature with no elongation in any direction. The observation of the post-regrowth AFM signifies that at high growth temperatures, the patterned surface is degrading rather than planarising, as evidenced by the lack of shape change to the nanohole and non-uniform infilling of the nanoholes after material deposition [68] (discussed later).
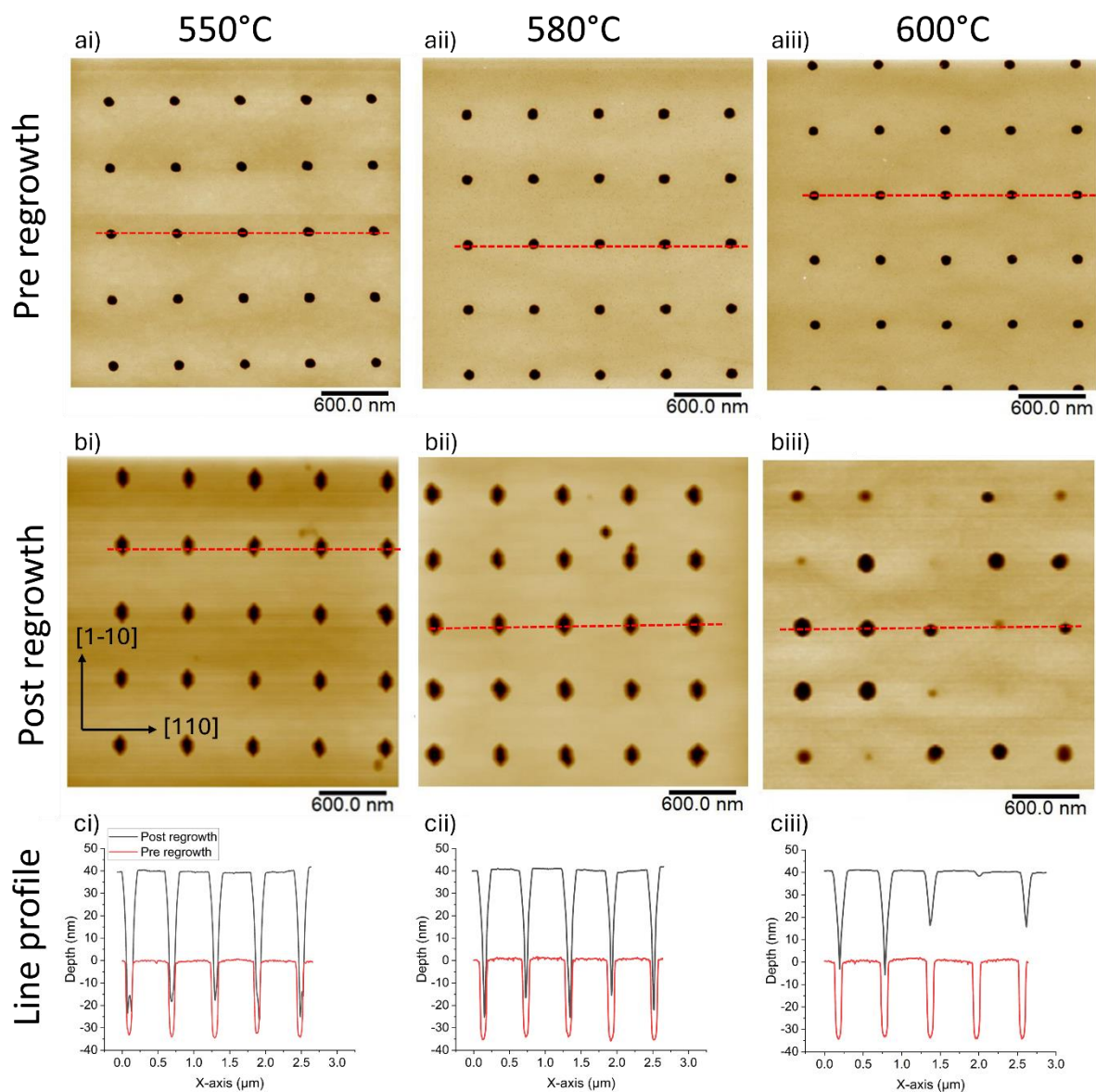
Figure 6- 12 Temperature dependence SCQD growth with AFM images comparing the a) pre-regrowth, b) post-regrowth, and c) line profile of one row of nanoholes (Red dash line) for different growth temperatures i) 550°C, ii) 580°C, iii) 600°C.

Figure 6- 13 outlines the nanohole depth distribution across each growth temperature and compares the pre- and post-regrowth. The pre-regrowth depths have a slight variation with an average depth of (32.90 ± 0.65) nm, (35.5 ± 0.61) nm and (34.19 ± 0.61) nm for 550°C, 580°C and 600°C, respectively. In an ideal scenario, the etch depth is consistent across all the arrays across the three samples. However,

there will be slight variation in the etch rate across the different samples due to a range of factors, such as the positioning of the arrays with respect to the plasma and variation with the plasma power, which all impact the uniformity of the etched nanoholes. After regrowth, growth temperatures up to 600°C present comparable post-regrowth depths of (59.04 ± 5.33) nm and (54.85 ± 4.22) nm, with an infilling of 14nm and 20 nm after the regrowth for 550°C and 580°C, respectively. This indicates that at lower growth temperature the variation between 550°C and 580°C has very minor improvements towards planarisation of the nanohole and suggest a different growth parameter is involved in preventing planarisation.

For a growth temperature of 600°C, the average pit depth is (18.74 ± 16.36) nm, with an infilling of 55 nm, the highest observed. The wide variation in nanohole depth across the arrays is not suitable for further investigation. However, using higher growth temperature could be a viable method in achieving planarisation. Typically, high temperature is not used on pattern substrate during oxide removal and patterned growth as this has shown to cause the pattern to collapse [84] and cause planarisation of the hole profile [87] at temperatures as low as 500°C. This results in enlarging the pattern profiles and reduction to the depth due to out-diffusion. Method such as hydrogen [192], gallium [77] or indium [73] assisted de-oxidation was developed to reduce the high temperatures required to remove oxides. In addition, the evidence of the nanoholes degrading over planarisation is the lack of shape changes observed. Schneider et al, has demonstrated the effects of infilling of nanoholes after layer growth is the elongation of the nanohole along the [1-10] orientation [68], where this is observed even at lower growth temperatures where lack of planarisation occurs. Other literature also support similar changes to the nanohole profile due to the infilling of nanoholes [55] [75]. Due to the uncertainty of whether a higher growth temperature (above 550°C) is beneficial or detrimental to the patterned substrate and reducing the depth of the nanoholes, the growth temperature is kept at 550°C, which has previously been shown to maintain a smooth surface growth without damaging the pattern in our growth process.
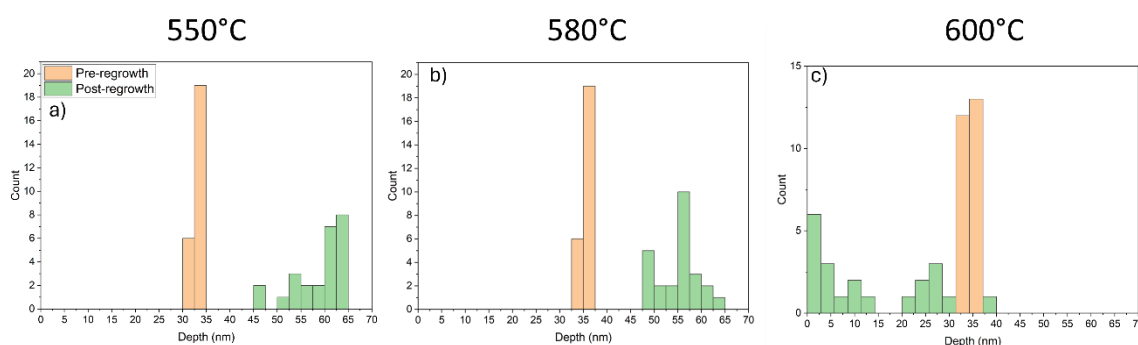
Figure 6- 13 Histogram comparing the pre-growth and post-regrowth nanohole depth for growth temperatures a) 550°C, b) 580°C, and c) 600°C. The nanohole depth measures are based on the AFM images captured in Figure 6- 12.

Thin layer deposition with growth interrupts

Changing the method of depositing the GaAs buffer layer was also investigated with a series of thin GaAs layers with growth interrupts. For this investigation, 2 nm thick GaAs were deposited, followed by a 30-second pause; this was repeated 20 times with a total thickness of 40 nm with a growth temperature of 550°C. Depositing a thin layer and annealing will promote the diffusion of gallium across the patterned surface and preferred deposition into the patterned regions caused by the large facets from the etched pits. Figure 6- 14 summarise the effects from 20 stacks of 2nm GaAs layer growth with AFM images and analysis of the nanohole depth change. The pre-regrowth AFM shows ideal regrowth conditions with uniform etched nanoholes on a clean and flat surface comparable to previous observations. After regrowth, no additional etch pits are formed with no evidence of planarisation from the nanoholes. Similar to previous growths, the nanoholes with elongation along [1-10] and maintain similar nanohole shape. Some of the nanohole shapes do have slight variations due to partial infilling, and the line profile provides better visibility on the change in etch pits after material deposition. In a cross-sectional view, the previous parabola-shaped nanohole has changed to irregularly shaped pits in some positions, as shown in Figure 6- 14c. The depth distribution is summarised in Figure 6- 14d, with the average depth changes from (34.66 ± 0.91) nm to (63.73 ± 7.92) nm, a ~11 nm infilling after 40 nm GaAs is deposited. When compared to a standard 40 nm thick GaAs deposition, a larger distribution of nanohole depth is presented, suggesting the infilling of nanoholes is inconsistent and random. The method of deposition proposed in this section is ineffective and unsuitable for SC growth. This conclusion is drawn from the fact that there was no observable difference when compared to the control sample, which deposited 40 nm of GaAs in a single growth step. This suggests that the method did not produce the desired effect of allowing gallium to diffuse more readily into the etch pits.
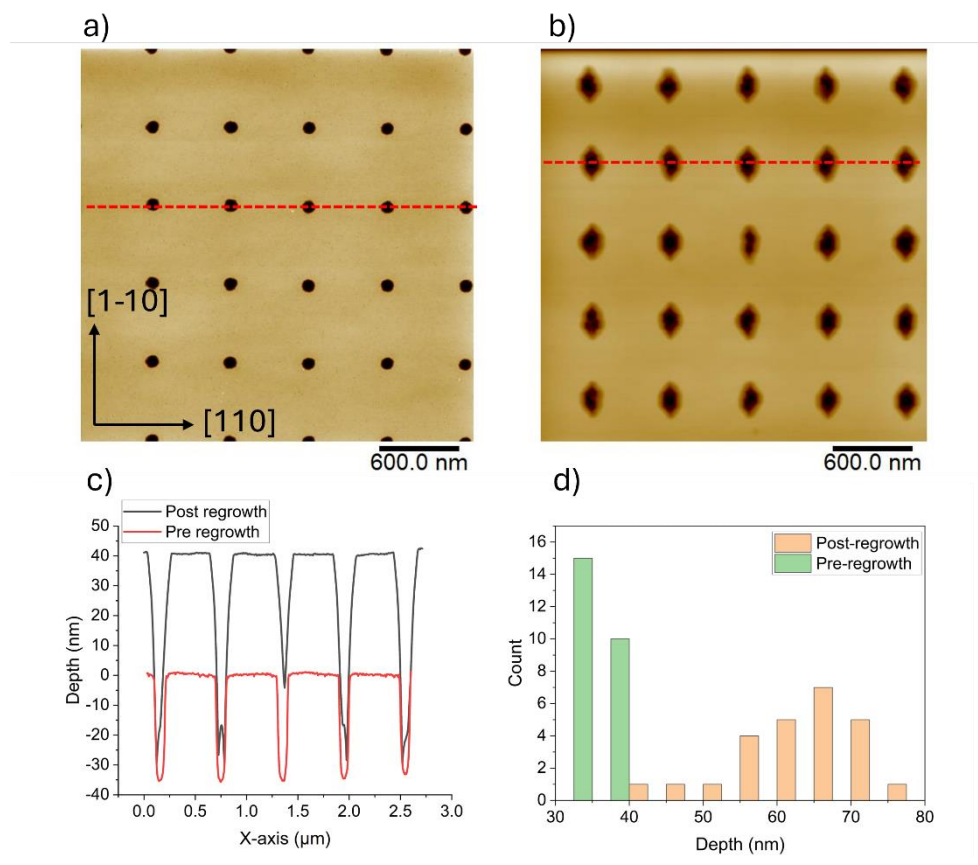
Figure 6- 14 Summary of the effects of 20x 2nm GaAs layers with a 30-second pause with AFM images of a) pre-regrowth, b) post-regrowth, c) line profile of a row of nanoholes along [110] orientation (red dashed line) and d) depth histogram of all nanoholes from the AFM images.

V/III ratio

MBE growth is typically carried out in group V rich conditions so the arrival rate of group III atoms determines the growth rate for GaAs layers. Therefore, lower gallium flux decreases the growth rate and results in slower layer growth. Comparing older SC growth, which achieved planarisation (see Figure 6- 6), with recent SC growths, the V/III ratios differ from 10:1 calculated for these previous planarised samples and 20:1 for doped waveguide growth and recent growth runs in this chapter. Therefore, a set of samples investigating the effects of the V/III ratio was grown, keeping the growth rate of GaAs the same as previously; the flux rate for arsenic was adjusted to control the V/III ratio. The arsenic flux was adjusted over gallium to observe the effects of the diffusion of gallium across the surface while keeping the total amount of gallium deposited the same.

Three different V/III ratios, 20:1, 11:1 and 10:1, are compared and the result of this parameter is summarised in Figure 6- 15. The surface quality is unaffected by the change in the V/III ratio, and no defects or additional etch nanoholes are found for the pre- and post-regrowth surfaces for all samples shown. With a V/III ratio of 20:1 as the control sample, no deviation from previously observed change in nanoholes and planarisation was observed. The nanohole continues to elongate along the [1-10]

orientation as previously found, and similar observations are found with other V/III ratios used in this growth set. Evidence of nanohole infilling is presented with a reduced V/III ratio, and the infilling matches closely with the amount of GaAs deposited during regrowth. For 11:1, the average nanohole depths change from (46.27 ± 1.21) nm to (53.89 ± 7.10) nm, and for 10:1, the depth changes from (44.16 ± 0.99) nm to (45.14 ± 7.31) nm. After taking into account the 40 nm GaAs deposited, the average infilling of nanohole was 32nm and 39 nm for 11:1 and 10:1, respectively. This infilling is uniform across the array, unlike previous results where only randomly selected nanoholes were planarised. Out of the two ratios, the 10:1 V/III ratio has a slightly higher infill rate, which is preferred. However, in our case, infilling of nanoholes only matches the rate of deposition (i.e. ~35 nm growth in the holes compared to 40 nm deposition), contrary to literature where infilling of nanoholes was seen to be higher than the planar surface [67]. Regardless, this study provides clear evidence that it is the V/III ratio that has the biggest effect on planarisation and the control sample was not optimised for this parameter.
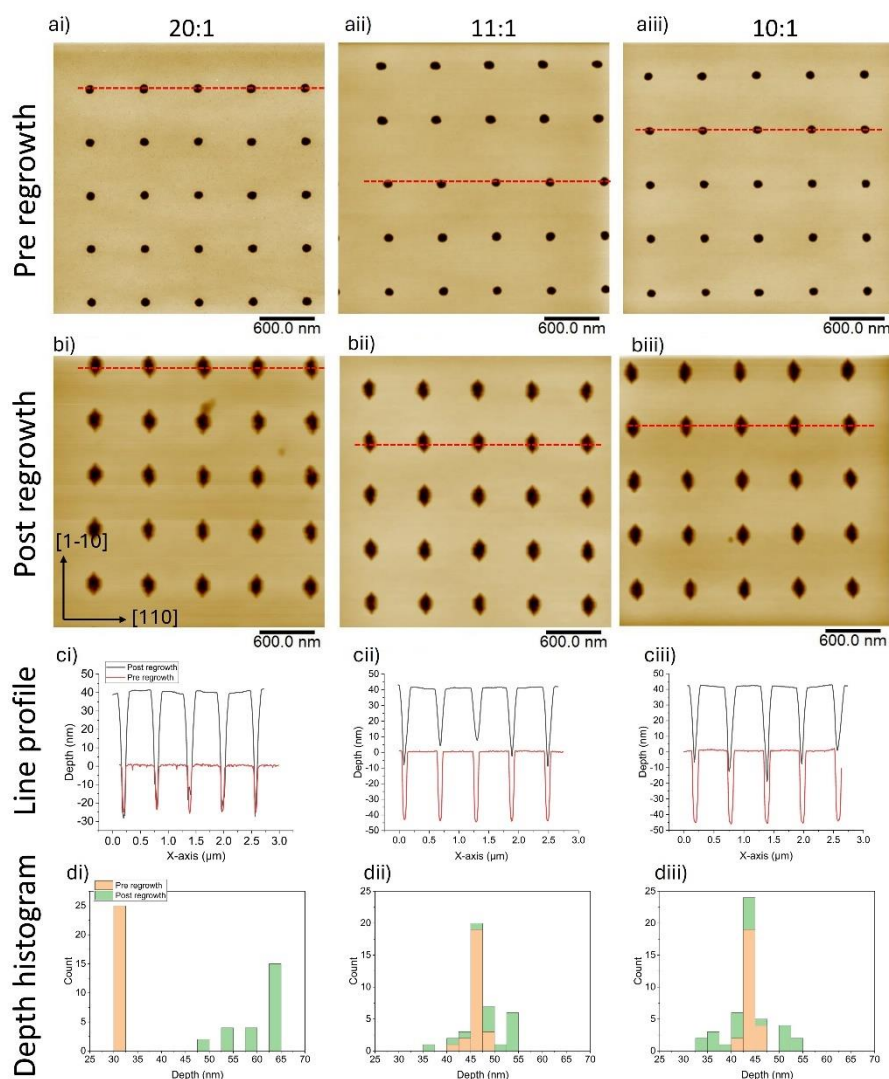
Figure 6- 15 Summary of the surface morphology comparing the a) pre-regrowth and b) post-regrowth AFM images, c) line profile of a row within the AFM along the [110] orientation, d) depth histogram with varying V/III ratio, i) 20:1, ii) 11:1, iii) 10:1. Infilling of the nanoholes around the same deposition amount is observed with nanohole elongating in the [1-10] orientation.

The planarisation of nanoholes was also achieved on other arrays with smaller nanoholes, which presumably is due to better infilling of the nanoholes with lower V/III ratio. An example of good planarisation is the 32D4 array, with a higher diffusion of indium of the nanoholes observed when compared to the 60D8 arrays. Figure 6- 16 shows a comparison between the nanohole profiles on the 32D4 arrays with different V/III ratios of 11:1 and 10:1. Using both ratios, after GaAs layer deposition, the nanohole shape maintains a round-shape profile instead of the hexagonal-shape found on the surface shown in non-planarised samples. The elongation along the [1-10] orientation is still present, but the diameter of the nanohole is reduced, which is attributed to the infilling of the nanohole. The shape profile at the surface of these arrays matches the shape change reported in the literature [55] [75]. The line profile further illustrates the infilling of the nanoholes while slightly increasing the nanohole diameter. With a V/III ratio of 11:1, the average depth changed from (28.25 ± 2.29) nm to

(14.19 ± 11.53) nm, a depth change of ~54 nm after 40 nm material deposition. This supports previous reports where the infilling of the nanohole rate is greater than the deposition rate across the planar surface [67]. When compared to a V/III ratio of 10:1, the average depth changes from (25.10 ± 4.65) nm to (6.69 ± 3.12) nm, a depth change of ~59 nm after 40 nm material deposition. This confirms that out of the two ratios used in this study, 10:1 is preferred as the nanoholes show better depth uniformity and good shape control, which will be used for further studies.

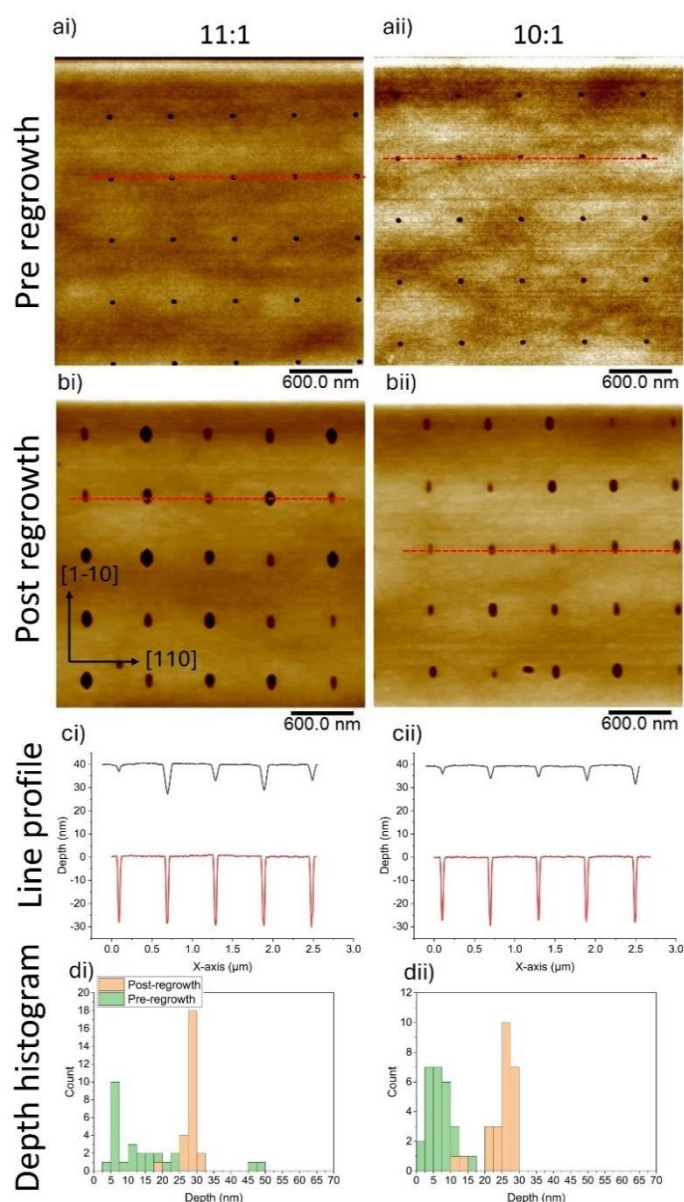*Figure 6- 16 Additional investigation towards smaller nanohole arrays, with a) pre-regrowth and b) post-regrowth AFM images, c) line profile of a row within the AFM along the [110] orientation, d) depth histogram with varying V/III ratio, i) 20:1, ii) 11:1, iii) 10:1. Uniform planarisation of nanoholes are demonstrated with lower V/III ratio, and shape change is minimised.*

Optimised growth conditions

This investigation to re-achieve planarisation on samples delves into examining both in-situ and ex-situ factors, which could enhance the infilling of etch pits on patterned surfaces. At low etch duration (depth) and high growth temperatures, random nanohole positions are planarised; however, this is not a viable solution as the rate of infilling is low and non-uniform across the arrays. Through manipulation of the V/III ratio, we were able to diminish the average depth of nanoholes to (6.69 ± 3.12) nm following 40 nm GaAs layer deposition. This moves the QD deposition interface away from the doped layers while maintaining a preferential nucleation site with the patterned array. Additionally, the correlation between etch duration and etch depth was optimised, allowing for etch pits to be formed without encroaching into the doped layers. Changes to the fabrication and growth process were made based on the results obtained in this investigation to ensure QD deposition is away from the doped layers. This includes a 9-second etch duration to yield a nanohole depth of ~10 nm and GaAs layers are grown with a V/III ratio of 10:1 during regrowth. With various parameters altered subsequent growth of QDs layer could be affected, therefore the next stage of the optimisation is to investigate the QD deposition conditions (2D to 3D transition time).

Optical structures

Having established conditions for good infilling primarily through adjustment of the V/III ratio, re-optimisation of the QD layer was investigated to ensure high occupancy and QD emissions are maintained. Two different 2D to 3D transition times (amount of InAs deposited) were investigated, 167 seconds and 163 seconds, which is below the standard 2D to 3D transition time for planar growths (170 seconds) previously defined for this reactor. Depositing InAs below the critical thickness are typically used in site-control growth as the minimum requirement for QD nucleation is found to be lower than randomly nucleated QDs due to the preferential indium diffusion to the nanoholes [21] [70]. After QD deposition, the sample is annealed for 60 seconds to improve uniformity and QD occupation. The QD layer is then capped with an 85 nm GaAs capping layer at the same temperature to maintain 170 nm thickness requirement for waveguide structures. The samples are then cooled down and removed from the reactor for low temperature (4K) μPL measurements using *Setup 2* (See Photoluminescence (PL) section for more details). For these samples, rapid feedback of the QD properties and occupancy is important as this enables the ability to make minor changes to the growth conditions for better QD properties.

Figure 6- 17 shows PL images of the QD arrays at the 0.6 μm pitch with different transition times. In both images, QD emissions in the form of the pattern are presented, showing that the pattern has successfully acted as the preferential nucleation site during the QD deposition. The QD occupancy across the arrays shows a significant difference depending on the 2D-3D transition times used. For

samples with a 167-second transition time, arrays either contain zero or high-density QD occupancy with poor emission intensity. The arrays with high-density QD occupancy also do not favour any specific nanohole size or e-beam dose arrays nor towards the centre of all the patterns or the edges. The reason the occupation of arrays is random is currently unknown, one suggestion could be due to a variation in nanohole formation across the different pattern parameters. For samples with a 163-second transition time, a low density of QD emissions within arrays is found, but this is consistent across most of the arrays in this sample. Some arrays exhibit high-density occupation across half of an array, but there is no explanation for the cause. While it is not possible to confirm if all QD emissions are from SCQD, the presence of some QD matches the ordered positions within the pattern. For both samples, the presence of alignment markers is clearly visible, and the emission from these markers is comparable to the rest of the sample. This indicates uniform QD depositions across the alignment markers and nanohole, a positive feature which was previously observed (see Figure 4- 3). It is also important to note that the lack of emissions observed could be a mixture of no QD occupation and optically inactive QDs.
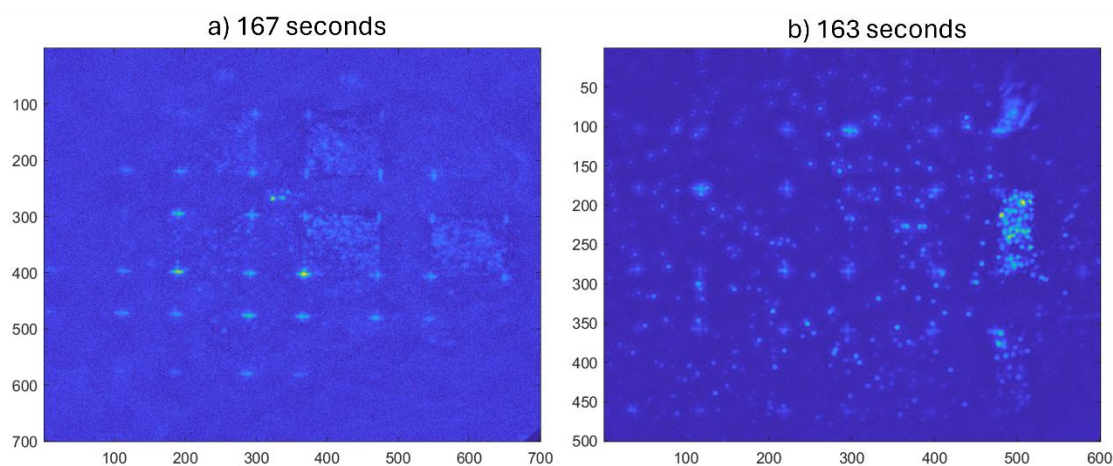
Figure 6- 17 PL images with different 2D to 3D transition times: a) 167 seconds and b) 163 seconds. Images captured are from the 0.6 μm pitch arrays with varying nanohole size and e-beam dose.

For optical characterisation of the QDs, a red laser with 1 μW excitation power was used to obtain the single dot spectrum measured. Figure 6- 18 presents the μPL spectrum of the 32D4 arrays with different transition times, which controls the density of QD formation. The results showed that a transition time of 167 seconds resulted in low density, sharp line emissions between 940nm and 980 nm. However, with a reduction of 4 seconds in the transition time, the density of dot-like emissions between 900 nm and 1000 nm increases significantly. The number of single dot emissions matches the density of QD emissions in the PL images shown in Figure 6- 17. The PL intensity between the two samples also differs significantly by up to 4 times, which indicates the difference in crystal quality and

the number of defects near the QDs [73]. Overall, both samples show QD emissions, but based on the number of QD emissions observed, the 2D-3D transition time of 163 seconds will be used in future QD layer growth.
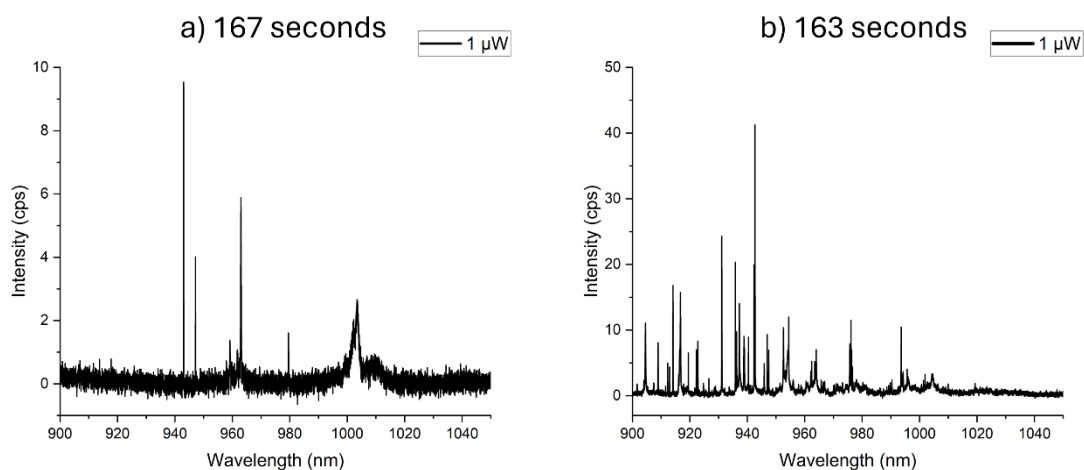
Figure 6- 18 µPL spectrum was measured with different 2D to 3D transition times, a) 167 seconds and b) 163 seconds. Acquisition settings of 1µW excitation power for 120 seconds were used on 32D4 array from the 0.6 µm pitch arrays.

Device characterisation

After resolving the lack of planarisation of doped structures, a repeat of the doped structures detailed in Figure 6- 1 was grown with the changes to growth conditions detailed in the previous section. Dr René Dost fabricated all samples into mesa diodes. The sample was then loaded into µPL setup (*Setup 2*) and cooled down to 4K for device and optical characterisation (we refer to Chapter 3 for the specific details on the setup). The diodes are initially excited by an LED for optical characterisation and 🔲 compare compares the PL images between the three diode structures with 0V bias. These images taken are from arrays within the 0.6 µm pitches as the high-density arrays provide quick identification of good SCQD emissions.

From these images, the Sample 1 diode had poor emissions from the pattern, with no clear indication of any QD or alignment markers. The Sample 2 diode has good QD emissions within arrays but also the presence of randomly nucleated QD emissions. The alignment markers are no longer visible, suggesting that QDs are not nucleated within the alignment markers and are more likely to nucleate within the nanoholes instead. For the Sample 3 diode, an ensemble-like emission is observed in the form of a pattern, but no single dot emissions could be identified. The changes to the emissions are impacted by the thin GaAs layer and subsequent indium flushing after QD deposition to control the height of SCQDs, which also diffuses exposed QD materials across the surface. For the Sample 1 and Sample 3 diodes, changing the bias voltage did not change the visibility of individual emissions. Therefore, no further measurements were taken from these samples. Only the Sample 2 diode

showed tuneable QD emissions by voltage bias. From the PL images, Sample 2 is the only sample with dot-like emissions, which warrants further investigation.
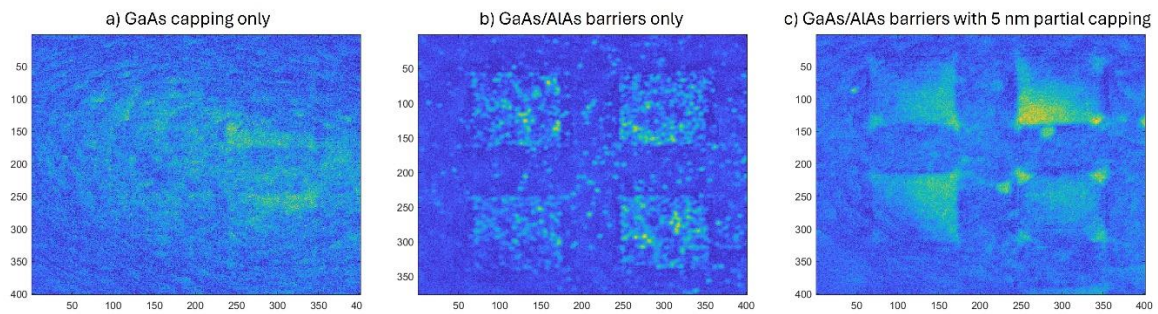
Figure 6- 19 Mesa diode structures PL images measured at 4K and 0V bias, a) GaAs capping only structure, b) GaAs/AlAs barrier, and c) GaAs/AlAs barriers with 5 nm thin GaAs layer for indium flushing is compared while excited by an LED. Images contain arrays from the 0.6 μm pitch pattern showing a variety of QD occupations.

Figure 6- 20 shows the IV curve of the three-mesa diode fabricated from the Sample 2 sample connecting to different pitches. A voltage bias of -0.5V to a maximum of 2V was applied to the diode as further increases could potentially damage the device. None of the diodes exhibit poor electrical conductivity (see Figure 6- 3a), as comparable IV curves are produced across the three diodes. Unlike previous attempts, when forward-biased, the current does not saturate, and a reasonable current is drawn. The diodes fabricated from other structures, Sample 1 and Sample 3, also presented comparable IV curves ruling out the possibilities of poorly fabricated diode structures. Thus this provides a good indication of a successful diode fabrication compared to previous attempts with poor IV curves (see Figure 6- 2).

From Sample 2, PL images of the different pitches were also investigated to observe QD occupancy. No emissions from the ordered array were found with a pitch size of 1.2 μm, but increasing the pitch size to 2.4 μm presented several arrays with good QD occupancy from the ordered array. Figure 6- 21a shows the PL image of the 2.4 μm pitch arrays with QD emissions, which were identified as 40D7, 40D8, 50D7 and 50D8 arrays. The PL image also shows the presence of defects which stretched across the 40D7 array, and the other identified arrays had clear and ordered arrays of QDs with varying intensities are also presented. Other obscuring features in this pitch are the metal contacts, illustrated at the bottom of the PL image, which block the majority of the arrays in this pitch. At 4.8 μm pitch, the difficulty in identifying arrays increases dramatically due to the low density of each array (7 x 7). This, compounded with no visibility of any alignment markers and a high density of randomly nucleation QDs within the pattern regions, makes it difficult to identify any arrays. One potential array was found; however, we are not confident in this finding. Some resemblance of an ordered array was demonstrated, but no further measurement was taken from this array due to the uncertainty. Figure

6 Doped site-control quantum dot growth and characterisation

6- 21b shows the potential array at 4.8 μm pitch, where the properties of the array are unknown due to the lack of markers.
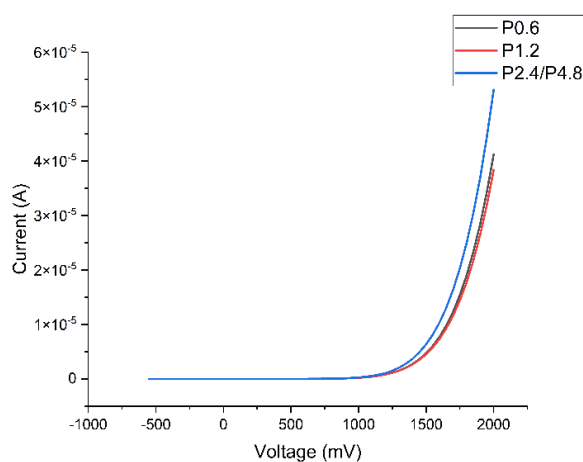
Figure 6- 20 IV characterisation on the barrier-only mesa diode across the different pitches. Three mesa diodes were fabricated of a single pattern, with 0.6 μm and 1.2 μm pitch forming individual diodes, with the third diode being a combination of 2.4 μm and 4.8 μm.
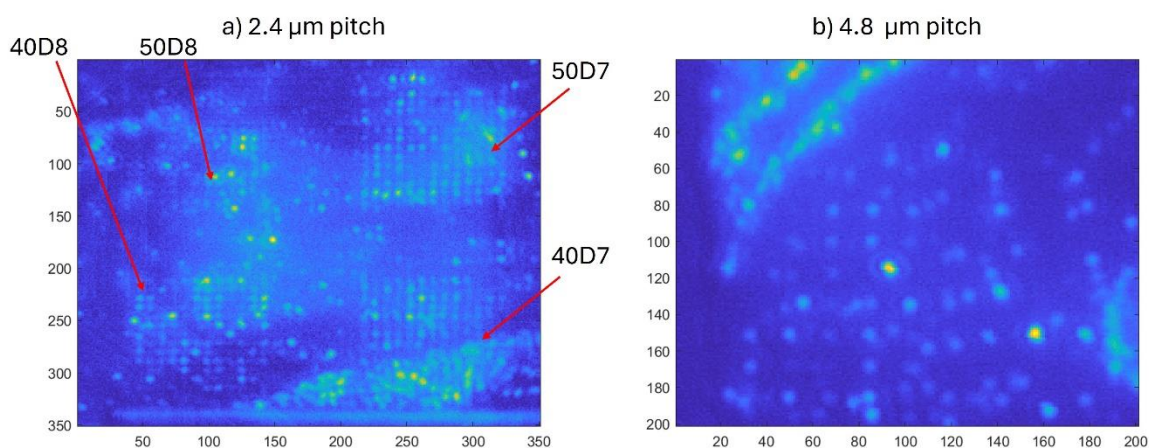
Figure 6- 21 Barrier-only mesa diode comparing the visibility of the different pitch arrays, PL images measured at 4K and 0V bias. a) 2.4 μm pitch showing 4 arrays (40D7, 40D8, 50D7, 50D8) and b) 4.8 μm pitch showing one potential array.

With the presence of ordered QD arrays at the 2.4 μm pitch, the effects of QCSE were studied. By altering the bias voltage applied between -0.5V to 2.0V, the QD emissions can be controlled electrically. The minimum turn-on voltage was -0.5V, but a greater population of QDs turn-on was around 0.0V to 0.5V. Increasing the bias voltage beyond 0.5V leads to marginal improvements to the number of QD emissions, but incremental improvements to PL intensity are observed which are dependent on the bias voltage. With high positive bias voltage this results in charge injection into the QDs, allowing emissions from the QD from higher energy levels. The QD occupation differs depending on the array investigated due to a variety of factors, such as nanohole size. The 40D8 arrays (highlighted in red) show an occupation rate of ~60% at 0.5V bias. Here, we assume that the bright

regions have QD emissions while the dark regions have no QD emissions. At this stage, this is an initial measurement for identifying QD occupancy, where additional measurements performed later will allow for proper characterisation of each position. The PL image captures QD emission anywhere between 900 nm to 1200 nm (detector limits). Therefore, the PL images are only useful in providing an initial assessment of QD occupation.

By adding a variable filter to the setup, it is possible to quickly identify the QD wavelength range for each position within an array. This can be achieved by subtracting the PL intensity from two PL images at different filter positions, which filter out different wavelength ranges. Figure 6- 23a shows the summary of the wavelength range of each position occupied, where each position is defined by (x, y). A series of QDs with similar wavelength emissions can be found in proximity to each other. The identified groups of QD emit in the emission range from 938 nm to 1000 nm, but a large number of QDs emitted above 1000 nm also exist (red). The detection efficiency decreases significantly above 1000 nm, and the possible wavelengths in this range extend to 1200 nm due to the detection limit, making them unsuitable for additional characterisation. The PL intensity from each wavelength range can also be calculated by measuring the transmission at various positions of the variable filter. Figure 6- 23b highlights the QD intensity as a function of wavelength. The brightest wavelength dots emit at 950 nm, and when compared to the wavelength map, only a single pair of QD emitting at this wavelength is found (shown later). For other wavelength ranges with similar brightness, QD emitting between 960 nm to 970 nm has a range of QDs that are neighbouring each other. Five positions within this array fit these criteria: positions *(5, 12), (6, 8), (7, 8), (7, 10) and (7, 12),* where a voltage sweep can be applied to determine if the quantum confinement stark effect can be used to tune QDs to emit at the same wavelength.
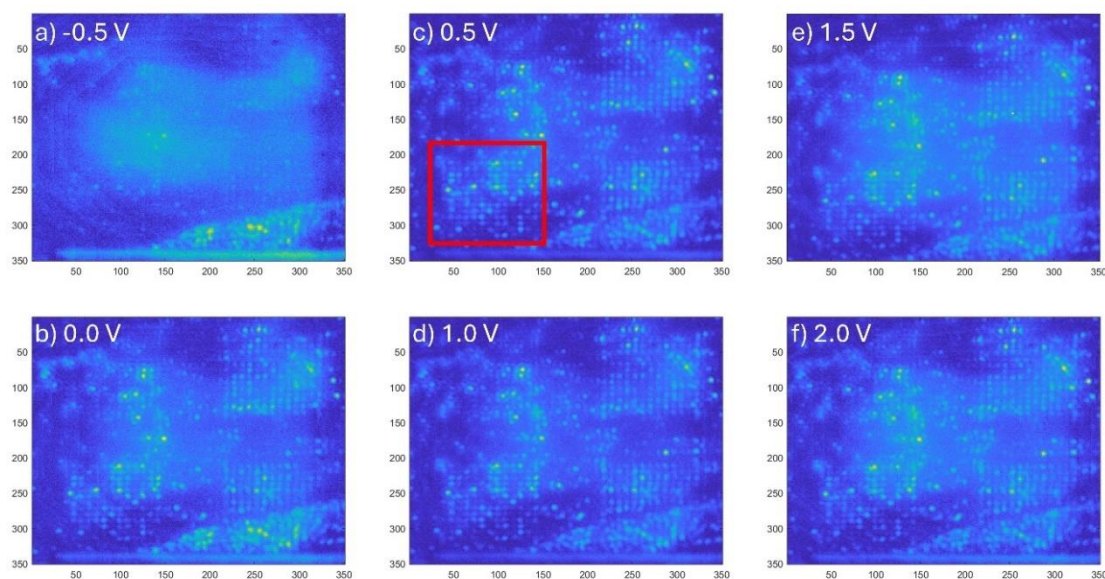
Figure 6- 22 PL images of 2.4 μm pitch with varying voltage bias, a) -0.5 V, b) 0.0 V, c) 0.5 V, d) 1.0 V, e) 1.5 V and f) 2.0V. QD emissions are turned electrically, and the ideal array for further investigation for emission wavelength and tuning is highlighted in a red box.
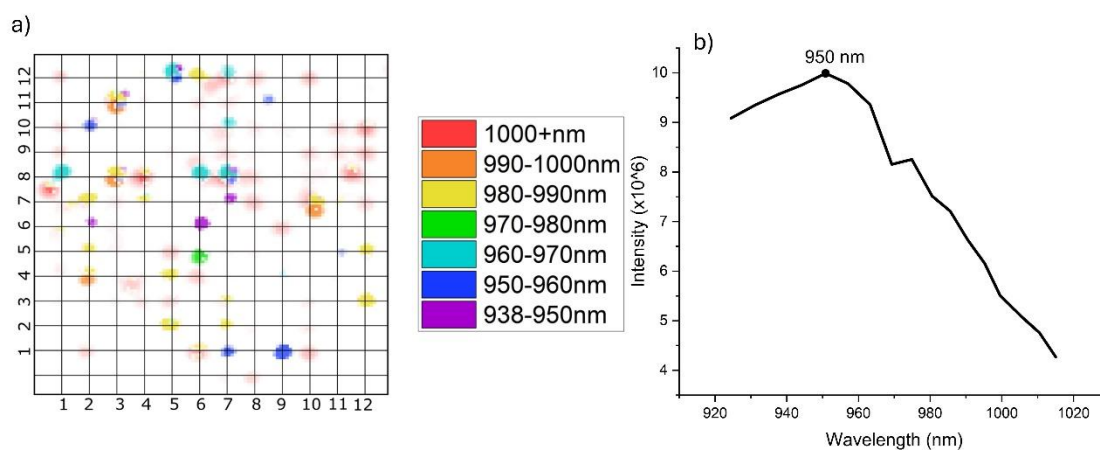
Figure 6- 23 Summary of the mesa diode characterisation with a) wavelength distribution of SCQD within the array and b) the emission intensity as a function of wavelength. Where five QD positions with good optical properties can be compared: position (5,12), (6, 8), (7, 8), (7, 10) and (7, 12).

Quantum Confinement Stark Effect for Single Dots

For each of the positions, *(5,12), (6, 8), (7, 8), (7, 10) and (7, 12)*, the μPL spectrum was taken with a voltage biased at 0.5V and shown in Figure 6- 24a. Regardless of the five locations measured, multiple QD emissions (minimum of two peaks) with large linewidth are found. The presence of multiple peaks in each position has been identified as the presence of multiple states such as excitons (X^0, X^- and X^+) and biexciton (XX) emission. The lowest linewidth of 169.1 μeV is obtained at position (7, 8), evidence that further studies are required to improve the uniformity of QD shape to reduce the linewidths [159]. The lowest linewidth with a dry-etching process was achieved by Schneider et al., with linewidths of ~60 μeV [86] and for other fabrication methods (wet etch), linewidths of ~20 μeV [186].

The current attempts of using indium flushing on a doped waveguide structure were proven to be unsuccessful, as no QD emission was observed. The previous study of growth technique is shown in this thesis (see Growth optimisation: Indium flushing), and the literature has demonstrated that varying thin GaAs capping thickness during the indium flushing step is capable of improving QD linewidths and FSS [57] [59]. Therefore, in a future study, re-investigating the indium flushing technique on a doped waveguide structure would be beneficial.

Figure 6- 24b shows the contour plot of the emission wavelength as a function of bias voltage for each position. The tuning of each position is independent of each other with an applied voltage bias. With a voltage bias of 0.5V, the limit of tuning for each position was reached, and the subsequent increase to bias voltage showed minimal changes to the wavelength. The brightest emissions are also obtained around 0.5V bias for all positions measured. For 4 out of 5 positions, QD emissions are maintained up to a max voltage bias of 1.2V before no emissions are detected, while position *(6, 8)* maintains QD emissions up to 2V bias. The QCSE enables tuning of any of the QDs up to ± 2 nm by controlling the bias voltage. In comparison, it is not possible to tune all five positions into the same wavelength; two different wavelength resonances can be achieved with separate groups of QDs. Position (*5, 12*), *(6, 8) and (7, 8)* can be tuned to emit at ~976 nm. In contrast, positions *(7, 10) and (7, 12)* can be tuned to emit at 967 nm, provided that each position can be biased independently. Another matchup between these 5 positions is also found but not discussed, as the bias conditions required lead to poor QD emissions in these positions. In summary, convincing evidence suggesting pairs or even groups of QDs neighbouring each other can be tuned into the same wavelength emissions has been presented. To advance the development of SCQD based on current results, the ability to individually tune and excite QDs within an array is crucial, as the current diode structure excites and tunes the entire sample rather than individual arrays or QDs. Large linewidths across the array are also areas which could be improved by optimising growth conditions for highly uniform QDs [59].
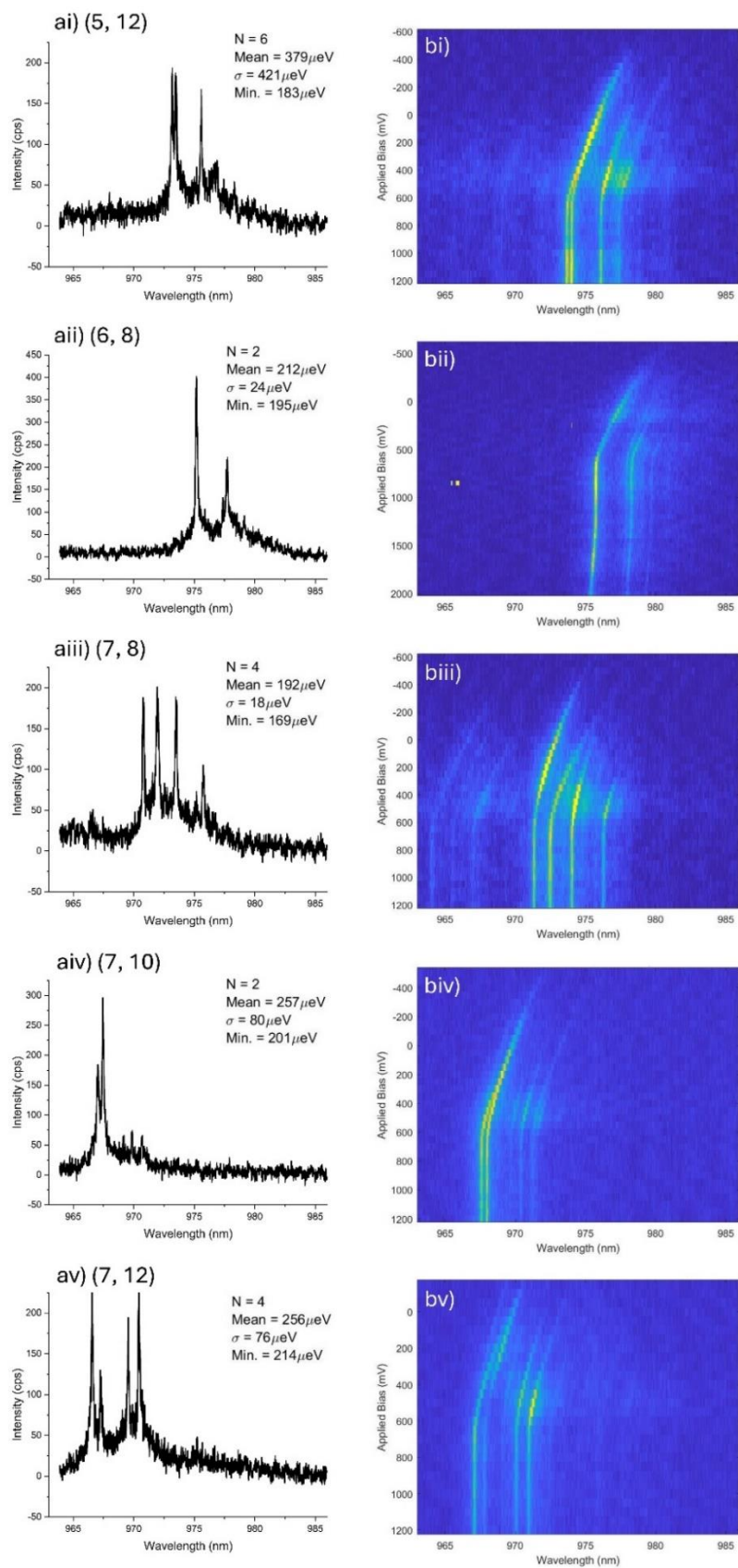
Figure 6- 24 Summary of the five different positions: i) position (5, 12), ii) position (6, 8), iii) position (7, 8), iv) position (7, 10), v) position (7,12). All position has comparable emission wavelengths, and the a) μPL spectrum with 0.5 V bias and b) Contour plot of the emission wavelength as a function of bias voltage, where pairs of QDs can be tuned to the same wavelength emissions.

QD mapping

Figure 6- 25 presents a QD map which displays the narrowest linewidth and the equivalent emission wavelength. The wavelength presented in this QD map differs from the wavelength distribution presented in Figure 6- 23a, showing the brightest QD emission. An example includes the previously measured positions (*5, 12), (6, 8) and (7, 8)* with the lowest linewidth observed with an emission wavelength of (974 ± 1) nm compared to the wavelength range of 960 to 970nm. The previously investigated positions are highlighted in orange, showing comparable wavelengths while being adjacent to each other. The QD occupancy has also decreased within the QD array, with 37 out of 144 positions (~25%) showing QD emissions. The significant decrease in density compared to the initial assessment of 60% QD occupancy. This can be explained as QD emissions above 1100 nm not included, as any emission above this range is not suitable for our intended application and linewidth larger than 500 μeV is observed. When compared to the undoped waveguide structures (discussed in QD mapping), with a QD occupancy rate of ~50% at 40D3 and 50D3 arrays, which only accounted for QD emissions with linewidth less than 150 μeV. Significant improvements to the growth process are needed to both improve the occupancy rate and reduce QD linewidth. Known solutions to increase high occupancy rates, including controlling the nanohole size [74] and depth [59], have previously been shown to be effective and to reduce linewidth, which is important to improving QD uniformity within ordered arrays [79] [155].

Other positions with comparable wavelength and linewidth were also identified, including positions *(6, 6) and (7, 7)*, as neighbouring positions; however, they were determined to be unsuitable due to the large linewidth observed. The lowest linewidth recorded in the QD map is at position *(9, 1)* with a value of 99.3 μeV, with a comparable emission *(7, 1)* and the respective spectrum is shown in Figure 6- 26. Unfortunately, despite being the lowest linewidth positions, these emissions are still a large distance from the target linewidth (< 50 μeV) required to perform other experiments, such as Hong-Ou-Mandel, to investigate indistinguishable photon emission from two QDs [185].
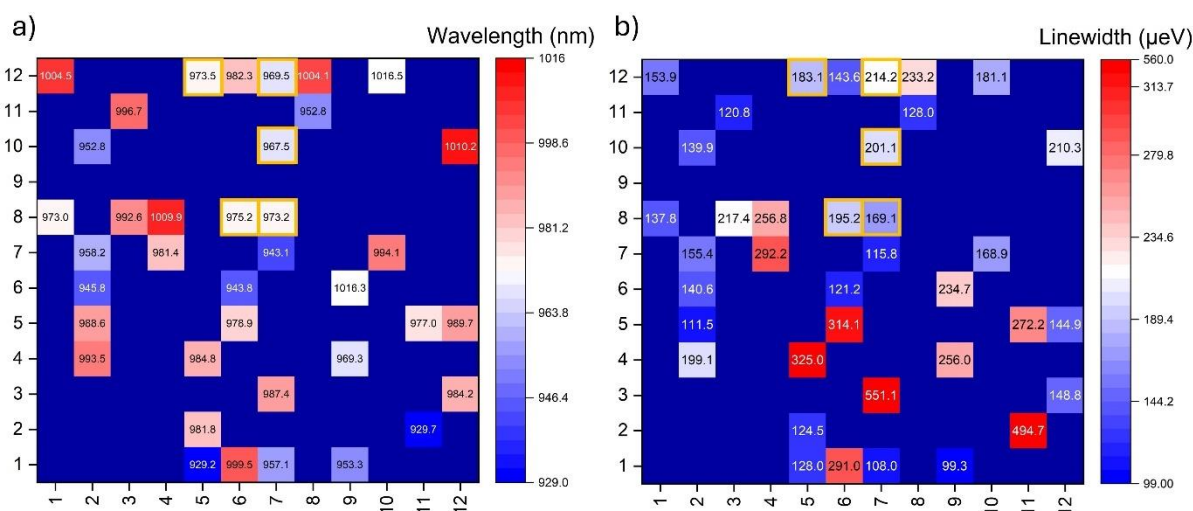
Figure 6- 25 QD mapping of a) wavelength and b) linewidth with a 0.5V bias and excited with a 3.3V LED. The map displays the best linewidth conditions, and the previously measured positions are highlighted in orange.
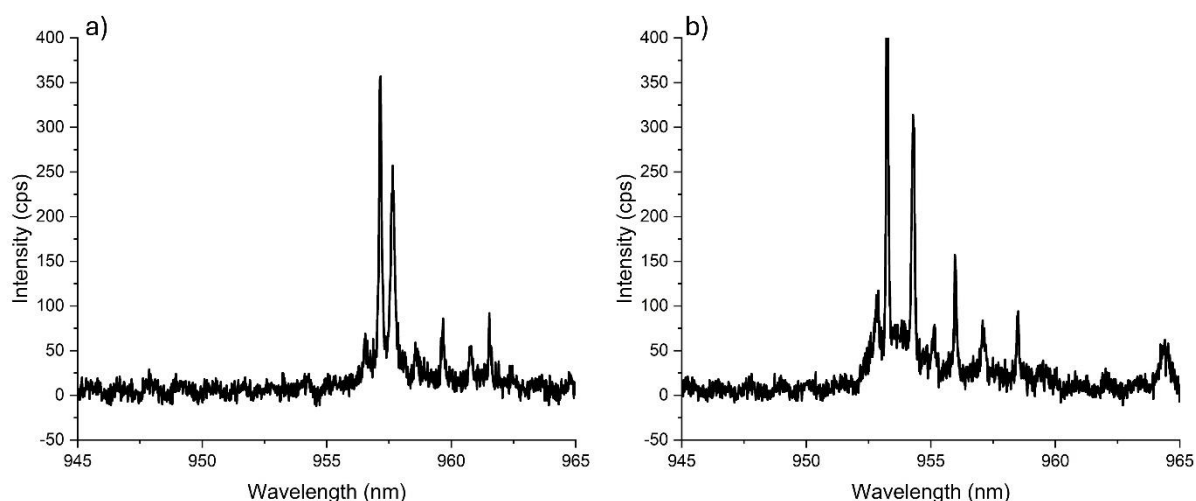
Figure 6- 26 μPL spectrum at 4K for a) position (7, 1) and b) position (9, 1) measured at 0.5V bias and excitation power of 3.3V LED.

Summary

The growth and characterisation of doped waveguide structures as mesa diodes have been presented in this chapter. Initial growth attempts indicate that the lack of planarisation results in QD deposition close to the doped layers, which prevents QD emissions. Adjusting the V/III ratio to 10:1 has improved the infilling of the nanoholes and achieved planarisation, which enables QD emissions. Still, other in-situ and ex-situ parameters, including etched depth and growth temperature, provided negligible improvement with a V/III ratio of 20:1. Therefore, revisiting these parameters with the adjusted V/III ratio could allow better control over the infilling of the nanoholes.

In the successful growth of doped waveguide structures, three different structures were grown. Only the structure with an AlAs/GaAs barrier produced QD emissions from positioned QD, which are easily

121

identifiable. The remaining structures produced very high-density QD emissions with poor distinguishability at each position. One growth attempt used the indium flushing technique but did not show good optical emission. However, previous studies have demonstrated indium flushing on undoped site-control structures to be an effective method of controlling QD properties (see Chapter 4). Therefore, reinvestigation towards ideal indium flushing conditions could be a viable solution in improving QD linewidths [57].

The device fabrication and characterisation of the Sample 2 structure have shown promising results where groups of QDs have emission wavelengths close enough to be tuned into the same wavelength with the QCSE effect. For future development of SCQD samples, the development of a 2-step etching process is required. This is to increase the visibility of the planarised pattern by etching the nanohole and alignment markers separately to achieve two different depth profiles but maintain the planarisation of the nanohole. This will assist future device fabrication and enable the capability to tune single QDs within an array. The results obtained while showing positive success in site-controlled dots with demonstration of QCSE tuning also highlight the need for further investigation of growth optimisation since the current optimised growth conditions have reduced QD occupancy and produced QD emission with linewidths exceeding 100 µeV. Parameters such as growth temperature [22] or growth rates [45] have previously demonstrated the potential to enhance QD shape uniformity [50], making them important factors to consider in future growth attempts.

7 Postgrowth Rapid Thermal Annealing

In the previous chapters, we demonstrated how different growth parameters and the use of a patterned surface can be suitable methods to control the positioning of QDs and optimise the optical properties. In this chapter, we switch focus towards InAs/InP droplet epitaxy QDs grown by metal-organic vapour phase epitaxy (MOVPE) and the effects of rapid thermal annealing (RTA) as an alternative post-growth method for QD tuning. The growth of InAs/InP QDs is well-established within the group by Dr Elisa M. Sala [195] [196]. However, continued development towards suitable QDs for quantum applications such as quantum key distribution (QKD) is still ongoing. This includes better control and understanding of the peak ensemble observed beyond 1600 nm and goals of shifting the peak emissions towards the C-band and O-band while removing the background noise generated for as-grown samples previously seen [195]. This is an area of interest that remains unexplored, and it is an excellent candidate for photonics applications and quantum light-emitting diodes at the telecom C-band [26]. RTA is a known technique that alters the shape and composition of QDs by controlling annealing temperature or duration, allowing the shifting of the dot emission wavelength, and improving PL intensity and linewidth [120] [121]. When annealing, determining the type of capping method influences the migration of atoms [120]. In this study, the effects of proximity capping [122] [126] and dielectric capping [128] were examined. The use of a capping layer serves as a method to protect the surface from excess degradation when annealed at high temperatures and, depending on the method, impacts the outdiffusion and intermixing of atoms between adjacent layers.

MOVPE is a chemical vapour deposition which uses metal organics to produce single or polycrystalline thin films. In contrast to MBE, this method does not require ultra-high vacuum conditions and, therefore, is a fast and low-cost alternative to produce high-quality epitaxial layers. As the name suggests, it uses metal-organics instead of solid sources, which are compounds containing direct metal-carbon bonds such as metal carbonyls or metal alkyls. Typical precursors for III/V semiconductors for group III metals, include trimethylgallium (TMGa), trimethylaluminium (TMAl), or trimethylindium (TMIn) and for group V precursors hydride gases are typically used, which include phosphine (PH_3) and arsine (AsH_3).

Growth conditions

All the samples used in this chapter were grown by Dr Elisa M. Sala in a closed-coupled showerhead MOVPE *Aixtron* reactor. The structure was grown on an InP (100) substrate using H_2 as carrier gas. Indium droplets are deposited on a 300 nm InP buffer grown at 620°C. The droplets are deposited at a constant TMIn flow of 2.6 μmol min^{-1} for 35 seconds at 320°C and then crystallised into InAs QDs under an AsH_3 flow while ramping the temperature to 520°C. Previous studies optimise the QD's

growth to achieve high-quality InAs QDs for emissions at 1550 nm at low temperatures [35] [196]. After the droplets crystallisation into InAs QDs, an InP capping layer of 20 nm was deposited at the same crystallisation temperature of 520°C, and a further 80 nm InP was grown at 620°C to bury the QDs entirely. The sample was then cooled down and removed from the growth chamber. For the dielectric cap, a 100 nm SiO_2 capping layer (40 nm/min) was deposited by Plasma-enhanced chemical vapour deposition (PECVD) to protect the surface during RTA. For samples with a proximity cap during annealing, a separate InP sacrificial substrate was placed on top of the sample. Figure 7- 1 shows a simple diagram of the InAs/InP QD grown with the different capping methods used in the RTA study. The samples were cleaved into 5 x 5 mm^2 pieces before being annealed at temperatures ranging from 650°C and 850°C for 30 seconds. For each annealing temperature, a new sample piece was used to directly compare the temperature effects while the annealing duration was fixed. After annealing, each sample was measured using the PL mapper to measure the room temperature PL. Low-temperature µPL (*Setup 1*, for details, see Chapter 3 was also measured for SiO_2 capped samples. The response of the InGaAs detector on the LT-µPL system is limited to 1600 nm, so single QD emission at longer wavelengths may not be detected.
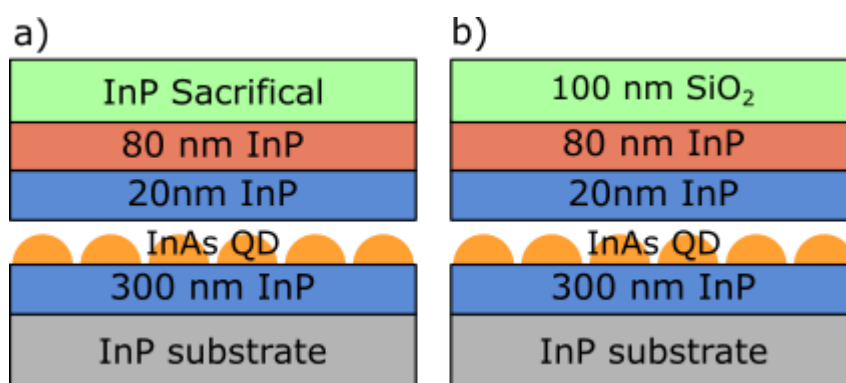
Figure 7- 1 A simple diagram of the InAs/InP QD structure grown with the different capping methods used in the RTA study: a) proximity capping with InP sacrificial substrate and b) dielectric capping with 100 nm SiO2 capping layer.

Dielectric capping vs. proximity capping

Figure 7- 2 summarises the difference between the proximity cap and SiO_2 cap with different annealing temperatures. Emission shifting only occurs at high temperatures (> 800°C), regardless of the capping method used. For proximity cap samples, a blueshift of 357 nm occurs at 850°C, where emission shifting at this temperature is caused by material degradation that occurs across the surface. Literature has linked material degradation to the generation of dislocations are created due to intermixing and outdiffusion [126]. Decreasing the annealing temperatures, the ensemble emissions and the emission intensity experience subtle changes. The results presented contradict the literature, as temperatures as low as 700°C have demonstrated the ability to control the ensemble of emissions [113] [123]. One possible reason for this is that the InP sacrificial cap limits the amount of outdiffusion

of indium or phosphorus atoms, restricting the ability to control emission properties, but eventually, material degradation occurs due to the excessively high annealing temperatures used (850°C) [120] [133]. The use of a SiO_2 cap with annealing temperatures up to 750°C did not result in any emission shifting. Instead, the integral intensity shows an initial improvement when compared to the as-grown sample. When annealing at 800°C, it enables a blueshift of 334 nm and increases the integral intensity. For both capping methods, surface degradation was observed when annealing from 800°C; however, only with a SiO2 cap does this cause any emissions shifting due to the outdiffusion of atoms to the SiO_2 layer (discussed later). For the SiO_2 cap, annealing at 850°C, the degradation across the structure is sufficiently bad that no optical emissions are observed [120] [126].
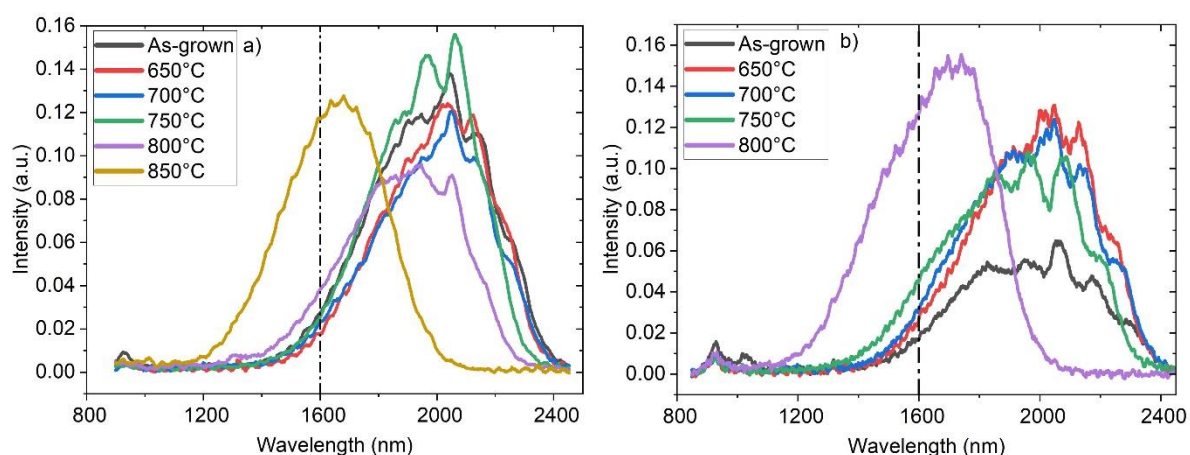
Figure 7- 2 Room temperature PL emissions with different annealing temperatures from 650°C to 850°C. Different capping methods were compared: a) proximity capping with sacrificial InP substrates and b) 100 nm SiO2 dielectric capping—dot-Dash line indicating the μPL detector's cut-off.

Figure 7- 3 summarises the PL properties between proximity capping and SiO_2 capping. The use of SiO_2 capping enables blueshifting 50°C lower than proximity capping. Otherwise, the blueshifting of emissions has similar trends between the two capping methods where, at low temperatures, annealing does not promote emissions shifting. Still, once a temperature threshold is reached (800°C/850°C depending on the capping method used), a large blueshift is achieved. The FWHM of the ensemble PL emissions, regardless of the cap used, show no discernible trends, but general improvements are found after annealing. At annealing temperatures where blueshifting occurs, for proximity capping at 850°C, the FWHM improves by 13%, while for SiO_2 capping at 800°C, the FWHM improves by 24%. Other temperature also shows some evidence that FWHM is broadening, such as at 750°C for SiO2 capping where FWHM broadens by 1%. The degradation observed appears to be random; therefore, it is difficult to ascertain if repeating annealing would result in the same result.

The integral intensity ratio (I/I_0) is defined as the annealed sample's integral intensity (I) divided by the as-grown integral intensity (I_0). The results are presented in Figure 7- 3b, showing negligible

improvement with the proximity capping with the highest intensity achieved at 750°C with an $I/I_0 =$ 1.2. The other annealing temperature with proximity capping the intensity is comparable to the as-grown PL intensity, which again can be linked to the lack of outdiffusion [120] [133]. With less outdiffusion of the atoms from the structures, fewer dislocations are formed, which limits the amount of intermixing. For the SiO_2 cap, the intensity improves by a minimum of ~80% when annealing from 650°C to 750°C. There appears to be an initial increase in PL intensity prior to emission shifting, which is a demonstration of a reduction in defects and improving InAs QD quality [73]. Increasing to 800°C, a twofold improvement in emission intensity is achieved compared to as-grown. For the SiO_2 cap, there is a significant change in thermal expansion coefficient mismatch between SiO_2 (~0.52 × 10^{-6} °C^{-1}) and InP (~4.6 × 10^{-6} °C^{-1}), which causes compressive stress at the interface region during annealing, allowing indium or group V intermixing [125]. The dramatic improvement achieved within a 50°C increment suggests that the effects of the intermixing of indium and group V atoms occur between 750°C to 800°C for the SiO_2 cap. Therefore, samples annealed between 750°C to 800°C with 10°C increments were investigated further.
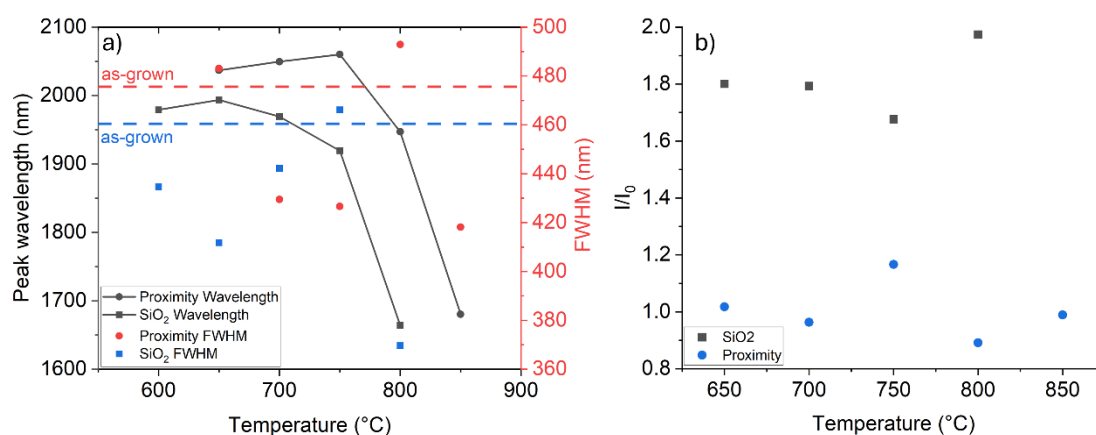
Figure 7- 3 Gaussian fitted analysis summary comparing the different capping methods used, proximity (circle) vs. SiO$_2$ (square), across different parameters, a) wavelength (black) vs. FWHM (Red/Blue) where the dashed line is as-grown linewidths and b) integral intensity ratio (I/I$_0$), as a function of temperature.

Surface defects

From the initial annealing attempts shown Figure 7- 2, the introduction of defects is visible from 800°C, which matches with literature where the formation of surface defects from 800°C and above is due to degradation of the material from microcracks formed on the surface [120]. However, in the subsequent annealing attempts with low temperatures (<700°C), surface defects were found on the surface; hence, an investigation of the question of reproducibility was performed and the cause for the introduction of these surface defects at low temperatures.

To examine when surface defects form, the annealing temperature is decreased until the defect formation is no longer visible. The presence of defect formation persisted down to 550°C, and at 500°C, no defect was found after annealing. Figure 7- 4 shows a microscope image (10x) of the surface of the SiO_2 capped samples after annealing at 550°C, 600°C and 700°C. When annealed at 550°C, no evidence that the surface defects were formed from any contamination or existing defect was found. Figure 7- 4c,d shows different surface defect patterns when annealing at 700°C for 30s. One attempt is similar to lower temperature annealing (600°C) with narrow microcracks (Figure 7- 4c), while the other annealing attempt at 700°C (Figure 7- 4d) matches higher temperature annealing (750°C, shown later) with a thick microcrack across the surface. The initial suggestion of the cause of these microcracks was that the annealer required re-calibration of the thermocouples. However, this was later disproved when the machine was serviced, and no improvements were found, which then suggests that this could be related to the sample preparation and the capping method.

25 µm
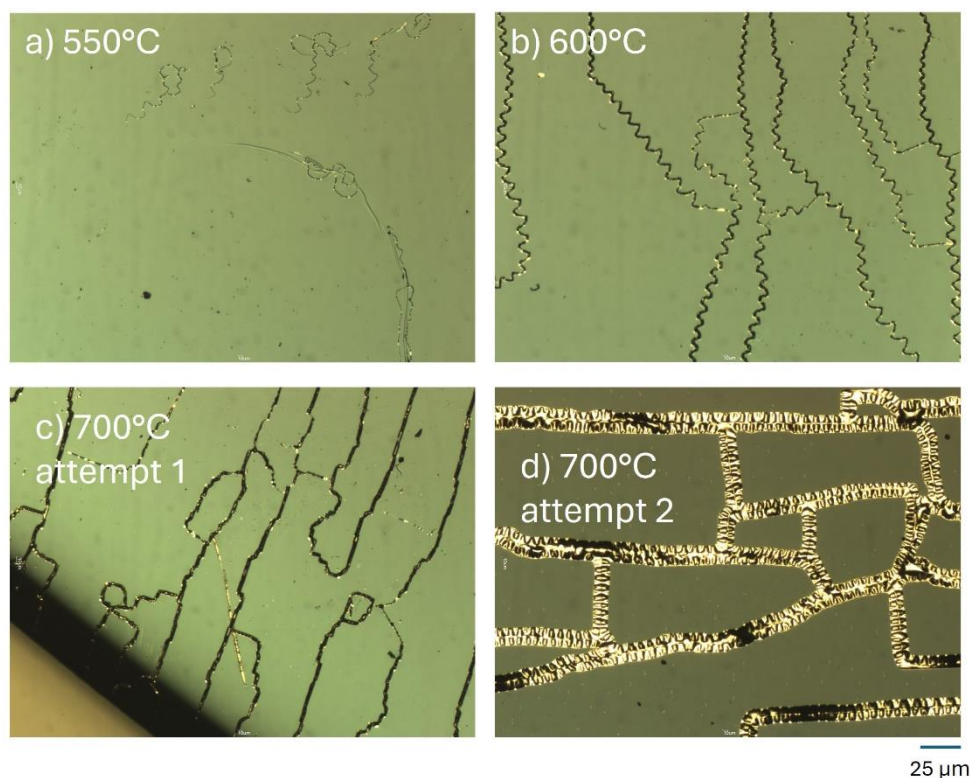
Figure 7- 4 A series of microscope images (10x lens) with different annealing temperatures, a) 550°C, b) 600°C, c-d) 700°C. The formation of surface defects is present with temperatures as low as 550°C, and at high temperatures, the formation of defects is inconsistent.

To understand the possible causes of the defects, energy-dispersive X-ray (EDX) spectroscopy was used to analyse the types of elements present on the sample surface [197]. Figure 7- 5 presents the EDX analysis of the range of elements present on a SiO_2 surface annealed at 700°C. From the list of atoms presence, silicon and oxygen atoms are expected due to the SiO_2 layer, but additional peaks for indium and phosphorus atoms are also present on the surface. This supports the findings presented

in the literature that, outdiffusion of the capping layer onto the SiO_2 takes place when annealing [120] [126]. The outdiffusion of the InP capping layer is an important mechanism for RTA as this creates vacancies where intermixing between the interlayers and encourages improvement to PL emissions. For InAs/GaAs structures, literature has shown only gallium (group III) to be available for outdiffusion [101], as opposed to InAs/InP structures where outdiffusion occurs for group V atoms. Chia et al, have described the effect of outdiffusion of group V over due to the large difference in thermal expansion coefficient between SiO_2 and InP. This could explain the cause of surface defects as the intensity of indium and phosphorous atoms are similar to the silicone and oxygen atoms measured on the surface, suggesting a significant number of indium and phosphorus atoms was diffused onto the SiO_2 layer. As such, we believe that the InP outdiffusion introduces large dislocations before the outdiffusion towards the SiO_2 surface. The lack of arsenic atom presence on the EDX scans suggests that intermixing between QD and the adjacent layers only affects the atoms closest to the QDs and not the entire InP layers.
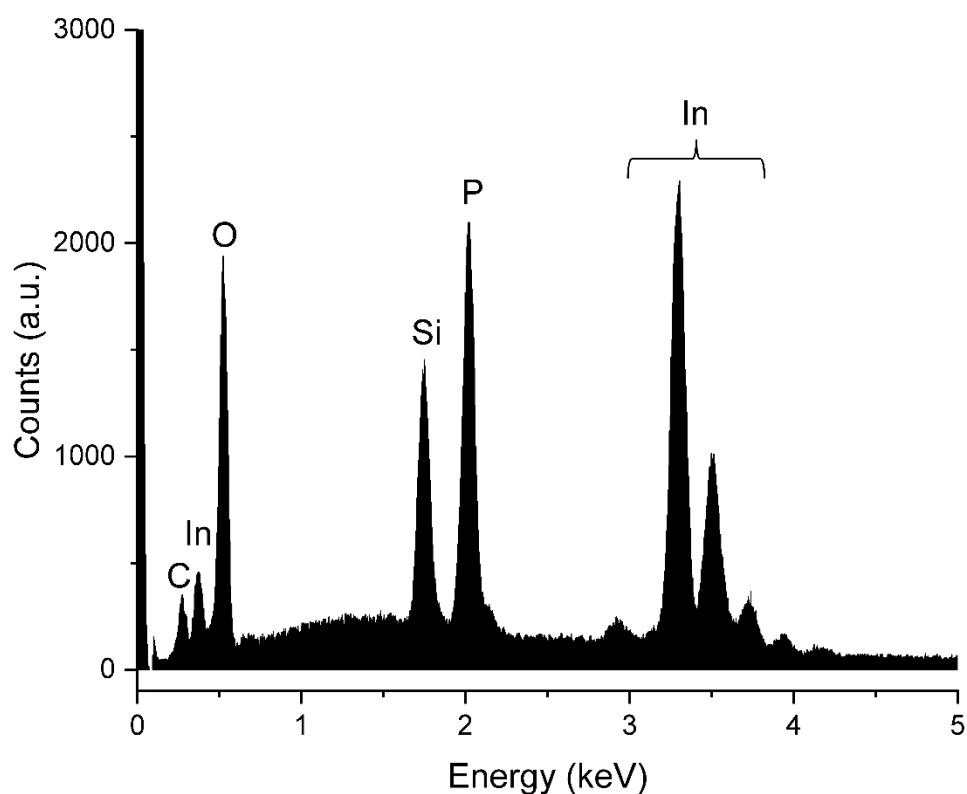
Figure 7- 5 EDX analysis of the types of elements present on a sample surface after annealing at 700°C for 30 seconds. The key elements which would be present on the surface are highlighted.

Upon closer examination of the sample annealed at 750°C with surface defects, evidence that the defects are generated at the InP capping layer is found. Figure 7- 6a shows the microscope image of a SiO_2 capped sample annealed at 750°C with an inset showing a magnification of the possible origin of surface defects origin where the surface appears to have been damaged, and interlayer material is visible. While annealing at low temperatures, small quantities of these defects propagate to the surface. To confirm if this statement is true, the SiO_2 layer was removed through HF etching at 40 nm/min for 2.5 minutes, and the defect remained on the InP surface, as shown in Figure 7- 6b. Figure 7- 6c-d shows an SEM image of a defect along with the type of material present on the surface. A large presence of indium and phosphorus on the surface is detected, with phosphorus only visible on the defect-free surface and indium visible across the entire surface. We believe that the defect is made up of metallic indium, and the lack of phosphorus has been desorbed into the surroundings during annealing. In the literature, there are mixed results, Barik et al, have presented annealing results up to 850°C for both SiO_2 and TiO_2 without any presence of microcracks [133]. While Chia et al, have reported the formation of microcracks but only when annealed at 900°C for SiO_2 and SiN_x [120]. Currently, we believe the formation of microcracks previously observed in our initial samples (see Figure 7- 1) is attributed to high-temperature annealing caused by excessive outdiffusion of atoms, but the 2nd attempt at annealing resulted in defects formed at lower annealing temperatures (>550°C), which we suspect is from a different origin compared to what has been a state in literature. The initial assumption suggests that this is the introduction of contamination during the SiO_2 deposition process. However, attempting to anneal SiO_2 capped samples from a previous batch with produced defect-free samples was unsuccessful and also produced surface defects in later attempts. As the surface defects cannot be removed with better surface preparation, the next possible explanation could be a variation in the annealing temperature where the initial samples were annealed at a significantly lower temperature. Therefore, a set of samples was annealed at 700°C and 800°C where the room temperature PL emissions were compared.
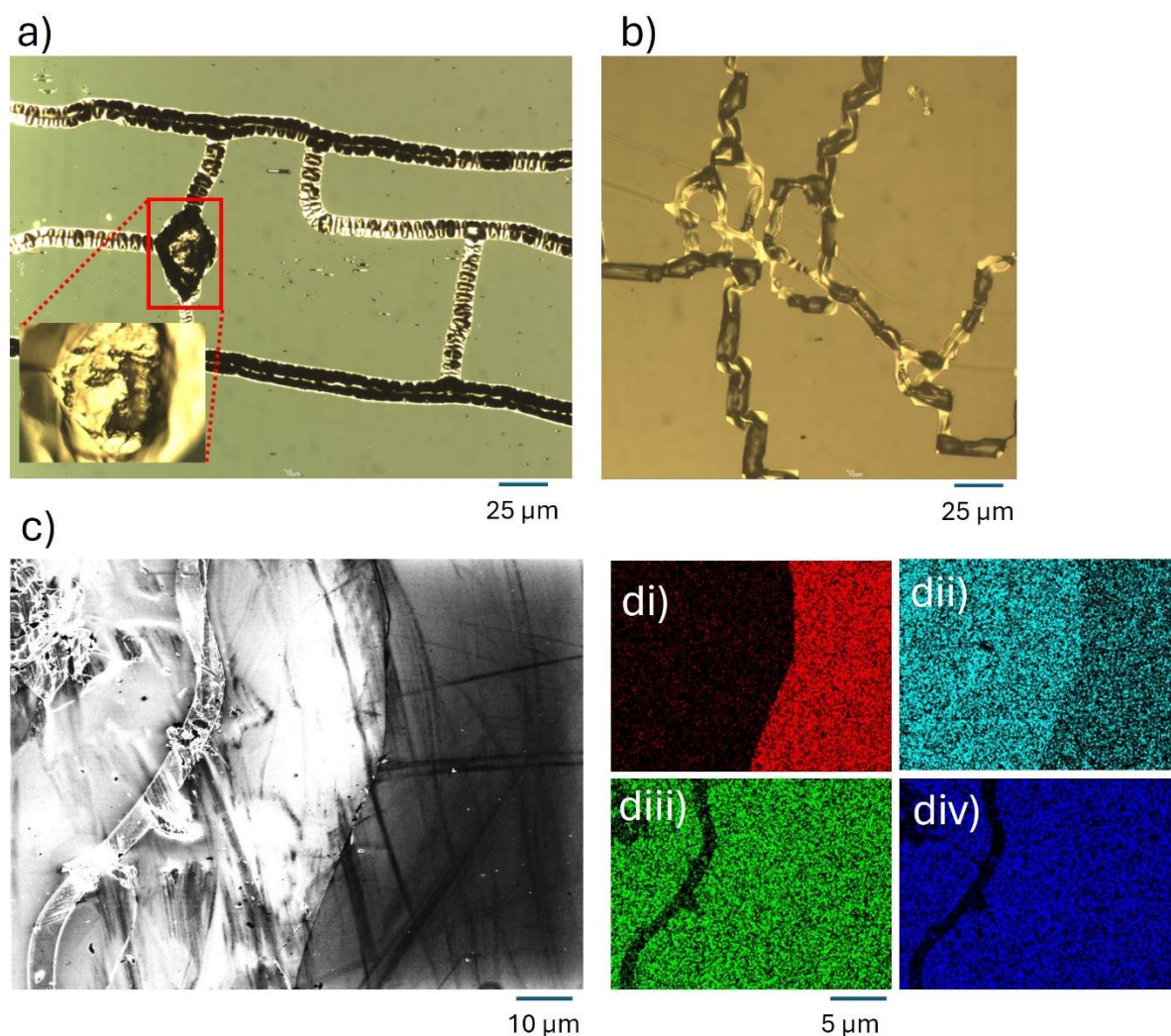
Figure 7- 6 Identifying the origins of the defect generation through microscope images of the surface annealed at 750°C shows the a) SiO2 surface and b) InP surface after HF etching of the SiO₂ layer. The surfaces presented are of arbitrary locations from the same sample before and after HF etching, c) SEM image of the surface defect with the presence of the defect originating from the InP capping layer, d) EDX image of different atom presence, i) phosphorus, ii) indium, iii) silicone iv) oxygen.

Figure 7- 7 compares the room temperature PL ensemble between the *defect-free* samples and the *surface-defect* sample at different annealing temperatures. To clarify, when annealed at 700°C, defect-free samples did not form any defects and maintained a flat surface. In contrast, the *surface-defect* samples resulted in defect formation, as seen in Figure 7- 4d. When annealed at 800°C, both samples result in defects forming on the surface, which are attributed to surface degradation. At 700°C, the increase in PL intensity from as-grown is maintained, and the lack of emission shifting of the ensemble between both samples indicates no differences in optical properties. For 800°C, minor differences are found, the first being the variation in integrated intensity. A decrease in intensity is observed with the *surface-defect* RTA attempts caused by light scattering on the defects. This is evidenced by the presence of a second-order laser peak at ~1300 nm. In addition, the peak wavelength has a difference of ~60 nm, which could be attributed to the sight variation in annealing conditions, such as the

placement of the sample during annealing or the difference in QD density between the different sample pieces used. Overall, the ensemble emissions are unaffected by the appearance of the surface defects; however, currently, no definitive explanation for the appearance of these defects in subsequent annealing experiments has been found. However, since the ensemble PL emission is unaffected, a continuation of the RTA studies with smaller annealing temperature increments (10°C) is performed to observe the effects of annealing between 750°C and 800°C with a SiO_2 capping layer.
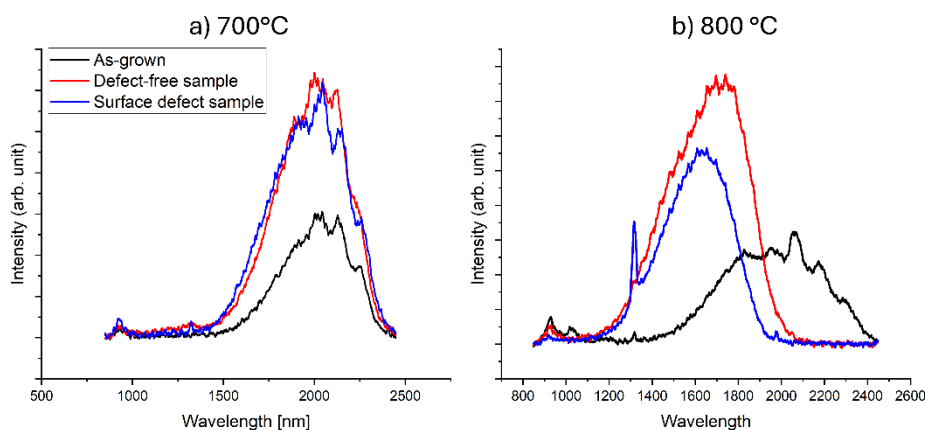
Figure 7- 7 Room temperature PL comparison between samples with SiO_2 cap when annealed at a) 750°C and b) 800°C between the defect-free sample and the surface-defect sample and as-grown sample.

Characterisation of RTA QDs

Another attempt in RTA was subsequently performed where the samples were coated with 100 nm of SiO_2 and annealed between 750°C and 800°C in 10°C increments for 30 seconds; the methodology used for the annealing process remained unchanged. During this annealing attempt, surface defects were still forming on the surface, but after confirming that the defects did not impact the surface, room temperature PL were measured on these samples. Figure 7- 8 shows the room temperature PL spectrum of the annealed samples between 750°C and 800°C. Compared to previous annealing attempts, shown in Figure 7- 2b, the annealing temperatures of 750°C and 800°C presented comparable improvements to ensemble emissions. This reaffirms that the appearance of surface defects does not impact the ensemble emissions after annealing. Incremental blueshift is achieved as the annealing temperature increases due to the different amounts of intermixing and outdiffusion of indium [120]. The PL intensity improves as expected at 750°C with a two-fold increase, but with subsequent increase in annealing temperature, PL intensity increases up to ~4.5 times at 770°C when compared to as-grown. The increase in integrated PL intensity can be attributed to the reduction of non-radiative recombination centres in the sample through annealing. Annealing beyond 770°C, the material quality begins to degrade [126], which generates dislocations and excessive outdiffusion of

indium atoms, resulting in poor PL emissions [124]. This is a known effect when annealing at extremely high temperatures and is observed during the previous annealing attempt.
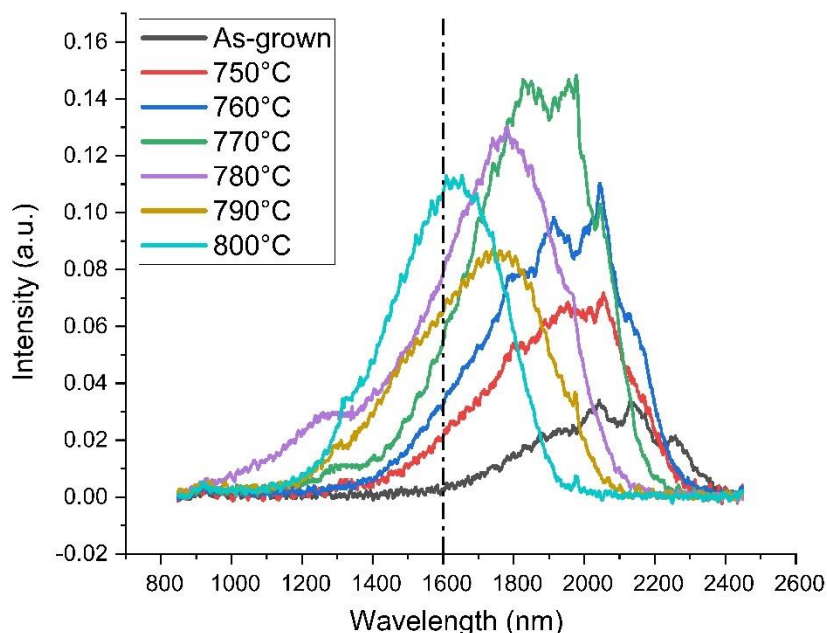
Figure 7- 8 Room temperature PL spectrum with different annealing temperatures between 750°C to 800°C with 10°C increment on InAs/InP QDs with SiO$_2$ cap. The spectrum obtained compares annealed samples to an as-grown sample as a reference.

The PL ensemble emission is Gaussian-fitted, and the results are summarised as a function of annealing temperatures, as shown in Figure 7- 9. The annealing process narrows the ensemble PL FWHM with the lowest FWHM of 329 meV (770°C), compared to 378 meV (as-grown), a 13% improvement. While no general trend is presented for FWHM, the narrowing of FWHM is related to the change in QD shape and compositions where highly uniform QD shapes often yield low FWHM [121] [123]. The emissions wavelength blueshifts linearly as a function of annealing temperature. The largest blueshift is found when annealed at 800°C with a shift of 430 nm towards ~1600nm, which is close to the detection limit for μPL (more details later). The size and composition of the QDs control emission shifting. This is affected by the intermixing of group V and indium atoms with adjacent layers [109], enabled by the outdiffusion of indium and phosphorus atoms, forming vacancies within the structure for intermixing to occur [120]. The annealing effect of InAs/InP differs significantly with InAs/GaAs QDs structures where such interaction is between In/Ga atoms only [113] [131]. By controlling the annealing temperature, it is possible to tune the optical properties of the QDs at room temperature. This allows for the ability to vary the emission wavelength and to understand better the

effects of RTA on single dot emissions, further analysis of the single dot spectrum of SiO2 capped samples was conducted using LT-µPL.
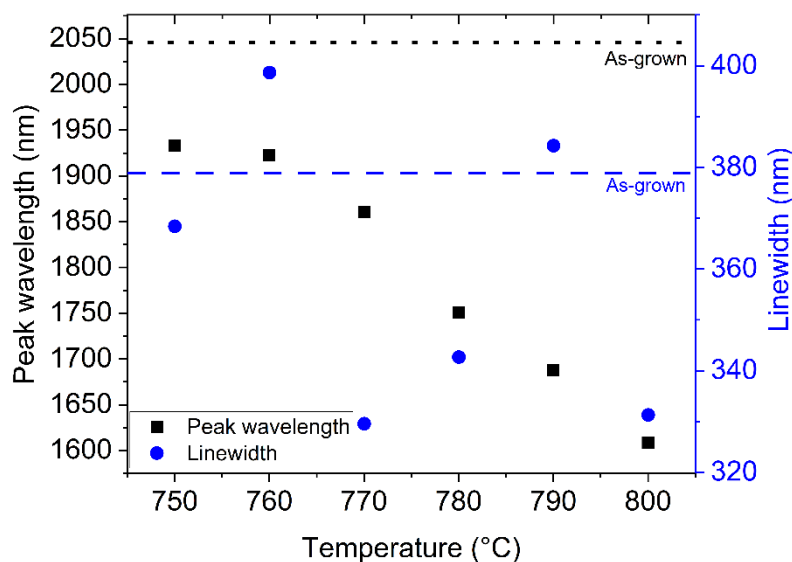
Figure 7- 9 Gaussian fitted analysis of annealing temperature against peak wavelength (squares) and linewidth (circles), with the dashed lines showing as-grown comparisons for the SiO₂ capped sample.

Low-temperature µPL

The annealed sample between 750°C and 800°C was loaded into the µPL, *Setup1* (See Photoluminescence (PL) for more detail) and cooled down to 5 K. The samples were excited through a fibre-coupled red diode laser with 1 µW excitation power, and the emissions were captured by an InGaAs detector and 600 lines/mm grating. Figure 7- 10 shows an example of the µPL spectrum of SiO$_2$ capped samples annealed at (a) 800°C, (b) 770°C, and (c) 750°C and (d) as-grown. In the as-grown sample, high-density QD emissions above 1400 nm are seen alongside background noise. The current assumption is that the background noise is caused by the significant charge noise, which broadens and coalesces emission peaks [23]. When annealing at 750°C, the background noise reduces due to the reduction of defects after annealing. QD emissions blueshift towards the 1300 nm range, along with a decrease in the density of QD emissions with no evidence of emission broadening. Increasing the annealing temperature to 770°C where the most significant improvement was observed, sharp dot-like emissions remain, and the background noise is suppressed. The QD emission does not blueshift and remains within the 1300 nm range. Increasing the annealing temperature up to 800°C results in the reappearance of large background noise, which covers the entire measurement range with atmosphere absorption in the range of 1350 nm to 1450 nm. The current assumption is that when the material degrades and forms microcracks, this induces dislocations which increase background noise. This would also explain the decrease in integrated intensity, as shown in Figure 7- 8 [128]. For

annealing temperatures between 750°C and 770°C, ideal QD emissions are detected with bright and narrow emission lines from single dots. To statistically confirm such a statement and analyse the QD distribution, multiple single spectrums were obtained at each annealing temperature.
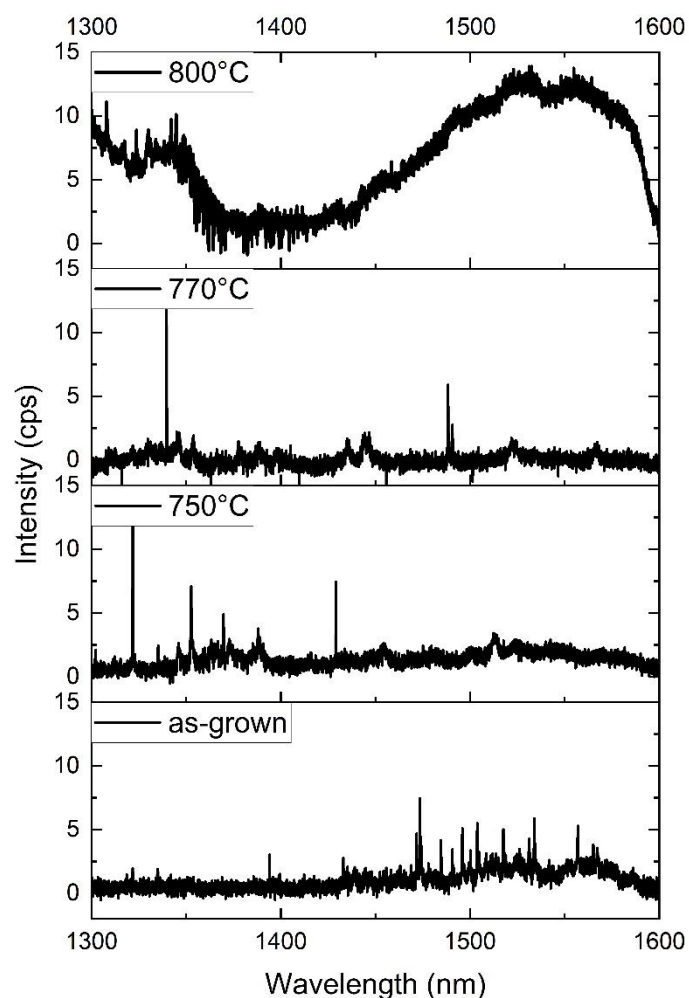
Figure 7- 10 μPL single dot spectrum of SiO₂ capped samples at 5K for a) 800°C, b) 770°C, c) 750°C, and d) as-grown.

Figure 7- 11a-g shows a comparison of sharp dot-like emission wavelengths between annealed and as-grown samples. The previous as-grown spectrum shown in Figure 7- 10 presented good emissions between 1400 nm and 1550 nm. When multiple locations are measured, comparable results are obtained. With increasing annealing temperature, we observe an additional dot-like distribution between 1300 nm and 1400 nm. When compared to the room temperature ensemble PL results shown in Figure 7- 8, the expectation is that a small number of QD would emit below 1400 nm at low temperatures for the as-grown sample as part of the short-wavelength edge of the QD distribution. For annealed samples, the short wavelength QD emissions should be blueshift towards 1200 nm and allow observation of single QD emissions between 1300 nm and 1400 nm from the μPL measurement.

The room temperature PL indicates that the distribution of QDs emission should extend across the whole measurement range for the µPL. Instead, no dot-like emissions are found above 1500 nm for samples annealed at 750°C and 760°C. This may be due to statistical variation in the spectrum, as QD emissions above 1500 nm are observed for samples annealed at a higher temperature. To aid in identifying the origin of the QD emissions after annealing, the two groups of emission lines in the spectrum are outlined: Group *1* is defined as the dot emissions below 1425 nm, corresponding to QDs emissions which have blueshift beyond the emissions from the as-grown sample, while *Group 2*, is emission above 1425 nm correspond to QD emissions that are blueshift due to annealing but are comparable to as-grown sample.

Figure 7- 11h-n shows the linewidth distribution for single QD emissions as a function of different annealing temperatures. For annealing temperatures of 770°C and above, an improvement in the linewidth distribution close to the detector spectral resolution of 20.9 µeV was seen. The lowest linewidth was achieved with a value of 22.0 µeV when annealed at 790°C. When annealing at 800°C, an increase in large linewidth QD emissions is consistent with material degradation and its effect in producing large background noise. For annealing temperatures below 770°C, the linewidth obtained is comparable to as-grown. In comparison, no difference was found between the two groups of dot emissions previously outlined, indicating that the linewidth is independent of emission shifting when annealed. Providing a suitable method of shifting single dot emissions while keeping a consistently low linewidth QD. The limited improvements to linewidth suggest a very uniform QDs shape prior to RTA, which is a known benefit when using droplet epitaxy for QD deposition [196] [198]. This could explain the lack of improvement with linewidth as emissions are blueshift, as while annealing will also improve the uniformity of QDs if the initial shape is very uniform initially, then the shape uniformity will be limited. In contrast, emission shifting is governed by the variation in QD size, which is observed with annealing, where QD shape is reduced due to intermixing with adjacent layers. This provides good evidence that RTA is a beneficial method in tuning DE QD emissions towards the C-band range, with no negative effects on the high uniformity of the QD shape.
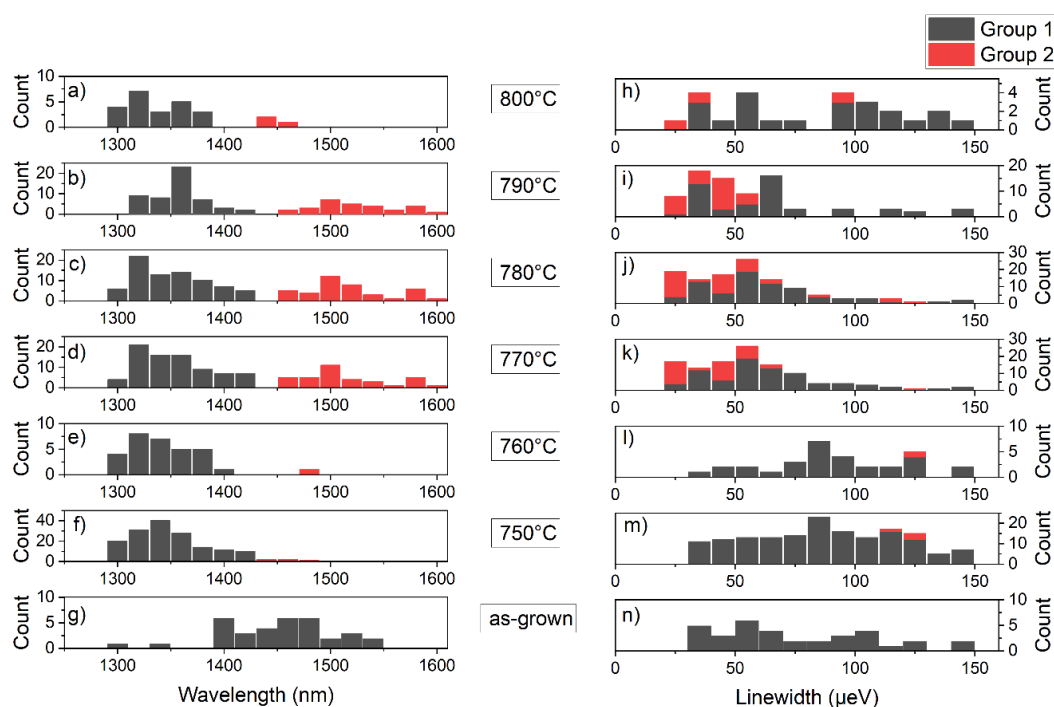
Figure 7- 11 Histogram analysis of multiple single dot emissions of SiO₂ capped sample for linewidth distribution of a) 800°C, b) 790°C, c) 780°C, d) 770°C, e) 760°C, f) 750°C, g) as-grown, and wavelength distribution of h) 800°C, i) 790°C, j) 780°C, k) 770°C, l) 760°C, m) 750°C, n) as-grown. Single dot emissions are further split QD emissions below 1425nm (Black/Group1) and above 1425nm (Red/Group2).

Summary

The ability to control the QD emissions by RTA on telecom InAs QDs on InP grown by droplet epitaxy has been examined. By varying the annealing temperature above 750°C, a controllable blueshift of QD ensemble emissions up to 430nm in RT-PL is achieved. Along with an increase in integrated intensity, a decrease in ensemble PL linewidth by ~15% is also observed. In low-temperature µPL, the ability to tune to single dot emissions is presented with blueshift emission towards the 1300 nm range and improving linewidth by up to 30% when controlling the annealing temperature. The tunability of the QD properties is linked to the intermixing and outdiffusion of indium and group V atoms. EDX analysis confirms the presence of indium and phosphorus in the SiO₂ capping layer after annealing, suggesting the outdiffusion of atoms from the InP cap layer. The presence of surface defects in the form of microcracks is also found in annealing temperatures as low as 550°C. Further research is necessary to investigate the defect form at low temperatures and identify potential methods to mitigate these issues. Interestingly, it has been demonstrated that despite the presence of defects, the overall ensemble PL emissions remain unaffected. Several potential approaches to improving the RTA method are outlined in the literature, in particular, low annealing temperatures for a longer period (e.g. 60 to 180 seconds at 650°C) [123] [128], have shown promising results.

8 Conclusion

The initial development of site-control InAs QDs on simple GaAs-only structures within the research group was previously reported with a demonstration of good QD occupancy and initial optical characterisation [109]. The focus of this project was to improve the current methods by using site-controlled InAs QD on waveguide structures for nanophotonics devices. This involves retaining high QD occupancy and optical properties previously achieved while implementing it into a waveguide structure to allow for device fabrication, which was successfully achieved.

Investigation on optimising QD growth with the use of various growth techniques (growth interrupts and indium flushing) for site-control QDs within an undoped waveguide structure was reported in Chapter 4. The use of growth interrupts after QDs growth was demonstrated to improve the FWHM of ensemble μPL emissions at low temperatures by reducing the size distribution of the QD within the arrays. Redshifting of emission was also shown to be dependent on the growth interrupt with a maximum redshift of 70 nm achieved. With a growth interrupt between 60 to 180 seconds, it is possible to achieve good QD occupancy with clear and bright QD emissions within arrays. This implies that some degree of growth interrupts is beneficial in allowing InAs to migrate across the surface and coalesce into uniform QD. The implementation of indium flushing controls the height of the quantum dot by interdiffusion of indium and gallium controlled by the thin GaAs layer after QD growth. This technique enabled additional control over the improved ensemble μPL emissions that was seen with growth interrupt-only structures [86]. Increasing the partial capping thickness up to 8 nm for the indium flushing technique allows for a redshifting of up to 80 nm and significant improvement to PL intensity by ~3 times. From both techniques, it was also shown that by increasing nanohole size results in the blueshift of emissions by ~30 nm and narrowing of FWHM by ~ 25 nm.

The optimised undoped waveguide structure with promising ensemble conditions was then characterised at a single dot level, outlined in Chapter 5. Positioned QD within an array yielded single dot emissions with easily identifiable exciton and biexciton emissions with relatively low linewidths achieved. Additional measurements using polarisation and temperature dependence were used to confirm the types of exciton species observed including the observation of charged excitons. Fine structure splitting of a neutral exciton had a value of 25.7 μeV, which is a significant improvement on many SCQDs demonstrated in the literature [162]. A QD map of the patterned arrays with good optical properties was then presented. Within the map, a series of QDs with comparable emissions in close proximity to each other was identified. This is a significant improvement to SCQDs, indicating the possibilities of tuning multiple QDs to emit the same wavelength with the use of quantum confinement stark effect on doped site-controlled structures. The lowest linewidth of 22.4 μeV, which

is close to the spectrometer detection limit (20.9 µeV), was also found and shows promise for the use of site-controlled QDs by this method in coherent quantum emitters and nanophotonic devices.

With the promising characterisation of single QD emissions in deterministic positions, development towards doped site-controlled waveguide structures was developed next and outlined in Chapter 6. The goal of this chapter was to achieve electrical tuning through the Stark effect in a diode structure and identify a series of QDs which can be tuned into the same wavelength. The introduction of doped layers, along with the lack of planarisation on the patterned regions, exerted a notable influence on QD emissions. This stemmed from charge suppression occurring when QDs are deposited with the doped layers [179]. To prevent this problem, readjusting the V/III ratio to a lower level improved the infilling of nanoholes and moved the QD growth interface away from the doped layer regions. Subsequent doped site-controlled waveguide growth presented an ordered array of QD emissions. The structure was then successfully fabricated into a mesa diode and was characterised optically and electrically. The ability to tune efficient QDs within an array by an electric field and have pairs (or groups) of QDs emit at the same wavelength, was achieved. A total of 5 SCQDs were identified which could be tuned into the same wavelength ranging between 960 nm to 970 nm - a significant development towards scalable QD devices.

In Chapter 7, the focus was shifted to InAs/InP QDs and the implementation of rapid thermal annealing to improve QD properties as a post-growth method. Different capping methods were compared with annealing temperatures between 650°C to 850°C. For both capping methods, annealing at temperatures below 800°C did not enable any shifting of PL emission in ensemble PL measurement. At 800°C, the use of the SiO_2 capping method enables blueshifting, which is at a temperature 50°C lower than seen with proximity capping. For proximity capping, aside from blueshifting of the ensemble emissions at 850°C, no additional improvement to optical properties was observed. In contrast, for SiO_2 capping, an increase in integral intensity was found at annealing temperatures as low as 650°C. When annealing SiO_2 between 750°C and 800°C, controlled blueshifting was achieved while maintaining a consistent improvement to integral intensity. In low-temperature PL, blueshifting of single dot emissions towards 1300 nm was achieved, along with the removal of background noise after annealing. In addition, an improvement in the linewidth distribution close to the detector spectral resolution (20.9 µeV) was observed. This presents an exciting post-growth solution to improve optical properties without complex processes or fabrication requirements.

Future work
The findings presented in this study unveil promising trajectories for future research. Within the areas of site-control QDs, both undoped and doped waveguide structures have shown significant

improvements and offer exciting opportunities for future development. Undoped site-control waveguides demonstrated in this thesis have shown significant improvement to the optical properties suitable for single photon emitters but further improvements towards this area are required. However, the current results achieved are already comparable to existing literature reports where nanophotonics devices such as optical resonators have been produced [13]. Therefore, one direction to explore is evolving undoped waveguide structures towards similar applications for cavity structures. Initial fabrication of nanobeam waveguide structures has been achieved, which requires further characterisation (see Figure 5- 19). Initial PL images show the presence of SCQD with high occupancy and a good coupling of QD emissions within the nanobeam towards the out coupler. We believe with minor improvements to the growth structures presented in this thesis, SCQDs in waveguide devices can be realised. Another direction for future development is providing greater statistics and uniformity measurements. The current status of SCQD, demonstrates the possibility of improving device yield within a small, patterned area, however, there has yet to be any reports on the scalability of such technology in a full wafer scale. As such a detail study of wafer uniformity and variation across large areas is important to prove that such technology can be easily scaled.

As for doped SC waveguide structures, initial characterisation of QD emissions has been achieved with some degree of tunability of the QDs. The initial success of fabricating device structures shows great advancement towards implementing SCQD as a building block for qubits. To realise this application, improvement in the linewidth of single dots is needed as, currently, it is too large for any additional investigation or experiments. To address this issue, a single QD with high symmetry is important. Therefore, improvement to uniformity through growth optimisation is needed. Indium flushing is one example of enhancing the uniformity of QDs, previously shown in Chapter 4. However, the current results in the doped structure were not successful. Therefore, it is recommended to reinvestigate the use of varying thin capping layers. Other potential parameters include growth temperature and growth rates, both of which impact the migration of InAs across the patterned surface. With optimised growth conditions, additional device fabrication and characterisation can be performed on these structures. These include basic diode structure but can also follow in the undoped waveguide future plan on developing nanobeam devices, to demonstrate the ability of resonant a series of SCQDs towards an out-coupler and enhancing the QD emissions.

Another area for future work is the overall pattern design for SCQDs. The current pattern in use provides a large range of pattern parameters (dose, pitch, nanohole size) which is great for research purpose in understanding how different etch pits affect QD growth. However, this is not useful for large scale or industrial applications, which focuses on uniformity and consistency. Therefore, future

progression should also focus selecting a specific pattern parameter that would be applied to a full wafer.

Lastly, rapid thermal annealing has shown to be a valuable method for post-growth tuning. Initial investigation has shown positive results on InAs/InP QDs with the ability to tune ensemble PL emission and control single dot emissions at low-temperature µPL. However, a detailed analysis of the current annealed sample, including fine structure splitting measurements, could be proven useful in identifying QD suitable for device fabrication. Attempts to remove the surface defect should also be investigated with the use of different capping methods or different annealing conditions, such as varying the annealing duration.

9 Reference

[1]   R. P. Feynman, "Simulating physics with computers," *International Journal of Theoretical Physics,* vol. 21, no. 6-7, pp. 467-488, 6 1982.

[2]   D. P. DiVincenzo and IBM, "The Physical Implementation of Quantum Computation," *Fortschritte der Physik,* vol. 48, no. 9-11, pp. 771-783, 2 2000.

[3]   S. Wehner, D. Elkouss and R. Hanson, "Quantum internet: A vision for the road ahead," *Science,* vol. 362, no. 6412, 10 2018.

[4]   G. E. Moore, "Cramming more components onto integrated circuits, Reprinted from Electronics, volume 38, number 8, April 19, 1965, pp.114 ff.," *IEEE Solid-State Circuits Society Newsletter,* vol. 11, no. 3, pp. 33-35, 2 2009.

[5]   R. Uppu, H. T. Eriksen, H. Thyrrestrup, A. D. Uğurlu, Y. Wang, S. Scholz, A. D. Wieck, A. Ludwig, M. C. Löbl, R. J. Warburton, P. Lodahl and L. Midolo, "On-chip deterministic operation of quantum dots in dual-mode waveguides for a plug-and-play single-photon source," *Nature Communications 2020 11:1,* vol. 11, no. 1, pp. 1-6, 7 2020.

[6]   J. Kołodyński, A. Máttar, P. Skrzypczyk, E. Woodhead, D. Cavalcanti, K. Banaszek and A. Acín, "Device-independent quantum key distribution with single-photon sources," *Quantum,* vol. 4, p. 260, 4 2020.

[7]   S. U. Hong, J. S. Kim, J. H. Lee, H. S. Kwack, W. S. Han and D. K. Oh, "Properties of self-assembled InAs quantum dots grown by various growth techniques," *Journal of Crystal Growth,* vol. 260, no. 3-4, pp. 343-347, 1 2004.

[8]   C. Zhu, M. Marczak, L. Feld, S. C. Boehme, C. Bernasconi, A. Moskalenko, I. Cherniukh, D. Dirin, M. I. Bodnarchuk, M. V. Kovalenko and G. Rainò, "Room-Temperature, Highly Pure Single-Photon Sources from All-Inorganic Lead Halide Perovskite Quantum Dots," *Nano Letters,* vol. 22, p. 42, 2022.

[9]   H. Wang, H. Y. Wang, A. Toma, T. A. Yano, Q. D. Chen, H. L. Xu, H. B. Sun and R. Proietti Zaccaria, "Dynamics of Strong Coupling between CdSe Quantum Dots and Surface Plasmon Polaritons in Subwavelength Hole Array," *Journal of Physical Chemistry Letters,* vol. 7, no. 22, pp. 4648-4654, 11 2016.

[10]   D. Hallett, A. P. Foster, D. Whittaker, M. S. Skolnick and L. R. Wilson, "Engineering Chiral Light-Matter Interactions in a Waveguide-Coupled Nanocavity," *ACS Photonics,* vol. 9, no. 2, pp. 706-713, 2 2022.

[11]   K. H. Lee, A. M. Green, R. A. Taylor, D. N. Sharp, J. Scrimgeour, O. M. Roche, J. H. Na, A. F. Jarjour, A. J. Turberfield, F. S. Brossard, D. A. Williams, G. Andrew and D. Briggs, "Registration

of single quantum dots using cryogenic laser photolithography," *Applied Physics Letters,* vol. 88, no. 19, p. 193106, 5 2006.

[12] M. Calic, C. Jarlov, P. Gallo, B. Dwir, A. Rudra and E. Kapon, "Deterministic radiative coupling of two semiconductor quantum dots to the optical mode of a photonic crystal nanocavity," *Scientific Reports 2017 7:1,* vol. 7, no. 1, pp. 1-7, 6 2017.

[13] A. Huggenberger, C. Schneider, T. Heindel, M. Kamp, S. Reitzenstein, S. Hofling, L. Worschech and A. Forchel, "Site-controlled In(Ga)As quantum dots with narrow emission linewidth for integration into nanophotonic devices," *2011 Int. Quantum Electron. Conf., IQEC 2011 and Conf. Lasers and Electro-Optics, CLEO Pacific Rim 2011 Incorporating the Australasian Conf. Optics, Lasers and Spectroscopy and the Australian Conf.,* pp. 216-218, 2011.

[14] I. Vurgaftman, J. R. Meyer and L. R. Ram-Mohan, "Band parameters for III-V compound semiconductors and their alloys," *Journal of Applied Physics,* vol. 89, no. 11 I, pp. 5815-5875, 2001.

[15] J. Li and L. W. Wang, "First principle study of core/shell structure quantum dots," *Applied Physics Letters,* vol. 84, no. 18, pp. 3648-3650, 5 2004.

[16] D. Bimberg, E. Stock, A. Lochmann, A. Schliwa, W. Unrau, M. Münnix, S. Rodt, A. Bakarov, J. A. Töfflinger, V. A. Haisler, A. I. Toropov and A. K. Kalagin, "Quantum dots for single- and entangled-photon emitters," *IEEE Photonics Journal,* vol. 1, no. 1, pp. 58-68, 6 2009.

[17] S. Bauer, V. Sichkovskyi, F. Schnabel, A. Sengül and J. P. Reithmaier, "Comparison between InP-based quantum dot lasers with and without tunnel injection quantum well and the impact of rapid thermal annealing," *Journal of Crystal Growth,* vol. 516, pp. 34-39, 6 2019.

[18] J. Huwer, R. M. Stevenson, J. Skiba-Szymanska, M. B. Ward, A. J. Shields, M. Felle, I. Farrer, D. A. Ritchie and R. V. Penty, "Quantum-dot-based telecommunication-wavelength quantum relay," *Physical Review Applied,* vol. 8, no. 2, p. 024007, 8 2017.

[19] N. S. Beattie, P. See, G. Zoppi, P. M. Ushasree, M. Duchamp, I. Farrer, D. A. Ritchie and S. Tomić, "Quantum Engineering of InAs/GaAs Quantum Dot Based Intermediate Band Solar Cells," *ACS Photonics,* vol. 4, no. 11, pp. 2745-2750, 11 2017.

[20] I. Mukhametzhanov, R. Heitz, J. Zeng, P. Chen and A. Madhukar, "Independent manipulation of density and size of stress-driven self-assembled quantum dots," *Applied Physics Letters,* vol. 73, no. 13, pp. 1841-1843, 9 1998.

[21] G. Biasiol, V. Baranwal, S. Heun, M. Prasciolu, M. Tormen, A. Locatelli, T. O. Mentes, M. A. Niño and L. Sorba, "Composition uniformity of site-controlled InAs/GaAs quantum dots," *Journal of Crystal Growth,* vol. 323, no. 1, pp. 176-179, 5 2011.

[22] R. Heitz, I. Mukhametzhanov, A. Madhukar, A. Hoffmann and D. Bimberg, "Temperature dependent optical properties of self-organized InAs/GaAs quantum dots," *Journal of Electronic Materials,* vol. 28, no. 5, pp. 520-527, 1999.

[23] J. Houel, A. V. Kuhlmann, L. Greuter, F. Xue, M. Poggio, R. J. Warburton, B. D. Gerardot, P. A. Dalgarno, A. Badolato, P. M. Petroff, A. Ludwig, D. Reuter and A. D. Wieck, "Probing single-charge fluctuations at a GaAs/AlAs interface using laser spectroscopy on a nearby InGaAs quantum dot," *Physical Review Letters,* vol. 108, no. 10, 3 2012.

[24] M. Abbarchi, T. Kuroda, C. Mastrandrea, A. Vinattieri, S. Sanguinetti, T. Mano, K. Sakoda and M. Gurioli, "Fine structure splitting of quantum dot excitons: Role of geometry and environment," *Physica E: Low-Dimensional Systems and Nanostructures,* vol. 42, no. 4, pp. 881-883, 2 2010.

[25] J. D. Plumhof, R. Trotta, A. Rastelli and O. G. Schmidt, "Experimental methods of post-growth tuning of the excitonic fine structure splitting in semiconductor quantum dots," 2012.

[26] M. Anderson, T. Müller, J. Skiba-Szymanska, A. B. Krysa, J. Huwer, R. M. Stevenson, J. Heffernan, D. A. Ritchie and A. J. Shields, "Coherence in single photon emission from droplet epitaxy and Stranski-Krastanov quantum dots in the telecom C-band," *Applied Physics Letters,* vol. 118, no. 1, 1 2021.

[27] M. Zieliński, "Vanishing fine structure splitting in highly asymmetric InAs/InP quantum dots without wetting layer," *Scientific Reports,* vol. 10, no. 1, 12 2020.

[28] G. S. Solomon, J. A. Trezza, A. F. Marshall and J. S. Harris, "Vertically Aligned and Electronically Coupled Growth Induced InAs Islands in GaAs," *Physical Review Letters,* vol. 76, no. 6, p. 952, 2 1996.

[29] J. M. Moison, F. Houzay, F. Barthe, L. Leprince, E. André and O. Vatel, "Self-organized growth of regular nanometer-scale InAs dots on GaAs," *Applied Physics Letters,* vol. 64, no. 2, pp. 196-198, 1 1994.

[30] A. Madhukar, Q. Xie, P. Chen and A. Konkar, "Nature of strained InAs three-dimensional island formation and distribution on GaAs(100)," *Applied Physics Letters,* vol. 64, no. 20, pp. 2727-2729, 5 1994.

[31] M. Z. M. Khan, T. K. Ng and B. S. Ooi, "Self-assembled InAs/InP quantum dots and quantum dashes: Material structures and devices," *Progress in Quantum Electronics,* vol. 38, no. 6, pp. 237-313, 2014.

[32] X. Yu, H. Jia, C. Dear, J. Yuan, H. Deng, M. Tang and H. Liu, "Optically enhanced single- and multi-stacked 1.55 μm InAs/InAlGaAs/InP quantum dots for laser applications," *Journal of Physics D: Applied Physics,* vol. 56, no. 28, p. 285101, 4 2023.

[33] E. Bauer and J. H. Van Der Merwe, "Structure and growth of crystalline superlattices: From monolayer to superlattice," *Physical Review B,* vol. 33, no. 6, p. 3657, 3 1986.

[34] J. H. Lee, Z. M. Wang, K. Sablon and G. J. Salamo, "Formation of hybrid molecules composed of Ga metal particle in direct contact with InGaAs semiconductor quantum ring," *Crystal Growth and Design,* vol. 8, no. 2, pp. 690-694, 2 2008.

[35] E. M. Sala, Y. I. Na, M. Godsland, A. Trapalis and J. Heffernan, "InAs/InP Quantum Dots in Etched Pits by Droplet Epitaxy in Metalorganic Vapor Phase Epitaxy," *Physica Status Solidi - Rapid Research Letters,* vol. 14, no. 8, 8 2020.

[36] D. D. Dukhan, S. V. Balakirev, N. E. Chernenko, M. M. Eremenko and M. S. Solodovnik, "Study of In/GaAs nanodroplet formation in conditions of non-stationary supersaturation during droplet epitaxy," *Journal of Physics: Conference Series,* vol. 2086, no. 1, 12 2021.

[37] S. V. Balakirev, N. E. Chernenko, M. M. Eremenko, O. A. Ageev and M. S. Solodovnik, "Independent control over size and surface density of droplet epitaxial nanostructures using ultra-low arsenic fluxes," *Nanomaterials,* vol. 11, no. 5, 2021.

[38] S. V. Balakirev, M. M. Eremenko, I. A. Mikhaylin, V. S. Klimin and M. S. Solodovnik, "Droplet epitaxy of In/AlGaAs nanostructures on the As-stabilized surface," *Journal of Physics: Conference Series,* vol. 1124, no. 2, 2018.

[39] J. H. Lee, Z. M. Wang and G. J. Salamo, "The control on size and density of InAs QDs by droplet epitaxy," *IEEE Transactions on Nanotechnology,* vol. 8, no. 4, pp. 431-436, 7 2009.

[40] R. S. R. Gajjela, E. M. Sala, J. Heffernan and P. M. Koenraad, "Control of Morphology and Substrate Etching in InAs/InP Droplet Epitaxy Quantum Dots for Single and Entangled Photon Emitters," *ACS Applied Nano Materials,* vol. 5, no. 6, pp. 8070-8079, 6 2022.

[41] J. Lee, Z. Wang, Y. Hirono, E. S. Kim, N. Kim, S. Park, C. Wang and G. J. Salamo, "Various configurations of in nanostructures on GaAs (100) by droplet epitaxy," *CrystEngComm,* vol. 12, no. 11, pp. 3404-3408, 11 2010.

[42] D. Leonard, K. Pond and P. M. Petroff, "Critical layer thickness for self-assembled InAs islands on GaAs," *Physical Review B,* vol. 50, no. 16, p. 11687, 10 1994.

[43] R. Hull and J. C. Bean, "Misfit dislocations in lattice-mismatched epitaxial films," *Critical Reviews in Solid State and Material Sciences,* vol. 17, no. 6, pp. 507-546, 1 1992.

[44] I. N. Stranski and L. Krastanow, "Zur Theorie der orientierten Ausscheidung von Ionenkristallen aufeinander," *Monatshefte für Chemie,* vol. 71, no. 1, pp. 351-364, 12 1937.

[45] P. B. Joyce, T. J. Krzyzewski, G. R. Bell, T. S. Jones, S. Malik, D. Childs and R. Murray, "Effect of growth rate on the size, composition, and optical properties of InAs/GaAs quantum dots grown by molecular-beam epitaxy," *Physical Review B,* vol. 62, no. 16, p. 10891, 10 2000.

[46] J. Sun, P. Jin and Z. G. Wang, "Extremely low density InAs quantum dots realized in situ on (100) GaAs," *Nanotechnology,* vol. 15, no. 12, pp. 1763-1766, 12 2004.

[47] L. Chu, M. Arzberger, G. Böhm and G. Abstreiter, "Influence of growth conditions on the photoluminescence of self-assembled InAs/GaAs quantum dots," *Journal of Applied Physics,* vol. 85, no. 4, pp. 2355-2362, 2 1999.

[48] L. H. Li, N. Chauvin, G. Patriarche, B. Alloing and A. Fiore, "Growth-interruption-induced low-density InAs quantum dots on GaAs," *Journal of Applied Physics,* vol. 104, no. 8, p. 83508, 10 2008.

[49] K. Iizuka, K. Mori and T. Suzuki, "Effects of growth interruption during the formation of InAs/GaAs self-assembled quantum dots grown by molecular beam epitaxy," *Microelectronics Journal,* vol. 34, no. 5-8, pp. 611-613, 5 2003.

[50] A. Huggenberger, S. Heckelmann, C. Schneider, S. Höfling, S. Reitzenstein, L. Worschech, M. Kamp and A. Forchel, "Narrow spectral linewidth from single site-controlled In(Ga)As quantum dots with high uniformity," *Applied Physics Letters,* vol. 98, no. 13, 3 2011.

[51] R. J. Coles, "Quantum Optical Circuits using III-V Nanophotonic Structures," White Rose eTheses Online, Sheffield, 2015.

[52] T. Hakkarainen, A. Schramm, J. Viheriälä and M. Guina, "Site-Controlled Epitaxy of InAs Quantum Dots on Nanoimprint Lithography Patterns," *Molecular Beam Epitaxy,* pp. 277-292, 1 2018.

[53] R. Seguin, A. Schliwa, S. Rodt, K. Pötschke, U. W. Pohl and D. Bimberg, "Size-dependent fine-structure splitting in self-organized InAs/GaAs quantum dots," 2006.

[54] J. M. García, G. Medeiros-Ribeiro, K. Schmidt, T. Ngo, J. L. Feng, A. Lorke, J. Kotthaus and P. M. Petroff, "Intermixing and shape changes during the formation of InAs self-assembled quantum dots," *Applied Physics Letters,* vol. 71, no. 14, pp. 2014-2016, 10 1997.

[55] C. J. Mayer, M. F. Helfrich and D. M. Schaadt, "Influence of hole shape/size on the growth of site-selective quantum dots," *Nanoscale Research Letters,* vol. 8, no. 1, pp. 1-7, 12 2013.

[56] R. Heitz, O. Stier, I. Mukhametzhanov, A. Madhukar and D. Bimberg, "Quantum size effect in self-organized InAs/GaAs quantum dots," *Physical Review B,* vol. 62, no. 16, p. 11017, 10 2000.

[57] F. Ferdos, S. Wang, Y. Wei, A. Larsson, M. Sadeghi and Q. Zhao, "Influence of a thin GaAs cap layer on structural and optical properties of InAs quantum dots," *Applied Physics Letters,* vol. 81, no. 7, pp. 1195-1197, 8 2002.

[58] S. Adhikary, N. Halder, S. Chakrabarti, S. Majumdar, S. K. Ray, M. Herrera, M. Bonds and N. D. Browning, "Investigation of strain in self-assembled multilayer InAs/GaAs quantum dot heterostructures," *Journal of Crystal Growth,* vol. 312, no. 5, pp. 724-729, 2 2010.

[59] H. Sasakura, S. Kayamori, S. Adachi and S. Muto, "Effect of indium-flush method on the control of photoluminescence energy of highly uniform self-assembled InAs quantum dots by slow molecular beam epitaxy growth," *Journal of Applied Physics,* vol. 102, no. 1, 2007.

[60] L. Goldstein, F. Glas, J. Y. Marzin, M. N. Charasse and G. Le Roux, "Growth by molecular beam epitaxy and characterization of InAs/GaAs strained-layer superlattices," *Applied Physics Letters,* vol. 47, no. 10, pp. 1099-1101, 11 1985.

[61] S. T. Moroni, T. H. Chung, G. Juska, A. Gocalinska and E. Pelucchi, "Statistical study of stacked/coupled site-controlled pyramidal quantum dots and their excitonic properties," *Applied Physics Letters,* vol. 111, no. 8, p. 83103, 8 2017.

[62] R. Heitz, A. Kalburge, Q. Xie, M. Grundmann, P. Chen, A. Hoffmann, A. Madhukar and D. Bimberg, "Excited states and energy relaxation in stacked InAs/GaAs quantum dots," *Physical Review B,* vol. 57, no. 15, p. 9050, 4 1998.

[63] C. H. Chan, C. H. Lee, Y. S. Huang, J. S. Wang and H. H. Lin, "Characterization of excitonic features in self-assembled InAs/GaAs quantum dot superlattice structures via surface photovoltage spectroscopy," *Journal of Applied Physics,* vol. 101, no. 10, p. 103102, 5 2007.

[64] P. B. Joyce, T. J. Krzyzewski, P. H. Steans, G. R. Bell, J. H. Neave and T. S. Jones, "Variations in critical coverage for InAs/GaAs quantum dot formation in bilayer structures," *Journal of Crystal Growth,* vol. 244, no. 1, pp. 39-48, 9 2002.

[65] J. Schuster, J. Aberl, L. Vukušić, L. Spindlberger, H. Groiss, T. Fromherz, M. Brehm and F. Schäffler, "Photoluminescence enhancement by deterministically site-controlled, vertically stacked SiGe quantum dots," *Scientific Reports 2021 11:1,* vol. 11, no. 1, pp. 1-13, 10 2021.

[66] V. G. Talalaev, J. W. Tomm, A. S. Sokolov, I. V. Shtrom, B. V. Novikov, A. T. Winzer, R. Goldhahn, G. Gobsch, N. D. Zakharov, P. Werner, U. Gösele, G. E. Cirlin, A. A. Tonkikh, V. M. Ustinov and G. G. Tarasov, "Tuning of the interdot resonance in stacked InAs quantum dot arrays by an external electric field," *Journal of Applied Physics,* vol. 100, no. 8, p. 83704, 10 2006.

[67] S. Kohmoto, T. Ishikawa and K. Asakawa, "InAs-dot/GaAs structures site-controlled by in situ EB lithography and self-organizing MBE growth," *Conference Proceedings - International Conference on Indium Phosphide and Related Materials,* pp. 769-772, 1998.

[68] C. Schneider, A. Huggenberger, M. Gschrey, P. Gold, S. Rodt, A. Forchel, S. Reitzenstein, S. Höfling and M. Kamp, "In(Ga)As/GaAs site-controlled quantum dots with tailored morphology

and high optical quality," *Physica Status Solidi (A) Applications and Materials Science,* vol. 209, no. 12, pp. 2379-2386, 12 2012.

[69] Y. R. Wang, I. S. Han and M. Hopkinson, "Fabrication of quantum dot and ring arrays by direct laser interference patterning for nanophotonics," *Nanophotonics,* vol. 12, no. 8, pp. 1469-1479, 4 2023.

[70] P. Atkinson, M. B. Ward, S. P. Bremner, D. Anderson, T. Farrow, G. A. Jones, A. J. Shields and D. A. Ritchie, "Site-control of InAs quantum dots using Ex-situ electron-beam lithographic patterning of GaAs substrates," *Japanese Journal of Applied Physics, Part 1: Regular Papers and Short Notes and Review Papers,* vol. 45, no. 4 A, pp. 2519-2521, 4 2006.

[71] K. Booker, Y. O. Mayon, C. Jones, M. Stocks and A. Blakers, "Deep, vertical etching for GaAs using inductively coupled plasma/reactive ion etching," *Journal of Vacuum Science & Technology B, Nanotechnology and Microelectronics: Materials, Processing, Measurement, and Phenomena,* vol. 38, no. 1, 1 2020.

[72] T. Xia, Y. J. Cho, M. Cotrufo, I. Agafonov, F. Van Otten and A. Fiore, "In-assisted deoxidation of GaAs substrates for the growth of single InAs/GaAs quantum dot emitters," *Semiconductor Science and Technology,* vol. 30, no. 5, pp. 1-6, 5 2015.

[73] S. Hussain, A. Pozzato, M. Tormen, V. Zannier and G. Biasiol, "Site-control of InAs/GaAs quantum dots with indium-assisted deoxidation," *Materials,* vol. 9, no. 3, 3 2016.

[74] B. A. Joyce and D. D. Vvedensky, "Self-organized growth on GaAs surfaces," *Materials Science and Engineering: R: Reports,* vol. 46, no. 6, pp. 127-176, 12 2004.

[75] J. Herranz, L. Wewior, B. Alen, D. Fuster, L. Gonzalez and Y. Gonzalez, "Role of re-growth interface preparation process for spectral line-width reduction of single InAs site-controlled quantum dots," *Nanotechnology,* vol. 26, no. 19, 5 2015.

[76] S. Kiravittaya, A. Rastelli and O. G. Schmidt, "Self-assembled InAs quantum dots on patterned GaAs(001) substrates: Formation and shape evolution," *Applied Physics Letters,* vol. 87, no. 24, pp. 1-3, 2005.

[77] P. Atkinson, S. Kiravittaya, M. Benyoucef, A. Rastelli and O. G. Schmidt, "Site-controlled growth and luminescence of InAs quantum dots using in situ Ga-assisted deoxidation of patterned substrates," *Applied Physics Letters,* vol. 93, no. 10, 2008.

[78] J. Yuan, H. Wang, R. P. Van Veldhoven, J. Wang, T. De Vries, B. Smalbrugge, C. Y. Jin, P. Nouwens, E. J. Geluk, A. Y. Silov and R. Nötzel, "Controlling polarization anisotropy of site-controlled InAs/InP (100) quantum dots," *Applied Physics Letters,* vol. 98, no. 20, 5 2011.

[79] L. O. Mereni, V. Dimastrodonato, R. J. Young and E. Pelucchi, "A site-controlled quantum dot system offering both high uniformity and spectral purity," *Applied Physics Letters,* vol. 94, no. 22, 2009.

[80] A. Mohan, M. Felici, P. Gallo, B. Dwir, A. Rudra, J. Faist and E. Kapon, "Polarization-entangled photons produced with high-symmetry site-controlled quantum dots," *Nature Photonics,* vol. 4, no. 5, pp. 302-306, 5 2010.

[81] G. Juska, E. Murray, V. Dimastrodonato, T. H. Chung, S. T. Moroni, A. Gocalinska and E. Pelucchi, "Conditions for entangled photon emission from (111)B site-controlled pyramidal quantum dots," *Journal of Applied Physics,* vol. 117, no. 13, p. 134302, 4 2015.

[82] K. D. Jöns, P. Atkinson, M. Müller, M. Heldmaier, S. M. Ulrich, O. G. Schmidt and P. Michler, "Triggered indistinguishable single photons with narrow line widths from site-controlled quantum dots," *Nano Letters,* vol. 13, no. 1, pp. 126-130, 1 2013.

[83] H. Z. Song, T. Usuki, S. Hirose, K. Takemoto, Y. Nakata, N. Yokoyama and Y. Sakuma, "Site-controlled photoluminescence at telecommunication wavelength from InAs/InP quantum dots," *Applied Physics Letters,* vol. 86, no. 11, pp. 1-3, 3 2005.

[84] S. Kiravittaya, H. Heidemeyer and O. G. Schmidt, "Growth of three-dimensional quantum dot crystals on patterned GaAs (0 0 1) substrates," *Physica E: Low-Dimensional Systems and Nanostructures,* vol. 23, no. 3-4 SPEC. ISS., pp. 253-259, 7 2004.

[85] G. Sęk, P. Poloczek, K. Ryczko, J. Misiewicz, A. Löffler, J. P. Reithmaier and A. Forchel, "Photoreflectance determination of the wetting layer thickness in the InxGa1-xAs/GaAs quantum dot system for a broad indium content range of 0.3-1," *Journal of Applied Physics,* vol. 100, no. 10, p. 103529, 11 2006.

[86] C. Schneider, A. Huggenberger, T. Sünner, T. Heindel, M. Strau, S. Göpfert, P. Weinmann, S. Reitzenstein, L. Worschech, M. Kamp, S. Höfling and A. Forchel, "Single site-controlled In(Ga)As/GaAs quantum dots: growth, properties and device," *Nanotechnology,* vol. 20, no. 43, p. 434012, 10 2009.

[87] K. M. Cha, I. Horiuchi, K. Shibata and K. Hirakawa, "Size-limiting effect of site-controlled inas quantum dots grown at high temperatures by molecular beam epitaxy," *Applied Physics Express,* vol. 5, no. 8, p. 085501, 8 2012.

[88] L. N. McCabe, "Epitaxial Growth of Spatially and Spectrally Controlled Quantum Dots and Quantum Dot Molecules," 2022.

[89] C. Ovenden, I. Farrer, M. S. Skolnick and J. Heffernan, "Nanoscale wafer patterning using SPM induced local anodic oxidation in InP substrates," *Semiconductor Science and Technology,* vol. 37, no. 2, p. 025001, 12 2021.

[90] M. Choi, M. Lee, S. Y. L. Park, B. S. Kim, S. Jun, S. I. Park, J. D. Song, Y. H. Ko and Y. H. Cho, "Single Quantum Dot Selection and Tailor-Made Photonic Device Integration using a Nanoscale-Focus Pinspot," *Advanced Materials,* vol. 35, no. 26, p. 2210667, 6 2023.

[91] T. W. Saucer, J. E. Lee, A. J. Martin, D. Tien, J. M. Millunchick and V. Sih, "Photoluminescence of patterned arrays of vertically stacked InAs/GaAs quantum dots," *Solid State Communications,* vol. 151, no. 4, pp. 269-271, 2 2011.

[92] R. Seguin, A. Schliwa, T. D. Germann, S. Rodt, K. Pötschke, A. Strittmatter, U. W. Pohl, D. Bimberg, M. Winkelnkemper, T. Hammerschmidt and P. Kratzer, "Control of fine-structure splitting and excitonic binding energies in selected individual InAs/GaAs quantum dots," *Applied Physics Letters,* vol. 89, no. 26, 2006.

[93] P. Joyce, T. Krzyzewski, G. Bell and B. Joyce, "Composition of InAs quantum dots on GaAs(001): Direct evidence for (In,Ga)As alloying," *Physical Review B,* vol. 58, no. 24, p. R15981, 12 1998.

[94] J. Q. Grim, A. S. Bracker, M. Zalalutdinov, S. G. Carter, A. C. Kozen, M. Kim, C. S. Kim, J. T. Mlack, M. Yakes, B. Lee and D. Gammon, "Scalable in operando strain tuning in nanophotonic waveguides enabling three-quantum-dot superradiance," *Nature Materials 2019 18:9,* vol. 18, no. 9, pp. 963-969, 7 2019.

[95] G. Ortner, I. Yugova, G. Baldassarri Höger Von Högersthal, A. Larionov, H. Kurtze, D. R. Yakovlev, M. Bayer, S. Fafard, Z. Wasilewski, P. Hawrylak, Y. B. Lyanda-Geller, T. L. Reinecke, A. Babinski, M. Potemski, V. B. Timofeev and A. Forchel, "Fine structure in the excitonic emission of InAs/GaAs quantum dot molecules," *Physical Review B - Condensed Matter and Materials Physics,* vol. 71, no. 12, 3 2005.

[96] F. Findeis, M. Baier, E. Beham, A. Zrenner and G. Abstreiter, "Photocurrent and photoluminescence of a single self-assembled quantum dot in electric fields," *Applied Physics Letters,* vol. 78, no. 19, pp. 2958-2960, 5 2001.

[97] J. Tatebayashi, Y. Ota, S. Ishida, M. Nishioka, S. Iwamoto and Y. Arakawa, "Site-controlled formation of InAs/GaAs quantum-dot-in-nanowires for single photon emitters," *Applied Physics Letters,* vol. 100, no. 26, 6 2012.

[98] A. Kaganskiy, F. Gericke, T. Heuser, T. Heindel, X. Porte and S. Reitzenstein, "Micropillars with a controlled number of site-controlled quantum dots," *Applied Physics Letters,* vol. 112, no. 7, p. 71101, 2 2018.

[99] P. Michler, Single Semiconductor Quantum Dots, P. Michler, Ed., Berlin, Heidelberg: Springer Berlin Heidelberg, 2009.

[100] T. Grange, N. Somaschi, C. Antón, L. De Santis, G. Coppola, V. Giesz, A. Lemaître, I. Sagnes, A. Auffèves and P. Senellart, "Reducing Phonon-Induced Decoherence in Solid-State Single-Photon Sources with Cavity Quantum Electrodynamics," *Physical Review Letters,* vol. 118, no. 25, p. 253602, 6 2017.

[101] J. Iles-Smith, D. P. McCutcheon, A. Nazir and J. Mørk, "Phonon scattering inhibits simultaneous near-unity efficiency and indistinguishability in semiconductor single-photon sources," *Nature Photonics,* vol. 11, no. 8, pp. 521-526, 7 2017.

[102] P. Lodahl, S. Mahmoodian and S. Stobbe, "Interfacing single photons and single quantum dots with photonic nanostructures," *Reviews of Modern Physics,* vol. 87, no. 2, pp. 347-400, 5 2015.

[103] C. Bentham, D. Hallett, N. Prtljaga, B. Royall, D. Vaitiekus, R. J. Coles, E. Clarke, A. M. Fox, M. S. Skolnick, I. E. Itskevich and L. R. Wilson, "Single-photon electroluminescence for on-chip quantum networks," *Applied Physics Letters,* vol. 109, no. 16, p. 161101, 10 2016.

[104] C. Schneider, T. Heindel, A. Huggenberger, T. A. Niederstrasser, S. Reitzenstein, A. Forchel, S. Höfling and M. Kamp, "Microcavity enhanced single photon emission from an electrically driven site-controlled quantum dot," *Applied Physics Letters,* vol. 100, no. 9, p. 91108, 2 2012.

[105] F. Biccari, A. Boschetti, G. Pettinari, F. La China, M. Gurioli, F. Intonti, A. Vinattieri, M. S. Sharma, M. Capizzi, A. Gerardino, L. Businaro, M. Hopkinson, A. Polimeni and M. Felici, "Site-Controlled Single-Photon Emitters Fabricated by Near-Field Illumination," *Advanced Materials,* vol. 30, no. 21, p. 1705450, 5 2018.

[106] W. Unrau, D. Quandt, J. H. Schulze, T. Heindel, T. D. Germann, O. Hitzemann, A. Strittmatter, S. Reitzenstein, U. W. Pohl and D. Bimberg, "Electrically driven single photon source based on a site-controlled quantum dot with self-aligned current injection," *Applied Physics Letters,* vol. 101, no. 21, p. 211119, 11 2012.

[107] M. H. Baier, C. Constantin, E. Pelucchi and E. Kapon, "Electroluminescence from a single pyramidal quantum dot in a light-emitting diode," *Applied Physics Letters,* vol. 84, no. 11, pp. 1967-1969, 3 2004.

[108] M. Mehta, D. Reuter, A. Melnikov, A. D. Wieck, S. Michaelis De Vasconcellos, T. Baumgarten, A. Zrenner and C. Meier, "Intentionally positioned self-assembled InAs quantum dots in an electroluminescent p–i–n junction diode," *Physica E: Low-dimensional Systems and Nanostructures,* vol. 42, no. 10, pp. 2749-2752, 9 2010.

[109] C. Ovenden, "Development and characterisation of site-controlled quantum dot arrays," White Rose eTheses Online, Sheffield, 2021.

[110] C. Dion, P. Desjardins, M. Chicoine, F. Schiettekatte, P. J. Poole and S. Raymond, "Drastic ion-implantation-induced inter-mixing during the annealing of self-assembled InAs/InP(001) quantum dots," *Nanotechnology,* vol. 18, no. 1, 1 2007.

[111] M. E. Reimer, M. Korkusiński, D. Dalacu, J. Lefebvre, J. Lapointe, P. J. Poole, G. C. Aers, W. R. McKinnon, P. Hawrylak and R. L. Williams, "Prepositioned single quantum dot in a lateral

electric field," *Physical Review B - Condensed Matter and Materials Physics,* vol. 78, no. 19, 11 2008.

[112] A. Muller, W. Fang, J. Lawall and G. S. Solomon, "Creating polarization-entangled photon pairs from a semiconductor quantum dot using the optical stark effect," *Physical Review Letters,* vol. 103, no. 21, 11 2009.

[113] A. Babiński, J. Jasiński, R. Bozek, A. Szepielow and J. M. Baranowski, "Rapid thermal annealing of InAs/GaAs quantum dots under a GaAs proximity cap," *Applied Physics Letters,* vol. 79, no. 16, pp. 2576-2578, 10 2001.

[114] S. Ramanathan, G. Petersen, K. Wijesundara, R. Thota, E. A. Stinaff, M. L. Kerfoot, M. Scheibner, A. S. Bracker and D. Gammon, "Quantum-confined Stark effects in coupled InAs/GaAs quantum dots," *Applied Physics Letters,* vol. 102, no. 21, p. 213101, 5 2013.

[115] R. B. Patel, A. J. Bennett, I. Farrer, C. A. Nicoll, D. A. Ritchie and A. J. Shields, "Two-photon interference of the emission from electrically tunable remote quantum dots," *Nature Photonics 2010 4:9,* vol. 4, no. 9, pp. 632-635, 7 2010.

[116] C. Heyn, L. Ranasinghe, M. Zocher and W. Hansen, "Shape-Dependent Stark Shift and Emission-Line Broadening of Quantum Dots and Rings," *Journal of Physical Chemistry C,* vol. 124, no. 36, pp. 19809-19816, 9 2020.

[117] R. Singh and G. Bester, "Lower bound for the excitonic fine structure splitting in self-assembled quantum dots," *Physical Review Letters,* vol. 104, no. 19, p. 196803, 5 2010.

[118] A. J. Bennett, M. A. Pooley, R. M. Stevenson, M. B. Ward, R. B. Patel, A. B. De La Giroday, N. Sköd, I. Farrer, C. A. Nicoll, D. A. Ritchie and A. J. Shields, "Electric-field-induced coherent coupling of the exciton states in a single quantum dot," *Nature Physics 2010 6:12,* vol. 6, no. 12, pp. 947-950, 10 2010.

[119] T. M. Hsu, Y. S. Lan, W. H. Chang, N. T. Yeh and J. I. Chyi, "Tuning the energy levels of self-assembled inas quantum dots by rapid thermal annealing," *Applied Physics Letters,* vol. 76, no. 6, pp. 691-693, 2 2000.

[120] C. K. Chia, S. J. Chua, S. Tripathy and J. R. Dong, "Group-V intermixing in InAs/InP quantum dots," *Applied Physics Letters,* vol. 86, no. 5, pp. 1-3, 1 2005.

[121] C. Dion, P. Desjardins, N. Shtinkov, F. Schiettekatte, P. J. Poole and S. Raymond, "Effects of grown-in defects on interdiffusion dynamics in InAsInP (001) quantum dots subjected to rapid thermal annealing," *Journal of Applied Physics,* vol. 103, no. 8, 2008.

[122] Z. Y. Zhang, P. Jin, C. M. Li, X. L. Ye, X. Q. Meng, B. Xu, F. Q. Liu and Z. G. Wang, "The evolution of InAs/InAlAs/InGaAlAs quantum dots after rapid thermal annealing," *Journal of Crystal Growth,* vol. 253, no. 1-4, pp. 59-63, 6 2003.

9 Reference

[123] J. F. Girard, C. Dion, P. Desjardins, C. Nì Allen, P. J. Poole and S. Raymond, "Tuning of the electronic properties of self-assembled InAs/InP(001) quantum dots by rapid thermal annealing," *Applied Physics Letters,* vol. 84, no. 17, pp. 3382-3384, 4 2004.

[124] W. Chaâbani, A. Melliti, M. A. Maaref, C. Testelin and A. Lemaître, "Rapid thermal annealing and modulation-doping effects on InAs/GaAs quantum dots photoluminescence dependence on excitation power," *Physica B: Condensed Matter,* vol. 493, pp. 53-57, 7 2016.

[125] T. Xiaohong, Y. Zongyou, T. Jinghua, D. Anyan and C. Mee Koy, "Selective intermixing of InAs/InGaAs/InP quantum dot structure with large energy band gap tuning," *IEEE Transactions on Nanotechnology,* vol. 7, no. 4, pp. 422-426, 7 2008.

[126] T. Yang, J. Tatebayashi, K. Aoki, M. Nishioka and Y. Arakawa, "Effects of rapid thermal annealing on the emission properties of highly uniform self-assembled InAs/GaAs quantum dots emitting at 1.3 µm," *Applied Physics Letters,* vol. 90, no. 11, 2007.

[127] A. O. Kosogov, P. Werner, U. Gösele, N. N. Ledentsov, D. Bimberg, V. M. Ustinov, A. Y. Egorov, A. E. Zhukov, P. S. Kop'ev, N. A. Bert and Z. I. Alferov, "Structural and optical properties of InAs-GaAs quantum dots subjected to high temperature annealing," *Applied Physics Letters,* vol. 69, no. 20, pp. 3072-3074, 11 1996.

[128] S. Malik, C. Roberts, R. Murray and M. Pate, "Tuning self-assembled InAs quantum dots by rapid thermal annealing," *Applied Physics Letters,* vol. 71, no. 14, pp. 1987-1989, 10 1997.

[129] J. J. Dubowski, R. Stanowski, D. Dalacu and P. J. Poole, "Precision tuning of InAs quantum dot emission wavelength by iterative laser annealing," *Optics and Laser Technology,* vol. 103, pp. 382-386, 7 2018.

[130] W. H. Jiang, H. Z. Xu, B. Xu, X. L. Ye, J. Wu, D. Ding, J. B. Liang and Z. G. Wang, "Priority communication Annealing effect on the surface morphology and photoluminescence of InGaAs/GaAs quantum dots grown by molecular beam epitaxy," *Journal of Crystal Growth,* vol. 212, pp. 356-359, 2000.

[131] S. J. Xu, X. C. Wang, S. J. Chua, C. H. Wang, W. J. Fan, J. Jiang and X. G. Xie, "Effects of rapid thermal annealing on structure and luminescence of self-assembled InAs/GaAs quantum dots," *Applied Physics Letters,* vol. 72, no. 25, pp. 3335-3337, 1998.

[132] W. Lei, Y. H. Chen, Y. L. Wang, B. Xu, X. L. Ye, Y. P. Zeng and Z. G. Wang, "Influence of rapid thermal annealing on InAs/InAlAs/InP quantum wires with different InAs deposited thickness," *Journal of Crystal Growth,* vol. 284, no. 1-2, pp. 20-27, 10 2005.

[133] S. Barik, L. Fu, H. H. Tan and C. Jagadish, "Impurity-free disordering of InAsInP quantum dots," *Applied Physics Letters,* vol. 90, no. 24, 2007.

[134] S. Thoms and D. S. Macintyre, "Investigation of CSAR 62, a new resist for electron beam lithography," *Journal of Vacuum Science & Technology B, Nanotechnology and*

Microelectronics: Materials, Processing, Measurement, and Phenomena, vol. 32, no. 6, p. 06FJ01, 11 2014.

[135] M. Stepanova, T. Fito, Z. Szabó, K. Alti, A. P. Adeyenuwo, K. Koshelev, M. Aktary and S. K. Dew, "Simulation of electron beam lithography of nanostructures," *Journal of Vacuum Science & Technology B, Nanotechnology and Microelectronics: Materials, Processing, Measurement, and Phenomena,* vol. 28, no. 6, pp. C6C48-C6C57, 11 2010.

[136] A. Raghunathan and J. G. Hartley, "Influence of secondary electrons in high-energy electron beam lithography," *Journal of Vacuum Science & Technology B, Nanotechnology and Microelectronics: Materials, Processing, Measurement, and Phenomena,* vol. 31, no. 1, p. 011605, 1 2013.

[137] R. Cheung, ;. B. Rong, ;. E. Van Der Drift, ;. W. G. Sloof, B. Rong, E. Van Der Drift and W. G. Sloof, "Etch mechanism and etch-induced effects in the inductively coupled plasma etching of GaN," *Journal of Vacuum Science & Technology B: Microelectronics and Nanometer Structures Processing, Measurement, and Phenomena,* vol. 21, no. 4, pp. 1268-1272, 7 2003.

[138] Kazuo Nojiri, Dry Etching Damage. In: Dry Etching Technology for Semiconductor, Cham: Springer, 2015.

[139] I. Farrer, J. J. Harris, R. Thomson, D. Barlett, C. A. Taylor and D. A. Ritchie, "Substrate temperature measurement using a commercial band-edge detection system," *Journal of Crystal Growth,* Vols. 301-302, no. SPEC. ISS., pp. 88-92, 4 2007.

[140] M. O'Steen, E. Readinger, M. Doran and D. Hanser, "Systems and technology for production-scale molecular beam epitaxy," *Molecular Beam Epitaxy: From Research to Mass Production,* pp. 657-680, 1 2013.

[141] Sasoka C, Kato Y and Usui A, "Temperature programmed desorption study of GaAs(loo>-c(4 x 4) and As. exposed (2 x 4) surfaces," *Surface Science Letters,* no. 265, pp. 239-244, 1998.

[142] D. Fuster, L. Ginés, Y. González, J. Herranz and L. González, "Low temperature oxide desorption in GaAs (111)A substrates," *Thin Solid Films,* vol. 537, pp. 70-75, 6 2013.

[143] T. M. Burke, E. H. Linfield, D. A. Ritchie, M. Pepper and J. H. Burroughes, "Hydrogen radical surface cleaning of GaAs for MBE regrowth," *Journal of Crystal Growth,* Vols. 175-176, no. PART 1, pp. 416-421, 1997.

[144] Y. Okada and J. S. Harris, "Basic analysis of atomic-scale growth mechanisms for molecular beam epitaxy of GaAs using atomic hydrogen as a surfactant," *Journal of Vacuum Science & Technology B: Microelectronics and Nanometer Structures Processing, Measurement, and Phenomena,* vol. 14, no. 3, pp. 1725-1728, 5 1996.

[145] G. R. Bell, N. S. Kaijaks, R. J. Dixon and C. F. McConville, "Atomic hydrogen cleaning of polar III–V semiconductor surfaces," *Surface Science,* vol. 401, no. 2, pp. 125-137, 4 1998.

[146] B. N. Popov, J. W. Lee and M. B. Djukic, "Hydrogen Permeation and Hydrogen-Induced Cracking," *Handbook of Environmental Degradation Of Materials: Third Edition,* pp. 133-162, 1 2018.

[147] K. G. Tschersich, J. P. Fleischhauer and H. Schuler, "Design and characterization of a thermal hydrogen atom source," *Journal of Applied Physics,* vol. 104, no. 3, p. 34908, 8 2008.

[148] D. Ugur, A. J. Storm, R. Verberk, J. C. Brouwer and W. G. Sloof, "Quantification of the atomic hydrogen flux as a function of filament temperature and H2 flow rate," *Journal of Vacuum Science & Technology A: Vacuum, Surfaces, and Films,* vol. 30, no. 3, p. 31603, 5 2012.

[149] K. G. Tschersich and V. Von Bonin, "Formation of an atomic hydrogen beam by a hot capillary," *Journal of Applied Physics,* vol. 84, no. 8, pp. 4065-4070, 10 1998.

[150] K. G. Tschersich, "Intensity of a source of atomic hydrogen based on a hot capillary," *Journal of Applied Physics,* vol. 87, no. 5, pp. 2565-2573, 3 2000.

[151] G. W. Wicks, E. R. Rueckwald and M. W. Koch, "Analysis of cracking efficiency of an atomic hydrogen source, and its effect on desorption of Al x Ga1– x As native oxides," *Journal of Vacuum Science & Technology B: Microelectronics and Nanometer Structures Processing, Measurement, and Phenomena,* vol. 14, no. 3, pp. 2184-2186, 5 1996.

[152] E. G. Lee, M. D. Kim and D. Lee, "Effect of the Carrier Capture Process on the Photoluminescence Intensity and the Decay Time of Semiconductor Quantum Dots," 2006.

[153] L. Yang, S. G. Carter, A. S. Bracker, M. K. Yakes, ;. Mijin, K. ;. Chul, S. Kim and P. M. Vora, "Optical spectroscopy of site-controlled quantum dots in a Schottky diode," *Appl. Phys. Lett,* vol. 108, p. 233102, 2016.

[154] C. Schneider, T. Heindel, A. Huggenberger, P. Weinmann, C. Kistner, M. Kamp, S. Reitzenstein, S. Höfling and A. Forchel, "Single photon emission from a site-controlled quantum dot-micropillar cavity system," *Applied Physics Letters,* vol. 94, no. 11, p. 111111, 3 2009.

[155] R. P. Mirin, ;. K. L. Silverman, ;. D. H. Christensen, ;. A. Roshko,). K. L. Silverman, D. H. Christensen and A. Roshko, "Narrow photoluminescence linewidths from ensembles of self-assembled InGaAs quantum dots," *Journal of Vacuum Science & Technology B: Microelectronics and Nanometer Structures Processing, Measurement, and Phenomena,* vol. 18, no. 3, pp. 1510-1513, 5 2000.

[156] T. M. Burke, S. J. Brown, M. P. Smith, E. H. Linfield, D. A. Ritchie, M. Pepper, K. B. Tang, R. E. Palmer and J. H. Burroughes, "Hydrogen radical cleaning and low energy electron stimulated desorption of surface contaminants for MBE regrowth of GaAs," *Applied Surface Science,* Vols. 123-124, pp. 308-312, 1 1998.

[157] J. Wu, Q. Jiang, S. Chen, M. Tang, Y. I. Mazur, Y. Maidaniuk, M. Benamara, M. P. Semtsiv, W. T. Masselink, K. A. Sablon, G. J. Salamo and H. Liu, "Monolithically Integrated InAs/GaAs

Quantum Dot Mid-Infrared Photodetectors on Silicon Substrates," *ACS Photonics,* vol. 3, no. 5, pp. 749-753, 5 2016.

[158] A. J. Bennett, R. B. Patel, J. Skiba-Szymanska, C. A. Nicoll, I. Farrer, D. A. Ritchie and A. J. Shields, "Giant Stark effect in the emission of single semiconductor quantum dots," *Applied Physics Letters,* vol. 97, no. 3, p. 31104, 7 2010.

[159] B. Tongbram, A. Ahmad, S. Sengupta, A. Mandal, J. Singhal, A. Balgarkashi and S. Chakrabarti, "Optimization of InAs quantum dots through growth interruption on InAs/GaAs quantum dot heterostructure," *Journal of Luminescence,* vol. 192, pp. 89-97, 12 2017.

[160] U. W. Pohl, K. Pötschke, A. Schliwa, F. Guffarth, D. Bimberg, N. D. Zakharov, P. Werner, M. B. Lifshits, V. A. Shchukin and D. E. Jesson, "Evolution of a multimodal distribution of self-organized InAs/GaAs quantum dots," *Physical Review B - Condensed Matter and Materials Physics,* vol. 72, no. 24, 12 2005.

[161] A. Convertino, L. Cerri, G. Leo and S. Viticoli, "Growth interruption to tune the emission of InAs quantum dots embedded in InGaAs matrix in the long wavelength region," *Journal of Crystal Growth,* vol. 261, no. 4, pp. 458-465, 2 2004.

[162] N. Matsumura, T. Haga, S. Muto, Y. Nakata and N. Yokoyama, "Lattice deformation and interdiffusion of InAs quantum dots on GaAs(100)," *Journal of Applied Physics,* vol. 89, no. 1, pp. 160-164, 1 2001.

[163] Z. R. Wasilewski, S. Fafard and J. P. McCaffrey, "Size and shape engineering of vertically stacked self-assembled quantum dots," North-Holland, 1999.

[164] S. Fafard, Z. R. Wasilewski, C. Allen, D. Picard, M. Spanner, J. P. McCaffrey and P. G. Piva, "Manipulating the energy levels of semiconductor quantum dots," American Physical Society, 1999.

[165] G. Costantini, A. Rastelli, C. Manzano, P. Acosta-Diaz, R. Songmuang, G. Katsaros, O. G. Schmidt and K. Kern, "Interplay between thermodynamics and kinetics in the capping of InAs/GaAs(001) quantum dots," *Physical Review Letters,* vol. 96, no. 22, 2006.

[166] M. E. Ikpi, P. Atkinson, S. P. Bremner and D. A. Ritchie, "The growth of GaAs and InAs dots on etched mesas: The effect of substrate temperature on mesa profile and surface morphology on dot distribution," *Journal of Crystal Growth,* vol. 311, no. 15, pp. 3911-3917, 7 2009.

[167] R. Leon, Y. Kim, C. Jagadish, M. Gal, J. Zou and D. J. Cockayne, "Effects of interdiffusion on the luminescence of InGaAs/GaAs quantum dots," *Applied Physics Letters,* vol. 69, no. 13, pp. 1888-1890, 9 1996.

[168] J. Skiba-Szymanska, A. Jamil, I. Farrer, M. B. Ward, C. A. Nicoll, D. J. Ellis, J. P. Griffiths, D. Anderson, G. A. Jones, D. A. Ritchie and A. J. Shields, "Narrow emission linewidths of

positioned InAs quantum dots grown on pre-patterned," *Nanotechnology,* vol. 22, no. 6, p. 065302, 1 2011.

[169] J. Canet-Ferrer, G. Munoz-Matutano, J. Herranz, D. Rivas, B. Alen, Y. Gonzalez, D. Fuster, L. Gonzalez and J. Martínez-Pastor, "Exciton and multiexciton optical properties of single InAs/GaAs site-controlled quantum dots," *Applied Physics Letters,* vol. 103, no. 18, p. 183112, 10 2013.

[170] X. Huang, J. Yang, C. Song, M. Rao, Y. Yu and S. Yu, "Self-assembled InAs/GaAs single quantum dots with suppressed InGaAs wetting layer states and low excitonic fine structure splitting for quantum memory," *Nanophotonics,* vol. 11, no. 13, pp. 3093-3100, 8 2022.

[171] P. Wyborski, M. Gawełczyk, P. Podemski, P. A. Wroński, M. Pawlyta, S. Gorantla, F. Jabeen, S. Höfling and G. Sęk, "Impact of MBE-grown (In,Ga)As/GaAs metamorphic buffers on excitonic and optical properties of single quantum dots with single-photon emission tuned to the telecom range," *Physical Review Applied,* vol. 20, no. 4, p. 044009, 10 2023.

[172] M. Nakayama, K. Suyama and H. Nishimura, "Biexciton formation in GaAs/AlAs type-II superlattices under extremely low excitation powers," *Physical Review B,* vol. 51, no. 12, p. 7870, 3 1995.

[173] L. Seravalli, G. Trevisi, P. Frigeri, D. Rivas, G. Muñoz-Matutano, I. Suárez, B. Aĺn, J. Canet and J. P. Martínez-Pastor, "Single quantum dot emission at telecom wavelengths from metamorphic InAs/InGaAs nanostructures grown on GaAs substrates," *Applied Physics Letters,* vol. 98, no. 17, p. 173112, 4 2011.

[174] R. Seguin, A. Schliwa, S. Rodt, K. Potschke, U. W. Pohl and D. Bimberg, "Size-dependent fine-structure splitting in self-organized InAs/GaAs quantum dots," *Physical review letters,* vol. 95, no. 25, 12 2005.

[175] H. Kim, J. S. Kim and J. D. Song, "Temperature-Dependent Exciton Dynamics in a Single GaAs Quantum Ring and a Quantum Dot," *Nanomaterials,* vol. 12, no. 14, 7 2022.

[176] K. P. O'Donnell and X. Chen, "Temperature dependence of semiconductor band gaps," *Applied Physics Letters,* vol. 58, no. 25, pp. 2924-2926, 6 1991.

[177] L. A. Larsson, M. Larsson, E. S. Moskalenko and P. O. Holtz, "Temperature and magnetic field effects on the transport controlled charge state of a single quantum dot," *Nanoscale Research Letters,* vol. 5, no. 7, pp. 1150-1155, 5 2010.

[178] Y. P. Varshni, "Temperature dependence of the energy gap in semiconductors," *Physica,* vol. 34, no. 1, pp. 149-154, 1 1967.

[179] W. Ouerghui, A. Melliti, M. A. Maaref and J. Bloch, "Dependence on temperature of homogeneous broadening of InGaAs/InAs/GaAs quantum dot fundamental transitions," *Physica E: Low-dimensional Systems and Nanostructures,* vol. 28, no. 4, pp. 519-524, 9 2005.

[180] T. Tran, A. Muller, C. K. Shih, P. S. Wong, G. Balakrishnan, N. Nuntawong, J. Tatebayashi and D. L. Huffaker, "Single dot spectroscopy of site-controlled InAs quantum dots nucleated on GaAs nanopyramids," *Applied Physics Letters,* vol. 91, no. 13, p. 133104, 9 2007.

[181] E. Seļuk, A. Y. Silov and R. Nötzel, "Single InAs quantum dot arrays and directed self-organization on patterned GaAs (311)B substrates," *Applied Physics Letters,* vol. 94, no. 26, p. 263108, 6 2009.

[182] N. I. Cade, H. Gotoh, H. Kamada, H. Nakano, S. Anantathanasarn and R. Nötzel, "Optical characteristics of single InAs/InGaAsP/InP (100) quantum dots emitting at 1.55 µm," *Applied Physics Letters,* vol. 89, no. 18, p. 181113, 10 2006.

[183] J. Tommila, C. Strelow, A. Schramm, T. V. Hakkarainen, M. Dumitrescu, T. Kipp and M. Guina, "The influence of temperature on the photoluminescence properties of single InAs quantum dots grown on patterned GaAs," *Nanoscale Research Letters,* vol. 7, no. 1, pp. 1-4, 6 2012.

[184] V. Donchev, K. F. Karlsson, E. S. Moskalenko, P. O. Holtz, B. Monemar, W. V. Schoenfeld, J. M. Garcia and P. M. Petroff, "Temperature study of the photoluminescence of a single InAs/GaAs quantum dot," *physica status solidi (c),* vol. 1, no. 3, pp. 608-611, 2 2004.

[185] F. Bouchard, A. Sit, Y. Zhang, R. Fickler, F. M. Miatto, Y. Yao, F. Sciarrino and E. Karimi, "Two-photon interference: the Hong–Ou–Mandel effect," *Reports on Progress in Physics,* vol. 84, no. 1, p. 012402, 12 2020.

[186] J. Große, M. von Helversen, A. Koulas-Simos, M. Hermann and S. Reitzenstein, "Development of site-controlled quantum dot arrays acting as scalable sources of indistinguishable photons," *APL Photonics,* vol. 5, no. 9, 9 2020.

[187] X. Shang, S. Li, H. Liu, X. Su, H. Hao, D. Dai, X. Li, Y. Li, Y. Gao, X. Dou, H. Ni and Z. Niu, "Single- and Twin-Photons Emitted from Fiber-Coupled Quantum Dots in a Distributed Bragg Reflector Cavity," *Nanomaterials,* vol. 12, no. 7, 4 2022.

[188] H. Dartsch, C. Tessarek, T. Aschenbrenner, S. Figge, C. Kruse, M. Schowalter, A. Rosenauer and D. Hommel, "Electroluminescence from InGaN quantum dots in a fully monolithic GaN/AlInN cavity," *Journal of Crystal Growth,* vol. 320, no. 1, pp. 28-31, 4 2011.

[189] G. Fasching, K. Unterrainer, W. Brezna, J. Smoliner and G. Strasser, "Tracing deeply buried InAsGaAs quantum dots using atomic force microscopy and wet chemical etching," *Applied Physics Letters,* vol. 86, no. 6, pp. 1-3, 2 2005.

[190] F. Cappelluti, M. Gioannini and A. Khalili, "Impact of doping on InAs/GaAs quantum-dot solar cells: A numerical study on photovoltaic and photoluminescence behavior," *Solar Energy Materials and Solar Cells,* vol. 157, pp. 209-220, 12 2016.

[191] T. Takebe, M. Fujii, T. Yamamoto, K. Fujita and T. Watanabe, "Orientation-dependent Ga surface diffusion in molecular beam epitaxy of GaAs on GaAs patterned substrates," *Journal of Applied Physics,* vol. 81, no. 11, pp. 7273-7281, 6 1997.

[192] Y. Okada, T. Fujita and M. Kawabe, "Growth modes in atomic hydrogen-assisted molecular beam epitaxy of GaAs," *Applied Physics Letters,* vol. 67, no. 5, pp. 676-678, 7 1995.

[193] F. Cesura, S. Vichi, A. Tuktamyshev, S. Bietti, A. Fedorov, S. Sanguinetti, K. Iizuka and S. Tsukamoto, "Droplet Free Self-Assembling of High Density Nanoholes on Gaas(100) Via Thermal Drilling".

[194] J. Tersoff, "Kinetic surface segregation and the evolution of nanostructures," *Applied Physics Letters,* vol. 83, no. 2, pp. 353-355, 7 2003.

[195] E. M. Sala, Y. I. Na, M. Godsland and J. Heffernan, "Self-assembled InAs QDs on InGaAsP/InP(100) by modified droplet epitaxy in MOVPE around the telecom C-band for quantum photonic applications," *physica status solidi (RRL) – Rapid Research Letters,* 9 2023.

[196] E. M. Sala, M. Godsland, A. Trapalis and J. Heffernan, "Effect of Cap Thickness on InAs/InP Quantum Dots Grown by Droplet Epitaxy in Metal–Organic Vapor Phase Epitaxy," *Physica Status Solidi - Rapid Research Letters,* vol. 15, no. 9, 9 2021.

[197] L. Hansen, F. Bensing and A. Waag, "InAs quantum dots embedded in silicon," *Thin Solid Films,* vol. 367, no. 1-2, pp. 85-88, 5 2000.

[198] S. V. Balakirev, M. S. Solodovnik and O. A. Ageev, "Hybrid Analytical–Monte Carlo Model of In/GaAs(001) Droplet Epitaxy: Theory and Experiment," *Physica Status Solidi (B) Basic Research,* vol. 255, no. 4, 4 2018.

10 Appendix

A.M.U (NEGATIVE)		A.M.U (POSITIVE)	
1	H	18,19	H_2O
16	O	24	C_2^-
17	OH^-	25	C_2H^-
27-30	Si	27	CN^-
23	Na^+	39	K^+
85	GaO^-	40	Ca^+
87	GaO^-	101	GaO_2^-
91	AsO^-	103	GaO_2^-
10-60	Hydrocarbons	107	AsO_2^-

Appendix A – A list of ions, fragments and charged species in the SIMS spectrum for negative mode and positive mode.

10 Appendix
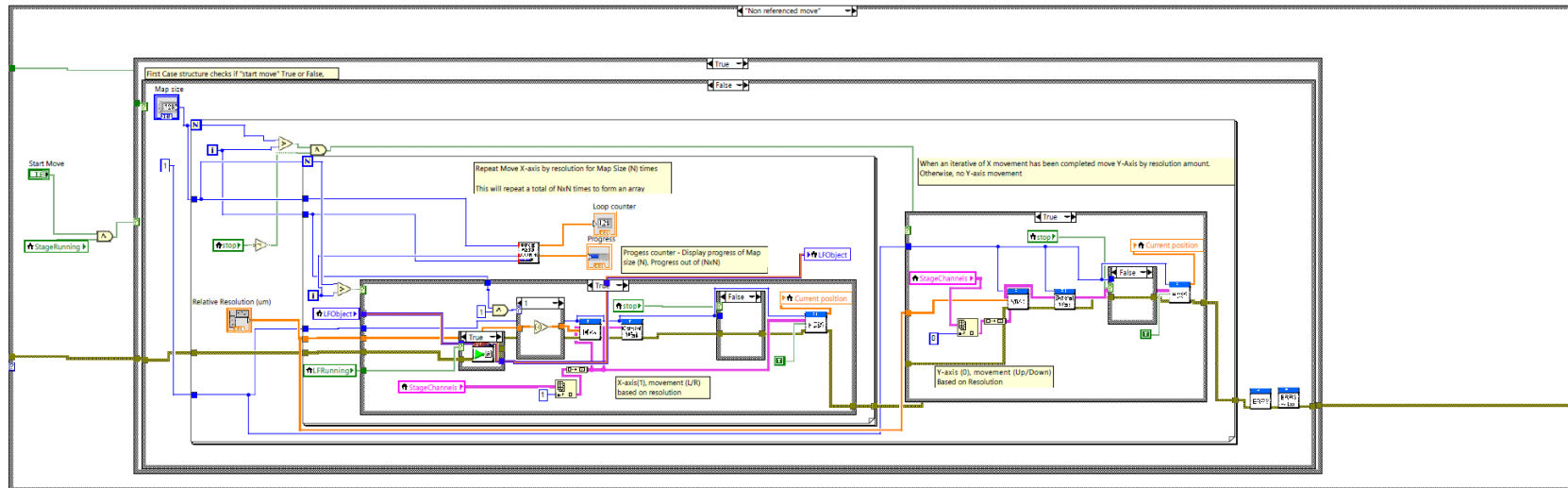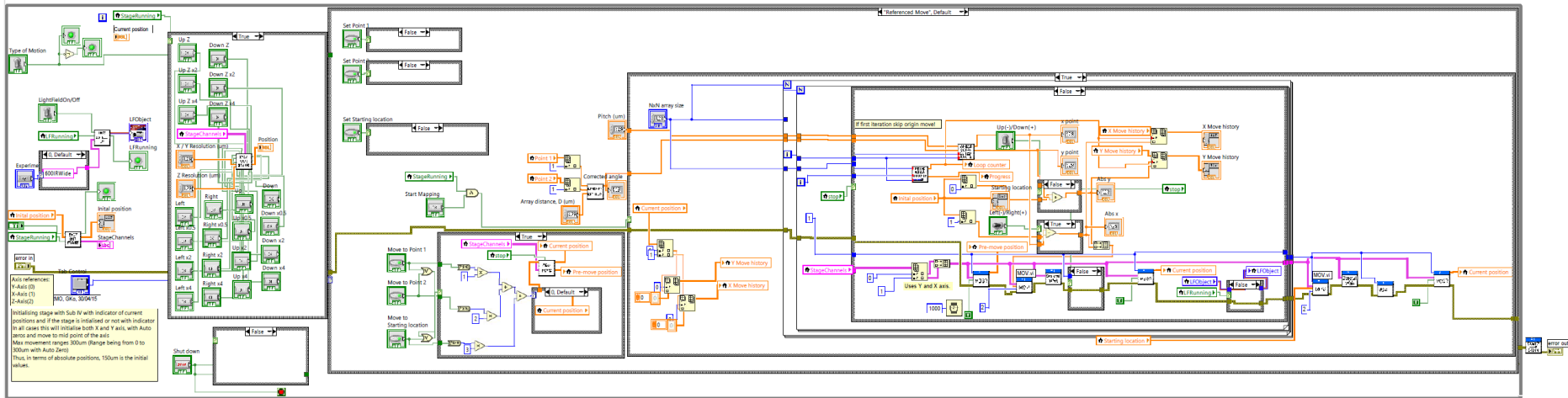
Appendix B – LabVIEW, object orientation programming solution, code used for nano-position program, with reference and non-reference automated moments. This is the backend of the program developed to allow for automated movement, PL acquisition and QD mapping. For open access to the code: https://github.com/ChakLamChan/uPL_Nanopositioner

Effects of Rapid Thermal Annealing on Telecom C-band InAs Quantum Dots on InP (100) Grown by Droplet Epitaxy

Chak Lam Chan[1*], Elisa Maddalena Sala[1,2], Edmund Clarke[1,2], Jon Heffernan[1,2]

[1]Department of Electronic and Electrical Engineering, The University of Sheffield, North Campus, Broad Lane, Sheffield, S3 7HQ, UK

[2]EPSRC National Epitaxy Facility, Department of Electronic and Electrical Engineering, The University of Sheffield, North Campus, Broad Lane, Sheffield, S3 7HQ, UK

*corresponding author

E-mail: clchan3@sheffield.ac.uk

Abstract

We demonstrate the effects of rapid thermal annealing (RTA) on emission from telecom C-band InAs/InP (100) quantum dots (QDs) grown by droplet epitaxy in Metal-Organic Vapour Phase Epitaxy (MOVPE). Room temperature photoluminescence (RT-PL) from the QD ensemble shows a tuned emission wavelength through the C-band and O-band while improving the emission intensity by ~4.5 times at an annealing temperature of 770°C. A blueshift of the QD emission up to 430 nm has been achieved. Low-temperature micro-photoluminescence (LT-µPL) demonstrates single QD emission from the annealed samples with an improvement in linewidth of up to 30%

1. Introduction

III-V quantum dots (QDs) play an important role in the active region of various devices for quantum technology applications, such as single photon emitters [1], entangled photon generation [2] and quantum relays [3]. Epitaxial QDs are usually fabricated by Stranski-Krastanov (SK) growth mode, [4] [5] but there may be limitations imposed on the growth conditions due to the lattice mismatch between substrate and epilayer [6] [7]. Droplet epitaxy (DE) is an alternative growth method which is more versatile compared to SK and allows for more flexibility in material choice and nanostructure fabrication [8]. Most importantly, highly symmetric QDs can be obtained using DE, showing reduced fine structure splitting (FSS) and longer coherence times [6] [7] [9]. Thus, QDs grown by the DE method are promising candidates as high-quality single-photon emitters [8] [10] [11] [12].

Altering the structure of the QDs using post-growth techniques can be used to obtain QDs with more favourable optical properties for photonics applications. For example, as-grown QDs may show a spectral distribution longer than the targeted wavelengths – in our case, the important telecoms C-band and O-band. The use of post-growth

methods, such as ion implantation [13], electric fields [13], and optical stark effect [14], have all been shown to control the QDs emission brightness [12], wavelength [15], and FSS [16]. Rapid thermal annealing (RTA) is a well-known technique that has been shown to improve the structural and optical properties of self-assembled QDs. [15] [17] [18] For instance, thermal treatments have been shown to remove defects and allow interdiffusion mechanisms to take place, resulting in shifted emission wavelengths [19], brightness enhancement [15] and reduction in the inhomogeneously-broadened linewidth of emission from the QD ensemble [20].

In this study, we investigate the effects of RTA on the optical properties of C-band emitting InAs/InP (100) QDs grown by DE in MOVPE. When annealed up to 800°C, a large room temperature photoluminescence (RT-PL) blueshift of 430 nm is observed, and the associated ensemble linewidth narrows by 15% (~50 meV). We also report on single-dot spectroscopy measured using low-temperature (5 K) micro-PL (LT-µPL), where a blueshift of single QD emission toward 1300 nm is observed, and single-dot linewidths showed an improvement by up to 30% (~20 µeV).

2. Methods

Samples were grown on epi-ready InP(001) in a closed-coupled showerhead (CCS) MOVPE reactor, using H_2 as carrier gas. No pre-treatment was used on the samples prior to growth. Indium droplets were deposited on a 300 nm InP buffer grown at 620°C. Droplets were deposited at 320°C and then crystallised into InAs QDs under an AsH3 flow while ramping the temperature to 520°C. The conditions used for QD growth were previously optimised to achieve high-quality InAs QDs showing low-temperature single-dot emission at wavelengths around 1550 nm [21] [22]. After droplet crystallisation into InAs QDs, an InP capping layer of 20 nm was deposited at the same crystallisation temperature of 520°C. A further 80 nm InP was grown at 620°C to bury the QDs entirely. We refer to our previous works for additional information on the growth sequence [21] [22]. Such QDs are grown from metallic droplets, however they will be strained after complete crystallisation and burying process with InP. A set of 5×5 mm^2 samples was annealed with the use of proximity capping between 650°C and 850°C (including an unannealed as-grown sample for reference), where sacrificial InP substrate was used to prevent the outdiffusion of group V atoms. [15] Another set of samples was capped with 100 nm SiO2 (40 nm/min) by plasma-enhanced chemical vapour deposition (PECVD) to protect the surface during RTA. After dielectric capping, the samples were cleaved into 5 x 5 mm^2 pieces before being annealed at temperatures ranging from 750°C to 800°C for 30 seconds including another reference sample (as-grown) which was SiO$_2$ capped but not annealed. For both set of experiments, samples were taken from locations on the wafer in close proximity to each other, to ensure the annealing affects would be comparable. The samples were cleaved into 5 x 5 mm^2 pieces before being annealed at temperatures ranging from 750°C to 800°C for 30 seconds. The samples were placed into two different PL setups for RT-PL and LT-µPL. For RT-PL, the samples were measured using an Accent RPM2000 PL mapper, with excitation from a 656 nm diode laser with the PL dispersed by a 150 g/mm grating and detected with a Hamamatsu G9208 InGaAs detector with an extended response up to 2200 nm. Next, the same QD samples were investigated by LT-µPL at 5K. For µPL, the samples were excited via a fibre-coupled 635 nm red diode laser at approximately 4.5 Wcm^{-2} with a Princeton Instruments SP2750 spectrometer and 600 lines/mm grating and a cooled PyLoN IR InGaAs detector. The response of the InGaAs detector on the LT-µPL system is limited to 1600

nm, so single QD emission at longer wavelengths may not be detected.

3. Results and discussions

3.1 Room temperature photoluminescence

Figure 1 shows the RT-PL spectra obtained from samples annealed at different temperatures with either proximity capping or SiO_2 capping. With proximity capping, we do not observe a blueshift of ensemble emission or significant changes in PL intensity up to an annealing temperature of 850°C as a results of lack of interdifussions between InAs QD and adjacent InP layers. While the ensemble does not shift under annealing, minor changes to the individual peaks of the ensemble are still observed, suggesting a gradual degradation of the sample or outdiffusion of indium atoms, which could impact the carrier dynamics. With the use of SiO_2 capping, the PL intensity doubles starting at 750°C to a maximum increase in PL intensity of ~4.5 times at 770°C when compared to as-grown. Subsequent annealing temperatures give no further improvement in PL intensity. This is consistent with previous reports of an increase of ~3 times in PL intensity from InAs/InP QDs with annealing when compared to an as-grown sample [23]. The PL intensity increase can be attributed to an annealing-

induced reduction in defects and other non-radiative recombination centres [24] [25] [26]. Increasing the annealing temperature above 770°C results in the degradation of the material quality, causing the generation of unwanted dislocations and outdiffusion of indium atoms [17] [23] [27]. We also observe a general narrowing of the ensemble PL FWHM with increasing annealing temperature, as shown in Figure 2, with the lowest FWHM of 329 meV (770°C), compared to 378 meV (as-grown). The FWHM of the as-grown ensemble is large but comparable with that observed by other groups for InAs/InP QDs emitting at these wavelengths [29][30]. Modified growth conditions that blueshift the QD emission towards 1550 nm, such as indium-flush [30] or growth on InGaAs interlayers [31][32], yield QD ensembles with narrower FHWM but we would still expect annealing to result in a further reduction in FWHM for QDs grown using these techniques. For RTA, the narrowing of FWHM is linked to the changing of the QD shape and compositions, as demonstrated by other groups [23] [28] [33]. This is made possible with the use of SiO_2 layers, which have previously been demonstrated to allow for promotion to impurity-free vacancy disordering, an additional mechanism assisting indium and group-V outdiffusion [30]. This results in the blueshift of
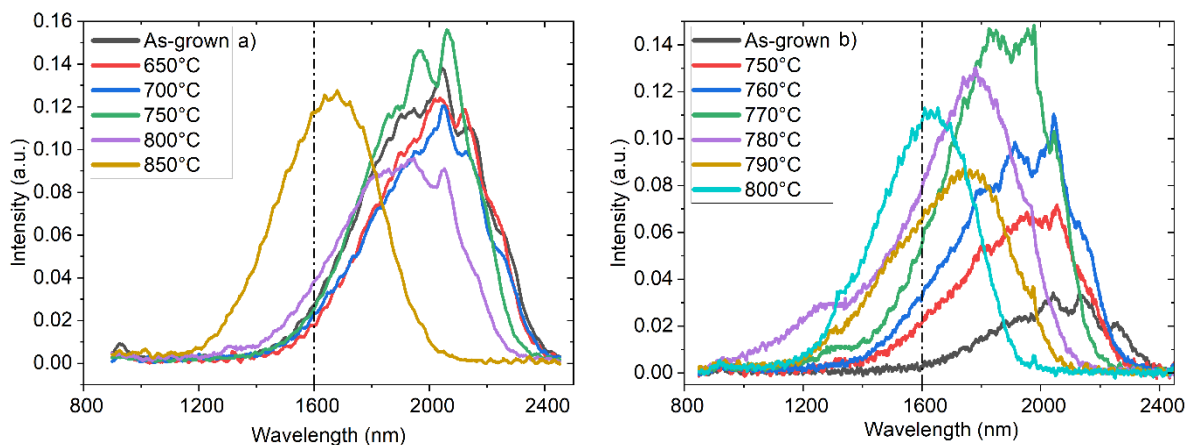

Figure 1 Room temperature PL for a) proximity cap between annealing temperature 650°C to 850°C compared with as-grown, b) SiO₂ cap with annealing temperature 750°C to 800°C compared with as-grown. Dot-Dash line indicating the µPL detector's cut-off.
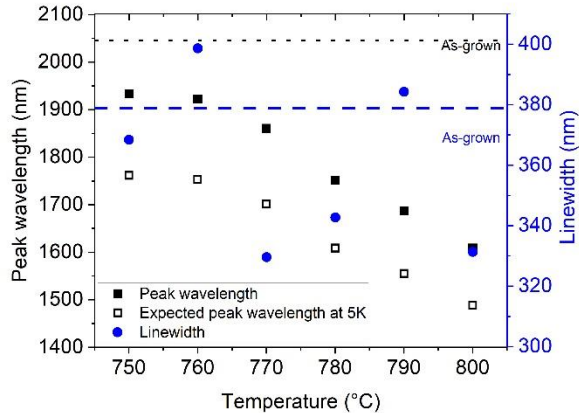
Figure 2 Gaussian fitted analysis of annealing temperature against peak wavelength (solid squares) and linewidth (circles), with the dashed lines showing as-grown comparisons for SiO₂ capped sample. The expected peak wavelength of the ensemble at 5K, according to the Varshni relation, is also included (open squares) [34].

emission from compositional changes in the QDs due to intermixing as well as narrowing of the ensemble linewidth due to the increase in QD size and uniformity of the QD ensemble [33]. We also observe the formation of microcracks during high-temperature annealing [23]. The disappearance of individual peaks across the ensemble could also be attributed to the degradation of the sample and linked to the outdiffusion of indium atoms from the structure into the SiO₂ layer.

The peak wavelength emissions can be controlled by varying the annealing temperature, as summarised in Figure 2. Comparing the different capping methods used, we observed a change in annealing temperature by 50°C before blueshifting occurred. One known cause is the significant difference in thermal expansion coefficients between SiO₂ ($\sim 0.52 \times 10$-6 °C^{-1}) and InP ($\sim 4.6 \times 10$-6 °C^{-1}). This causes compressive stress at the interface region during annealing, which will allow for group-V intermixing more readily [35]. This mechanism is in contrast with InAs/GaAs QDs structures where such interaction is between In/Ga atoms instead [19] [36] [37]. The

effect of indium and group-V outdiffusion is also a common mechanism alongside intermixing of As/P atoms across the interfaces of InAs QDs and InP barriers [28] [33]. This results in the largest blueshift of 430 nm, which is observed with an annealing temperature of 800°C with SiO₂ capping. The improvement in optical properties is attributed to the change in the capping method, which allows vacancies to form when outdiffusion of indium and group-V atoms [23] while also protecting the surface from excessive surface degradation [17]. Repeating the same annealing experiement on different regions of the same produce comparable PL results. As such, we ascribe such effects to the use of different capping methods. With promising results from RT-PL, single dot spectrum of the SiO₂ capped sample was measured using LT-µPL to understand the effects RTA has on single dot emissions.
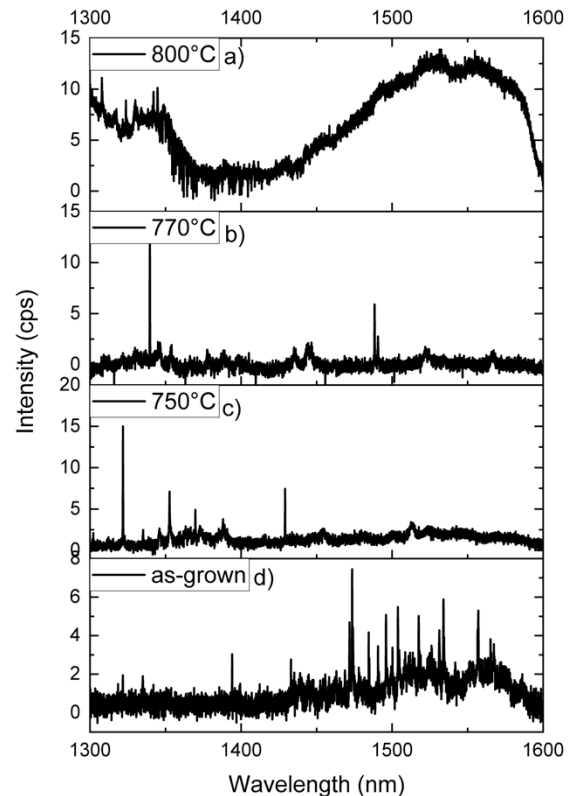

Figure 3 µPL single dot spectra of SiO₂ capped samples at 5K for a) 800°C, b) 770°C, c) 750°C, d) as-grown.

3.2 Low temperature micro-photoluminescence

The RT-PL measurements presented in Figure 1 allow us to identify the wavelength range of the whole ensemble. Still, when considering the portion of the ensemble visible by LT-µPL (5K), this is limited by the detection range (1300 nm to 1600 nm). We expect an average emission blueshift of ~150 nm for the QD ensemble between room temperature and 5 K following the Varshni relation, shown in Figure 2 [38]. Annealing the samples blueshifts the ensemble emission towards the detection range of the LT-µPL so the spectrums obtained from the as-grown sample are from QDs at the short-wavelength edge of the ensemble. The sample annealed at 780°C would best represent the peak ensemble range of QDs, which has improved linewidth distribution when compared to the as-grown sample, the short-wavelength edge. Similarly, at higher annealing temperatures,

emissions originating from the long-wavelength edge of the QD distribution have comparable linewidths to the peak of the ensemble for the as-grown sample.

Figure 3 shows examples of µPL spectra of SiO2 capped samples annealed at (a) 800°C, (b) 770°C, (c) 750°C and (d) as-grown. In the as-grown sample, a high density of sharp emissions from single quantum dots is seen alongside background noise. The background noise observed is possibly caused by significant charge noise, leading to emission broadening and coalescence of emission peaks [39]. At 750°C, the background noise is quenched, most likely due to a reduction of defects after annealing. Blueshifting of sharp dot-like emissions is observed after annealing, emitting around 1300 nm. The density of dot-like emissions has decreased, but there is no evidence of emission broadening. At 770°C, we observe the most significant improvement in linewidth while

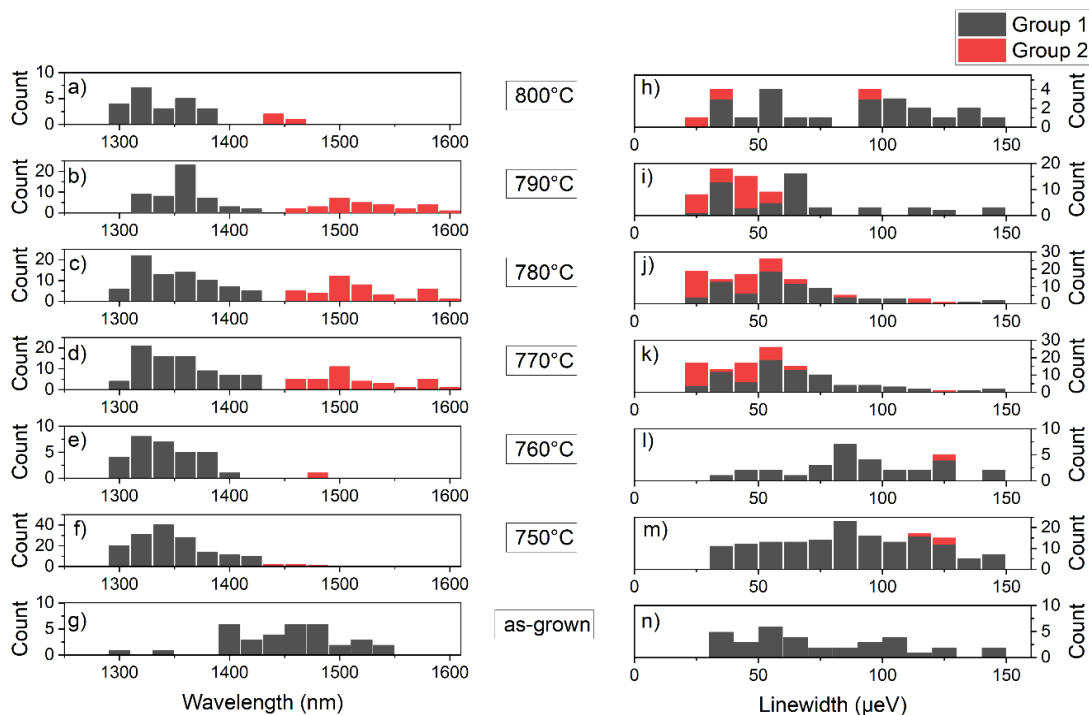**Figure 4** Histogram analysis of multiple single dot emissions of SiO₂ capped sample at 5K for wavelength distribution of a) 800°C, b) 790°C, c) 780°C, d) 770°C, e) 760°C, f) 750°C, g) as-grown, and linewidth distribution of h) 800°C, i) 790°C, j) 780°C, k) 770°C, l) 760°C, m) 750°C, n) as-grown. Single dot emissions are further split QD emissions below 1425nm (Black/Group1), above 1425nm (Red/Group2).

maintaining dot-like sharp emissions and a significant reduction in background noise. At 800°C, background noise reappears, which extends across the entire range with the atmosphere absorption range from 1350 nm to 1450 nm. We believe factors such as microcrack formation cause the observed increase in background noise at high annealing temperatures. This is also consistent with the observed reduction in integrated PL intensity shown in Figure 1 [23]. Between 750°C and 770°C, bright, narrow emission lines from single QDs can be detected in the range 1300 to 1500 nm. To statistically analyse the distribution of single dot-like emissions, multiple single spectra were obtained at each annealing temperature [38].

Figure 4a-g shows a comparison of sharp dot-like emissions between annealed and as-grown QDs. As-grown single spectra show good emission between 1400 nm to 1550 nm, with comparable results when multiple locations across the sample are measured. With increasing annealing temperature, we observe additional dot-like emission between 1400 nm and our short-wavelength measurement limit of 1300 nm. By comparison, with the room temperature ensemble PL shown in Figure 1 and the expected peak ensemble wavelength at the low temperature shown in Figure 2, the QD distribution shown in Figure 4 matches the expected wavelengths according to Varshni's relation. For the annealed samples, the blueshift will shift the short-wavelength side of the ensemble below 1300 nm at low temperature, allowing observation of single QD emission between 1300 and 1400 nm in our µ-PL measurements. With increasing annealing temperature, we may obtain a blueshift of the emission beyond the short-wavelength limit of our measurements at 1300 nm from an increased number of QDs in the distribution due to the outdiffusion of indium from the QDs. It is surprising that we do not observe single QD

emission >1500 nm for the samples annealed at 750 and 760°C. This may be due to statistical variations in the spectra, as we observe QD emission >1500 nm for samples annealed at higher temperatures, and the room temperature PL suggests that the QDs observed in µPL are on the short-wavelength side of the QD distribution for all samples. QD emission around 1400 nm may be suppressed by atmospheric absorption, with fewer emission lines from the QDs being above the noise floor of the detector and resulting in an apparent bimodal wavelength distribution in the data presented in Figure 4. The sudden formation of bimodal distribution on a single-dot level is currently still unknown. This could be the linked to the disappearance of individual peaks observed in Figure 1, where the high temperature used may have caused outdiffusion of indium atoms from the QDs, affecting the QD morphology and thus the carrier dynamics [40].

To understand how RTA affected single QD properties and its relationship between emission shifting and linewidth, we define two groups of emission lines in the spectra from the annealed samples: Group 1 is defined as dot emissions below 1425 nm corresponding to QDs whose emission has been blueshifted to wavelengths shorter than the emission from the as-grown sample, while Group 2 is emissions above 1425 nm, corresponding to QDs whose emission will also have been blueshifted due to annealing but are emitting at wavelengths comparable to the as-grown sample. Figure 4h-n shows the linewidth distribution for single QD emission as a function of different annealing temperatures. Below 770°C, the linewidths are comparable to those obtained from the as-grown sample. For annealing temperature of 770°C and above, we observe an improvement in the linewidth distributions, with the lowest linewidth of 22.0 µeV (790°C), close to the detector spectral resolution of 20.9 µeV. An increase in the number of emission

lines with large linewidth for the sample annealed at 800 ℃ is consistent with material degradation, that may also contribute to the increased background emission observed for this sample. We do not observe a significant difference in the linewidths of emission lines from QDs in Groups 1 and 2, where low linewidth QDs are maintained across the wavelength range. This demonstrates that the improvement to linewidth is not dependent on emission wavelength and demonstrates that the use of RTA can be beneficial for improving the QD linewidth for samples targeting either the O-band or the C-band.

4. Conclusion

In conclusion, we have examined the impact of RTA on telecom InAs QDs on InP grown by droplet epitaxy in MOVPE. By varying the annealing temperature above 750°C, a controllable blueshift of the QD ensemble emission up to 430 nm under RT-PL conditions is observed. RTA also increases the integrated intensity and decreases the PL linewidth. In μPL, the emission of the QDs can be blueshifted to the O-band. At annealing temperatures of 770°C and above, we achieved an improvement of 30% (~20 μeV) in single QD emission linewidth. Control of the annealing temperature gives the ability to adjust the emission wavelength and reduce the emission linewidth from single dots, enhancing the potential of InAs/InP DE QDs embedded in quantum devices.

Acknowledgements

References

[1]   P. Michler, A. Kiraz, C. Becher, W. V. Schoenfeld, P. M. Petroff, L. Zhang, E. Hu and A. Imamoğlu, *Science,* vol. 290, no. 5500, pp. 2282-2285, 12 2000.

[2]   R. M. Stevenson, R. J. Young, P. Atkinson, K. Cooper, D. A. Ritchie and A. J. Shields, *Nature 2006 439:7073,* vol. 439, no. 7073, pp. 179-182, 1 2006.

[3]   J. Huwer, R. M. Stevenson, J. Skiba-Szymanska, M. B. Ward, A. J. Shields, M. Felle, I. Farrer, D. A. Ritchie and R. V. Penty, *Physical Review Applied,* vol. 8, no. 2, p. 024007, 8 2017.

[4]   L. Goldstein, F. Glas, J. Y. Marzin, M. N. Charasse and G. Le Roux, *Applied Physics Letters,* vol. 47, no. 10, pp. 1099-1101, 11 1985.

[5]   D. J. Eaglesham and M. Cerullo, *Physical Review Letters,* vol. 64, no. 16, p. 1943, 4 1990.

[6]   M. Anderson, T. Müller, J. Skiba-Szymanska, A. B. Krysa, J. Huwer, R. M. Stevenson, J. Heffernan, D. A. Ritchie and A. J. Shields, *Applied Physics Letters,* vol. 118, no. 1, 1 2021.

[7]   J. Skiba-Szymanska, R. M. Stevenson, C. Varnava, M. Felle, J. Huwer, T. Müller, A. J. Bennett, J. P. Lee, I. Farrer, A. B. Krysa, P. Spencer, L. E. Goff, D. A. Ritchie, J. Heffernan and A. J. Shields, *Physical Review Applied,* vol. 8, no. 1, 7 2017.

[8]   M. Gurioli, Z. Wang, A. Rastelli, T. Kuroda and S. Sanguinetti, *Nature Materials,* vol. 18, no. 8, pp. 799-810, 8 2019.

[9]   T. Müller, J. Skiba-Szymanska, A. B. Krysa, J. Huwer, M. Felle, M. Anderson, R. M. Stevenson, J. Heffernan, D. A. Ritchie and A. J. Shields, *Nature Communications,* vol. 9, no. 1, 12 2018.

[10]   R. S. R. Gajjela, E. M. Sala, J. Heffernan and P. M. Koenraad, *ACS Applied Nano Materials,* vol. 5, no. 6, pp. 8070-8079, 6 2022.

[11]   E. M. Sala, Y. I. Na, M. Godsland and J. Heffernan, Phys. Status Solidi RRL, 18: 2300340, 2024.

[12]   C. L. Phillips, A. J. Brash, M. Godsland, N. J. Martin, A. Foster, A. Tomlinson, R. Dost, N. Babazadeh, E. M. Sala, L. Wilson, J. Heffernan, M. S. Skolnick and A. M. Fox, *Scientific Reports 2024 14:1,* vol. 14, no. 1, pp. 1-9, 2 2024.

[13] C. Dion, P. Desjardins, M. Chicoine, F. Schiettekatte, P. J. Poole and S. Raymond, *Nanotechnology,* vol. 18, no. 1, 1 2007.

[14] M. E. Reimer, M. Korkusiński, D. Dalacu, J. Lefebvre, J. Lapointe, P. J. Poole, G. C. Aers, W. R. McKinnon, P. Hawrylak and R. L. Williams, *Physical Review B - Condensed Matter and Materials Physics,* vol. 78, no. 19, 11 2008.

[15] A. Muller, W. Fang, J. Lawall and G. S. Solomon, *Physical Review Letters,* vol. 103, no. 21, 11 2009.

[16] A. Babiński, J. Jasiński, R. Bozek, A. Szepielow and J. M. Baranowski, *Applied Physics Letters,* vol. 79, no. 16, pp. 2576-2578, 10 2001.

[17] J. D. Plumhof, R. Trotta, A. Rastelli and O. G. Schmidt, *Nanoscale Research Letters,* vol. 7, p. 336, 2012.

[18] W. Chaâbani, A. Melliti, M. A. Maaref, C. Testelin and A. Lemaître, *Physica B: Condensed Matter,* vol. 493, pp. 53-57, 7 2016.

[19] J. M. García, G. Medeiros-Ribeiro, K. Schmidt, T. Ngo, J. L. Feng, A. Lorke, J. Kotthaus and P. M. Petroff, *Applied Physics Letters,* vol. 71, no. 14, pp. 2014-2016, 10 1997.

[20] T. Yang, J. Tatebayashi, K. Aoki, M. Nishioka and Y. Arakawa, *Applied Physics Letters,* vol. 90, no. 11, 2007.

[21] S. J. Xu, X. C. Wang, S. J. Chua, C. H. Wang, W. J. Fan, J. Jiang and X. G. Xie, *Applied Physics Letters,* vol. 72, no. 25, pp. 3335-3337, 1998.

[22] E. M. Sala, M. Godsland, A. Trapalis and J. Heffernan, *Physica Status Solidi - Rapid Research Letters,* vol. 15, no. 9, 9 2021.

[23] E. M. Sala, Y. I. Na, M. Godsland, A. Trapalis and J. Heffernan, *Physica Status Solidi - Rapid Research Letters,* vol. 14, no. 8, 8 2020.

[24] C. K. Chia, S. J. Chua, S. Tripathy and J. R. Dong, *Applied Physics Letters,* vol. 86, no. 5, pp. 1-3, 1 2005.

[25] J. W. L. Sakai and P. C. Morais, *Solid State Communications,* vol. 120, no. 2-3, pp. 89-93, 2001.

[26] W. H. Jiang, H. Z. Xu, B. Xu, X. L. Ye, J. Wu, D. Ding, J. B. Liang and Z. G. Wang, *Journal of Crystal Growth,* vol. 212, pp. 356-359, 2000.

[27] E. G. Lee, M. D. Kim and D. Lee, *Journal of the Korean Physical Society,* vol. 48, no. 6, pp. 1228-1232, 2006.

[28] S. Malik, C. Roberts, R. Murray and M. Pate, *Applied Physics Letters,* vol. 71, no. 14, pp. 1987-1989, 10 1997.

[29] S. Hasan, O. Richard, C. Merckling and W. Vandervorst, *Journal of Crystal Growth*, vol. 557, no. 126010, 2021.

[30] X. Yu, H. Jia, C. Dear, J. Yuan, H. Deng, M. Tang and H. Liu, *Journal of Physics D: Applied Physics*, vol. 56, no. 285101, 2023.

[31] K. Park, P. Moon, E. Ahn. S. Hong, E. Yoon, J. W. Yoon, H. Cheong and J.-P. Leburton, *Applied Physics Letters*, vol. 86, no. 223110, 2005.

[32] E. M. Sala, M. Godsland, Y. I. Na, A. Trapalis and J. Heffernan, *Nanotechnology* **33** 065601, 2022

[33] C. Dion, P. Desjardins, N. Shtinkov, F. Schiettekatte, P. J. Poole and S. Raymond, *Journal of Applied Physics,* vol. 103, no. 8, 2008.

[34] Y. P. Varshni, *Physica,* vol. 34, no. 1, pp. 149-154, 1 1967.

[35] J. F. Girard, C. Dion, P. Desjardins, C. Nì Allen, P. J. Poole and S. Raymond, *Applied Physics Letters,* vol. 84, no. 17, pp. 3382-3384, 4 2004.

[36] S. Barik, L. Fu, H. H. Tan and C. Jagadish, *Applied Physics Letters,* vol. 90, no. 24, 2007.

[37] A. O. Kosogov, P. Werner, U. Gösele, N. N. Ledentsov, D. Bimberg, V. M. Ustinov, A. Y. Egorov, A. E. Zhukov, P. S. Kop'ev, N. A. Bert and Z. I. Alferov, *Applied Physics Letters,* vol. 69, no. 20, pp. 3072-3074, 11 1996.

[38] T. M. Hsu, Y. S. Lan, W. H. Chang, N. T. Yeh and J. I. Chyi, *Applied Physics Letters,* vol. 76, no. 6, pp. 691-693, 2 2000.

[39] T. Xiaohong, Y. Zongyou, T. Jinghua, D. Anyan and C. Mee Koy, *IEEE Transactions on Nanotechnology,* vol. 7, no. 4, pp. 422-426, 7 2008.

[40] W. Lei, Y. H. Chen, Y. L. Wang, B. Xu, X. L. Ye, Y. P. Zeng and Z. G. Wang, *Journal of Crystal Growth,* vol. 284, no. 1-2, pp. 20-27, 10 2005.

[41]   N. A. Jahan, C. Hermannstädter, J.H. Huh, H. Sasakura, T. J. Rotter, P. Ahirwar, G. Balakrishnan, K. Akahane, M. Sasaki, H. Kumano and I. Suemune, *Journal of Applied Physics,* vol. vol. 113, no. 033506, 2013.